

MODELING, OPTIMIZATION AND CONTROL OF HYBRID
POWERTRAINS

LUCA DE PASCALI



Modeling of vehicle hybrid power-trains and design of optimal control strategies
for energy management

Doctoral School in Materials, Mechatronics and Systems Engineering
Department of Industrial Engineering
University of Trento

Luca De Pascali: *Modeling, optimization and control of hybrid powertrains*,
Modeling of vehicle hybrid power-trains and design of optimal control
strategies for energy management, © August 2019

SUPERVISORS:
Francesco Biral
Enrico Bertolazzi

LOCATION:
Trento

ABSTRACT

To cope with the increasing demand of a more sustainable mobility, the main Original Equipment Manufacturers are producing vehicles equipped with hybrid propulsion systems that increase the overall vehicle efficiency and mitigate the emission problem at a local level. The newly gained degrees of freedom of the hybrid powertrain need to be handled by advanced energy management techniques that allow to fully exploit the system capabilities.

In this thesis we propose an optimal control approach to the solution of the energy management problem, putting emphasis on the importance of accurate models for the reliability of the optimization solution.

In the first part of the thesis we address the energy management problem for a hybrid electric vehicle, including the mitigation of the battery aging mechanisms. We show that, with an optimal management strategy, we could extend the battery life up to 25% for some driving cycles while keeping the fuel savings performance substantially unaltered.

In the second part of the thesis we focus on the hydrostatic hybrid transmission, a different hybridization solution that is able to fulfill the high power demand of heavy duty off-highway vehicles. Also in this case, we formulate the energy management problem as an optimal control problem, dealing with the complexity introduced by the discrete valve actuations in the framework of mixed-integer optimal control. We show that, using hydraulic accumulators to recover energy from the regenerative braking, we could reduce fuel consumption up to 13% for a typical driving cycle.

In the third and last part of the thesis we show how the optimization approach can be used to systematically design and calibrate control algorithms, casting the calibration problem into a Linear Matrix Inequality. We first develop a non-overshooting closed-loop control for the actuation pressure of a wet clutch, proving the effectiveness of the control on an experimental setup.

Finally, we focus on the design of a dead-zone based kinematic observer for the estimation of the lateral velocity of a road vehicle. The structure of the observer presents good noise rejection performance, allowing for the selection of a higher observer gain that improves the estimation accuracy.

PUBLICATIONS

- [1] M. Cocetti, S. Donnarumma, L. De Pascali, M. Ragni, F. Biral, F. Panizzolo, P.P. Rinaldi, A. Sassaro, and L. Zaccarian. "Hybrid non-overshooting set-point pressure regulation for a wet clutch." In: *IEEE/ASME transactions on mechatronics* (2019), to appear.
- [2] L. De Pascali, F. Biral, and S. Onori. "Development and validation of a temperature dependent electrochemical battery model for gr/NMC lithium cells." In: *IEEE/ASME transactions on vehicular technology* (submitted), to appear.
- [3] L. De Pascali, M. Cocetti, F. Biral, A. Palazzetti, F. Panizzolo, P.P. Rinaldi, A. Sassaro, and L. Zaccarian. "LMI-based non-overshooting pressure control design for a wet clutch." In: *Control Applications (CCA), 2016 IEEE Conference on*. IEEE. 2016, pp. 329–334.
- [4] L. De Pascali, M. Cocetti, S. Tarbouriech, L. Zaccarian, and F. Biral. "A kinematic observer with adaptive dead-zone for vehicles lateral velocity estimation." In: *Advanced Motion Control (AMC), 2018 IEEE International Workshop on*. IEEE. 2018.
- [5] L. De Pascali, F. Biral, M.G. Bort, and L. Serrao. "Fuel Economy Off-Line Optimization Strategies of Hydraulic Hybrid Vehicle Modeled with Continuous and Discrete Controls." In: *Journal of Dynamic Systems, Measurement and Control* (submitted), to appear.
- [6] G. Valenti, L. De Pascali, and F. Biral. "Estimation of longitudinal speed profile of car drivers via bio-inspired mirroring mechanism." In: *2018 21st International Conference on Intelligent Transportation Systems (ITSC)*. IEEE. 2018, pp. 2140–2147.

*To the optimist, the glass is half full.
To the pessimist the glass is half empty.
To the engineer, the glass is twice as big as it needs to be.*

— Unknown

ACKNOWLEDGMENTS

I would like to thank my advisors Francesco Biral and Enrico Bertolazzi, for supporting me throughout these three challenging years. I owe Francesco a lot of what I became from both the scientific and personal point of view. His esteem and trust in my work gave me the confidence in pursuing my own path and his guidance always led my research in the right direction. Thanks to Enrico, for the many precious advices and for giving me the tools for completing my research. Thanks to Luca Zaccarian, his genuine passion for his job is, and always will be, a source of inspiration. Thanks to Daniele Bortoluzzi for his valuable teaching advices, and thanks also for having accepted to be part of the committee.

I am grateful to Matteo Corno and Roberto Lot for thoroughly reviewing my thesis and for having accepted to be part of the committee, their advices allowed to greatly improve the quality of my work.

Thanks to Simona Onori for giving me the chance to work at CU-ICAR on battery modeling and optimization projects and for her valuable feedbacks on my research work.

I would like to express my sincere gratitude to Luca Poggio and Elena Ligabue from Ferrari, that funded the last year of my PhD. They gave me the great opportunity to work in their team on the study of the battery for the *SF90 Stradale*. The massive amount of data I had access to allowed me to achieve in this thesis exceptional results that would have been otherwise impossible to attain. A special thanks also to the hybrid team in Ferrari: thanks to Irene Donà, Matteo Tassinari, Angelica Di Cola, Filippo Dragonas, Simone Pelloni and Andrea Luongo just to cite some, for their support and for the fun moments together.

Thanks to Dana Mechatronics Technology Center (DMTC), for funding part of my Ph.D. on the challenging problem of the energy management of the hydrostatic hybrid transmission. Having the possibility to use the experimental data from the prototype vehicle greatly increased the value of the results presented in this thesis. Thanks to Luca Balboni and Lorenzo Serrao for the guidance on such a demanding project, I am happy and grateful to be their colleague now.

Thanks to Dana Rexroth Transmission Systems (DRTS), in particular thanks to Pier Paolo Rinaldi and Alex Sassaro, for the challenging project on the non-overshooting control of the wet clutch. I grew up a lot working with you and you taught me the importance of the teamwork.

Thanks to Maserati, in particular to Paolo Lombardi and Plinio Mascarucci for giving me the chance to work on the optimization of fuel savings strategies for an electric hybrid car.

Thanks to all the friends I met in Greenville: Sana, Jasprit, Harikesh, Disha, Dyuti, Hesam, Roberto, Sunny, Umberto, Gabriele, Simone, Francesco and Zifan. I now have a pal in every part of the world.

Thanks to Matteo Cocetti, Mirko Brentari and Matteo Ragni for their sincere friendship. I could not have hoped for better friends to spend these years of PhD with, I admire them both as professionals and as persons. The enriching conversations and the time spent with these three guys are among the most precious moments of this journey.

My gratitude goes also to all my friends and loved ones: thanks to my hike and climb companions Lorenzo and Gianluigi, thanks to Marilina and Gianfranco for always finding a seat at their table for me, thanks to the open-space fellows and thanks also to the students that followed my lectures.

I would like thank my parents, Clara and Claudio, for their constant support and for teaching me the importance of always finding happiness in everything I do. Thanks to my sister Elena and my brother Nicola, for always standing by me when I needed them.

In the end, I cannot say enough thanks to Chiara, who has always been by my side, even when I was on the other side of the ocean, even when I was more in the office than at home. She is the most supportive and empathic person I know, and most of my achievements would not have been possible without her love.

CONTENTS

1	INTRODUCTION	1
1.1	Motivations and objectives	1
1.2	Introduction to hybrid vehicles	3
1.2.1	Series Hybrid	4
1.2.2	Parallel Hybrid	4
1.2.3	Power-split hybrid	5
1.3	The optimal control problem	7
1.3.1	Optimal control formulation	7
1.3.2	Discretization schemes for optimal control	10
I	THE HYBRID ELECTRIC TRANSMISSION	
2	BATTERY DYNAMICS AND AGING MODEL	19
2.1	The Electrochemical Model	22
2.1.1	Model Development	22
2.1.2	Model Parametrization	33
2.1.3	Conclusions	41
2.2	The Degradation Model	42
2.2.1	Aging Mechanisms	42
2.2.2	Calendar Aging	50
2.2.3	Cycle-induced Aging	53
2.2.4	Conclusions	62
Appendix of Chapter 2		71
2.A	Model parameters	71
2.B	Cycle aging dataset	73
3	OPTIMAL ENERGY MANAGEMENT STRATEGIES	79
3.1	Power-train Architecture Model	81
3.1.1	Driving cycle and longitudinal dynamics	82
3.1.2	Engine	84
3.1.3	Motor	85
3.1.4	Battery System	86
3.2	Battery life-aware energy management	90
3.2.1	Problem formulation	91
3.2.2	Solution method	92
3.2.3	Simulation results	93
3.3	Towards a run-time optimization	103
3.3.1	MPC problem formulation	103
3.3.2	Real-time solution of the optimal control problem	104

3.4	Conclusions	106
Appendix of Chapter 3		
3.A	Battery model parameters	113
3.B	Simulations result figures	115
II THE HYBRID HYDROSTATIC TRANSMISSION		
4	HYDROSTATIC TRANSMISSION MODEL	119
4.1	Model Design	121
4.1.1	Hydrostatic sub-system	122
4.1.2	Hydraulic accumulator sub-systems	125
4.1.3	Power Boost hub sub-system	126
4.1.4	Mechanical powertrain and longitudinal dynamics	128
4.2	Model Validation	130
4.2.1	Experimental setup	130
4.2.2	Performance assessment	130
5	MIXED INTEGER OPTIMAL CONTROL SOLUTION	135
5.1	Problem Formulation	136
5.1.1	Mixed-Integer Optimal Control	136
5.1.2	Regularized functions	137
5.1.3	Outer convexification and relaxation	138
5.2	Solution to Optimal Control Problem	139
5.2.1	Direct full discretization method	139
5.2.2	Sum-Up rounding	139
5.2.3	Multi-time switching penalty	140
5.3	Optimization Results	140
5.4	Conclusions	145
Appendix of Chapter 3		
5.A	List of Symbols	151
III OPTIMIZATION OF THE CONTROLLER PARAMETERS		
6	PRESSURE CONTROL OF A WET CLUTCH	155
6.1	Introduction	155
6.2	Experiment description and goals	156
6.3	Plant model and identification	157
6.3.1	Model selection	157
6.3.2	Identification of the output nonlinearity	158
6.3.3	Model identification	159
6.4	Control synthesis	161
6.4.1	LMI-based observer design	162
6.4.2	LMI-based state feedback design	164
6.5	Gains selection and experiments	169

6.5.1	Gain selection	169
6.5.2	Experimental validation of the control scheme	171
6.6	Conclusion	172
7	VEHICLE LATERAL VELOCITY ESTIMATION	175
7.1	Introduction	175
7.2	Vehicle models	177
7.2.1	Double track model	177
7.2.2	Kinematic model	177
7.3	Kinematic observer	178
7.3.1	A yaw-rate dependent kinematic observer	178
7.3.2	The effect of input/output noise	179
7.4	Dead-zone based kinematic observers	180
7.4.1	Overview on dead-zone observers	180
7.4.2	Yaw-rate dependent dead-zone observer	182
7.4.3	LMI-based optimization	185
7.5	Simulation results	186
7.6	Conclusions	188
8	CONCLUSIONS	195
8.1	Energy management of an electric hybrid vehicle	195
8.2	Mixed-integer optimal control of a hydrostatic power-train	196
8.3	Optimization for the design of the controller	197

LIST OF FIGURES

Figure 1.1	Topology of series hybrid. Solid black line: mechanical bus. Dashed turquoise line: electrical bus. Arrows: power flow direction. 4
Figure 1.2	Topologies of parallel hybrid. Solid black line: mechanical bus. Dashed turquoise line: electrical bus. Arrows: power flow direction. 5
Figure 1.3	Topology of power-split hybrid. Solid black line: mechanical bus. Dashed turquoise line: electrical bus. Arrows: power flow direction. 7
Figure 2.1	Schematic diagram of the cell section. 22
Figure 2.2	PDE solution of the stoichiometry at the anode and at the cathode (green dash-dot line) compared with our proposed realization (gray solid line) and with the controller canonical form (black dashed line). 31
Figure 2.3	Block diagram illustrating the input (current) and output (terminal voltage) relation. 32
Figure 2.4	Open Circuit Voltage (OCV) measured at different temperatures (circles). The calibrated model is represented by the solid line. 34
Figure 2.5	Experimental cell resistance and model prediction (surfaces). 36
Figure 2.6	Sketch of the MBH algorithm on a “funnel-like” function. 38
Figure 2.7	Comparison between experimental voltage and model prediction over pulse dataset. 39
Figure 2.8	Comparison between measured and predicted voltage for a current profile required for nine laps of the Fiorano track. 40
Figure 2.9	Comparison between measured and predicted voltage for a current profile required for one lap of the Nürburgring track. 41
Figure 2.10	SEI layer representation. 43
Figure 2.11	Open circuit potential at anode-side as a function of SOC. 45
Figure 2.12	Stress factor for capacity loss due to SEI formation. 46

- Figure 2.13 View of the anode overhang for a single layer of the cell. 47
- Figure 2.14 Measured residual capacity of the calendar aging tests. 50
- Figure 2.15 Comparison between measured calendar loss and model prediction. 52
- Figure 2.16 Residual capacity for each current profile. The markers indicate the capacity measured at the RPT and the solid lines are used to better visualize the trends. 57
- Figure 2.17 Stress factors of the cycle-induced aging in logarithmic scale. 60
- Figure 2.18 Comparison between model prediction and experimental cycle-induced aging. 61
- Figure 2.19 Cycle-induced aging model: contribution of the three aging terms. 62
- Figure 2.B.1 Voltage, SOC, current and temperature of the highway (**AS**) cycle. 73
- Figure 2.B.2 Voltage, SOC, current and temperature of the high speed (**AV**) cycle. 74
- Figure 2.B.3 Voltage, SOC, current and temperature of the combined (**C**) cycle. 74
- Figure 2.B.4 Voltage, SOC, current and temperature of the electric drive (**E-drive**) cycle. 75
- Figure 2.B.5 Voltage, SOC, current and temperature of the Fiorano (**FI**) cycle. 75
- Figure 2.B.6 Voltage, SOC, current and temperature of the hill (**NB**) cycle. 76
- Figure 2.B.7 Voltage, SOC, current and temperature of the free-way (**NV**) cycle. 76
- Figure 2.B.8 Voltage, SOC, current and temperature of the sustaining (**S**) cycle. 77
- Figure 2.B.9 Voltage, SOC, current and temperature of the Urban (**U**) cycle. 77
- Figure 3.1 Architecture of the pre-transmission parallel-hybrid power-train configuration (P1) under investigation. 82
- Figure 3.2 Engine fuel consumption rate in kg/h (blue solid lines) and torque limits (red dashed lines). 84
- Figure 3.3 Motor efficiency and power maps. 85
- Figure 3.4 Actual motor power computed for each element of the efficiency map from (3.4). 86

Figure 3.5	Optimal power split of the hybrid transmission.	94
Figure 3.6	Cell current, SOC and voltage.	95
Figure 3.7	Electric machine utilization.	96
Figure 3.8	Comparison of the battery SOC for different values of the Pareto coefficient α .	97
Figure 3.9	Comparison of the battery energy throughput for different values of the Pareto coefficient α .	98
Figure 3.10	Comparison of the SOC-weighted current throughput for different values of the Pareto coefficient α .	100
Figure 3.11	Pareto curves for the four concatenated driving cycles.	101
Figure 3.12	Comparison between SOC evolutions with $\alpha = 1$ during WLTC cycle using different horizon lengths.	106
Figure 3.B.1	Driving cycles considered in this work.	116
Figure 4.1	Dana Spicer [®] PowerBoost [®] driveline.	121
Figure 4.2	Scheme of the transmission in hydrostatic mode. The check valves CV_a and CV_b regulate the flow from the charge pump C, while RV_a and RV_b are the two relief valves.	122
Figure 4.3	Conceptual scheme of the PowerBoost Hub that connects the accumulators to the lines.	127
Figure 4.4	Architecture of the driveline.	129
Figure 4.5	Tele-boom handler used for experimental campaign.	131
Figure 4.6	Test track at Dana's facility in Arco, TN - Italy.	131
Figure 4.7	Comparison between measured and estimated pressure.	132
Figure 5.1	Engine working points in the two working modes.	142
Figure 5.2	Speed, power and optimal gear selection in hybrid mode.	143
Figure 5.3	Pumps and motor displacements in hybrid mode.	144
Figure 5.4	Lines and accumulators pressures in hybrid mode.	146
Figure 6.1	Time delay between the commanded step current and the pressure response.	157
Figure 6.2	Interpolation of the steady-state pairs (top) and residuals (bottom) normalized on the maximum pressure p_{\max} .	158
Figure 6.3	Validation of the identified model.	160
Figure 6.4	Block diagram of the proposed control algorithm consisting of the nonlinearity inversion φ^{-1} , an observer and a state feedback.	162

Figure 6.5	Trade-off curve between α and γ for the observer gain selection, based on construction (6.12), (6.13) applied to the identified transfer function. 164
Figure 6.6	Region of the complex plane where the closed-loop poles are confined in the design optimization. 165
Figure 6.7	Simulated step responses of the state-feedback loop (no observer) with the selections of Table 6.1. The bold curve corresponds to the experimental gains. 170
Figure 6.8	Simulation of the step responses in the three considered scenarios: state feedback (red), output feedback without delay (blue) and output feedback with delay (green). 171
Figure 6.9	Experimental closed loop response. 172
Figure 6.10	Comparison between the measure and the estimate of the state x_1 . 172
Figure 7.1	Comparison between the simulated (dashed line) and the estimated lateral velocity with the kinematic observer (green solid line) and the dead-zone observer (red solid line) during a step-like steering maneuver on the double track model, see Subsection 7.2.1. 187
Figure 7.2	Dead-zone “tube” overlapped to the output injection term (top) and filtering action of the dead-zone (bottom). 188

LIST OF TABLES

Table 1.1	List of parallel hybrid configurations. 6
Table 2.1	Calendar aging parameters. 51
Table 2.2	Cycle-induced aging parameters P with $T_{\text{ref}} = 298.15\text{ K}$ and $I_{\text{ref}} = 1\text{ C}$ (26 A). 59
Table 2.A.1	List of parameters of the gr/NMC 26.2Ah 3.8V Proto B cell. 71
Table 2.A.2	List of temperature dependent parameters of the gr/NMC 26.2Ah 3.8V Proto B cell. 72
Table 2.A.3	List of cell model variables. 73

Table 3.1	Hybrid vehicle parameters. 83
Table 3.2	Willan's coefficients 84
Table 3.3	Fuel savings with optimal energy management control of the hybrid electric vehicle. 96
Table 3.4	Fuel savings comparison for different values of the Pareto coefficient α . Savings are referred to the fuel consumption with only ICE. 99
Table 3.5	Reduction of the capacity degradation for $\alpha < 1$. 99
Table 3.6	Comparison of the fuel savings obtained using different horizon lengths of the WLTC cycle. Percentage relative to the ICE-only power-train consumption. 105
Table 3.7	Comparison of the battery aging obtained using different horizon lengths of the WLTC cycle. Percentage relative to the full horizon solution with $\alpha = 1$. 105
Table 3.A.1	List of parameters of the gr/NMC 2.0Ah 3.2V cell. 113
Table 3.A.2	List of temperature dependent parameters of the gr/NMC 2.0Ah 3.2V cell. 114
Table 4.1	Valves configuration in the PowerBoost Hub. When $HP_i, LP_i = 0$ the corresponding valve is closed, when $HP_i, LP_i = 1$ the corresponding valve is open, with $i = \{a, b\}$. 128
Table 4.2	Transmission ratios. 129
Table 4.3	Parameters longitudinal dynamics. 130
Table 5.A.1	List of States and Controls of the Optimal Control Problem. 151
Table 5.A.2	List of Parameters. Subscripts p, m ₁ , m ₂ refer to pump, motor 1 and motor 2. Subscripts hp, lp refer to high and low pressure accumulators respectively. 152
Table 6.1	Values resulting from the optimization discussed in Remark 2 and corresponding color in the curves of Figure 6.7. 168
Table 7.1	Parameter α and performance indicator for the sinusoidal steering test on the non-linear model. 187

INTRODUCTION

1.1 MOTIVATIONS AND OBJECTIVES

Mobility has always been a central part of people's life and has played a crucial role in the course of human progress. Despite recent problems with overcapacity and low profitability, which led to the automotive sector crisis of 2008-2010, the automotive industry retains a strong influence on the economy worldwide. Over 4 million people are employed directly by the OEMs (Original Equipment Manufacturers) and many more are indirectly involved.

Approximately 21% of carbon dioxide (CO₂), the main greenhouse gas, emissions in 2016 are attributable to road-vehicles, 15% of which owing to light-vehicles — cars and vans — and 6% to heavy-duty vehicle — trucks, buses and coaches [7]. This amount increases if we include also non-road vehicles, mainly in agricultural and construction equipment; a study of the International Council on Clean Transportation (ICCT) reports that almost 25% of the fine particulate matter and 15% of the NO_x emitted from mobile sources are produced by off-highway vehicles, mainly because of the milder emission-control regulations compared to the heavy-duty sector, although the vehicles share many similarities in the design the powertrain and in the exhaust emission control technologies [12]. The *global* effects of greenhouse gas emissions on global warming add to the *local* effect of noxious emissions in densely populated area, where high concentration of road and non-road vehicles endangers the health of the people and the quality of their life. Therefore, one of the major challenges of our time is the shift towards a more sustainable mobility; this is reflected by more restrictive regulations, both at a global level (more restrictive standard on car emissions and fuel consumptions) and at a local level (traffic block in the most polluted cities).

To cope with the increasing demand of a more sustainable mobility, all OEMs are producing car models with an electric propulsion system that is able to provide part (*Hybrid Electric Vehicles - HEV*) — or the totality (*Battery Electric Vehicles - BEV*) — of the required tractive effort. While this solution mitigates the emission problem at a *local* level, freeing the large urban area from the noxious emissions, many unsolved issues remain on the global scale: first, the *well-to-wheel* emissions remain substantially unaltered, because most of the electrical energy is still produced in

fossil fuel power plants; second, a capillary infrastructure of high power charging stations has to be built; finally, the most impelling challenge is the production, optimization and recycling of the energy storage unit, that, in the vast majority of the applications, is the lithium ion battery. All these points are influenced by political initiatives, such as large investments in renewable energies and infrastructures, and the global energy storage market will grow to reach 620 billion dollars in investments by 2040 as predicted by Bloomberg New Energy Finance (BNEF) [1].

The OEMs are then committed to offer an increasing number of HEV/BEV vehicles, able on one side to fulfill the emission regulations and on the other side to meet various customer concerns in terms of reliability (driving range, low maintenance, etc.), cost and performance. To deal with these ambitious challenges, OEM and Tier 1 suppliers have been developing increasingly complex hybrid powertrain systems.

Advanced control techniques are thus necessary to govern the newly gained degrees of freedom, in order to maximize the overall efficiency and reduce usage costs. The main objective of this thesis is to show, by means of several application examples, that the optimal control approach to the energy management problem can dramatically improve the efficiency of the hybrid powertrain by exploiting to the best its architecture. The optimal energy management strategy is computed starting from the mathematical model of the powertrain: this means that the more descriptive the powertrain model is, the more reliable the optimal control solution becomes. For this reason, in this work we put great emphasis on the systematic formulation and validation of mathematical models for the different powertrain components, that have to capture the behavior of the systems throughout a wide range of operating conditions.

Following this guideline, we study in Chapter 3 the problem of minimizing fuel consumptions in a Hybrid Electric Vehicle, including the mitigation of the of the battery aging mechanisms; this optimization problem is based on the thorough analysis and experimental validation of the battery electrochemical model of Chapter 2, that represents precisely the charge/discharge battery dynamics as well as the aging mechanisms under different temperatures, states-of-charge and current profiles.

Electrification is not the only solution to reduce carbon emissions and fuel consumption, especially in those applications where high power density is required. This is the case of heavy duty and off-highway vehicles, such as the telescopic-boom handler introduced in Chapter 4, where a hydrostatic transmission decouples the internal combustion engine from the wheel and the energy is recovered with a system of hydraulic accumulators connected to the hydrostatic transmission with an electronically actuated valve block. Compared to the battery, the

hydraulic accumulator is much cheaper, more robust and can withstand frequent peaks of power in a smaller volume, but has limited energy. The hydraulic powertrain has many degrees of freedom that have to be suitably controlled to reach the best fuel economy result. To this end, in Chapter 5 we address the energy management problem in the framework of optimal control, focusing on the hybrid dynamics — i.e. exhibiting both discrete (valves/clutches) and continuous (motor/pump displacements) dynamics — of the system.

We will finally see in Part iii how the optimization approach can be used not only to draw high level control trajectories, but also to systematically design and calibrate control algorithms. Indeed, once the control structure is defined, the calibration problem can be cast into a Linear Matrix Inequality [6] that is easily solved using standard off-the-shelf algorithms. This powerful tool is used first in Chapter 6 to design a non-overshooting control for the smooth engagement of a wet clutch, then it is used in Chapter 7 to calibrate a non-linear observer for the estimation of the vehicle lateral speed.

In the reminder of this first chapter we give in Section 1.2 an overview of the main hybrid powertrain architectures, discussing the advantages and disadvantages of each solution; moreover, in Section 1.3 we introduce the optimal control problem, starting from its general formulation and briefly detailing the solution approach adopted throughout this thesis.

1.2 INTRODUCTION TO HYBRID VEHICLES

In this section we give an overview of the three main hybrid powertrain architectures:

- **Series Hybrid:** the electric branch of the powertrain serves as prime mover so that the ICE can be fully decoupled from the wheels;
- **Parallel Hybrid:** the electric machine and the ICE are both mechanically coupled to the wheels;
- **Power-split Hybrid:** thanks to the power-split device, the planetary gear, the powertrain combines series and parallel operations.

The best selection among the three different configurations depends on several aspects, such as cost, complexity, weight and type of application. In the following we describe the three architectures for battery-powered electric hybrid vehicles, but the same considerations can be made also for other types of hybridization (e.g. hydrostatic hybrid).

1.2.1 Series Hybrid

The simplest hybrid architecture is the series hybrid configuration represented in Figure 1.1. The electric machine is directly connected to the wheel and serves as prime mover. This allows to decouple the wheels from the combustion engine, that operates as an auxiliary generator producing electrical power through an electrical generator to recharge the battery or to boost the primary electric motor. The electric machine has high efficiency over a wide speed range, therefore a mechanical transmission is usually not required, reducing the cost and the complexity of the powertrain. Since the electric motor is the prime mover, it should

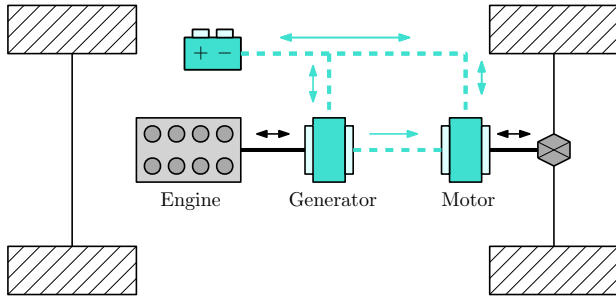


Figure 1.1: Topology of series hybrid. Solid black line: mechanical bus. Dashed turquoise line: electrical bus. Arrows: power flow direction.

be selected large enough to provide all the tractive effort required at the wheel; on the contrary, having the engine completely disconnected from the wheels, there is great freedom in choosing its load and speed to reach the highest possible efficiency. The main drawback of the series hybrid is the double energy conversion from mechanical to electrical in the generator and from electrical to mechanical in the electric motor; this introduces additional power losses when a direct connection between the engine and the wheels would be more efficient, e.g. at high speed.

1.2.2 Parallel Hybrid

In the parallel hybrid architecture, the wheels are mechanically connected both to the electric motor and to the engine. The power summation is thus mechanical rather than electrical as in the series case. As illustrated in Figure 1.2, there is only an electric machine that serves both as motor and generator, thus reducing the overall number of components resulting in a more cost effective solution. The common parallel architectures can be

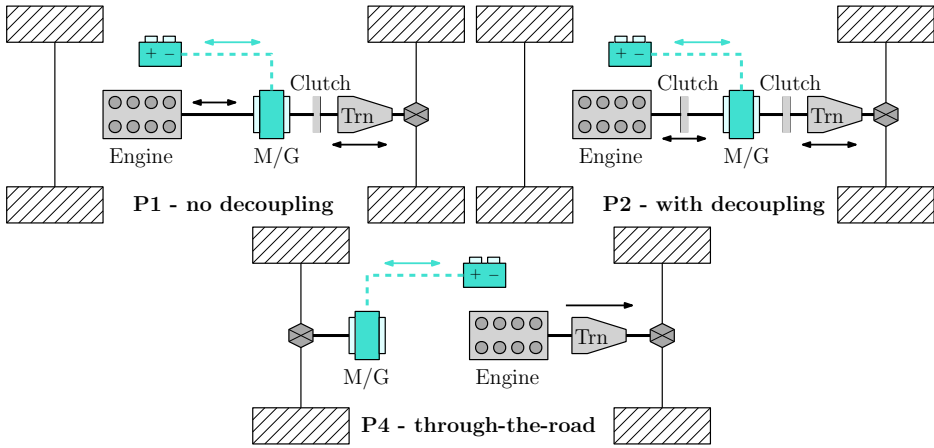


Figure 1.2: Topologies of parallel hybrid. Solid black line: mechanical bus. Dashed turquoise line: electrical bus. Arrows: power flow direction.

classified depending on the position of the electric machine with respect to the engine, as listed in Table 1.1. Since only one energy conversion is performed from electrical to mechanical (and vice-versa) in the electric motor, the parallel hybrid is potentially more efficient than the series configuration, and the direct connection of the engine to the wheels improves the efficiency at high speed. On the other side, the engine speed cannot be chosen as freely as in the previous case, deteriorating the performance in certain drive conditions. Moreover, the electric motor of the parallel hybrid drivetrain is usually less powerful compared to its series counterpart, unless significantly oversized, thus limiting the potential for high power operations and regenerative braking.

1.2.3 Power-split hybrid

The power-split hybrid configuration combines the features of the series and parallel architectures by means of a power-split device, usually a planetary gear set. As shown in Figure 1.3 the power-split configuration requires two electric machines, one (MG1) that works as a generator and the other (MG2) as a motor. The ring (R) of the planetary gear set is directly connected to the wheels and to the electric motor unit (MG2), therefore the vehicle speed is determined by the speed of MG2. The generator unit MG1 is connected to the sun (S) of the planetary gear, while the engine is connected to the carrier (C). This configuration

Configuration	Description
P0	The electric machine is connected to the engine through a belt on the front end accessory drive.
P1	The electric machine is connected directly to the engine crankshaft through a spur gear.
P2	Same as P1, but the electric machine can be disconnected from the engine with a clutch, allowing for pure electric drive.
P3	The electric machine is connected through a gearbox inside the transmission and its speed can be decoupled from the ICE speed.
P4	The electric machine is connected to the secondary shaft. Also called <i>through-the-road hybrid</i> .

Table 1.1: List of parallel hybrid configurations.

allows to vary the speed of the engine independently from the vehicle speed by controlling the speed of the electric machines, and for this reason is called *electrical continuous variable transmission (E-CVT)*. Part of the engine power is transmitted directly to the ring gear and thus to the wheels as in the parallel hybrid configuration; the remaining part of the mechanical power is transformed in electric power in the generator MG1 and stored in the battery or supplied to the motor MG2. This twice energy conversion is the source of the low efficiency of the variator, therefore the power-split architecture should be designed to minimize the power throughput over the electrical variator [9].

In conclusion, series hybrid architectures are usually the best option for vehicles traveling at low speed or for applications where the engine is small compared to the primary motor and serves solely as a *range extender* to improve the autonomy of the hybrid vehicle. The power-split architecture, thanks to the E-CVT and to the more sophisticated control techniques, surpasses parallel configurations in fuel economy and driving smoothness, without significantly increasing the mechanical complexity of the powertrain. Nevertheless, as stated in [10], parallel hybrid powertrains are still the best choice in vehicles that require good performance, higher maximum speed and towing capability.

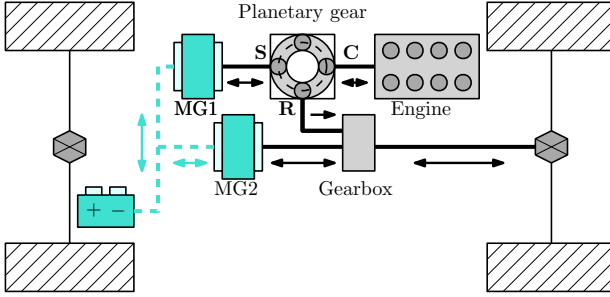


Figure 1.3: Topology of power-split hybrid. Solid black line: mechanical bus. Dashed turquoise line: electrical bus. Arrows: power flow direction.

1.3 THE OPTIMAL CONTROL PROBLEM

The main purpose of the activities presented in this thesis is the definition of control laws that lead to the desired behavior of a dynamical system within the bounds of the imposed constraints. The desired behavior is described by the minimization (or maximization) of a functional that represents an economic, energy, or time cost.

In this brief introduction to optimal control we detail the direct methods to the optimal control problem, a collection of techniques used to solve the optimization problems treated in this thesis.

1.3.1 Optimal control formulation

We focus in this chapter on the optimal control solution for continuous-time non-linear systems, whose evolution over time is described by a set of non-linear ordinary differential equations (ODE)

$$\begin{aligned} \dot{\mathbf{x}}(t) &= \mathbf{f}(\mathbf{x}(t), \mathbf{u}(t)), \quad \forall t \in [t_0, t_f] \\ \mathbf{x}(t_0) &= \mathbf{x}_0. \end{aligned} \quad (1.1)$$

The system evolves over the finite time horizon $t \in [t_0, t_f] \subset \mathbb{R}$ and starts at the initial time t_0 with initial state \mathbf{x}_0 . $\mathbf{x} : [t_0, t_f] \rightarrow \mathbb{R}^{N_x}$ is the continuous-valued state vector, $\mathbf{u} : [t_0, t_f] \rightarrow \mathbb{R}^{N_u}$ is the continuous-valued control vector and the vector field $\mathbf{f} : \{\mathbb{R}^{N_x} \times \mathbb{R}^{N_u}\} \rightarrow \mathbb{R}^{N_x}$ is the vector field that describes the dynamics of the system.

We impose some regularity conditions on the dynamics vector field $\mathbf{f}(\cdot)$ and on the admissible control $\mathbf{u}(\cdot)$ in order to guarantee *well-posedness* of the system, meaning that there exists a unique solution $\mathbf{x}(\cdot)$ to (1.1) for every choice of the initial state \mathbf{x}_0 and every admissible control

$\mathbf{u}(\cdot)$. First, we assume that $\mathbf{u}(\cdot)$ is *piecewise-continuous*, namely that it has only a finite number of discontinuities on every bounded interval and is limited from the right and from the left at each of these discontinuities. Second, we say that $\mathbf{x}(\cdot)$ is *absolutely continuous*, that means that $\mathbf{x}(\cdot)$ is continuous everywhere, continuously differentiable almost everywhere¹ and satisfies

$$\mathbf{x}(t) = \mathbf{x}(t_0) + \int_{t_0}^t \mathbf{f}(\mathbf{x}(\tau), \mathbf{u}(\tau)) \, d\tau.$$

Finally, to enforce uniqueness of the solution we assume that $\mathbf{f}(\cdot, \mathbf{u}(t))$ is *Lipschitz continuous* w.r.t. $\mathbf{x}(\cdot)$, that means that there exists a Lipschitz constant $0 \leq L_z \leq \infty$ such that

$$\begin{aligned} \|\mathbf{f}(\mathbf{x}_1, \mathbf{u}(t)) - \mathbf{f}(\mathbf{x}_2, \mathbf{u}(t))\| &\leq L_z \cdot \|\mathbf{x}_1 - \mathbf{x}_2\|, \\ \forall \mathbf{x}_1, \mathbf{x}_2 \in \mathbb{R}^{N_x}, \forall \mathbf{u}(t) \in \mathbb{R}^{N_u}, \forall t \in [t_0, t_f] \end{aligned}$$

In the setting of optimal control we seek for a functions in the infinite-dimensional state and control spaces that minimizes a given cost functional, which is defined in its most general form as the *Bolza functional*

$$J = m(\mathbf{x}(t_f)) + \int_{t_0}^{t_f} \ell(\mathbf{x}(t), \mathbf{u}(t)) \, dt \quad (1.2)$$

that comprises both the integral — or *Lagrange* — functional and the terminal — or *Mayer* — functional.

The solution of the optimal control problem must fulfill a set of constraints both on the states and on the control, that are expressed as

$$\begin{aligned} \mathbf{x}(\cdot) &\in \mathcal{X} \\ \mathbf{u}(\cdot) &\in \mathcal{U}. \end{aligned} \quad (1.3)$$

The constraints formulation in (1.3) comprises of both box constraints and control saturations, namely

$$\begin{aligned} \mathbf{x}_{\text{lb}} &\leq \mathbf{x}(\cdot) \leq \mathbf{x}_{\text{ub}} \\ \mathbf{u}_{\text{lb}} &\leq \mathbf{u}(\cdot) \leq \mathbf{u}_{\text{ub}} \end{aligned}$$

and of path constraints in the form of

$$\mathbf{g}(\mathbf{x}(\cdot), \mathbf{u}(\cdot), \cdot) \leq \mathbf{0}, \quad (1.4)$$

¹ Almost everywhere means that the derivative can be discontinuous on countable points of measure zero.

where $\mathbf{g} : \mathbb{R}^{N_x} \times \mathbb{R}^{N_u} \times \mathbb{R} \rightarrow \mathbb{R}^{N_g}$ described the relations between the states and the controls during the optimization horizon.

Finally, for the optimal control to be well-posed, we need to define the boundary conditions, that describe the initial and final values of the state trajectories:

$$\boldsymbol{\psi}(\mathbf{x}(t_0), \mathbf{x}(t_f)) \leq \mathbf{0}, \quad (1.5)$$

with $\boldsymbol{\psi} : \mathbb{R}^{N_x} \times \mathbb{R}^{N_x} \rightarrow \mathbb{R}^{N_\psi}$. Usually the boundary conditions in (1.5) are separable over the time horizon, in this case we define the *decoupled* boundary conditions

$$\begin{aligned} \boldsymbol{\psi}_0(\mathbf{x}(t_0)) &\leq \mathbf{0} \\ \boldsymbol{\psi}_f(\mathbf{x}(t_f)) &\leq \mathbf{0}. \end{aligned}$$

In the optimal control problem the task is finding the admissible control function $\mathbf{u}^*(\cdot) \in \mathcal{U}$ that generates the admissible state trajectory $\mathbf{x}^*(\cdot) \in \mathcal{X}$ such that the cost functional in (1.2) is minimized and the boundary conditions (1.5) are satisfied. This is formulated collecting all the conditions as

$$\begin{aligned} \min_{\mathbf{u}(\cdot)} \quad & m(\mathbf{x}(t_f)) + \int_{t_0}^{t_f} \ell(\mathbf{x}(t), \mathbf{u}(t)) dt \\ \text{s.t.} \quad & \dot{\mathbf{x}}(t) = \mathbf{f}(\mathbf{x}(t), \mathbf{u}(t)) \\ & \boldsymbol{\psi}(\mathbf{x}(t_0), \mathbf{x}(t_f)) \leq \mathbf{0} \\ & \mathbf{x}(t) \in \mathcal{X} \\ & \mathbf{u}(t) \in \mathcal{U}, \quad \forall t \in [t_0, t_f]. \end{aligned} \quad (1.6)$$

Three main groups of methods exist to find the solution of the optimal control (1.6): the dynamic programming methods [2], the *indirect* methods [13], [11] and the *direct* methods [3], [5], [8]. A brief while exhaustive introduction of the three methods can be found in [4].

The dynamic programming methods are based on the Hamilton-Jacobi-Bellman's principle of optimality, that states that any tail of an optimal trajectory is an optimal trajectory too; this allows to find the optimal trajectory proceeding recursively backwards starting from the final condition. The dynamic programming approach is the only one that guarantees sufficient conditions for the optimality and, in its discrete version, embodies by construction the formulation of switched dynamics and discrete control; on the other side, the complexity of the dynamic programming methods explodes for high dimensional problems, which makes this method practically unfeasible for systems with more than three or four states.

The *indirect* methods are extremely accurate and can manage even high dimensional problems. They solve a two-point boundary value problem that originates from the Pontryagin's first-order necessary (not sufficient!) conditions for optimality. The first-order necessary conditions introduce a set of new equations (adjoint equations) and new variables (adjoint variables) that are non-physical quantities; the initialization of such non-physical quantities is likely the most relevant issue of the indirect methods, since a bad initialization of the adjoint variables could lead to very ill-conditioned numerical solutions. Moreover, indirect methods cannot easily handle path constraints in the form of (1.4), because it is necessary to make an a priori estimate of the constrained-arc sequence.

Finally, the *direct* methods are based on a suitable discretization of the infinite dimensional state and control space. The resulting finite dimensional optimization problem can be solved using standard non-linear programming technique, as semi-quadratic programming (SQP) or interior point methods. In the remainder of this work we will focus on this family of techniques, because of their larger domain of convergence compared to the *indirect* methods and also because of their better scalability to high dimensional systems. In the following we will deepen the discretization strategies used to approximate the infinite dimensional optimal control problem and transform it into a finite dimensional constrained optimization problem.

1.3.2 Discretization schemes for optimal control

In the setting of the *direct* solution of the optimal control we have to find numerically approximations of the optimal control trajectories $\mathbf{u}^*(\cdot)$ over the time horizon $t \in [t_0, t_f]$. This procedure is based on the discretization of the problem formulation in (1.6) on the (not necessarily equidistant) time grid

$$\mathbb{G}_N = \{t_0 < t_1 < \dots < t_N = t_f\} \quad (1.7)$$

with step sizes $h_j := t_{j+1} - t_j$, $j = 0, \dots, N - 1$. Often, the grid \mathbb{G}_N will be divided in equidistant intervals of size $t_s = \frac{t_N - t_0}{N}$ and we can thus find the grid points as $t_j = t_0 + jh$, $j = 0, \dots, N$. Such discretization changes dramatically the nature of our problem: the objective functional becomes an objective function and the infinite dimensional state and control space shrinks to a finite dimensional space.

1.3.2.1 Control discretization

The first step of the *direct* solution approach is the discretization of the control trajectory. As stated in [8], the admissible control space \mathcal{U} is replaced by some M -dimensional subspace

$$\mathcal{U}^M \subset \mathcal{U}$$

where $M \in \mathbb{N}$ is finite.

Let $\mathcal{B} = \{B_1, \dots, B_M\}$ be a basis of \mathcal{U}^M , then every $\mathbf{u}^M \in \mathcal{U}^M$ can be written as

$$\mathbf{u}_M(\cdot) := \sum_{i=1}^M \omega_i B_i(\cdot) \quad (1.8)$$

with coefficients $\boldsymbol{\omega} = \{\omega_1 \dots \omega_M\}^\top \in \mathbb{R}^{N_u \times M}$. Notice that we can write the dependency of the control as $\mathbf{u}_M(t) = \mathbf{u}_M(t, \boldsymbol{\omega})$

In [8] it is suggested to select basis functions having *local support*, thus avoiding cubic splines, Hermite polynomials or polynomials; such selection may lead to numerical instabilities since a variation of one component of the weight vector $\boldsymbol{\omega}$ may affect the whole control $\mathbf{u}_M(t, \boldsymbol{\omega})$ for all $t \in [t_0, t_f]$.

Therefore basis functions with local support are preferred, in particular we focus on a B -spline representation. We start introducing the B -splines by defining an auxiliary grid \mathbb{G}_N^k , with $k \in \mathbb{N}$ as ([8]):

$$\mathbb{G}_N^k = \{\tau_i | i = 1, \dots, N + 2k - 1\}$$

that has auxiliary points

$$\tau_i := \begin{cases} t_0, & \text{if } 1 \leq i \leq k \\ t_{i-k}, & \text{if } k+1 \leq i \leq N+k-1 \\ t_N, & \text{if } N+k \leq i \leq N+2k-1. \end{cases}$$

The *elementary B-splines* $B_i^k(\cdot)$ of order k , $i = 1, \dots, N+k-1$ are defined by the recursion

$$B_i^1(t) := \begin{cases} 1, & \text{if } \tau_i \leq t < \tau_{i+1} \\ 0, & \text{otherwise} \end{cases}$$

$$B_i^k(t) := \frac{t - \tau_i}{\tau_{i+k-1} - \tau_i} B_i^{k-1}(t) + \frac{\tau_{i+k} - t}{\tau_{i+k} - \tau_{i+1}} B_{i+1}^{k-1}(t).$$

The control is then parametrized, for a fixed $k \in \mathbb{N}$, choosing $\mathbf{u}_M(\cdot)$ from the set

$$\mathcal{U}^M := \left\{ \sum_{i=1}^{N+k-1} \omega_i B_i^k(\cdot) \mid \omega_i \in \mathbb{R}^{N_u}, i = 1, \dots, N+k-1 \right\}.$$

Finally, we must take into account that the higher the value of k , the more smooth the approximation is. It is common to adopt B -splines of order one (piecewise constant approximation) or order two (continuous and piecewise linear approximation), that, even if they result in a not so smooth control trajectory the complexity of the resulting optimization problem is greatly reduced.

1.3.2.2 State discretization - Runge-Kutta integration scheme

The second step of the *direct* solution approach is the discretization of the initial value problem (1.1). The simplest discretization approaches are the explicit (or forward) Euler method

$$\begin{aligned} \mathbf{x}_{j+1} &= \mathbf{x}_j + h_j \mathbf{f}(\mathbf{x}_j, \mathbf{u}_j), \quad j = 0, \dots, N-1 \\ \mathbf{x}_0 &= \mathbf{x}(t_0). \end{aligned}$$

with $\mathbf{x}_j = \mathbf{x}(t_j)$ and $\mathbf{u}_j = \mathbf{u}(t_j)$, and the implicit (or backwards) Euler:

$$\begin{aligned} \mathbf{x}_{j+1} &= \mathbf{x}_j + h_j \mathbf{f}(\mathbf{x}_{j+1}, \mathbf{u}_{j+1}), \quad j = 0, \dots, N-1 \\ \mathbf{x}_0 &= \mathbf{x}(t_0). \end{aligned}$$

Both approaches are naturally subject to an approximation error w.r.t. the true solution that propagates at every step. In order to reduce such error higher order approximation can be used to approximate the right-hand-side function of the dynamics; such approach comprises a family of different discretization methods that are grouped under the name of Runge-Kutta methods. Let us first write the exact solution for the state at time t_{j+1} , $j = 0, \dots, N-1$ as

$$\mathbf{x}_{j+1} = \mathbf{x}_j + \int_{t_j}^{t_{j+1}} \mathbf{f}(\mathbf{x}(t), \mathbf{u}(t)) dt.$$

To improve the accuracy of the integration method, similarly to the control discretization procedure, we have to evaluate the dynamics function over an auxiliary grid: we subdivide the time step of the main grid \mathbb{G}_N in L subintervals (L -stage Runge-Kutta methods) with intermediate time points $\tau_{l,j}$, $j = 0, \dots, N$ such that

$$\tau_{l,j} = t_j + c_l h_j, \quad l = 1, \dots, L$$

with

$$0 \leq c_1 \leq c_2 \leq \cdots \leq c_L \leq 1.$$

The L -stage Runge-Kutta method is obtained by approximating the integral with the *stage derivatives* $s_l(\cdot)$, $l = 1, \dots, L$ at the L intermediate points as

$$\int_{t_j}^{t_{j+1}} \mathbf{f}(\mathbf{x}(t), \mathbf{u}(t)) dt \approx h_j \sum_{l=1}^L b_l s_l(\mathbf{x}(t_j), \mathbf{u}(t_j)) \quad (1.9a)$$

where the l -th stage derivative is defined as

$$s_l(\mathbf{x}(t_j), \mathbf{u}(t_j)) := \mathbf{f} \left(\mathbf{x}(t_j) + h_j \sum_{q=1}^L a_{l,q} s_q(\mathbf{x}(t_j), \mathbf{u}(t_j)), \mathbf{u}(t_j + c_l h_j) \right) \quad (1.9b)$$

for $l = 1, \dots, L$. The Runge-Kutta method is called *explicit* if $a_{l,q} = 0$ for each $q \geq l$, otherwise it is called *implicit*. The value of the control at the intermediate points $\tau_{l,j} = t_j c_l h_j$, with $l = 1, \dots, L$ is evaluated according to the selected control discretization method in (1.8).

The numerical solution to the initial value problem in (1.1) is finally approximated by the recursion

$$\begin{aligned} \mathbf{x}_{j+1} &= \mathbf{x}_j + h_j \Phi_j(\mathbf{x}(t_j), \mathbf{u}(t_j)) \\ \mathbf{x}_0 &= \mathbf{x}(t_0) \end{aligned}$$

with

$$\Phi_j(\mathbf{x}(t_j), \mathbf{u}(t_j)) = \sum_{l=1}^L b_l s_l(\mathbf{x}(t_j), \mathbf{u}(t_j)) \quad j = 0, \dots, N-1$$

and the l -th stage $s_l(\mathbf{x}(t_j), \mathbf{u}(t_j))$ as in (1.9b). The parameters b_l , c_l , $a_{l,q}$ and L are defined by the Runge-Kutta method.

1.3.2.3 Full discretization approach

After evaluating both the Bolza functional (1.2) and the constraints over the time grid \mathbf{G}_N , we can write the infinite-dimensional optimal control problem in (1.6) as the finite-dimensional non-linear optimization problem as follows:

$$\begin{aligned} \min_{\substack{\mathbf{u}_0, \dots, \mathbf{u}_N \\ \mathbf{x}_0, \dots, \mathbf{x}_N}} \quad & m(\mathbf{x}_N) + \sum_{j=0}^{N-1} h_j \ell(\mathbf{x}_j, \mathbf{u}_j) \\ \text{s.t.} \quad & \mathbf{x}_{j+1} = \mathbf{x}_j + h_j \Phi_j(\mathbf{x}(t_j), \mathbf{u}(t_j)) \quad j = 0, \dots, N-1 \\ & \psi(\mathbf{x}_0, \mathbf{x}_N) \leq \mathbf{0} \\ & \mathbf{x}_j \in \mathcal{X} \quad j = 0, \dots, N \\ & \mathbf{u}_j \in \mathcal{U} \quad j = 0, \dots, N. \end{aligned} \quad (1.10)$$

The direct solution method based on the formulation of the optimization problem in (1.10), where both the continuous-valued control space and the continuous-valued state space are discretized, is called *direct collocation* method. Notice that the optimization variables are both the discretized control vector \mathbf{u}_j and the discretized state vector $\mathbf{x}_j, j = 0, \dots, N$. Finally, we decided in (1.10) to approximate the Lagrange term using a simple forward Euler method, but any other higher order method can be used to improve the accuracy of the approximation.

The finite-dimensional optimization problem is then solved numerically by a non-linear programming method as the interior point method [14] or the sequential quadratic programming (SQP) method [8].

BIBLIOGRAPHY OF CHAPTER 1

- [1] Bloomberg New Energy Finance (BNEF). *Energy Storage is a \$620 Billion Investment Opportunity to 2040*. Bloomberg New Energy Finance (BNEF), 2019. URL: <https://about.bnef.com/blog/energy-storage-620-billion-investment-opportunity-2040/>.
- [2] Dimitri P Bertsekas, Dimitri P Bertsekas, Dimitri P Bertsekas, and Dimitri P Bertsekas. *Dynamic programming and optimal control*. Vol. 1. 2. Athena scientific Belmont, MA, 1995.
- [3] John T. Betts. *Practical Methods for Optimal Control and Estimation Using Nonlinear Programming*. 2010, p. 434. ISBN: 9780898716887. DOI: [10.1137/1.9780898716887](https://doi.org/10.1137/1.9780898716887).
- [4] Francesco Biral, Enrico Bertolazzi, and Non-member Paolo Bosetti. "Notes on Numerical Methods for Solving Optimal Control Problems." In: *IEEJ Journal of Industry Applications* 5.2 (2015), pp. 154–166. DOI: [10.1541/ieejjia.5.154](https://doi.org/10.1541/ieejjia.5.154).
- [5] Thomas J Böhme and Benjamin Frank. "Hybrid Systems, Optimal Control and Hybrid Vehicles." In: *Cham, CH: Springer International* (2017).
- [6] Stephen Boyd, Laurent El Ghaoui, Eric Feron, and Venkataramanan Balakrishnan. *Linear matrix inequalities in system and control theory*. Vol. 15. Siam, 1994.
- [7] The European Commission. *Road transport: Reducing CO₂ emissions from vehicles*. The European Commission, 2019. URL: https://ec.europa.eu/clima/policies/transport/vehicles_en.
- [8] Matthias Gerdt. *Optimal control of ODEs and DAEs*. Walter de Gruyter, 2012.
- [9] Alan G Holmes and Michael Roland Schmidt. *Hybrid electric powertrain including a two-mode electrically variable transmission*. US Patent 6,478,705. 2002.
- [10] Jimmy Kapadia, Daniel Kok, Mark Jennings, Ming Kuang, Brandon Masterson, Richard Isaacs, Alan Dona, Chuck Wagner, and Thomas Gee. "Powersplit or Parallel-Selecting the Right Hybrid Architecture." In: *SAE International Journal of Alternative Powertrains* 6.1 (2017), pp. 68–76.

- [11] Donald E Kirk. *Optimal control theory: an introduction*. Courier Corporation, 2012.
- [12] Joseph Kubsh. *Managing emissions from non-road vehicles*. The International Council on Clean Transportation (ICCT), 2017. URL: <https://www.theicct.org/publications/managing-emissions-non-road-vehicles>.
- [13] Daniel Liberzon. *Calculus of variations and optimal control theory: a concise introduction*. Princeton University Press, 2011.
- [14] Andreas Wächter and Lorenz T Biegler. “On the implementation of an interior-point filter line-search algorithm for large-scale non-linear programming.” In: *Mathematical programming* 106.1 (2006), pp. 25–57.

Part I

THE HYBRID ELECTRIC TRANSMISSION

The electric-hybrid powertrain comprises of several components that contribute to provide the power demanded by the driver. The battery in hybrid cars are accountable for the improved fuel economy that has become central to the technology, providing power to the electric motor that assists the engine and storing the otherwise wasted kinetic energy during regenerative braking. Technology is making great leaps forward with the lithium battery, but in order to avoid possible safety threats this component is typically oversized and employed within overly conservative safety bounds. For this reason, a thorough knowledge of the battery system has a pivotal role in reducing costs and maximizing the performance of the hybrid powertrain.

The research presented in this chapter aims at the study and characterization of a lithium-ion high voltage battery for the new Ferrari sport road car *SF90 Stradale*, equipped with a parallel hybrid powertrain with a P2 electric machine and two P4 electric motors mounted on the wheel hubs of the rear axle.

The research is divided into two main activities: in the first activity (Section 2.1) we study the cell voltage dynamics and we propose a new variant of the electrochemical battery model that extends the validity of the reduced-order model also for non-constant temperatures. This feature, that has never been previously addressed in the literature for this order reduction strategy, is of paramount importance if we want to capture the battery behavior in all the operating conditions, while keeping the formulation simple. In the second activity (Section 2.2) we focus on the degradation of the battery performances and we will propose a semi-empirical model to describe the capacity losses as a consequence of storage conditions and charge/discharge cycles. The proposed semi-empirical aging model gathers several other models proposed in the literature that partially describe the aging processes, in order to get a good prediction of the battery deterioration in all driving conditions. Both the charge/discharge dynamics model and the battery aging model are validated against a large amount of measured data.

The physics-based electrochemical model describes terminal voltage dynamics as a consequence of impedance variations due to diffusion processes occurring inside the cell. Its formulation is more involved than

the standard equivalent circuit models, but the increase complexity can be justified by several advantages:

- electrochemical model is more accurate when the battery is driven far from the equilibrium; indeed, the typical equivalent circuits that comprises just one or two RC-parallel branches are not accurate for long charges or discharges or for high current values.
- the equivalent circuit model lump the electric properties of the cell with equivalent electrical elements (capacitors and resistors); the capacity and resistance values varies with temperature and state-of-charge (SOC), therefore we need many experimental data in all conditions to characterize this value. This is not the case for the equivalent circuit model, since due to its physics-based structure it is easier to extrapolate the cell behavior even for SOC values and temperatures not available in the experimental dataset.
- the dependency of the electric elements of the equivalent circuit model on temperature and SOC is usually obtained through interpolation of a static map; conversely, the electrochemical model is based only on constant parameters that determine the terminal voltage through continuous and continuously differentiable functions. The smooth structure of the electrochemical model allows to use gradient-based techniques for solving optimization problem, e.g. in an optimal control framework.
- electrochemical model allows to observe the internal state of the battery, which is a strong benefit if we want to model the aging mechanisms that occur mainly at the anode side.

In this research we propose a reduced-order version of the full-order electrochemical model that can be suitable for control and fast simulation purposes.

It is well-known that battery degradation occurs both during charge and discharge cycles and during long storage periods. Several studies revealed, thanks to post-mortem analyses, that battery degradation is the result of many mechanisms, most of which occur at the anode-side, like solid-electrolyte-interphase growth, lithium plating, passive electrode effect and electrode degradation. A precise physics-based aging model should represent individually these intertwined degradation mechanisms, but only their combined effect on the performance losses is detectable from non-invasive current/voltage measurements; this prevents the possibility of validating the models with reliable experimental data.

An example should clarify this concept: solid-electrolyte-interphase (SEI)

is a layer that covers the anode active material that results from the side-reaction between the electrolyte and the anode-graphite, and consumes cyclable lithium ions reducing the overall capacity; it is a self-inhibiting reaction because it occurs on a “clean” anode surface, namely a surface not covered by SEI layer. While the battery undergoes charge/discharge current cycles, the repeated intercalation of lithium ions leads to cracking of the anode active material, thus exposing new “clean” surface for the SEI reaction to occur. From current/voltage measurements we will notice a fast degradation of the battery capacity, but it would be impossible to determine how much of such loss is to ascribe to the SEI formation and how much to the electrode cracking.

For these reasons, the empirical models, based only on the observation of the overall battery degradation from experimental data, have gained increasing interest in the research community. These models are extremely simple and relate the battery degradation to the time and to the energy throughput; nevertheless they are strongly dependent on the available experimental dataset and they do not exploit any knowledge of the internal states of the battery nor of the dependency on the main aging mechanisms.

In this study we propose a slightly different approach which is half-way between the physics-based and the empirical model, recently proposed in some studies as the *semi-empirical model*. This approach takes advantage of the (little) knowledge that we have of the degradation mechanisms and build a model structure based on the qualitative dependency of the degradation processes on the aging conditions. For instance it is shown by many studies that lithium plating occurs during charges at cold temperature, and this is accentuated for higher current values at high SOC; therefore the semi-empirical model will comprise of a term that recalls this trend.

The outline of this work is organized as follows: in Section 2.1 we introduce the electrochemical battery model, we show how to reduce the model order and we calibrate the many unknown model parameters. In Section 2.2 we discuss battery aging separating the aging mechanism into two groups: aging during storage (calendar aging) and aging during battery usage (cycle-induced aging); we show how to design and calibrate the semi-empirical model thanks to an extensive experimental campaign of many lithium-ion cells aged under different conditions.

2.1 THE ELECTROCHEMICAL MODEL

2.1.1 Model Development

Unlike the empirical equivalent circuit models, that are widely used in real-time estimation and control applications (see e.g. [19, 36, 38]), the macroscopic porous-electrode model proposed by Doyle and Newman in [10, 34] is able to capture the spatial and temporal lithium-ion concentration dynamics in a wider range of operating conditions. As suggested in [40], the capability of the physics-based electrochemical model to predict proximity to saturation and depletion conditions allows for a less conservative design of the control strategy, in particular in high power applications; moreover, aging phenomena like SEI formation and loss of active material caused by the side reactions taking place in the anode, can be directly related to the variation of electrochemical parameters like active material volume fraction and SEI layer thickness [22]. Figure 2.1 represents a schematic cutaway of a single layer of the Li-ion cell. The cell

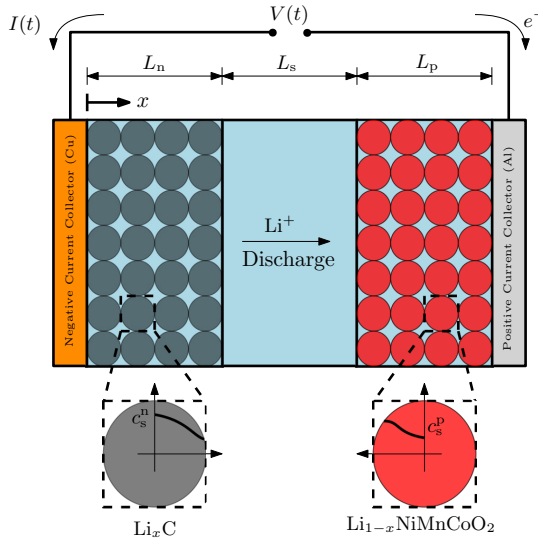
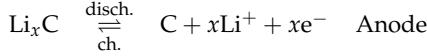


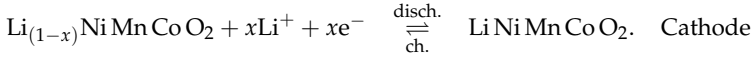
Figure 2.1: Schematic diagram of the cell section.

is built by several of these layers, that comprise of a slurry of negative active material (typically graphite) coated onto a copper foil and a slurry of positive active material (metal oxide) coated onto an aluminum foil, that are separated by a polymeric material. These layers are then rolled,

folded or stacked depending on the desired final form factor and finally inserted in a can filled with liquid (or gel) electrolyte. During discharge, the lithium intercalated in the graphite layers diffuses to the surface of the solid-phase electrode and undergoes the following anodic oxidation



releasing Li^+ -ions in the electrolyte. The polymeric separator serves as electronic insulator and forces the electrons to follow an external path through the current collectors and the external load. The Li^+ -ions move in the electrolyte by diffusion and ionic conduction until they reach the positive electrode where they undergoes the cathodic reduction reaction



The resulting solid-phase Li then diffuses from the surface to the center of the positive active material, generating a concentration gradient along the thickness of the particle as indicated in Figure 2.1.

2.1.1.1 Full order model

In this section we provide a short overview of the four coupled PDE governing mass and charge conservation in the solid and liquid phase. We indicate with the superscript p, n, s the quantities related to the positive, negative and separator domain respectively, while the subscripts s, e refer to the solid and liquid phase. All the symbols with their meaning and unit are listed in Table 2.A.1, 2.A.2 and 2.A.3 in Appendix 2.A.

We assume the reaction rate for the intercalation process $j^i(x, t)$, $i = p, n$ to be constantly distributed along the domains' thickness i.e.

$$j^i(x, t) = j^i(t) = \mp \frac{I(t)}{A^i L_i}, \quad i = p, n \quad (2.1)$$

where $I(t) > 0$ is a discharge current; this allows to approximate the porous electrode by a single spherical particle whose capacity is equivalent to that of the electrode [17].

The conservation of lithium-ion in a spherical particle of active material is described by the Fick's law for mass diffusion, i.e.

$$\frac{\partial c_s^i(r, t)}{\partial t} = \frac{D_s^i}{r^2} \frac{\partial}{\partial r} \left(r^2 \frac{\partial c_s^i(r, t)}{\partial r} \right) \quad i = p, n \quad (2.2)$$

where r is the radial coordinate and the boundary conditions

$$\begin{aligned} \left[\frac{\partial c_s^i(r, t)}{\partial r} \right]_{r=0} &= 0 \\ \left[D_s^i \frac{\partial c_s^i(r, t)}{\partial r} \right]_{r=R_s^i} &= \frac{-j^i(t)}{a_s^i F} \quad i = p, n, \end{aligned}$$

impose the symmetry at the particle center and characterize the flux of Li^+ at the particle surface.

The conservation of lithium ions in the liquid phase is described by linear diffusion, namely

$$\varepsilon_e \frac{\partial (c_e^i(x, t))}{\partial t} = \frac{\partial}{\partial x} \left(D_e^{\text{eff}} \frac{\partial c_e^i(x, t)}{\partial x} \right) + \frac{(1 - t_0^+)}{F} j^i(t) \quad (2.3)$$

where the electrode tortuosity is taken into account by the Bruggeman relation $D_e^{\text{eff}} = D_e \varepsilon_e^\gamma$. The boundary conditions

$$\begin{aligned} \left[\frac{\partial c_e^n(x, t)}{\partial x} \right]_{x=0} &= \left[\frac{\partial c_e^p(x, t)}{\partial x} \right]_{x=L} = 0 \\ \left[D_n^{\text{eff}} \frac{\partial c_e^n(x, t)}{\partial t} \right]_{x=L_n} &= \left[D_s^{\text{eff}} \frac{\partial c_e^s(x, t)}{\partial t} \right]_{x=L_n} \\ c_e^n(L_n, t) &= c_e^s(L_n, t) \\ \left[D_s^{\text{eff}} \frac{\partial c_e^s(x, t)}{\partial t} \right]_{x=L_n+L_s} &= \left[D_p^{\text{eff}} \frac{\partial c_e^p(x, t)}{\partial t} \right]_{x=L_n+L_s} \\ c_e^s(L_n + L_s, t) &= c_e^p(L_n + L_s, t) \end{aligned}$$

guarantee zero flux at the current collectors and continuity of flux and concentration at the interface between the domains.

The conservation of charge in the solid phase is determined by the infinite-dimensional form of the Ohm's law for the electric potential, i.e.

$$\sigma^{\text{eff}, i} \frac{\partial^2 \phi_s^i(x, t)}{\partial x^2} = j^i(x, t) \quad i = p, n \quad (2.4)$$

with the boundary conditions that express the electric fields at the current collectors and at the domain interfaces:

$$\begin{aligned} \left[\sigma^{\text{eff}} \frac{\partial \phi_s^n(x, t)}{\partial x} \right]_{x=0} &= -\frac{I(t)}{A} \\ \left[\sigma^{\text{eff}} \frac{\partial \phi_s^p(x, t)}{\partial x} \right]_{x=L_c} &= +\frac{I(t)}{A} \\ \left[\frac{\partial \phi_s^n(x, t)}{\partial x} \right]_{x=L_n} &= \left[\frac{\partial \phi_s^p(x, t)}{\partial x} \right]_{x=L_s+L_n} = 0, \end{aligned}$$

where σ^{eff} is the effective solid phase conductivity and $I(t)$ is the current applied to the cell.

In the liquid phase the conservation of charge is described by both the flux due to the potential gradient (as in the solid phase) and the flux due to the concentration gradient, namely

$$\frac{2R_g T \kappa^{\text{eff}} (t_0^+ - 1)}{F} (1 + \beta) \frac{\partial \ln(c_e^i(x, t))}{\partial x} + \kappa^{\text{eff}} \frac{\partial \phi_e^i(x, t)}{\partial x} = \mp j^i(t) L^i \quad i = p, s, n \quad (2.5)$$

where the Bruggeman relation $\kappa^{\text{eff}} = \kappa \varepsilon_e^\gamma$ defines the effective ionic conductivity of the electrolyte. The activity coefficient β is chosen equal to zero in [8], while other authors express a dependency on the concentration [39, 41], namely $\beta = \frac{d(\ln f_\pm)}{d(\ln c_e)}$; we will treat β as a tunable parameter independent of the Li^+ concentration as in [31], whose dependency on temperature is expressed by

$$\beta = \beta_{\text{ref}} \exp \left[E_{\text{act}, \beta} \left(\frac{1}{T_{\text{ref}, \beta}} - \frac{1}{T} \right) \right]^{\rho_\beta}.$$

The boundary conditions define the electric potential for the electrolyte at the current collectors and at the domains interfaces, i.e.¹

$$\begin{aligned} \left[\frac{\partial \phi_e^n}{\partial x} \right]_{x=0} &= \left[\frac{\partial \phi_e^p}{\partial x} \right]_{x=L_c} = 0 \\ \left[\left(\kappa_n^{\text{eff}} \frac{\partial \phi_e^n}{\partial x} \right) + \left(\frac{\kappa_D^{\text{eff}}}{c_{e0}} \frac{\partial c_e^n(x, t)}{\partial x} \right) \right]_{x=L_n} &= \\ &= \left[\left(\kappa_s^{\text{eff}} \frac{\partial \phi_e^s}{\partial x} \right) + \left(\frac{\kappa_D^{\text{eff}}}{c_{e0}} \frac{\partial c_e^s(x, t)}{\partial x} \right) \right]_{x=L_n} \end{aligned}$$

¹ We used the shorthand notation $\kappa_D^{\text{eff}} = \frac{2RT \kappa^{\text{eff}} (t_0^+ - 1)}{F} (1 + \beta)$.

$$\left[\left(\kappa^{\text{eff}} \frac{\partial \phi_e^{\text{s}}}{\partial x} \right) + \left(\frac{\kappa_{\text{D}}^{\text{eff}}}{c_{\text{e}0}} \frac{\partial c_e^{\text{s}}(x, t)}{\partial x} \right) \right]_{x=L_n+L_s} = \left[\left(\kappa^{\text{eff}} \frac{\partial \phi_e^{\text{p}}}{\partial x} \right) + \left(\frac{\kappa_{\text{D}}^{\text{eff}}}{c_{\text{e}0}} \frac{\partial c_e^{\text{p}}(x, t)}{\partial x} \right) \right]_{x=L_n+L_s}$$

$$\phi_e^{\text{s}}(L_n + L_s, t) = \phi_e^{\text{p}}(L_n + L_s, t)$$

The three PDEs in (2.2), (2.3) and (2.5) are coupled by the intercalation current density $j^i(t)$, that is governed by the Butler-Volmer kinetics

$$j^i(t) = a_{\text{s}}^i i_0^i(t) \left\{ \exp \left(\frac{\alpha_{\text{a}} F}{R_{\text{g}} T} \eta^i(t) \right) - \exp \left(- \frac{\alpha_{\text{c}} F}{R_{\text{g}} T} \eta^i(t) \right) \right\}, \quad i = \text{p, n} \quad (2.6)$$

where the exchange current density $i_0^i(x, t)$ depends both on solid concentration and electrolyte concentration according to

$$i_0^i(t) = k^i \sqrt{c_e^i(t) (c_{\text{s, max}}^i - c_{\text{s}}^i(R_{\text{s}}^i, t)) c_{\text{s}}^i(R_{\text{s}}^i, t)}. \quad i = \text{p, n} \quad (2.7)$$

The overpotential is the magnitude of the potential drop resulting from the polarization of the electrode, caused by resistance to the passage of current [34]; in other words overpotential is the extra potential which must be applied to an electrode to initiate the electrochemical reaction. Notice that $\eta^i(x, t) > 0$ produces an anodic current, indeed the net current direction depends on the sign of the overpotential. The surface overpotential is then defined as the difference between the actual potential and the equilibrium potential, namely

$$\eta^i(t) = \phi_{\text{s}}^i(t) - \phi_e^i(t) - U^i(t). \quad i = \text{p, n} \quad (2.8)$$

The functional forms of the open circuit voltage (OCV) $U^i(t)$, $i = \text{p, n}$ for the lithiated graphite (U^{n}) and for the Lithium Nickel Manganese Cobalt Oxide (U^{p}) are reported in appendix 2.A.

Overpotential is related to the intercalation current density via Butler-Volmer kinetics, thus inverting 2.6 and assuming $\alpha_{\text{a}} = \alpha_{\text{c}} = \alpha$ we get the explicit expression for the overpotential:

$$\eta^i(t) = \frac{R_{\text{g}} T}{\alpha F} \sinh^{-1} \left[\frac{j^i(t)}{a_{\text{s}}^i i_0^i(t)} \right]. \quad i = \text{p, n} \quad (2.9)$$

Finally we can compute terminal voltage $V(t)$ as the difference between solid potentials at the current collectors plus a term that takes the contact and SEI film resistance into account:

$$V(t) = \phi_{\text{s}}^{\text{p}}(t) - \phi_{\text{s}}^{\text{n}}(t) - R_{\Omega} I(t). \quad (2.10)$$

Solving 2.8 for $\phi_s^i(x, t)$ and substituting in 2.10 yields

$$V(t) = U^P(t) - U^n(t) + \eta^P(t) - \eta^n(t) + \phi_e^P(L, t) - \phi_e^n(0, t) - R_\Omega I(t). \quad (2.11)$$

Equation (2.11) expresses the relation between the current applied to the battery (galvanostatic input) and the resulting terminal output voltage.

2.1.1.2 Reduced order model

The two PDEs in (2.2) and (2.3) characterize the diffusion phenomena in the solid electrodes and in the liquid phase and predict the concentrations of lithium ions, that are used to compute the half-cell equilibrium potential and overpotential to finally get the terminal voltage through 2.11. Since the PDE system is not tractable for the design of on-line control and estimation algorithms, many researchers have proposed different approaches to reduce the order of the model, spanning from finite difference methods [6, 9, 35] to Galerkin orthogonal decomposition [3, 5, 7, 14, 30].

We resort in this work to the frequency-based model order reduction proposed in [15], where the diffusion dynamics (2.2) is Laplace transformed and the solution of the resulting ODE leads to the infinite dimensional transfer function

$$\frac{\tilde{C}_s^i(r, s)}{I(s)} = \pm \frac{[R_s^i]^2 \exp((R_s^i - r)\zeta^i) [\exp(2r\zeta^i) - 1]}{[R_s^i \zeta^i \exp(2R_s^i \zeta^i) + R_s^i \sqrt{\zeta^i} - \exp(2R_s^i \zeta^i) + 1] \gamma^i}, \quad (2.12)$$

where $\zeta^i = \sqrt{\frac{s}{D_s^i}}$ and $\gamma^i = D_s^i a_s^i F A^i L^i r$ for $i = p, n$. Equation (2.12)

is eventually approximated at the particle surface (i.e. at $r = R_s^i$, $i = p, n$) by Padé rational polynomials. We indicate with upper case letters the Laplace transform of the lower case variables. This approach is particularly appealing because it reduces the system to a linear transfer function with few states (depending on the truncation order) and is based on an analytical solution that can be easily generalized to higher orders. The authors of [31] have shown that a third order approximation is sufficient to capture with good accuracy dynamics up to 2.5 Hz, that carry 90% of the the signal power in typical HEV applications; the third order transfer function from the input current to the solid-electrolyte interface concentration $C_{s,e}^i(s) = C_s^i(R_s^i, s)$, $i = p, n$ becomes

$$\frac{\tilde{C}_{s,e}^i(s)}{I(s)} = \pm \frac{21 \left[\frac{1}{a_s^i F A [R_s^i]^3 L^i} s^2 + \frac{60 D_s^i}{a_s^i F A [R_s^i]^3 L^i} s + \frac{495 [D_s^i]^2}{a_s^i F A [R_s^i]^5 L^i} \right]}{s^3 + \frac{189 D_s^i}{[R_s^i]^2} s^2 + \frac{3465 [D_s^i]^2}{[R_s^i]^4} s}. \quad (2.13)$$

While the surface concentration determines the equilibrium voltage and the overpotential in 2.11, the cell State of Charge is related the volume-averaged (or bulk) concentration $c_{s,\text{avg}}^i(t)$, defined in [15] as the spherical integral of 2.12, leading to

$$\begin{aligned} \frac{\tilde{c}_{s,\text{avg}}^i(s)}{I(s)} &= \pm \frac{\int_0^{R_s^i} C_s^i(s,r)(4\pi r^2)dr}{(4/3)\pi[R_s^i]^3} \\ &= \pm \frac{3}{R_s^i L^i A^i F a_s^i} \frac{1}{s} \quad i = p, n \end{aligned} \quad (2.14)$$

Following similar steps, the Lithium concentration at the negative and positive current collectors becomes

$$\begin{aligned} \frac{\tilde{c}_e(0,s)}{I(s)} &= - \frac{2.9351(t_0^+ - 1)}{\epsilon_e L F A^n \left(s + \frac{9.5842 D_e^{\text{eff}}}{L^2} \right)} \\ \frac{\tilde{c}_e(L,s)}{I(s)} &= + \frac{3.1463(t_0^+ - 1)}{\epsilon_e L F A^p \left(s + \frac{9.8710 D_e^{\text{eff}}}{L^2} \right)}, \end{aligned} \quad (2.15)$$

for the considered cell geometry, namely $L_n = \frac{2}{3}L$, $L_s = \frac{1}{4}L$ and $L_p = \frac{7}{20}L$. It is worth mentioning that the numerical coefficients appearing in 2.15 depend only on battery geometry (layers' thickness) and therefore remain unchanged during battery life. The tilde in (2.13), (2.14) and (2.15) indicates a deviation from the equilibrium value at the initial time instant t_0 , namely $c_{s,\{e,\text{avg}\}}^i(t) = c_{s,\{e,\text{avg}\}}^i(t_0) + \tilde{c}_{s,\{e,\text{avg}\}}^i(t)$ and $c_e(\{0,L\},t) = c_e(\{0,L\},t_0) + \tilde{c}_e(\{0,L\},t)$.

By introducing the normalized bulk concentration corresponding to the discharged and charged cell, $\theta_{0\%}^i$ and $\theta_{100\%}^i$ respectively, we can relate the cell SOC to the bulk concentration of the two electrodes as

$$\begin{aligned} \text{SOC}(t) &= \frac{\frac{c_{s,\text{avg}}^i(t)}{c_{s,\text{max}}^i} - \theta_{0\%}^i}{\theta_{100\%}^i - \theta_{0\%}^i} \\ &= \text{SOC}(t_0) + \frac{\frac{\tilde{c}_{s,\text{avg}}^i(t)}{c_{s,\text{max}}^i}}{\theta_{100\%}^i - \theta_{0\%}^i} = \text{SOC}(t_0) + \widetilde{\text{SOC}}(t) \end{aligned} \quad (2.16)$$

Notice that 2.16 enforces conservation of lithium ions and allows to write a relation between the bulk concentration at the cathode and the bulk concentration at the anode. Moreover, the concentration operating range can be converted to the cell capacity expressed in ampere-seconds according to

$$Q_N = \mp L^i A^i F \epsilon_s^i c_{s,\text{max}}^i (\theta_{100\%}^i - \theta_{0\%}^i) \quad i = p, n \quad (2.17)$$

$$\begin{aligned}
 A &= \begin{bmatrix} -\frac{189D_s^p}{[R_s^p]^2} & -\frac{3465[D_s^p]^2}{[R_s^p]^4} & 0 & 0 & \frac{189D_s^p(\theta_{100\%}^p - \theta_{0\%}^p)c_{s,\max}^p}{[R_s^p]^2} \\ 1 & 0 & 0 & 0 & -(\theta_{100\%}^p - \theta_{0\%}^p)c_{s,\max}^p \\ 0 & 0 & -\frac{189D_s^n}{[R_s^n]^2} & -\frac{3465[D_s^n]^2}{[R_s^n]^4} & -\frac{189D_s^n(\theta_{100\%}^n - \theta_{0\%}^n)c_{s,\max}^n}{[R_s^n]^2} \\ 0 & 0 & 1 & 0 & (\theta_{100\%}^n - \theta_{0\%}^n)c_{s,\max}^n \\ 0 & 0 & 0 & 0 & 0 \end{bmatrix}, \\
 B &= \begin{bmatrix} \frac{7}{\varepsilon^p F A^p L^p} \\ -\frac{[R_s^p]^2}{15 D_s^p \varepsilon^p F A^p L^p} \\ \frac{7}{\varepsilon^n F A^n L^n} \\ -\frac{[R_s^n]^2}{15 D_s^n \varepsilon^n F A^n L^n} \\ -\frac{1}{Q_N} \end{bmatrix}, \quad C = \begin{bmatrix} 1 & 0 & 0 & 0 & 0 \\ 0 & 0 & -1 & 0 & 0 \\ 0 & 0 & 0 & 0 & 1 \end{bmatrix}.
 \end{aligned} \tag{2.19b}$$

It is interesting to notice that by substituting (2.14) and (2.17) in (2.16) and using the definition of active surface $a_s^i = 3e^i/R_s^i$ we get

$$SOC(t) = SOC(t_0) - \frac{1}{Q_N} \int_{t_0}^t I(\tau) d\tau = SOC(t_0) + \widetilde{SOC}(t), \tag{2.18}$$

which is the Coulomb counting method for computing SOC.

The lithium conservation allows us to represent the positive and negative electrodes dynamics using only five states (instead of six) exploiting the relation between the volume-averaged concentrations. We propose in the following a reduced order state-space realization for the electrodes dynamics transfer function in (2.13), that is formulated as

$$\begin{aligned}
 \dot{x}(t) &= Ax(t) + Bu(t), \quad \text{with } x \in \mathbb{R}^5, u \in \mathbb{R} \\
 y(t) &= Cx(t), \quad \text{with } y(t) = \begin{bmatrix} \tilde{c}_{s,e}^p(t) \\ \tilde{c}_{s,e}^n(t) \\ \widetilde{SOC}(t) \end{bmatrix} \in \mathbb{R}^3
 \end{aligned} \tag{2.19a}$$

where the state space matrices are reported in (2.19b). Because the state matrix is non-full rank, the steady-state $x_{ss} \in \mathbb{R}^5$ must be sought in the kernel of the matrix A ; thus, given the non-zero initial condition on the

SOC variation $\widetilde{SOC}(t_0) = \widetilde{SOC}_0$ after some algebraic manipulation the steady state becomes

$$x_{ss} = \begin{bmatrix} (\theta_{100\%}^p - \theta_{0\%}^p)c_{s,max}^p \widetilde{SOC}_0 \\ 0 \\ -(\theta_{100\%}^n - \theta_{0\%}^n)c_{s,max}^n \widetilde{SOC}_0 \\ 0 \\ \widetilde{SOC}_0 \end{bmatrix} \quad (2.20)$$

where $\widetilde{c}_{s,avg0}^i$ is the bulk concentration variation at the initial time $t = t_0$. By computing the system steady state output y_{ss} through matrix C we see that the surface concentration at the anode and at the cathode converges to the initial bulk concentration, indeed

$$y_{ss} = \begin{bmatrix} \widetilde{c}_{s,avg0}^p \\ \widetilde{c}_{s,avg0}^n \\ \widetilde{SOC}_0 \end{bmatrix}, \quad (2.21)$$

where we used (2.16) to relate the bulk concentration to the SOC.

2.1.1.3 Temperature Dependency

The solid phase diffusion coefficients D_s^i and the kinetic constants k^i increase with temperature according to the Arrhenius-like equation

$$\Gamma(T) = \Gamma_{ref} \exp \left[-\frac{E_{act,\Gamma}}{R_g} \left(\frac{1}{T} - \frac{1}{T_{ref,\Gamma}} \right) \right]. \quad (2.22)$$

Similarly, lower values of the contact and film resistance R_Ω at higher temperature are described by changing the sign in front of the exponential argument in 3.10.

The parameters of the transfer functions in (2.13) vary with temperature, therefore we need to carefully select a proper state-space realization in order to avoid non-physical behaviors in the simulation; other authors, e.g. [41], suggest to convert the transfer function using a canonical realization, but this choice leads to a loss of accuracy when the temperature varies over the simulation. To show how the selection of the state-space influences the model performances, we compare in Figure 2.2 our proposed model in (2.19) with the minimal realization in controller canonical form and with the numeric solution of the PDE. As expected, in the first part of the simulation the two realizations exhibit the same behavior and are in good accordance with the numeric solution, because the two formulations

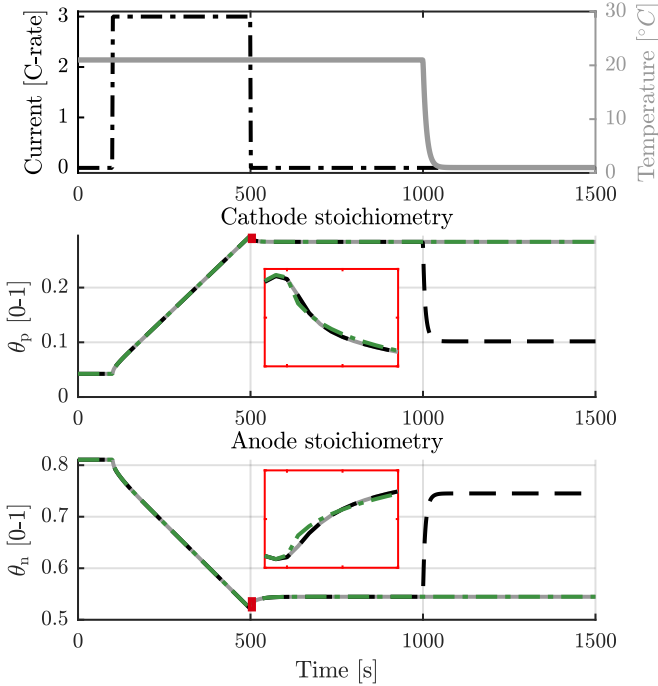


Figure 2.2: PDE solution of the stoichiometry at the anode and at the cathode (green dash-dot line) compared with our proposed realization (gray solid line) and with the controller canonical form (black dashed line).

are input-output equivalent for the same constant temperature; when the temperature changes at $t = 1000$ s the stoichiometry of the two electrodes modeled by the controller realization moves from its steady state and, contrarily to our realization, deviates from the analytic solution.

2.1.1.4 Input-output relationship

The equations detailed in the previous sections determine the relation between the input current and the terminal voltage according to the scheme in Figure 2.3.

As already discussed, the model behavior depends on the temperature that must be provided as input of the system. The model requires also the

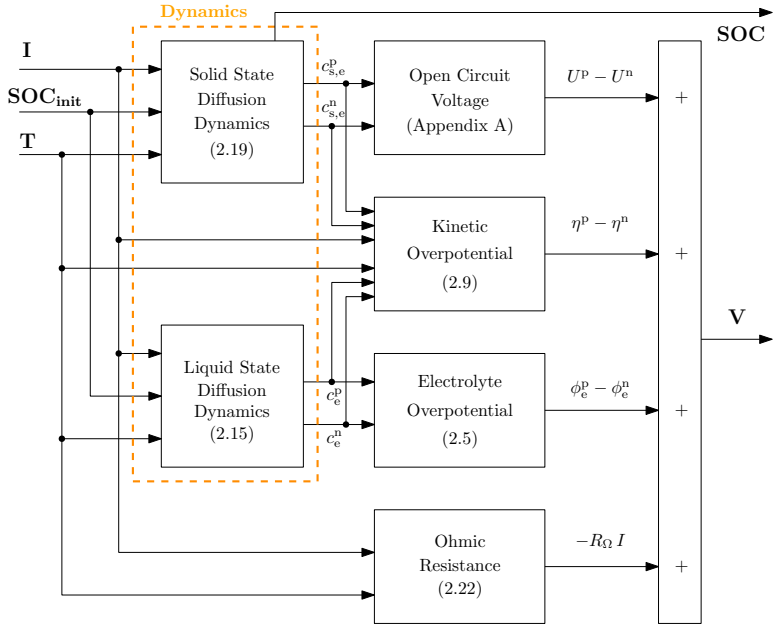


Figure 2.3: Block diagram illustrating the input (current) and output (terminal voltage) relation.

initial state-of-charge value (or directly the initial states if the simulation starts from a non-equilibrium conditions).

2.1.2 Model Parametrization

In this section we describe the parametrization procedure used for determining the value of the unknown parameters of the battery model described in Section 2.1. This approach is widely inspired by the work of Marcicki et al. [31], where the authors propose to exert the cell with specific current inputs in order to selectively reduce the number of parameters appearing in the output voltage formulation. We explicitly formulate the non-linear programming (NLP) problems relative to each phase of the parametrization procedure and we finally illustrate the approach that we used to seek the global optimal parameters.

2.1.2.1 Parametrization description

The parameters associated with the geometry of the cell are selected from [41], where a similar cell is studied; the electrolyte properties are taken from the extensive study by Valøen et al. in [42], where the authors have experimentally measured the properties of the LiFeP₆-based electrolyte at different temperature and concentration values.

We sort the remaining unknown parameters, that determine the capacity, resistance and relaxation properties of the cell, into three groups. The electrode volume fractions and the initial stoichiometry ratios influence the equilibrium potential and the capacity of the cell, while its internal impedance is instead related to the kinetic constants and to the contact resistance; finally, the temperature dependent diffusion coefficients regulate the relaxation dynamics of the cell.

CAPACITY RELATED PARAMETERS at equilibrium, the terminal voltage corresponds to the difference between the half cells overpotential, namely

$$\lim_{\substack{I(t)=0 \\ t \rightarrow \infty}} V(t) = U^P \left(\frac{c_{s,\text{avg}}^P}{c_{s,\text{max}}^P} \right) - U^n \left(\frac{c_{s,\text{avg}}^n}{c_{s,\text{max}}^n} \right), \quad (2.23)$$

The OCV dependence on the stoichiometry is described by the functional forms reported in Appendix 2.A.

By discharging the battery with a fixed current for a known time interval and letting the cell rest for enough time (2 hours) until it reaches the equilibrium, we can associate the experimental OCV data OCV_{exp} to the corresponding SOC obtained by Coulomb counting.

The NMC chemistry is characterized by a small hysteresis, therefore we assume with good approximation that the OCV map is the average between charge and discharge values. The volume-averaged concentration $c_{s,\text{avg}}^i$ can be related to the SOC through (2.16), while the initial and final degree of lithiation $\theta_{100\%}^i$ and $\theta_{0\%}^i$ are linked by the definition of cell capacity (2.17). This allows us to write the parametrization problem as the minimization of the squared error between the measured and the estimated OCV in the four optimization variables $\theta_{0\%}^p$, $\theta_{0\%}^n$, ϵ_s^p and ϵ_s^n , i.e.

$$\min_{\theta_{0\%}^i, \epsilon_s^i} \left\| \text{OCV}_{\text{exp}} - \lim_{\substack{I(t)=0 \\ t \rightarrow \infty}} V(t) \right\| \quad (2.24)$$

subject to (2.16), (2.17) and (2.23)

The solution of this optimization problem with the methods described in Section 2.1.2.2 leads to the results reported in Figure 2.4, where the model prediction is represented with a black solid line and the circles indicate the experimental OCV measured at different temperature values. We report in Figure 2.4 the OCV values in charge and discharge to show that only a negligible hysteresis is present for this chemistry and the identified model is able to accurately predict the OCV in both conditions.

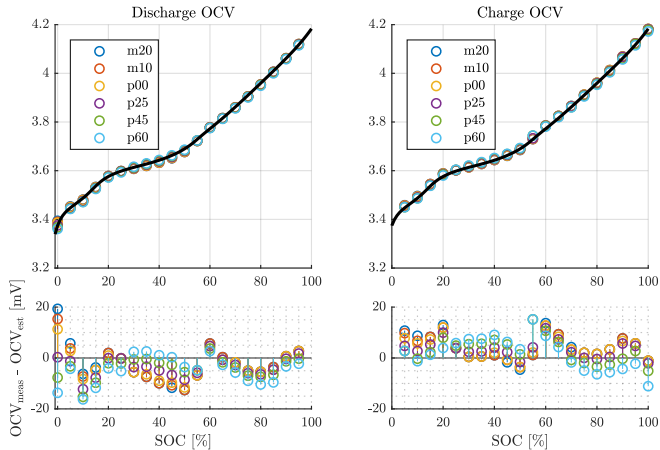


Figure 2.4: Open Circuit Voltage (OCV) measured at different temperatures (circles). The calibrated model is represented by the solid line.

RESISTANCE RELATED PARAMETERS The initial overpotential is known to vary with temperature, current amplitude and SOC, therefore we collected the cell voltage response at different current steps for various temperatures (-20°C , 0°C , 25°C , 40°C) and different SOC (10%, 30%, 50%, 70%, 90%).

If the current step is applied at time $t = t_{\text{st}}$ and $I(t_{\text{st}}^-) = 0$, we divide the instantaneous voltage drop $V(t_{\text{st}}^+) - V(t_{\text{st}}^-)$ by the current amplitude $I(t_{\text{st}}^+)$ and we get the experimental initial overpotential R_{exp} . In the short time interval $(t_{\text{st}}^+ - t_{\text{st}}^-)$ the slow diffusion dynamics can be neglected, therefore the concentration-dependent terms in (2.11) remain constant; this allows to isolate the the ohmic and kinetic temperature-dependent overpotential as

$$\begin{aligned}
 R(t_{\text{st}}^+) &= - \frac{V(t_{\text{st}}^+) - V(t_{\text{st}}^-)}{I(t_{\text{st}}^+)} \\
 &= - \frac{\eta^{\text{P}}(t_{\text{st}}^+) - \eta^{\text{n}}(t_{\text{st}}^-)}{I(t_{\text{st}}^+)} - \frac{\phi_{\text{e}}^{\text{P}}(t_{\text{st}}^+) - \phi_{\text{e}}^{\text{n}}(t_{\text{st}}^-)}{I(t_{\text{st}}^+)} + R_{\Omega} \\
 &= - \frac{RT}{\alpha F I(t_{\text{st}}^+)} \left(\sinh^{-1} \left[\frac{j^{\text{P}}(t_{\text{st}}^+)}{a_{\text{s}}^{\text{P}} i_0^{\text{P}}(t_{\text{st}}^+)} \right] - \sinh^{-1} \left[\frac{j^{\text{n}}(t_{\text{st}}^+)}{a_{\text{s}}^{\text{n}} i_0^{\text{n}}(t_{\text{st}}^+)} \right] \right) \\
 &\quad + \frac{1}{\kappa^{\text{eff}}} \left(\frac{L^{\text{P}}}{A^{\text{P}}} + \frac{L^{\text{n}}}{A^{\text{n}}} \right) + R_{\Omega}
 \end{aligned} \tag{2.25}$$

Notice that, since the function \sinh^{-1} preserves the sign of its argument, the first term in (2.25) is always positive for a non-zero current. The exchange current density $i_0^i(t_{\text{st}})$ depends on the solid and liquid concentrations as in (3.7c) through the unknown kinetic coefficient k^i that, similarly to the ohmic resistance R_{Ω} , depends on temperature according to the Arrhenius-like equation (3.10); we can now cast the parametrization as an optimization problem of the form

$$\begin{aligned}
 &\min_{k_{\text{ref}}^i, E_{\text{act},k}^i, R_{\Omega,\text{ref}}, E_{\text{act},R_{\Omega}}} \quad \left\| R_{\text{exp}} - R(t_{\text{st}}^+) \right\| \\
 &\text{subject to} \quad (3.7c), (3.10) \text{ and } (2.25),
 \end{aligned} \tag{2.26}$$

where the electrolyte conductivity depends on temperature according to the functional form illustrated in [42]. In Figure 2.5 we plot the model surfaces at constant temperature that approximate the experimental data (circles) at different SOC and current applied. The model surfaces approximate well the lower resistance values at higher temperature; moreover it is evident that the effect of the kinetic overpotential is accentuated at low temperature and for small SOC values, more specifically low current values lead to higher resistance.

The physics-based nature of the electrochemical model allows to extrapolate the resistance behavior even when only few measurements are

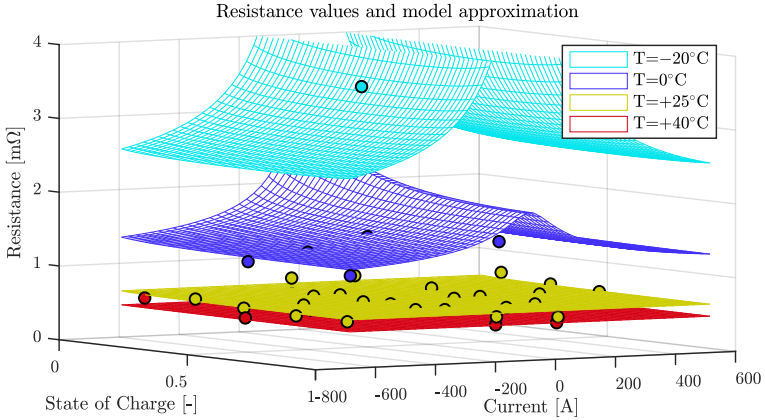


Figure 2.5: Experimental cell resistance and model prediction (surfaces).

taken at a specific condition, e.g. at very low temperatures (-20°C) and for small SOC values.

DIFFUSION RELATED PARAMETERS While the liquid phase dynamics is defined by the coefficients characterized in [42] computed at the average concentration of $c_{e,\text{avg}} = 1.2 \text{ mol/cm}^3$, the electrodes temperature-dependent diffusion coefficients have to be estimated using the dynamic information of our dataset. In this work we used the measurements from constant charge/discharge current pulses acquired at different temperatures and SOC values; with long enough pulses (approx 60 s) we excite the system in the frequency range from 5 Hz to nearly 0 Hz, which covers the typical usage of the hybrid vehicle and corresponds to the frequency domain in which the reduced-order model of Section 2.1.1.2 is valid.

We set-up the identification procedure by first re-sampling the dataset over the time grid $\mathbf{G}_N = \{t_0, t_1, \dots, t_{st}, \dots, t_N\}$, with N intervals and variable time steps $h_{k+1} = t_{k+1} - t_k$, $k = 0 \dots N$; we design the grid so that it is thicker near the rising and falling edges of the current step in order to capture the fast variations in the current and voltage values. We then discretize the reduced order solid-phase diffusion dynamics (2.19) over the same grid \mathbf{G}_N following the generic one-step method $\psi(\cdot)$ as

$$x(t_{k+1}) = x(t_k) + \psi(x, I, T), \quad (2.27)$$

starting from the initial condition $x(t_0) = x_0$. In this work we used the 4th order Runge-Kutta method [16] for the discretization of the solid and liquid diffusion dynamics, that guarantees good accuracy with few

discretization points at the cost of evaluating more values of the dynamic functions.

The parametrization problem is formulated, similarly to the previous steps, as the minimization of the squared error between the experimental and the simulated terminal voltage, i.e. $\Delta V(t_k) = V_{\text{exp}}(t_k) - V(t_k)$, for every points of the time grid. The problem is solved simultaneously for the N_I current and N_T temperature profiles and for the N_S initial SOC, namely

$$\begin{aligned} \min_{D_{s,\text{ref}}^i, E_{\text{act},D_s}^i} \quad & \sum_{j_i, j_T, j_S=1}^{N_I, N_T, N_S} \sum_{k=0}^N \Delta V(t_k, I_{j_i}(t_k), T_{j_T}(t_k), \text{SOC}_{0,j_S})^2 \\ \text{subject to} \quad & (2.11), (2.19), (3.10) \text{ and } (2.27) \\ & \theta_{0\%}^i \gtrsim \theta^i(t_k) \gtrsim \theta_{100\%}^i, \quad i = \text{p, n} \end{aligned} \quad (2.28)$$

for $t_k \in \mathbb{G}_N$. Wrong values of the activity coefficients could lead to non feasible solid phase concentrations, therefore we have constrained in problem (2.28) the stoichiometries θ^i at the two electrodes to stay within the maximum and minimum values resulting from (2.24) in order to ensure the robustness of the solution algorithm.

Notice that this minimization is valid also when the temperature varies during the test, because we have shown that the proposed state space realization (3.9) is able to approximate the partial differential equation (2.2) also for non-constant temperatures. This means that we could perform the parametrization of the diffusion coefficients even with longer cycles at higher current values, that are more representative of the standard HEV usage.

The simultaneous solution over different temperatures, current amplitudes and initial SOC of the parametrization problem allows to find the best set of parameters in a wide range of conditions, but we could easily incur in local minima. Metaheuristic optimization algorithms [2] (e.g. particle swarm [11]) allow to explore the space of the solutions and are in general less prone to converge to local minima, but they exhibit fairly slow convergence when dealing with large size problems and cannot easily handle complex constraints. For these reasons, standard non-linear least squares algorithms are more appealing for the solution of problem (2.28), but they could more easily get stuck in a local optimum. Nevertheless, it is reasonable to assume that the best set of parameters could be found in the vicinity of the local solution. This is the fundamental principle behind the Monotonic Basin Hopping (MBH) [25], a quasi-global optimization algorithm that exploits the “funnel like” structure of many optimization problems to explore the space of solutions by means of local

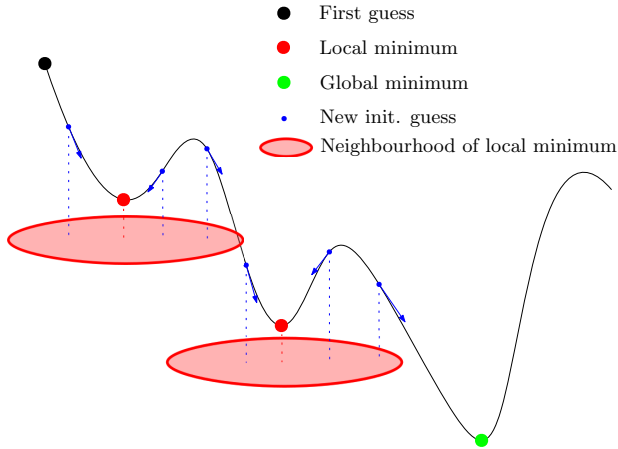


Figure 2.6: Sketch of the MBH algorithm on a “funnel-like” function.

searches. In the following section we will briefly illustrate the main steps of this optimization algorithm.

2.1.2.2 NLP Solution Method: Monotonic Basin Hopping

Similarly to the multi-start optimization methods [43], where many local searches are performed starting from different initial guesses sampled randomly within the allowable bounds, also the MBH algorithm repeats many local optimization starting from different initial guesses, yet selecting them in a neighborhood of a local minimum; if a better minimum is found, the algorithm will start the following local optimizations in the vicinity of this new optimal solution, otherwise an “impatience” counter is incremented. The iterations continue until a stopping condition (in general an iterations number limit or CPU time) is met. Figure 2.6 sketches the idea of the MBH working principle on a multi-minima function.

In this work we used the MBH version proposed in [13], where, once the local search finds the best minimum in the funnel, a new global search starting from a randomly selected point is performed with the aim of exploring the entire solution space. In the same work, the authors shown that the efficiency and robustness of the algorithm can be improved by selecting the random initial guess from long tail distributions (like Cauchy or bi-polar Pareto).

In the following section we present the validation results of the parametrization procedure.

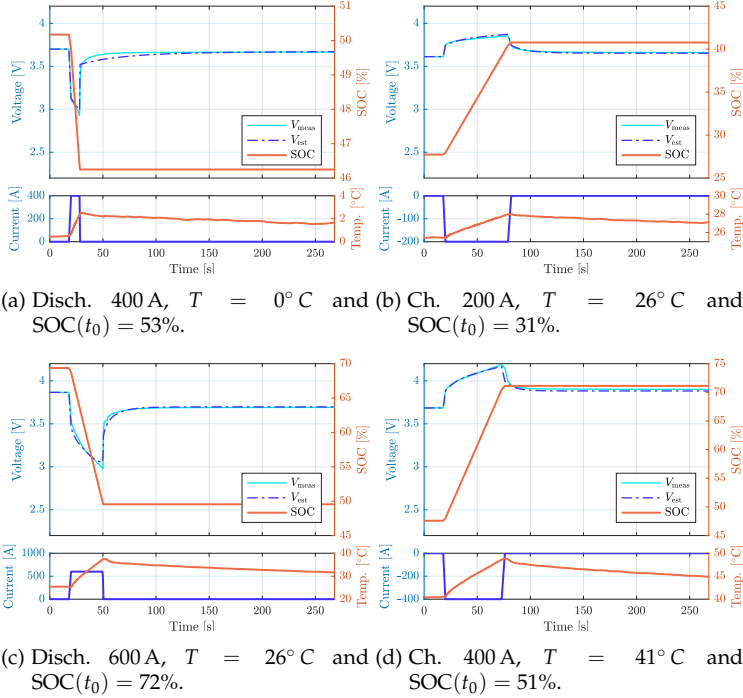


Figure 2.7: Comparison between experimental voltage and model prediction over pulse dataset.

2.1.2.3 Model validation

We test the validity of the parametrization procedure by comparing the cell voltage estimated by the model with the measured cell voltage subject to two current profiles at two different temperatures.

First, we examine the behavior of the model using current pulses of different amplitudes; from Figure 2.7 we see that the model follows with good accuracy the measured voltage for all temperature, voltage and initial SOC, even though the simulated relaxation dynamics seems faster than the actual one. The SOC evolution is computed by integrating the precise current measurement of the battery cyclers according to the Coulomb counting method in (2.18). As it is proved in many other works, the addition of the electrolyte dynamics and the liquid state diffusion to the model favors a good prediction at higher C-rates.

Because the aim of this work is to model the battery system for a high-performance hybrid electric car, it is crucial to assess the goodness of our model in situations characteristic of the specific application. To this end, we present in Figure 2.8 the comparison between the estimated and measured terminal voltage resulting from a current profile required for completing nine laps of the Fiorano track. Our model is able to predict

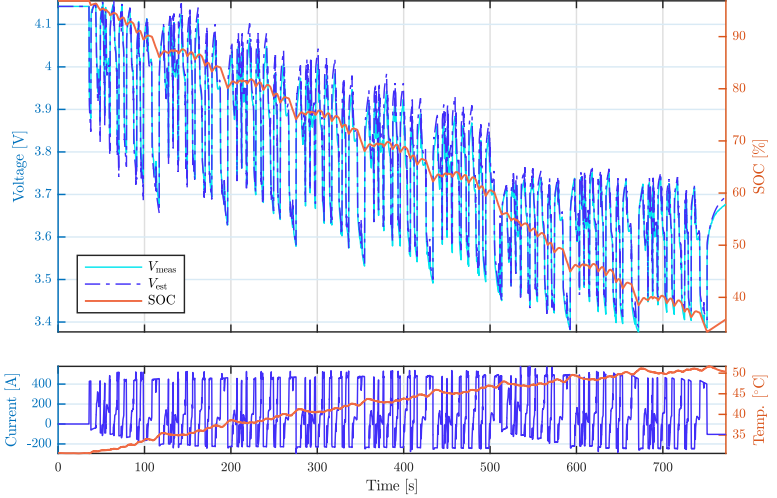


Figure 2.8: Comparison between measured and predicted voltage for a current profile required for nine laps of the Fiorano track.

the measured voltage with an acceptable prediction error: the goodness of fit (GoF) is quantified using the Normalized Root Mean Squared Error (NRMSE), and is defined as

$$\begin{aligned} \text{GoF}[\%] &= (1 - \text{NRMSE}) \cdot 100 \\ &= \left(1 - \frac{\|V_{\text{exp}} - V\|}{\|V_{\text{exp}} - \bar{V}_{\text{exp}}\|} \right) \cdot 100 \end{aligned}$$

where V is the estimated terminal voltage, \bar{V}_{exp} is the average measured voltage value and $\| \cdot \|$ indicates the 2-norm of a vector. For the test in Figure 2.8, the resulting goodness of fit is equal to $\text{GoF} = 88.02\%$.

Another common reference circuit to assess a sport car performance is the Nürburgring track. In Figure 2.9 we compare the predicted and the experimental terminal voltage resulting from a current profile required for completing one lap of the Nürburgring track. The goodness of fit

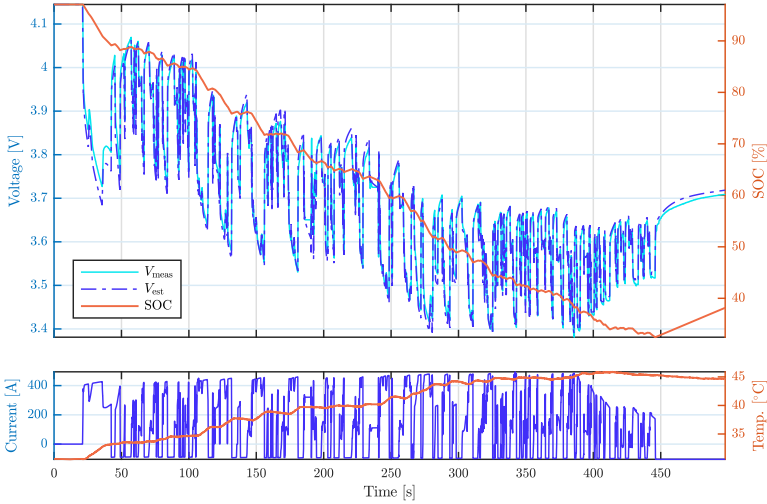


Figure 2.9: Comparison between measured and predicted voltage for a current profile required for one lap of the Nürburgring track.

is equal to $\text{GoF} = 88.96\%$, which is similar to the previous case, thus certifying the repeatability of the results.

The good fitting outcome certifies the validity of the parametrization procedure, nevertheless it is not possible to determine whether the identified parameters correspond to their exact physical value. Indeed, the values resulting from the three optimization problems are just the parameters that best fit the experimental curves and there is no experimental evidence that they match the actual physical quantities.

2.1.3 Conclusions

In this section we have reported the full-order electrochemical model, also known as Doyle-Fuller-Newman (DFN) model by detailing the system of Partial Differential Equations and the other governing equations. We thus proposed a model order reduction technique based on an approximation of the solid and liquid diffusion transcendent transfer function, and we suggested a realization of the resulting 5th order system that takes into account the temperature variations.

We formulated the identification problem as a non-linear programming problem using three different tests for each group of parameters and we described the technique used for the robust solution of the NLP problem.

Finally, we compared the model prediction of the cell terminal voltage with the experimental voltage measured applying current profiles which are typical of the battery applications.

In the next chapter we will introduce the battery degradation mechanisms and we will propose a model to capture the capacity losses.

2.2 THE DEGRADATION MODEL

The degradation of battery performances over time can be traced back to a series of complex and intertwined processes. The battery deterioration is determined both by capacity fade—the loss of available energy deliverable by the battery—and by power fade—the drop of the battery ability to deliver or to absorb power. Capacity fade is usually associated to the loss of cyclable lithium ions as a consequence of side-reactions at the electrode, while power fade is related to the rise of the internal impedance caused by alterations of the electrode structure and by the formation of a passivating layer at the anode-side.

It is well-established that most of the battery aging mechanisms occur at the anode-side [24], thus many researches focus on the analysis of different anode materials in order to extend battery life and to improve its performance.

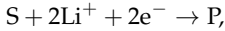
Battery aging is usually split into two categories: *calendar aging* and *cycle-induced aging*; the former refers to the deterioration of the battery performance after long storage times, while the latter concerns the—usually faster—power and capacity fade as a consequence of charge and discharge cycles. From a system perspective, this classification is highly convenient because we can plan an appropriate experimental campaign in order to observe the aging behavior in the two distinct situations; nevertheless we should bare in mind that the aging processes that occur during the storage time continue also when the battery is subject to charge and discharge cycles and are affected by the changes of the internal state induced by the applied current.

2.2.1 Aging Mechanisms

In this section we list the main aging mechanisms and we discuss how they affect the two aforementioned situations. An extensive overview of these mechanisms can be found in the survey works [1] and [18].

2.2.1.1 Solid electrolyte interphase growth

The high potential difference between the liquid electrolyte and the negative solid electrode activates an irreversible side-reaction at the interface between the two phases that produces a coating around the anode particle, called solid-electrolyte-interphase (SEI) layer. Given the solvent reactants S , the generic SEI formation reaction at the anode surface is written as



where P is the product of the irreversible reactions between the lithium ions and the carbon-based compounds of the electrolyte. The SEI is formed by a “mosaic” of such products as pictured in Figure 2.10.

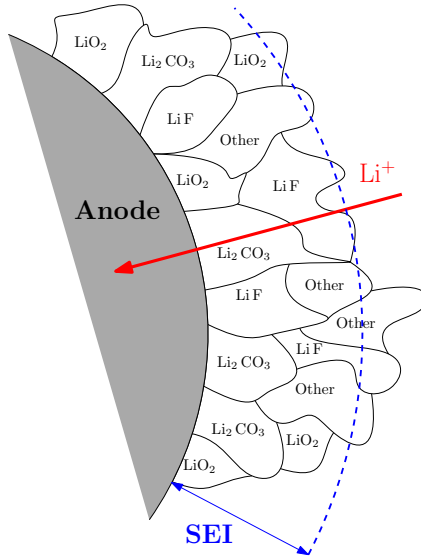


Figure 2.10: SEI layer representation.

In the first stages of the battery life this layer is beneficial for the electrode, because it slows down further SEI formation reactions but it still permits the passage of the lithium ions that intercalate in the anode; however, as the layer thickness grows consuming lithium ions in the irreversible reaction of SEI formation, the path of the lithium ions through the SEI becomes more tortuous and this results in a rise of the cell impedance. In other words, the SEI forms a passivating coating

around the anode by consuming cyclable lithium ions, thus causing both capacity and power fade.

The irreversible side-reaction occurs even when no current is applied to the battery, meaning that the deterioration of the performance caused by the SEI formation is observable after long storage periods. Indeed, it is widely accepted that SEI is the main cause of the battery calendar aging [12, 23, 24, 45, 46].

The SEI formation is the most well-known aging mechanism and there exist many empirical and electro-physical models that relate the growth rate of the layer to the storage SOC and temperature. Both empirical and electrochemical models agree on the hypothesis that the SEI growth rate is proportional to the square root of the storage time. This is in accordance with the intuition that the thicker the SEI layer, the slower the formation of new layers is; in other words, the side-reaction that forms new SEI is a self-inhibiting reaction and slows down with time.

In this work we adopt a slightly modified version the physics-based SEI formation model presented in [22], where the capacity loss Q_{sei} is computed by integrating the side-reaction rate as

$$Q_{\text{sei}} = \int_0^t i_{\text{sei}}(t) A^n dt \quad (2.29)$$

where $i_{\text{s}}(t)$ is the side-reaction current density that is described by a Butler-Volmer kinetics relation governed by the kinetic overpotential for the side-reaction

$$\eta_{\text{sei}}(t) = \eta^n(t) + U^n(t) - U_{\text{sei}}, \quad (2.30)$$

where η^n and U^n are the anode overpotential (3.7b) and the equilibrium potential respectively and U_{sei} is the equilibrium potential for the solvent reduction reaction. The diffusion of the solvent reactant through the SEI, that follows the Arrhenius-like trend in (3.10), is assumed to be the limiting factor for the side-reaction to occur; under this assumption, we can neglect the lithium diffusion through the electrode bulk and come up with a simple formulation of the capacity loss, which is

$$Q_{\text{sei}}(t) = \int_0^t -\frac{k_{\text{sei}} \exp\left[-\frac{E_{\text{sei}}}{R_{\text{g}}}\left(\frac{1}{T(t)} - \frac{1}{T_{\text{ref,sei}}}\right)\right]}{2\left(1 + \lambda \exp\left[\frac{\alpha F}{R_{\text{g}} T(t)} \eta_{\text{sei}}(t)\right]\right)} \sqrt{t} dt, \quad (2.31)$$

where k_{sei} , E_{sei} , λ and α are tuning parameters and the SEI overpotential is as in (2.30). In Section 2.2.2 we will show how to tune the model parameters based on storage data.

The exponential term at the numerator of (3.12) captures the faster capacity loss experienced at high temperature due to the faster diffusion

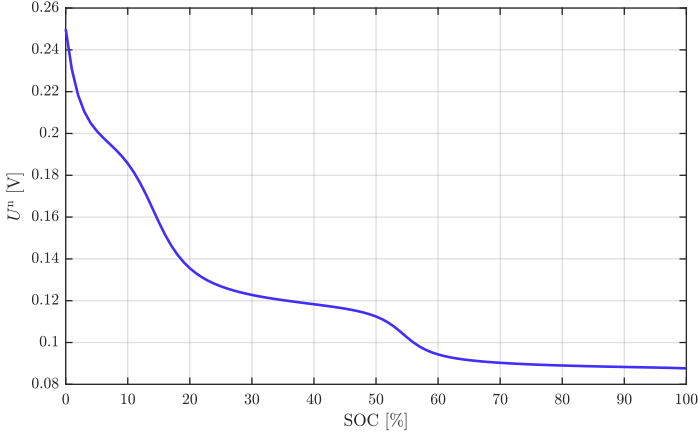


Figure 2.11: Open circuit potential at anode-side as a function of SOC.

of the solvent reactant through the SEI layer.

It is also interesting to notice that higher SEI overpotential values leads to a lower capacity loss rate. According to (2.30), low anode-side open circuit potential and kinetic overpotential correspond to low $\eta_{\text{sei}}(\cdot)$ that leads to faster aging; as reported in Figure 2.11 higher SOC levels maps to lower equilibrium potential, meaning that the cell ages faster when it is stored at higher SOC. Finally, we should notice from (2.30) that a negative (charging) current leads to a negative anode-side kinetic overpotential $\eta_n(\cdot)$, that greatly reduces SEI overpotential and consequently accelerates SEI formation.

If the battery is stored in a controlled temperature environment at a constant SOC, then the integral in (2.30) can be analytically solved because all the time-dependent variables are constant and the kinetic overpotential is zero, yielding

$$\begin{aligned}
 Q_{\text{sei}}(t) &= -\frac{k_{\text{sei}} \exp\left[-\frac{E_{\text{sei}}}{R_g} \left(\frac{1}{T} - \frac{1}{T_{\text{ref,sei}}}\right)\right]}{\left(1 + \lambda \exp\left[\frac{\alpha F}{R_g T} (U^n(\text{SOC}) - U_{\text{sei}})\right]\right)} \sqrt{t} \\
 &= -\varphi_{\text{sei}}(T, \text{SOC}) \sqrt{t},
 \end{aligned} \tag{2.32}$$

where the SEI stress intensity factor $\varphi_{\text{sei}}(T, \text{SOC})$ depends on temperature and SOC according to the trend of Figure 2.12.

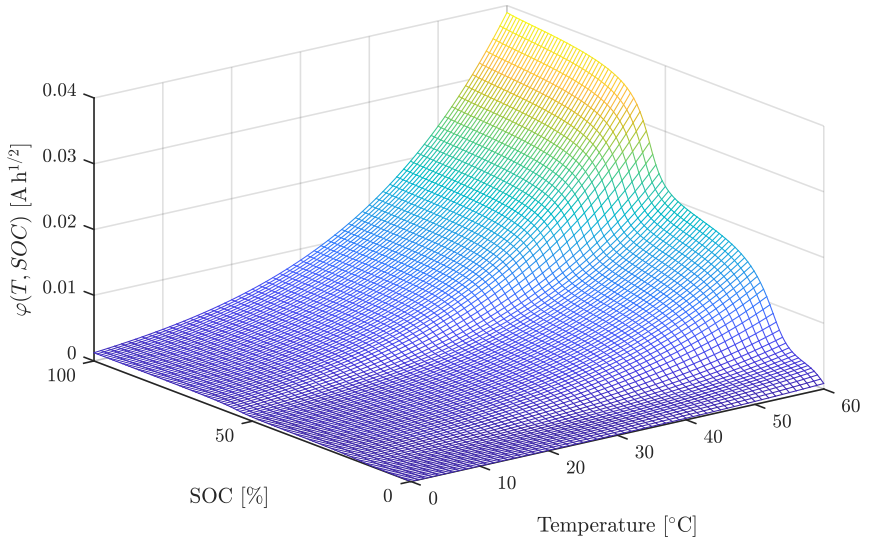


Figure 2.12: Stress factor for capacity loss due to SEI formation.

2.2.1.2 Anode overhang

In recent studies [26–28, 44], an apparent rise of the recovery capacity after storage have been observed for certain storage conditions in the early stages of battery life. This effect has been explained by the *passive electrode effect*, that is related to the part of anode area that has no counter electrode (cathode), named *anode overhang* (see Figure 2.13). This geometrical excess of the anode is used to avoid lithium plating effects at the edge of the electrode. If a concentration gradient exists between the overhang and the part of the anode overlapped by the cathode, the lithium slowly migrates from the region at higher concentration to the region at lower concentration, until the equilibrium is reached.

The area of the anode overhang A_{aoh} is simply computed by subtracting the area of the two electrodes, namely

$$A_{\text{aoh}} = A^{\text{n}} - A^{\text{p}}. \quad (2.33)$$

At the initial storage time t_0 , we assume that the lithium concentration in the central part of the anode $c_{\text{s,avg}}^{\text{n}}(t_0)$ —computed from initial SOC according to (2.16)—is smaller than (higher than) the concentration of lithium in the overhang $c_{\text{aoh}}(t_0)$; this concentration gradient gives rise to the lateral diffusion of lithium from (to) the overhang to (from) the

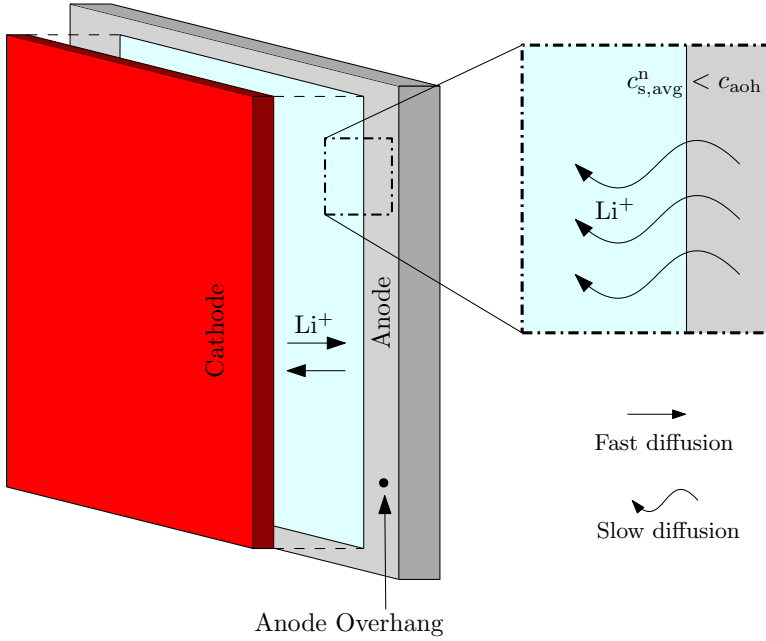


Figure 2.13: View of the anode overhang for a single layer of the cell.

part of the anode overlapped by the cathode that tends to equilibrate the concentration of the overall anode area at the weighted average value

$$\begin{aligned}
 c_{\text{eq}} &= \frac{c_{\text{s,avg}}^{\text{n}}(t_0)(A^{\text{n}} - A_{\text{aoh}}) + c_{\text{aoh}}(t_0)A_{\text{aoh}}}{A^{\text{n}}} \\
 &= \frac{A^{\text{P}}}{A^{\text{n}}}c_{\text{s,avg}}^{\text{n}}(t_0) + \frac{(A^{\text{n}} - A^{\text{P}})}{A^{\text{n}}}c_{\text{aoh}}(t_0).
 \end{aligned} \tag{2.34}$$

The lateral diffusion through the solid phase due to the passive electrode effect is much slower than the diffusion through the electrolyte due to charge/discharge cycles, but for long storage time it can sensibly alter the measurement of the recovery capacity releasing (or draining) cyclable lithium ions.

We model the lateral diffusion dynamics as a simple second order linear system of the form

$$\begin{bmatrix} \dot{c}_{\text{s,avg}}^{\text{n}}(t) \\ \dot{c}_{\text{aoh}}(t) \end{bmatrix} = \begin{bmatrix} -\frac{1}{\tau_{\text{T}}} & \frac{1}{\tau_{\text{T}}} \\ \frac{1}{\tau_{\text{aoh}}} & -\frac{1}{\tau_{\text{aoh}}} \end{bmatrix} \begin{bmatrix} c_{\text{s,avg}}^{\text{n}}(t) \\ c_{\text{aoh}}(t) \end{bmatrix}. \tag{2.35}$$

The two concentrations at the equilibrium are

$$c_{s,\text{avg}}^n(t \rightarrow \infty) = c_{\text{aoh}}(t \rightarrow \infty) = c_{\text{eq}} \quad (2.36)$$

with c_{eq} as in (2.34) if and only if the time constants in (2.35) are related according to

$$\tau_{\text{aoh}} = \frac{(A_n - A_p)}{A_p} \tau_{\Gamma}. \quad (2.37)$$

This follows from the analytic solution of the linear system (2.35), which is

$$\begin{bmatrix} c_{s,\text{avg}}^n(t) \\ c_{\text{aoh}}(t) \end{bmatrix} = \exp \left(\begin{bmatrix} -\frac{1}{\tau_{\Gamma}} & \frac{1}{\tau_{\Gamma}} \\ \frac{1}{\tau_{\text{aoh}}} & -\frac{1}{\tau_{\text{aoh}}} \end{bmatrix} t \right) \begin{bmatrix} c_{s,\text{avg}}^n(t_0) \\ c_{\text{aoh}}(t_0) \end{bmatrix},$$

that at the equilibrium ($t \rightarrow \infty$) becomes

$$\begin{bmatrix} c_{s,\text{avg}}^n(t \rightarrow \infty) \\ c_{\text{aoh}}(t \rightarrow \infty) \end{bmatrix} = \frac{1}{\tau_{\Gamma} + \tau_{\text{aoh}}} \begin{bmatrix} \tau_{\Gamma} & \tau_{\text{aoh}} \\ \tau_{\Gamma} & \tau_{\text{aoh}} \end{bmatrix} \begin{bmatrix} c_{s,\text{avg}}^n(t_0) \\ c_{\text{aoh}}(t_0) \end{bmatrix}$$

that fulfills (2.36) if and only if (2.37) is valid.

The only unknown parameters are the time constant τ_{Γ} and the initial anode overhang concentration $c_{\text{aoh}}(t_0)$, that should be calibrated on experimental measurements of the calendar aging. It is useful to define an equivalent anode overhang state of charge as

$$\text{SOC}_{\text{aoh}}(t) = \frac{\frac{c_{\text{aoh}}(t_0)}{c_{s,\text{max}}^n} - \theta_{0\%}^n}{\theta_{100\%}^n - \theta_{0\%}^n}. \quad (2.38)$$

The capacity loss associated to the anode overhang effect—that can be both positive or negative depending on the initial concentration gradients—is computed considering the variation of lithium concentration in the central part of the anode from its initial value that leads, according to (2.17), to a capacity loss (or increase) in units of Ah equal to

$$Q_{\text{aoh}}(t) = \frac{1}{3600} A^n L^n \varepsilon_s^n F \left(c_{s,\text{avg}}^n(t) - c_{s,\text{avg}}^n(t_0) \right). \quad (2.39)$$

2.2.1.3 Mechanical stress, electrode cracking and dendrite formation

The continuous intercalation and de-intercalation of lithium ions during charge and discharge cycles creates mechanical stresses at the electrodes. These stresses alter the structure of the electrode, reducing the contact surfaces among the electrode particles and thus increasing the impedance

of the battery. Moreover, high current values can fracture the electrode and, at the anode, exposing new surface for the electrolyte reduction reaction, thus accelerating the formation of new SEI. An interesting approximated model that describes the coupled effect of electrode cracking and SEI formation has been recently presented in [29].

Low potential values at the anode-side during high current charge favor lithium being plated as metal, resulting in the growth of metallic dendrites. Besides the obvious capacity fade (loss of lithium in the metallic lithium formation) and the impedance increase (metallic lithium impedes the lithium intercalation reaction), the lithium dendrites may penetrate the separator leading to internal short circuits. The authors of [21] have observed depositions of lithium plating in the samples aged at higher temperatures, suggesting a strong dependency of temperature of the plating reaction. This result contradicts the common knowledge that the formation of metallic dendrites is faster and more hazardous at low temperatures [4, 20]. This suggests that the definition of a precise model of lithium plating should rely on an extensive experimental campaign in order to shed light on the unknown variables that regulate this hazardous phenomenon.

Even though a unified modeling strategy is far to be found, many studies propose semi-empirical aging models that aim at capturing the main aging effects rather than trying to isolate the specific mechanisms. Such models are usually fairly simple and can be adopted in fast simulations. Because most of the parameters of the model are not related to physical quantities, they have to be calibrated on experimental values, therefore their validity is limited to the individual type of cell studied. Moreover, even the structure of the model could change from cells of different chemistries or different scope (power- or energy-specific cells). Nevertheless, most of the models describe the capacity loss as the sum of one (or more) term proportional to the the square-root of the current throughput and one term which is linear with the current throughput.

The aging model presented in this work blends some models already presented and validated in the literature with new models proposed to describe the characteristic aging of the Ferrari battery. Indeed, thanks to an extensive experimental campaign, we were able to collect aging data in several operating conditions and we found that none of the models already presented in the literature were able to fully capture the capacity fade of the battery. We have detailed in the previous sections the anode overhang and the SEI formation mechanisms, we will see in Section 2.2.2 how these two effects contribute to the calendar aging. Then, we will treat in Section 2.2.3 the cyclic aging effects, developing and integrating the recent results presented in the work by Schimpe et al. [37] to build

a model that can predict the capacity fade effects in different operating conditions.

2.2.2 Calendar Aging

We assume that the superposition of the aging effects detailed in Section 2.2.1 can be applied for both the calendar aging mechanisms. This allows us to write the overall capacity loss during storage as the sum of the contributions of the SEI formation (3.12) and of the anode overhang effect (2.39), yielding

$$Q_{\text{cal}}(t) = Q_{\text{sei}}(t) + Q_{\text{aoh}}(t). \quad (2.40)$$

To characterize the unknown parameters of the calendar aging model, we need to design an extensive experimental campaign that should represent different storage conditions. Two cells were stored at four different temperatures (25° C, 30° C, 45° C and 50° C) and three different SOC (50%, 75% and 95%), for a total of 24 cells tested. The average measured capacity for the first 24 weeks are reported in Figure 2.14.

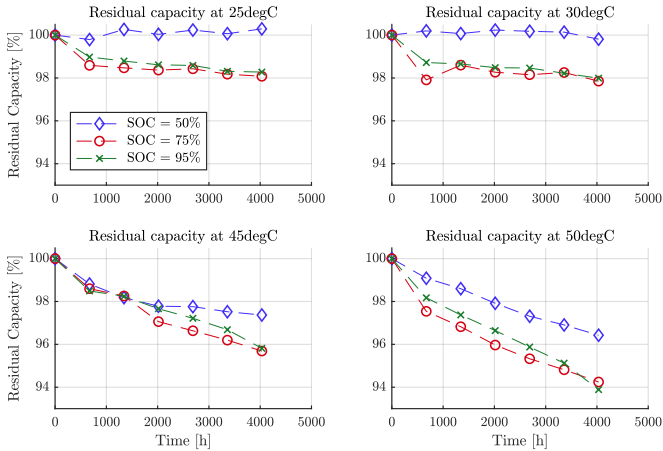


Figure 2.14: Measured residual capacity of the calendar aging tests.

It is interesting to notice that the samples stored at lower temperatures (25° C and 30° C) and low SOC (50%) exhibit almost no loss in the measured capacity; this could be explained with the migration of lithium from the anode overhang into the central part of the an-

ode that balances the loss of lithium in the SEI formation, namely $Q_{\text{sei}}(t) \approx -Q_{\text{aoh}}(t) \rightarrow Q_{\text{sei}}(t) \approx 0$.

It is worth to mention the unexpected behavior of the cells stored at 95% SOC, that seem to age slower than the samples stored at 75% SOC: this trend cannot be explained by the afore-mention model that predicts faster aging at higher storage SOC. A similar behavior have been also observed in [12] for the first 260 days of storage, after which the trend is reversed and the capacity loss of the sample stored at 95% SOC becomes faster as expected by the physics of aging reactions. We believe that after a sufficiently long storage time also our samples stored at 95% SOC will exhibit a faster aging, as shown by the last measurements of the cell stored at 50° C. We couldn't find any satisfying explanation to this unexpected behavior, that should be investigated with post-mortem analyses in a dedicated experimental campaign.

Since the temperature and SOC conditions remain constant throughout the storage time, we could resort to the analytic solution of the SEI formation dynamics (2.32), while the solution of the AOH dynamics (2.35) follows by the linear system theory. This allows us to compare the measured capacity loss of the N_{meas} measurements with the capacity loss predicted by the SEI growth model at constant conditions described by (2.32); the identification of the model parameters is formulated as usual as the minimization of the prediction error and the results are reported in Table 2.1 In Figure 2.15 we compare the experimental data and the model

	Symbol	Value
SEI formation	k_{sei}	$7.30 \cdot 10^{10}$
	E_{sei}	$5.86 \cdot 10^4$
	λ	$8.20 \cdot 10^5$
	α	0.52
	U_{sei}	0.4
Anode Overhang	τ_{Γ}	$2.39 \cdot 10^5$
	$\text{SOC}_{\text{aoh}}(t_0)$	0.83

Table 2.1: Calendar aging parameters.

prediction over a storage time of 8 years. The predicted residual capacity remain close to the nominal capacity in the first storage years, mainly because the side reaction kinetics at low SOC and low temperature is extremely slow, moreover the higher initial SOC of the anode overhang

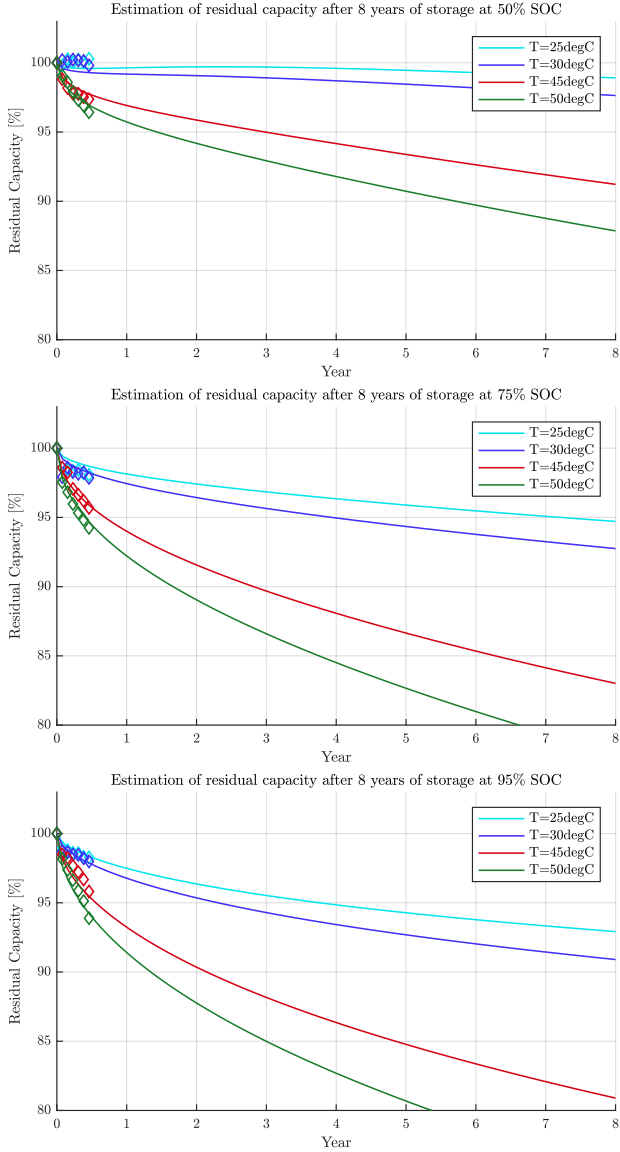


Figure 2.15: Comparison between measured calendar loss and model prediction.

favors the migration of lithium ions from the overhang to the central part of the electrode.

2.2.3 Cycle-induced Aging

As previously stated in Section 2.2.1, many mechanisms concur in the loss of capacity and impedance increase of the battery during charge and discharge cycles.

It is not possible to separately characterize the different degradation mechanisms using only measurements of the residual capacity and impedance, since battery degradation is the result of the combined accumulation of such mechanisms. Nevertheless, some of them prevail in specific conditions: for instance it is widely accepted (with some exceptions — see [21]) that the lithium plating is the main cause of battery degradation at low temperature, while SEI formation dominates at high temperature. Bearing this in mind, in order to improve the prediction of the residual battery life over a wide range of operating conditions, we should give the aging model a structure that mimics the separation of the aging processes.

In this work we use the semi-empirical cycle aging model proposed in [37], where three capacity loss contributions are used to describe the degradation dynamics under three different conditions: high temperature, low temperature and high SOC at low temperature. In the following we recall the model equations and we detail the procedure to identify the model parameters using capacity loss data from realistic charge/discharge cycles.

2.2.3.1 Model description

The assumption of superposition of the aging effects allows us to write the overall capacity loss as the sum of all the mechanisms that contribute in battery degradation; using $Q_{\text{cyc}}(t)$ to indicate the capacity loss due to current cycles at time t we could write the overall capacity loss as the sum of SEI, AOH and cycle contributions as

$$Q_{\text{tot}}(t) = Q_{\text{sei}}(t) + Q_{\text{aoh}}(t) + Q_{\text{cyc}}(t). \quad (2.41)$$

Notice that during charge and discharge cycles, we must consider that both the anode overpotential $\eta_{\text{n}}(\cdot)$ and the open circuit potential $U_{\text{n}}(\cdot)$ are not constant, thus also the SEI overpotential $\eta_{\text{sei}}(\cdot)$ in (2.30) varies with time and the analytic solution (2.32) for the SEI loss is no more valid.

According to [37], the cycle capacity loss $Q_{cyc}(\cdot)$ is the sum of three terms, each representing a specific condition, namely

$$Q_{cyc}(t) = Q_{ht}(t) + Q_{lt}(t) + Q_{lt,hs}(t) \quad (2.42)$$

where the subscripts lt, ht and lt,hs indicate the losses at high temperature, low temperature and high SOC at low temperature respectively.

At high temperature, the dominant cycle-induced loss mechanism is the faster growth of the SEI layer as a consequence of the perturbation of the anode structure; indeed, the charge and discharge cycles induce mechanical strains in the electrode, leading to the formation of small cracks that expose new active surface for the side reaction to happen. The experimental trends of the capacity loss—we will discuss them in the next section—suggest a dependency on the square-root of the total current throughput $\Gamma_{tot}(t) = \int_0^t V(t)|I(t)| dt$; this, similarly to the SEI formation, indicates a self-inhibiting tendency of the loss mechanism. The cycle-induced capacity loss at high temperature is formulated as

$$Q_{ht}(t) = \int_0^t \underbrace{k_{ht} \exp \left[-\frac{E_{ht}}{R_g} \left(\frac{1}{T(t)} - \frac{1}{T_{ref}} \right) \right]}_{\varphi_{ht}(t)} \frac{V(t)|I(t)|}{2\sqrt{\Gamma_{tot}(t)}} dt \quad (2.43)$$

where the dependency on temperature of the stress factor $\varphi_{ht}(\cdot)$ is captured by an Arrhenius like equation. If the temperature remains constant throughout the cycle and the initial current throughput $\Gamma_{tot}(0) = 0$, we could solve the integral in (2.43) as

$$\begin{aligned} Q_{ht}(t) &= \varphi_{ht} \int_0^t \frac{V(t)|I(t)|}{2\sqrt{\Gamma_{tot}(t)}} dt \\ &= \varphi_{ht} \int_0^{\Gamma_{tot}(t)} \frac{1}{2\sqrt{\Gamma_{tot}}} d\Gamma_{tot} \\ &= \varphi_{ht} \sqrt{\Gamma_{tot}(t)}, \end{aligned}$$

where we highlighted the dependency on square-root of the current throughput and we used the change of variable $d\Gamma_{tot} = V(t)|I(t)| dt$.

At low temperature, the primary aging mechanism is lithium plating, which is associated to transport limitations inside the anode when a charging current is applied to the cell. This is taken into account in the model by introducing a dependency of the stress factor on the charge current and by considering only charge-current throughput $\Gamma_{ch}(t) = \int_0^t V_{ch}(t)|I_{ch}(t)| dt$

in the formulation. The capacity loss at low temperature is thus formulate as

$$Q_{lt}(t) = \int_0^t \varphi_{lt}(t) V_{ch}(t) |I_{ch}(t)| dt, \quad (2.44)$$

where the stress factor $\varphi_{lt}(\cdot)$ depends on temperature and charge current according to

$$\varphi_{lt}(t) = k_{lt} \exp \left[\frac{E_{lt}}{R_g} \left(\frac{1}{T(t)} - \frac{1}{T_{ref}} \right) \right] \exp \left[\beta_{lt} \frac{|I_{ch}(t)| - I_{ref}}{Q_{nom}} \right].$$

Notice that the Arrhenius dependency in (2.44) is opposite to the one in (2.43), meaning that this mechanism is faster at lower temperature values. Similarly to the previous case, if we keep the temperature constant and we apply the same constant charge current to the battery, we can analytically solve the integral (2.44) and get

$$Q_{lt}(t) = \varphi_{lt} \sqrt{\Gamma_{ch}(t)}.$$

The plating of metallic lithium occurs when the anode potential $\phi_s^n(\cdot)$ reaches negative values. Recall from (2.8) that the overall potential at the anode-side can be expressed as

$$\phi_s^n(t) = U^n(t) + \eta^n(t) + \phi_e^n,$$

therefore negative potentials at the anode can be reached for negative values of the overpotential—i.e. when a charging current is applied—and when the equilibrium potential $U^n(t)$ is small. The latter condition occurs, according to Figure 2.11, at high SOC; this is confirmed by experimental aging data collected from cells that are subject to charging current at high SOC. Contrarily to the other terms, here a linear dependence on the charge-current throughput has been introduced to better fit the experimental data. The capacity loss equation for charge cycles at low temperature and high SOC is here defined as

$$Q_{lt,hs}(t) = \int_0^t \varphi_{lt,hs}(t) V_{ch}(t) |I_{ch}(t)| dt, \quad (2.45)$$

where the stress factor $\varphi_{lt,hs}(\cdot)$ depends on temperature and current similarly to (2.44), and a new term is added to take SOC-dependency into account, namely

$$\begin{aligned} \varphi_{lt,hs}(t) = & k_{lt,hs} \exp \left[\frac{E_{lt,hs}}{R_g} \left(\frac{1}{T} - \frac{1}{T_{ref}} \right) \right] \\ & \exp \left[\beta_{lt,hs} \frac{|I_{ch}(t)| - I_{ref}}{Q_{nom}} \right] \left(\frac{\text{sign}(\text{SOC}(t) - \text{SOC}_{ref}) + 1}{2} \right). \end{aligned}$$

If we consider constant conditions as in the previous cases, the stress intensity factor is constant and the analytic solution of the integral becomes

$$Q_{lt,hs}(t) = \varphi_{lt,hs} \Gamma_{ch}(t),$$

showing a linear dependency of the capacity loss on the charge energy throughput.

Now that the model structure is defined, we need to calibrate its parameters with an extensive experimental campaign that is representative of the operating conditions of the cell. In the next sections we present the data collection and we discuss how to calibrate the model bypassing the need of time-consuming simulations of the aging process.

2.2.3.2 *Experimental validation of the aging model*

The semi-empirical cycle aging model has to be valid for all the typical charge/discharge cycles that the cell is expected to undergo throughout its life. For this reason nine different current profiles, reported in Appendix 2.B, were designed to cover the widest number of possible driving scenarios: from urban to circuit, from highway to hill road, etc.

The current profiles were run continuously on the cells, monitoring voltage, temperature and SOC. The test was stopped when the residual cell capacity reached 80% of its initial nominal value. To track the evolution of the battery capacity, a reference performance test (RPT²) is carried out every increment of 14 kWh of energy passing in the cell. Since the average power of each cycle is different, the RPTs are taken after a diverse number of repetitions and in different days depending on the cycle. The residual capacity for each cycle is reported in Figure 2.16.

It is clear from the data that two profiles, the Fiorano (**FI**) cycle and the high speed (**AV**) cycle cause a much faster deterioration of the cell capacity, while the remaining seven profiles follow a similar trend.

MODEL PARAMETRIZATION The experimental cycle-induced capacity loss $Q_{cyc}^{exp}(\cdot)$ is computed from (2.41) by subtracting the estimated capacity loss due to SEI growth and to AOH from the experimental total loss for each RPT, namely

$$Q_{cyc}^{exp}(t_j) = Q_{tot}^{exp}(t_j) - (Q_{sei}(t_j) + Q_{aoh}(t_j)), \quad j = 1, \dots, n_{rpt}$$

where n_{rpt} is the total number of RPTs of a given current profile. The capacity loss due to SEI growth and to AOH is estimated considering the temperature and current variations over the entire test.

2 The RPT is a standard test used to measure cell capacity and resistance.

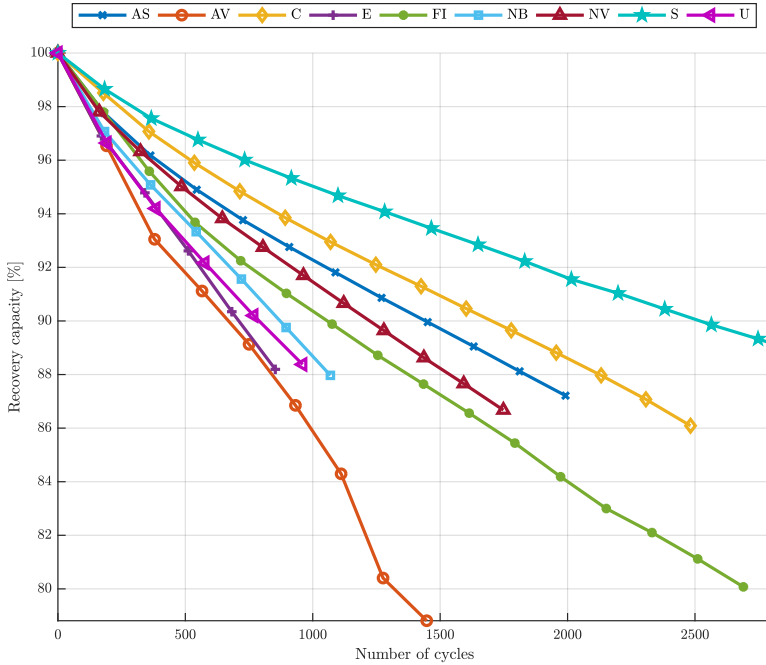


Figure 2.16: Residual capacity for each current profile. The markers indicate the capacity measured at the RPT and the solid lines are used to better visualize the trends.

The optimal model parameters minimize the modeling error, thus we determine their value by solving the non-linear least-squares problem

$$\min_P \sum_{j=1}^{n_{\text{rpt}}} \left[Q_{\text{cyc}}^{\text{exp}}(t_j) - Q_{\text{cyc}}(t_j) \right]^2,$$

where P is a vector that contains the unknown model parameters listed in Table 2.2 and the simulated cycle-induced loss is computed from (2.42). Considering the capacity loss contributions (2.43), (2.44) and (2.45), we can write the total cycle-induced losses at time t_j as

$$\begin{aligned} Q_{\text{cyc}}(t_j) &= \int_0^{t_j} \left[\varphi_{\text{ht}}(t) \frac{V(t)|I(t)|}{2\sqrt{\Gamma_{\text{tot}}(t)}} + \varphi_{\text{lt,hs}}(t) V_{\text{ch}}(t) |I_{\text{ch}}(t)| \right. \\ &\quad \left. + \varphi_{\text{lt}}(t) \frac{V_{\text{ch}}(t) |I_{\text{ch}}(t)|}{2\sqrt{\Gamma_{\text{ch}}(t)}} \right] dt \\ &= \int_0^{t_j} q_{\text{cyc}}(t) dt \\ &= \int_0^{t_{j-1}} q_{\text{cyc}}(t) dt + \int_{t_{j-1}}^{t_j} q_{\text{cyc}}(t) dt \\ &= Q_{\text{cyc}}(t_{j-1}) + \int_{t_{j-1}}^{t_j} q_{\text{cyc}}(t) dt. \end{aligned}$$

This means that we can compute the capacity loss of the RPT at time t_j as the sum of the capacity loss at time t_{j-1} and the integral of $q_{\text{cyc}}(\cdot)$ from t_{j-1} to t_j , which is considerably faster than computing the integral over the total time interval from $t_0 = 0$ to t_j . This recursive computation is of paramount importance to speed-up the non-linear least squares solution algorithm.

We used the non-linear least-squares solver `lsqnonlin` of the Optimization Toolbox in Matlab and provided the derivative of the cost function w.r.t. the unknown parameters P to find the minimizer of the aforementioned problem. In order to better explore the space of the solutions we combined the non-linear least-squares solver with the Monotonic Basin Hopping algorithm detailed in Section 2.1.2.2. We used the data from five different current profiles (corresponding to the driving cycles C, FI, U, AV and E) as identification dataset, and we employed the remaining four (S, NB, NV and AS) to validate the results. The values of the identified parameters are listed in Table 2.2, while the stress factors surfaces are illustrated in Figure 2.17. It is interesting to notice that the stress factor for the aging mechanism at low temperature $\varphi_{\text{lt}}(\cdot)$ does not manifest any dependency on the current intensity; indeed, the value of β_{lt} in Table 2.2 is extremely small and can be approximated to zero.

	Symbols (P)	Value
High Temperature	k_{ht}	$1.56 \cdot 10^{-6}$
	E_{ht}	$8.06 \cdot 10^5$
Low Temperature	k_{lt}	2.26
	E_{lt}	$9.62 \cdot 10^4$
	β_{lt}	$9.58 \cdot 10^{-8}$
Low Temperature, High SOC	$k_{lt,hs}$	$7.91 \cdot 10^{-11}$
	$E_{lt,hs}$	$1.04 \cdot 10^5$
	$\beta_{lt,hs}$	2.13

Table 2.2: Cycle-induced aging parameters P with $T_{ref} = 298.15\text{K}$ and $I_{ref} = 1\text{C}$ (26 A).

MODEL VALIDATION In this section we compare the capacity loss predicted by the identified model with the experimental capacity loss of the identification and validation dataset. Moreover, we use the recent aging dataset from the new cell prototype (*Proto C*) to assess the accuracy of the model with a slightly different cell type.

In Figure 2.18 the solid lines represent the model predictions while the circles indicate the experimental value. It can be noticed that the prediction error remains within a band of $\pm 3\%$ and is comparable both in the identification and in the validation dataset. The model is able to describe the aging trends, in particular it is able to capture the much faster capacity degradation of the driving cycles FI and AV.

The urban driving cycle (U-cycle) exhibits the largest approximation error (3% for the last sample); indeed, the model predicts a smaller value of capacity loss which is reasonable considering the not so severe current profile in Figure 2.B.9. Further tests are required on the same current profile to study the incidence of other factors that have not been considered in this study.

It is now interesting to inspect the single contributions of the three terms composing the overall cycle-induced aging in Figure 2.19, where the model prediction (solid line) and the single contributions (dashed lines) are plotted together with the experimental data from the *Proto B2* cell (green circles) and from the newest *Proto C* cell (red squares). The separate visualization of the different driving cycles make it easier to assess the goodness of the proposed aging model, also for the cycles with slower degradation—except for the already mentioned U-cycle.

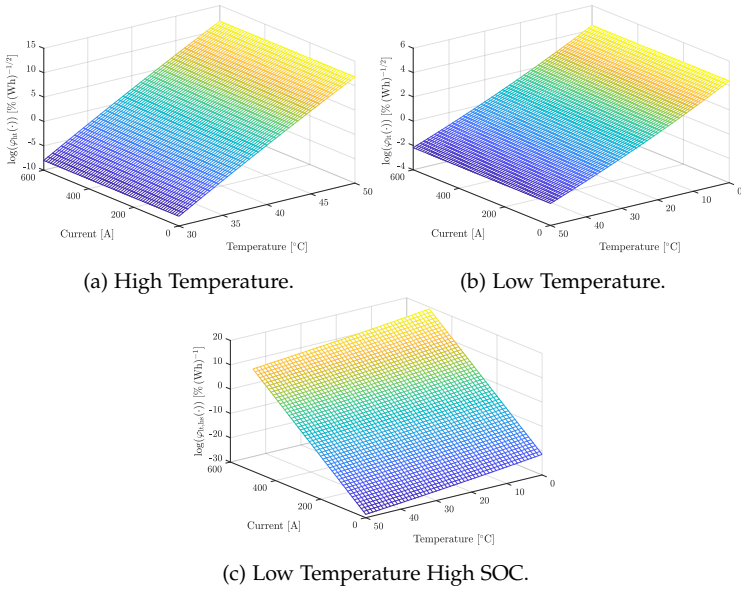
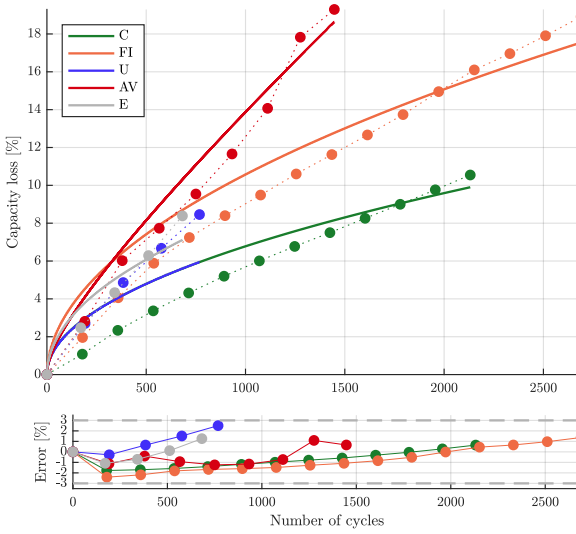


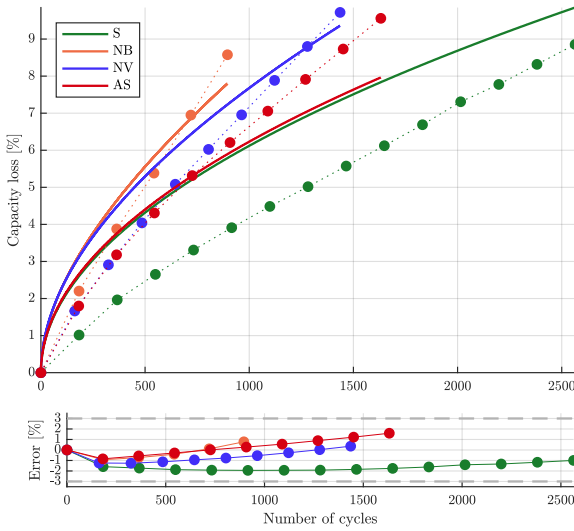
Figure 2.17: Stress factors of the cycle-induced aging in logarithmic scale.

The low temperature aging term is responsible for almost the totality of the capacity loss for seven driving cycles (C, S, E, U, NB, NV and AS). Recall that, from (2.44), this term depends solely on the temperature and on the charge energy throughput; this means that most of the degradation phenomena take place during battery charge; this is in good accordance with other studies, e.g. [32] and [33], where the authors state that aging occurs mainly during charging.

Nevertheless, a model that comprises only the low-temperature term would not be able to accurately predict the severe deterioration measured on the FI-cycle and on the AV-cycle dataset. The capacity loss during the Fiorano driving cycle (FI-cycle) is greatly affected by the high temperature caused by the high charge/discharge currents as illustrated in Figure 2.B.5; this agrees with the trend of the stress factors in Figure 2.17, where we should acknowledge that for temperature values above 45°C the high-temperature stress factor is several order of magnitude larger than the low-temperature stress factor. The fast capacity degradation of the AV-cycle is due to the linear dependency on the charge energy throughput caused by the frequent charges above 80% SOC, indeed the AV-cycle is the only one showing a well-defined dependency on the low-temperature high-SOC aging term.



(a) Identification dataset.



(b) Validation dataset.

Figure 2.18: Comparison between model prediction and experimental cycle-induced aging.

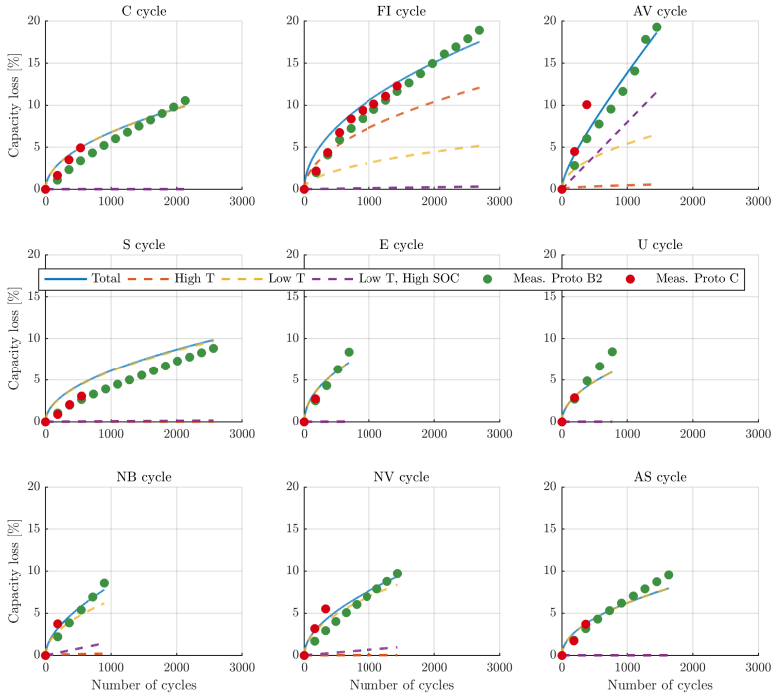


Figure 2.19: Cycle-induced aging model: contribution of the three aging terms.

2.2.4 Conclusions

In this section we presented the aging mechanisms that contribute to the deterioration of the battery performances during its usage and also while the cell is stored.

We have introduced the Solid Electrolyte Inter-phase as the main source of capacity loss and impedance rise during the storage of the battery. We have explained the negligible capacity loss during storage at low SOC with the passive electrode effect that causes the lithium ions to migrate from the outside of the anode to the inside.

Finally, we have proposed a model to describe the capacity loss induced by charge/discharge cycles and we found out that temperature and frequent charges are the main factors affecting battery deterioration.

We compared our model with the data collected during an extensive experimental campaign that aimed at aging the battery with reference current profiles.

BIBLIOGRAPHY OF CHAPTER 2

- [1] Anthony Barré, Benjamin Deguilhem, Sébastien Grolleau, Mathias Gérard, Frédéric Suard, and Delphine Riu. “A review on lithium-ion battery ageing mechanisms and estimations for automotive applications.” In: *Journal of Power Sources* 241 (2013), pp. 680–689.
- [2] Leonora Bianchi, Marco Dorigo, Luca Maria Gambardella, and Walter J Gutjahr. “A survey on metaheuristics for stochastic combinatorial optimization.” In: *Natural Computing* 8.2 (2009), pp. 239–287.
- [3] Adrien M Bizeray, Shi Zhao, Stephen R Duncan, and David A Howey. “Lithium-ion battery thermal-electrochemical model-based state estimation using orthogonal collocation and a modified extended Kalman filter.” In: *Journal of Power Sources* 296 (2015), pp. 400–412.
- [4] MICHEL Broussely, S Herreyre, Ph Biensan, P Kasztejna, K Nechev, and RJ Staniewicz. “Aging mechanism in Li ion cells and calendar life predictions.” In: *Journal of Power Sources* 97 (2001), pp. 13–21.
- [5] Long Cai and Ralph E White. “An efficient electrochemical–thermal model for a lithium-ion cell by using the proper orthogonal decomposition method.” In: *Journal of the Electrochemical Society* 157.11 (2010), A1188–A1195.
- [6] Matteo Corno, Nimitt Bhatt, Sergio M Savaresi, and Michel Verhaegen. “Electrochemical model-based state of charge estimation for Li-ion cells.” In: *IEEE Transactions on Control Systems Technology* 23.1 (2015), pp. 117–127.
- [7] Thanh-Son Dao, Chandrika P Vyasarayani, and John McPhee. “Simplification and order reduction of lithium-ion battery model based on porous-electrode theory.” In: *Journal of Power Sources* 198 (2012), pp. 329–337.
- [8] Domenico Di Domenico, Giovanni Fiengo, and Anna Stefanopoulou. “Lithium-ion battery state of charge estimation with a Kalman filter based on an electrochemical model.” In: *Control Applications, 2008. CCA 2008. IEEE International Conference on. Ieee.* 2008, pp. 702–707.

- [9] D Domenico, Anna Stefanopoulou, and G Di Fiengo. "PSM: Lithium-Ion Battery State of Charge (SOC) and Critical Surface Charge (CSC) Estimation using an Electrochemical Model-driven Extended Kalman Filter." In: *submitted to a special issue of ASME Journal of Dynamic Systems, Measurements and Control* (2009).
- [10] Marc Doyle and John Newman. "The use of mathematical modeling in the design of lithium/polymer battery systems." In: *Electrochimica Acta* 40.13-14 (1995), pp. 2191–2196.
- [11] Soren Ebbesen, Pascal Kiwitz, and Lino Guzzella. "A generic particle swarm optimization Matlab function." In: *American Control Conference (ACC), 2012*. IEEE. 2012, pp. 1519–1524.
- [12] Madeleine Ecker, Nerea Nieto, Stefan Käbitz, Johannes Schmalstieg, Holger Blanke, Alexander Warnecke, and Dirk Uwe Sauer. "Calendar and cycle life study of Li (NiMnCo) O₂-based 18650 lithium-ion batteries." In: *Journal of Power Sources* 248 (2014), pp. 839–851.
- [13] Jacob A Englander and Arnold C Englander. "Tuning monotonic basin hopping: improving the efficiency of stochastic search as applied to low-thrust trajectory optimization." In: (2014).
- [14] Guodong Fan, Ke Pan, Marcello Canova, James Marcicki, and Xiao Guang Yang. "Modeling of Li-Ion cells for fast simulation of high C-Rate and low temperature operations." In: *Journal of The Electrochemical Society* 163.5 (2016), A666–A676.
- [15] Joel C Forman, Saeid Bashash, Jeffrey Stein, and Hosam Fathy. "Reduction of an electrochemistry-based Li-ion battery health degradation model via constraint linearization and Padé approximation." In: *ASME 2010 Dynamic Systems and Control Conference*. American Society of Mechanical Engineers. 2010, pp. 173–183.
- [16] Matthias Gerdt. *Optimal control of ODEs and DAEs*. Walter de Gruyter, 2012.
- [17] Meng Guo, Godfrey Sikha, and Ralph E White. "Single-particle model for a lithium-ion cell: Thermal behavior." In: *Journal of The Electrochemical Society* 158.2 (2011), A122–A132.
- [18] Kelsey B Hatzell, Aabhas Sharma, and Hosam K Fathy. "A survey of long-term health modeling, estimation, and control of lithium-ion batteries: Challenges and opportunities." In: *American Control Conference (ACC), 2012*. IEEE. 2012, pp. 584–591.

- [19] Xiaosong Hu, Scott J Moura, Nikolce Murgovski, Bo Egardt, and Dongpu Cao. "Integrated optimization of battery sizing, charging, and power management in plug-in hybrid electric vehicles." In: *IEEE Transactions on Control Systems Technology* 24.3 (2016), pp. 1036–1043.
- [20] J Jaguemont, L Boulon, and Y Dubé. "A comprehensive review of lithium-ion batteries used in hybrid and electric vehicles at cold temperatures." In: *Applied Energy* 164 (2016), pp. 99–114.
- [21] K Jalkanen, J Karppinen, L Skogström, T Laurila, M Nisula, and K Vuorilehto. "Cycle aging of commercial NMC/graphite pouch cells at different temperatures." In: *Applied energy* 154 (2015), pp. 160–172.
- [22] Xing Jin, Ashish Vora, Vaidehi Hoshing, Tridib Saha, Gregory Shaver, R Edwin García, Oleg Wasynczuk, and Subbarao Varigonda. "Physically-based reduced-order capacity loss model for graphite anodes in Li-ion battery cells." In: *Journal of Power Sources* 342 (2017), pp. 750–761.
- [23] Stefan Käbitz, Jochen Bernhard Gerschler, Madeleine Ecker, Yusuf Yurdagel, Brita Emmermacher, Dave André, Tim Mitsch, and Dirk Uwe Sauer. "Cycle and calendar life study of a graphite | $\text{LiNi}_{\frac{1}{3}}\text{Mn}_{\frac{1}{3}}\text{Co}_{\frac{1}{3}}\text{O}_2$ Li-ion high energy system. Part A: Full cell characterization." In: *Journal of Power Sources* 239 (2013), pp. 572–583.
- [24] Mohammad Kassem, Julien Bernard, Renaud Revel, Serge Pelissier, François Duclaud, and C Delacourt. "Calendar aging of a graphite/LiFePO₄ cell." In: *Journal of Power Sources* 208 (2012), pp. 296–305.
- [25] Robert H Leary. "Global optimization on funneling landscapes." In: *Journal of Global Optimization* 18.4 (2000), pp. 367–383.
- [26] Meinert Lewerenz and Dirk Uwe Sauer. "Evaluation of cyclic aging tests of prismatic automotive LiNiMnCoO₂-Graphite cells considering influence of homogeneity and anode overhang." In: *Journal of Energy Storage* 18 (2018), pp. 421–434.
- [27] Meinert Lewerenz, Jens Münnix, Johannes Schmalstieg, Stefan Käbitz, Marcus Knips, and Dirk Uwe Sauer. "Systematic aging of commercial LiFePO₄ | Graphite cylindrical cells including a theory explaining rise of capacity during aging." In: *Journal of Power Sources* 345 (2017), pp. 254–263.
- [28] Meinert Lewerenz, Georg Fuchs, Lisa Becker, and Dirk Uwe Sauer. "Irreversible calendar aging and quantification of the reversible capacity loss caused by anode overhang." In: *Journal of Energy Storage* 18 (2018), pp. 149–159.

- [29] J Li, K Adewuyi, N Lotfi, RG Landers, and J Park. "A single particle model with chemical/mechanical degradation physics for lithium ion battery State of Health (SOH) estimation." In: *Applied Energy* 212 (2018), pp. 1178–1190.
- [30] Ji Liu, Guang Li, and Hosam K Fathy. "A computationally efficient approach for optimizing lithium-ion battery charging." In: *Journal of Dynamic Systems, Measurement, and Control* 138.2 (2016), p. 021009.
- [31] James Marcicki, Marcello Canova, A Terrence Conlisk, and Giorgio Rizzoni. "Design and parametrization analysis of a reduced-order electrochemical model of graphite/LiFePO₄ cells for SOC/SOH estimation." In: *Journal of Power Sources* 237 (2013), pp. 310–324.
- [32] Scott J Moura, Jeffrey L Stein, and Hosam K Fathy. "Battery-health conscious power management in plug-in hybrid electric vehicles via electrochemical modeling and stochastic control." In: *IEEE Transactions on Control Systems Technology* 21.3 (2013), pp. 679–694.
- [33] Scott J Moura, Joel C Forman, Saeid Bashash, Jeffrey L Stein, and Hosam K Fathy. "Optimal control of film growth in lithium-ion battery packs via relay switches." In: *IEEE Transactions on Industrial Electronics* 58.8 (2011), pp. 3555–3566.
- [34] John Newman and Karen E Thomas-Alyea. *Electrochemical systems*. John Wiley & Sons, 2012.
- [35] Sourav Pramanik and Sohel Anwar. "Electrochemical model based charge optimization for lithium-ion batteries." In: *Journal of Power Sources* 313 (2016), pp. 164–177.
- [36] Umberto Sartori, Francesco Biral, Enrico Bertolazzi, and Simona Onori. "On-Line power management optimization of a hybrid electric vehicle with Non linear MPC and battery re-charge equivalent cost." In: *Industrial Electronics Society, IECON 2016-42nd Annual Conference of the IEEE*. IEEE. 2016, pp. 5094–5100.
- [37] Michael Schimpe, ME von Kuepach, M Naumann, HC Hesse, K Smith, and A Jossen. "Comprehensive Modeling of Temperature-Dependent Degradation Mechanisms in Lithium Iron Phosphate Batteries." In: *Journal of The Electrochemical Society* 165.2 (2018), A181–A193.
- [38] Lorenzo Serrao, Simona Onori, Antonio Sciarretta, Yann Guezennec, and Giorgio Rizzoni. "Optimal energy management of hybrid electric vehicles including battery aging." In: *American Control Conference (ACC), 2011*. IEEE. 2011, pp. 2125–2130.

- [39] Kandler A Smith. "Electrochemical modeling, estimation and control of lithium ion batteries." In: (2006).
- [40] Kandler A Smith. "Electrochemical control of lithium-ion batteries [applications of control]." In: *IEEE Control Systems* 30.2 (2010), pp. 18–25.
- [41] Tanvir R Tanim, Christopher D Rahn, and Chao-Yang Wang. "A temperature dependent, single particle, lithium ion cell model including electrolyte diffusion." In: *Journal of Dynamic Systems, Measurement, and Control* 137.1 (2015), p. 011005.
- [42] Lars Ole Valøen and Jan N Reimers. "Transport properties of LiPF₆-based Li-ion battery electrolytes." In: *Journal of The Electrochemical Society* 152.5 (2005), A882–A891.
- [43] David J Wales and Jonathan PK Doye. "Global optimization by basin-hopping and the lowest energy structures of Lennard-Jones clusters containing up to 110 atoms." In: *The Journal of Physical Chemistry A* 101.28 (1997), pp. 5111–5116.
- [44] Jörn Wilhelm, Stefan Seidlmayer, Peter Keil, Jörg Schuster, Armin Kriele, Ralph Gilles, and Andreas Jossen. "Cycling capacity recovery effect: A coulombic efficiency and post-mortem study." In: *Journal of Power Sources* 365 (2017), pp. 327–338.
- [45] Qi Zhang and Ralph E White. "Calendar life study of Li-ion pouch cells." In: *Journal of Power Sources* 173.2 (2007), pp. 990–997.
- [46] Qi Zhang and Ralph E White. "Calendar life study of Li-ion pouch cells: Part 2: Simulation." In: *Journal of Power Sources* 179.2 (2008), pp. 785–792.

APPENDIX OF CHAPTER 2

2.A MODEL PARAMETERS

Description	Unit	Symbol	Value	Source
Faraday Constant	C mol^{-1}	F	96487	-
Gas Constant	J (mol K)^{-1}	R_g	8.3140	-
Nominal Capacity	Ah	Q_N	26.2	datasheet
Bruggeman coefficient	-	γ	2.8	tuned
Transference number	-	t_0^+	0.39	[1]
Mean electrolyte concentration	mol cm^{-3}	$c_{e,\text{avg}}$	$1.25 \cdot 10^{-3}$	[3]
Electrode Area	cm^2	A^P	$1.2116 \cdot 10^4$	geometry
		A^N	$1.3243 \cdot 10^4$	
Layer thickness	cm	L^P	$6.2 \cdot 10^{-3}$	geometry
		L^S	$2.63 \cdot 10^{-3}$	
		L^N	$6.3 \cdot 10^{-3}$	
Volume Fraction	-	ϵ^P	0.3525	id. (2.24)
		ϵ^S	0.69	
		ϵ^N	0.4684	
Max. Li-ion concentration	mol cm^{-3}	$c_{s,\text{max}}^P$	0.0518	[3]
		$c_{s,\text{max}}^N$	0.0311	
Initial stoichiometry	-	$\theta_{0\%}^P$	0.7261	id. (2.24)
		$\theta_{0\%}^N$	0.0466	
Final stoichiometry	-	$\theta_{100\%}^P$	0.0134	id. (2.24)
		$\theta_{100\%}^N$	0.8509	
Particle Radius	cm	R_s^P	$5 \cdot 10^{-4}$	[3]
		R_s^N	$5 \cdot 10^{-4}$	
Active surface	cm^{-1}	a_s^P	$2.1150 \cdot 10^3$	geometry
		a_s^N	$2.8104 \cdot 10^3$	

Table 2.A.1: List of parameters of the gr/NMC 26.2Ah 3.8V Proto B cell.

Description	Unit	Symbol	Value	Source
Kinetic coeff. ref. value	$\text{A cm}^{\frac{3}{2}} \text{mol}^{-\frac{3}{2}}$	$k_{\text{ref}}^{\text{P}}$	$6.618 \cdot 10^4$	id. (2.26)
		$k_{\text{ref}}^{\text{n}}$	$3.248 \cdot 10^2$	
- ref. temperature	K	$T_{\text{ref},k}^{\text{P}}$	268	tuned
		$T_{\text{ref},k}^{\text{n}}$	293	
- activation energy	J mol^{-1}	$E_{\text{act},k}^{\text{P}}$	$5.320 \cdot 10^4$	id. (2.26)
		$E_{\text{act},k}^{\text{n}}$	$1.291 \cdot 10^4$	
Diffusion coeff. ref. value	$\text{cm}^2 \text{s}^{-1}$	$D_{\text{s,ref}}^{\text{P}}$	$3.041 \cdot 10^{-10}$	id. (2.28)
		$D_{\text{s,ref}}^{\text{n}}$	$1.497 \cdot 10^{-10}$	
- ref. temperature	K	$T_{\text{ref},D_s}^{\text{P}}$	293	tuned
		$T_{\text{ref},D_s}^{\text{n}}$	293	
- activation energy	J mol^{-1}	$E_{\text{act},D_s}^{\text{P}}$	$7.777 \cdot 10^3$	id. (2.28)
		$E_{\text{act},D_s}^{\text{n}}$	$1.022 \cdot 10^4$	
Contact resistance ref. value		$R_{\Omega,\text{ref}}$	$4.528 \cdot 10^{-4}$	id. (2.26)
- ref. temperature	K	$T_{\text{ref},R_{\Omega}}$	296	tuned
- activation energy	J mol^{-1}	$E_{\text{act},R_{\Omega}}$	$1.863 \cdot 10^3$	id. (2.26)
Activity coeff. ref. value		β_{ref}	3.75	tuned
- ref. temperature	K	$T_{\text{ref},\beta}$	338	tuned
- activation energy	J mol^{-1}	$E_{\text{act},\beta}$	140	tuned
- exponential	J mol^{-1}	ρ_{β}	0.3	tuned

Table 2.A.2: List of temperature dependent parameters of the gr/NMC 26.2Ah 3.8V Proto B cell.

Open Circuit Voltage

The open circuit voltage for the LiNiMnCoO_2 electrode (cathode) depends on the stoichiometric ratio $z = \frac{c_s^{\text{P}}}{c_{\text{s,max}}^{\text{P}}}$ according to

$$U^{\text{P}}(z) = 72.11z^6 - 162.15z^5 + 132.59z^4 - 48.39z^3 + 9.11z^2 - 2.68z + 4.299 \quad z \in [0; 1]$$

The half-cell OCV for the lithiated graphite anode is [2]

$$U^{\text{n}}(y) = 0.1493 + 0.8493 \exp(-61.79y) + 0.3824 \exp(-665.8y) - \exp(39.42y - 41.92) \\ - 0.03131 \tan^{-1}(25.59y - 4.099) - 0.009434 \tan^{-1}(32.49y - 15.74) \quad y \in [0; 1],$$

$$\text{with } y = \frac{c_s^{\text{n}}}{c_{\text{s,max}}^{\text{n}}}.$$

Description	Symbol	Unit
Lithium-ion concentration	c_k^i	mol cm^{-3}
Intercalation current density	j^i	A cm^{-3}
Current density in the liquid phase	i_e^i	A cm^{-3}
Exchange current density	i_0^i	A cm^{-2}
Temperature	T	K
Surface overpotential	η^i	V

Table 2.A.3: List of cell model variables.

2.B CYCLE AGING DATASET

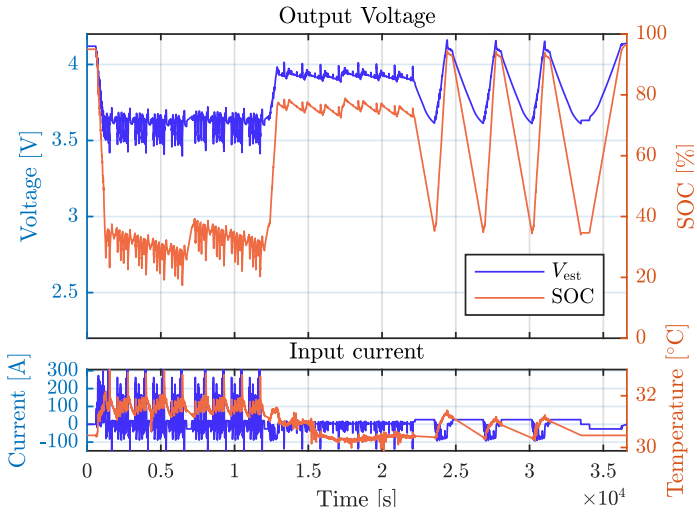


Figure 2.B.1: Voltage, SOC, current and temperature of the highway (AS) cycle.

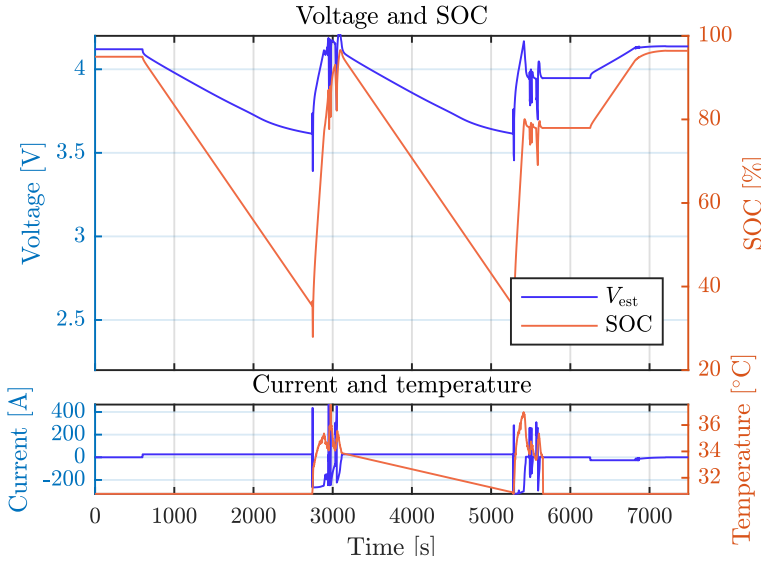


Figure 2.B.2: Voltage, SOC, current and temperature of the high speed (AV) cycle.

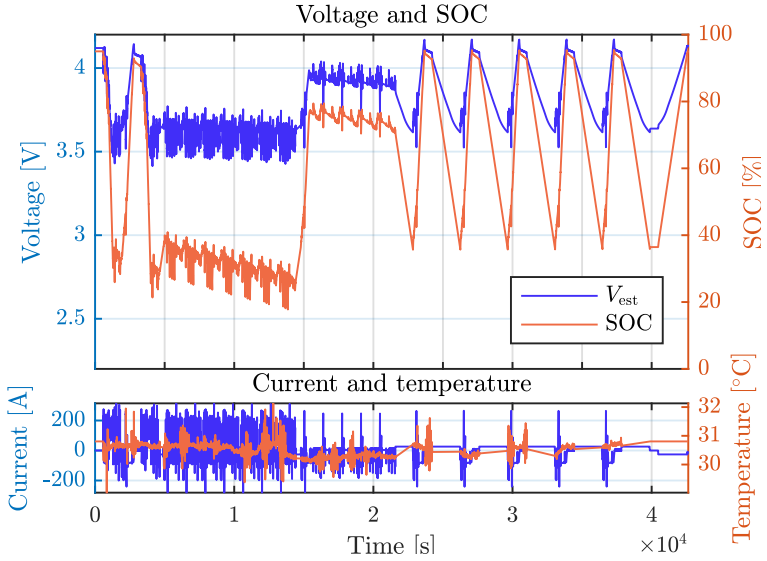


Figure 2.B.3: Voltage, SOC, current and temperature of the combined (C) cycle.

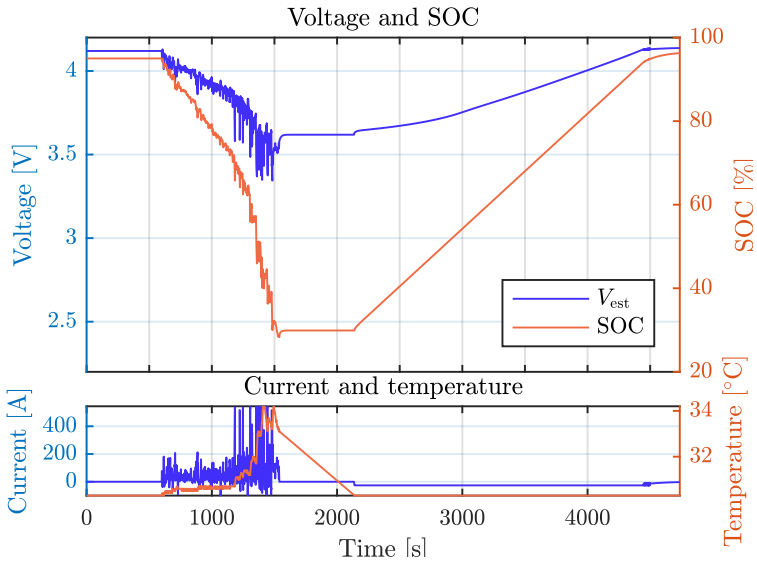


Figure 2.B.4: Voltage, SOC, current and temperature of the electric drive (**E-drive**) cycle.

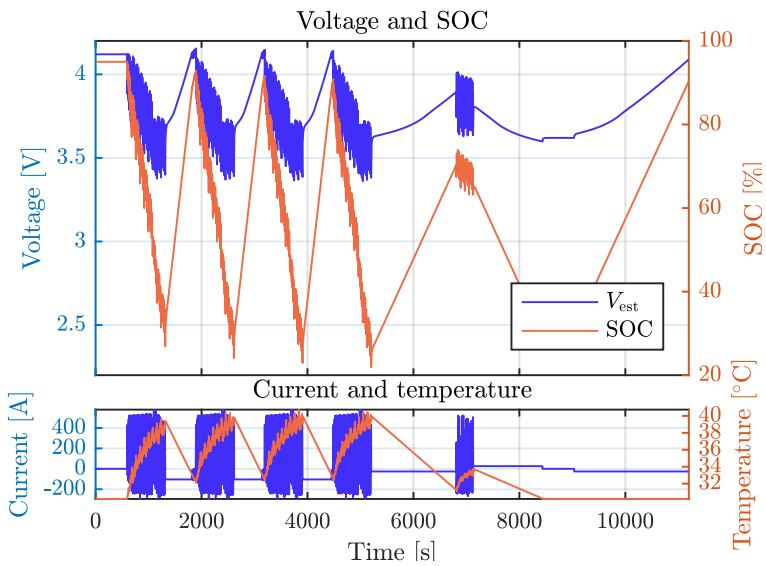


Figure 2.B.5: Voltage, SOC, current and temperature of the Fiorano (**FI**) cycle.

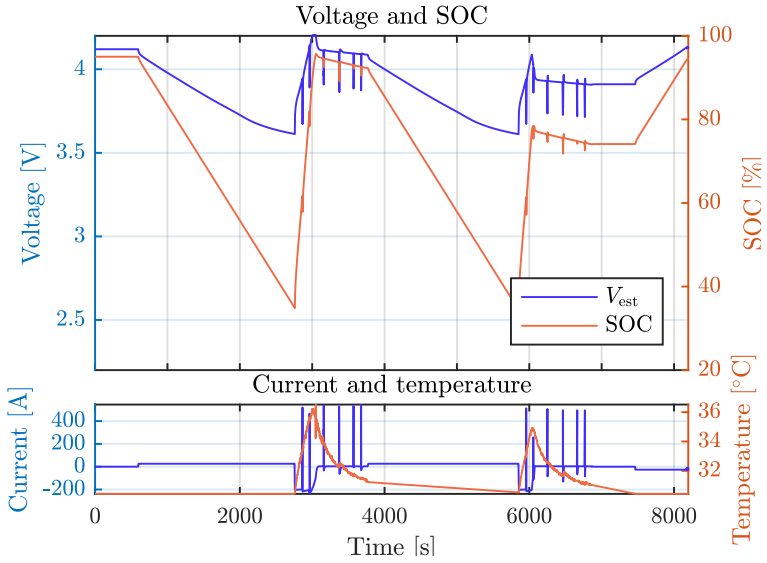


Figure 2.B.6: Voltage, SOC, current and temperature of the hill (NB) cycle.

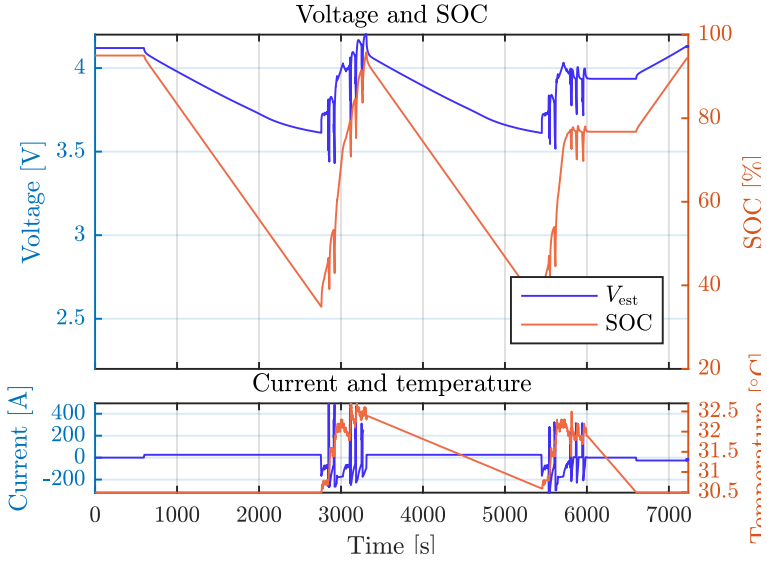


Figure 2.B.7: Voltage, SOC, current and temperature of the freeway (NV) cycle.

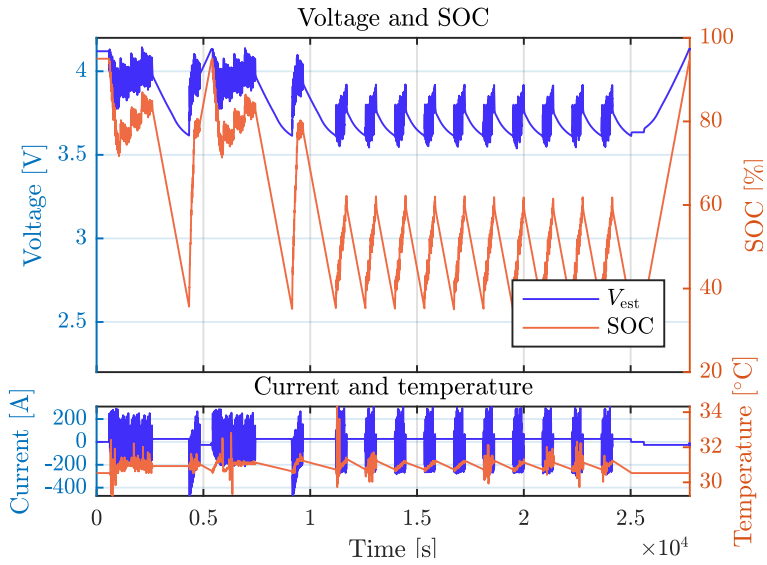


Figure 2.B.8: Voltage, SOC, current and temperature of the sustaining (S) cycle.

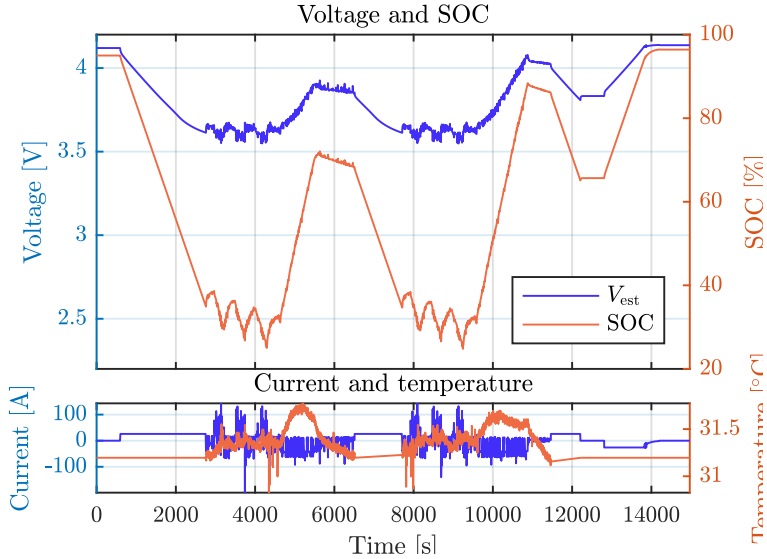


Figure 2.B.9: Voltage, SOC, current and temperature of the Urban (U) cycle.

The increasing concerns about the reduction of greenhouse gases have moved the joint interest of governments, industries and academies towards the development of a clean and sustainable mobility. Hybrid electric vehicles (HEV) are blending the transition towards the full-electric mobility, since they run on both electric and petrol power, in a proportion that is dependent on the level of hybridization of the power-train architecture: from start&stop micro hybrid to plug-in hybrids where the internal combustion engine serves solely as a range extender that supports the main electric motor. All the hybrid electric vehicles have at least two power-sources that contribute in deploying the required power at the wheels. If the required power at the wheels, considering the efficiency chain of the drive-line, is less than the sum of the maximum power of the electric motor and of the engine, then the system is redundant; this means that we can obtain the desired power at the wheels with infinitely many combinations of the power of the motor and of the engine. This gives us the possibility to decide how to allocate the power flows inside a transmission in order to pursuit, for instance, the minimization of the fuel consumed in a driving mission.

There is a vast literature on the definition of control strategies that aim at the optimization of the fuel economy in HEV, spanning from heuristic strategies as the thermostatic control logic of [12] and [33] to the widely adopted Equivalent Consumption Minimization Strategy (ECMS), found e.g. in [19], [23] and [17], based on the necessary optimality conditions stated by the Pontryagin Minimum Principle (PMP). The effectiveness of the PMP-based control algorithms is further improved for an electric bicycle in [8], exploiting the a-priori knowledge of the route information.

In recent years convex optimization has been spread in vehicular technology due to the availability of off-the-shelf free efficient solvers that allow to find the global optimal solution in fairly short computational time; the energy management problem is cast as a convex optimization problem in [18], [16] and [10], under rigorous simplifying assumptions that guarantee the existence and uniqueness of the optimal solution.

The study of optimal energy management strategies is also used to assess and compare the performances of different power-train architectures as in [4] and [31], where the authors resort to the optimal solution to the power-management problem to prove the advantages of the Continuous

Variable Transmission (CVT) compared to the Fixed Transmission (FT) in a parallel pre-transmission hybrid vehicle.

Most of the energy management algorithms found in the literature focus on how to split the power flows inside the transmission in order to reduce fuel consumption and satisfy the driver's torque (and consequently speed) requirements. The authors of [3] and [13] show that great improvements in fuel economy can be achieved by relaxing this constraint and by solving a joint optimization of the velocity profile and of the power-split inside the transmission.

The reduction of fuel consumption, and consequently of the cost associated to the vehicle usage, is the main objective of the most common energy management techniques; nevertheless, two other conflicting issues remain unsolved: first, in Plug-in HEV (P-HEV) the electric energy stored in the battery via grid charge is not free and, in some situations, it should be saved at the cost of higher fuel consumptions; second, as we have deeply discussed in Chapter 2, a frequent and severe usage of the battery leads to a fast deterioration of its performances, dictating an expensive replacement of the battery system after few years. For these reasons, Formentin et al. propose in [6] the Total Cost Minimization Strategy (TCMS), that casts the energy management problem as a multi-objective optimization problem that takes into account battery aging, depth-of-discharge and, of course, fuel consumption. The increasing availability of simple and reliable battery aging models favors the development of new energy management strategies that trade off fuel consumption and battery degradation, as the ECMS algorithm presented in [24], [25] and the battery-health conscious power management in [14]. In [15] the authors propose a cell-balancing method based on relay switches that is able to reduce the growth of the Solid Electrolyte Interphase (SEI). The importance of a mindful management of charging operations in extending battery life is highlighted in [10], while battery internal-temperature control is treated in [20] as the prime method to slow down battery aging.

In all of the aforementioned articles, the battery system has been modeled with equivalent circuit models. The simplest equivalent circuit comprises a resistance in series with a voltage generator, and the state-of-charge is the only state; the model is able to capture the static relation between battery current and terminal voltage, but as thoroughly discussed in [9], the model is affected by a large error compared to the models that take voltage dynamics into account¹. This error is amplified in conditions far from the equilibrium, e.g. for high charge/discharge current values, long-lasting current bursts and for high or low SOC values;

¹ The RC-model, that adds a parallel Resistance-Capacitor branch in series to the voltage generator and the resistance, exhibits much better results in [9].

moreover, as we have seen in Chapter 2, the knowledge of the internal state of the battery given by the first-principle electrochemical battery model is of paramount importance for an accurate description of the aging dynamics. To the best of the authors knowledge, not many works have been presented that include the electrochemical battery model in the design of the energy management strategy. A remarkable exception is the work by Moura et al. that resort in [14] to an electrochemistry-based battery model for closed-loop verification and to find the set of admissible controls, but the optimal control problem is formulated using the simpler equivalent circuit model.

In this chapter we try to fill this gap by devising an energy management battery-health aware strategy for a parallel HEV based on the reduced order electrochemical model validated in Chapter 2. The accurate knowledge of the internal states of the battery allows to adopt less compelling constraints on the controls and on the battery state; moreover, by reducing the modeling errors with an accurate description of the voltage dynamics, we can better rely on the resulting control strategy.

The outline of this chapter is organized as follows: in Section 3.1 we describe the power-train model of the parallel HEV considered in this study, by also briefly recalling the main equations of the electrochemical model and of the capacity degradation model; in Section 3.2 we state the energy management problem and we show how to employ the result of the optimization to select the best operating temperature to maximize the fuel savings and to reduce the battery degradation. Finally, in Section 3.3 we see how the optimization problem can be cast in a Non-linear Model Predictive Control (N-MPC) framework and we evaluate the effect of the length of the horizon window on the overall energy saving performances.

3.1 POWER-TRAIN ARCHITECTURE MODEL

This project was partly developed with Maserati and Alfa Romeo group and aimed at investigating energy management strategies for a mild parallel hybrid electric vehicle. The configuration of the power-train architecture is illustrated in Figure 3.1 and consists of a 8-speed automatic transmission that can be disconnected from the rest of the power-train by means of a clutch system; the internal combustion engine is assisted by an electric motor that is fed by a low-voltage 48V battery and is connected to the crankshaft through a reduction ratio. The electric motor—or Internal Starter Generator (ISG) unit—is always connected to the crankshaft, because it is placed just after the engine and before the clutch; this simplifies the power-train construction but prevents the vehicle from traveling in pure electric mode. The electric motor unit is connected to the engine shaft through the reduction ratio $\gamma_{\text{mot}} > 1$, therefore $\omega_{\text{mot}}(t) = \omega_{\text{eng}}(t) \gamma_{\text{mot}}$. The engine torque $T_{\text{eng}}(\cdot)$ and the motor

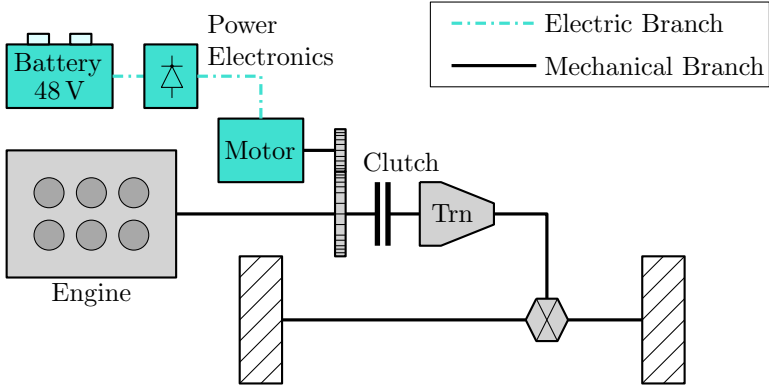


Figure 3.1: Architecture of the pre-transmission parallel-hybrid power-train configuration (P1) under investigation.

torque $T_{\text{mot}}(\cdot)$ sum up at the wheels giving the total torque $T_w(\cdot)$ that is expressed by

$$T_w(t) = (T_{\text{eng}}(t) - J_{\text{eng}} \dot{\omega}_{\text{eng}}(t) + T_{\text{mot}}(t) \gamma_{\text{mot}}) \eta_{\text{trn}}^{\text{sign}[a_x(t)]} \gamma_{\text{trn}}(t) \gamma_{\text{axle}} + T_{\text{brk}}(t), \quad (3.1)$$

where $a_x(\cdot)$ is the vehicle longitudinal acceleration and $T_{\text{brk}}(\cdot)$ is the torque exerted by the mechanical brakes on the wheels. The system parameters are listed in Table 3.1. The term $J_{\text{eng}} \dot{\omega}_{\text{eng}}(t)$ represents the extra-torque needed to accelerate the engine. The transmission ratio $\gamma_{\text{trn}}(t) \in \{\gamma_{\text{trn},1}, \dots, \gamma_{\text{trn},8}\}$ switches among the eight ratios according to the simple speed-based strategy

- if $\omega_{\text{eng}}(t) > \omega_{\text{eng,up}}$, up-shift
- if $\omega_{\text{eng}}(t) < \omega_{\text{eng,down}}$, down-shift

3.1.1 Driving cycle and longitudinal dynamics

We formulate the optimization problem by constraining the speed of the vehicle to follow the velocity profile imposed by the driving cycle. We solve the optimization over two driving cycles, with different speed and altitude profiles. In Figure 3.B.1 we report the speed and altitude profile for each cycles: the WLTP is used in type approval tests, e.g. for emissions assessment, for passenger cars and is characterized by four ramps reaching increasing speed values; the other cycle, called Vail2NREL, is a demanding extra-urban driving cycle that includes also

Description	Symbol	Value	Unit
Transmission efficiency	η_{trn}	0.95	-
Axle ratio	γ_{axle}	3.730	-
First Gear	$\gamma_{\text{trn},1}$	5.000	-
Second Gear	$\gamma_{\text{trn},2}$	3.200	-
Third Gear	$\gamma_{\text{trn},3}$	2.143	-
Fourth Gear	$\gamma_{\text{trn},4}$	1.720	-
Fifth Gear	$\gamma_{\text{trn},5}$	1.314	-
Sixth Gear	$\gamma_{\text{trn},6}$	1.000	-
Seventh Gear	$\gamma_{\text{trn},7}$	0.822	-
Eighth Gear	$\gamma_{\text{trn},8}$	0.640	-
Motor ratio	γ_{mot}	2.000	-
Vehicle mass	m_v	1750	kg
Dyn. wheel radius	r_w	0.31	m
Aerodyn. drag coeff.	c_f	0.28	kg m^{-1}
Rolling resistance coeff	$c_{\text{rr}0}$	0.02	-
Engine inertia	J_{eng}	$2.26 \cdot 10^{-2}$	kg m^2
Up-shift engine speed	$\omega_{\text{eng,up}}$	$4.77 \cdot 10^3$	rpm
Down-shift engine speed	$\omega_{\text{eng,down}}$	$2.87 \cdot 10^3$	rpm

Table 3.1: Hybrid vehicle parameters.

slope variations; finally, US06 is another driving cycle used for type approval test, mostly in the United States. The torque required at the wheels at time t is computed from the longitudinal dynamics equation

$$T_w(t) = \left(c_f v_x(t)^2 + m_v a_x(t) + g m_v (\sin[\sigma(t)] + c_{\text{rr}0} \cos[\sigma(t)]) \right) r_w, \quad (3.2)$$

where $\sigma_{\text{road}}(\cdot)$ is the road slope and $v_x(\cdot)$ is the longitudinal vehicle speed, both taken from the driving profiles of Figure 3.B.1. If we impose the vehicle speed and the road slope according to the selected driving profile in Figure 3.B.1, then the torque at wheel $T_w(\cdot)$ is known from (3.2).

3.1.2 Engine

The instantaneous fuel consumption map in Figure 3.2 is derived from the engine efficiency and depends on the torque and speed at the motor shaft. The 2D map is well approximated by Willan's lines approach

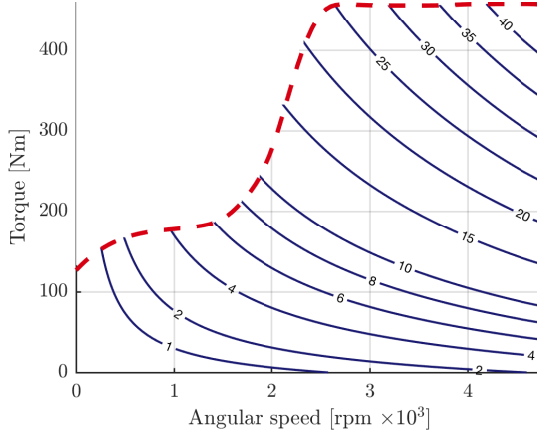


Figure 3.2: Engine fuel consumption rate in kg/h (blue solid lines) and torque limits (red dashed lines).

[21], that states that there exists an affine relationship between the fuel consumption rate \dot{m}_f - which is proportional to the power generated by the combustion through the specific calorific value - and the mechanical power output by the engine $P_{\text{eng}}(t) = \omega_{\text{eng}}(t) T_{\text{eng}}(t)$, therefore the instantaneous fuel consumption rate at time t becomes

$$\dot{m}_f(\omega_{\text{eng}}(t), T_{\text{eng}}(t)) = \alpha(\omega_{\text{eng}}(t)) P_{\text{eng}} + \beta(\omega_{\text{eng}}(t)), \quad (3.3)$$

with $\alpha(\omega_{\text{eng}}(\cdot)) = \sum_{i=0}^3 \alpha_i \omega_{\text{eng}}^{i-1}(\cdot)$ and $\beta(\omega_{\text{eng}}(\cdot)) = \sum_{i=0}^3 \beta_i \omega_{\text{eng}}^{i-1}(\cdot)$. The Willan's parameters used in this work are reported in Table 3.2.

	$i = 1$	$i = 2$	$i = 3$
α_i	$6.1454 \cdot 10^{-8}$	$-5.2369 \cdot 10^{-11}$	$7.4707 \cdot 10^{-14}$
β_i	$7.0402 \cdot 10^{-6}$	$8.3295 \cdot 10^{-7}$	$6.2962 \cdot 10^{-10}$

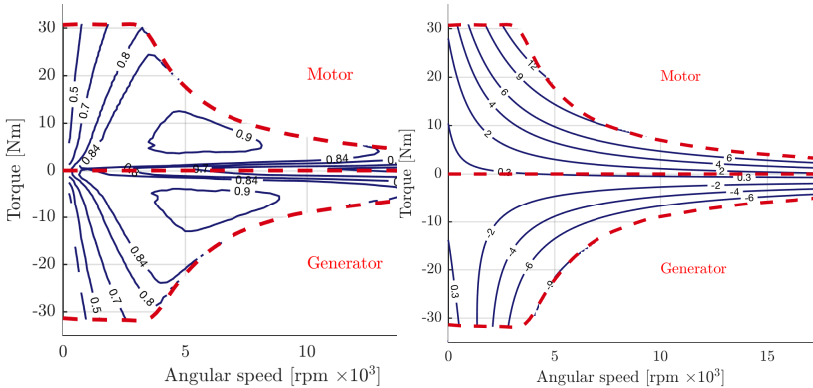
Table 3.2: Willan's coefficients

3.1.3 Motor

The electric motor—or internal starter generator (ISG) unit—of the 48V hybrid operates in two working modes: when working as a motor the ISG converts the electrical energy from the battery to mechanical energy at the shaft, while in generator mode it recovers the kinetic energy during a regenerative braking by transforming it to electrical energy that is stored in the battery. The overall power generated (generator mode) or absorbed (motor mode) by the ISG unit is computed considering the non-unitary efficiency $\eta_{\text{mot}}(t)$ that depends on the ISG shaft speed $\omega_{\text{mot}}(\cdot)$ and torque $T_{\text{mot}}(\cdot)$ as

$$P_{\text{mot}}(\omega_{\text{mot}}(t), T_{\text{mot}}(t)) = \begin{cases} \omega_{\text{mot}}(t) T_{\text{mot}}(t) \eta_{\text{mot}}(t) & T_{\text{mot}}(t) < 0, \text{ gen.} \\ \frac{\omega_{\text{mot}}(t) T_{\text{mot}}(t)}{\eta_{\text{mot}}(t)} & T_{\text{mot}}(t) \geq 0, \text{ mot.} \end{cases} \quad (3.4)$$

where $\eta_{\text{mot}}(\cdot)$ depends on the motor characteristics and is usually represented by iso-efficiency lines as in Figure 3.3a. If we approximate



(a) Motor/generator efficiency contours (b) Approximated motor power contours and torque limits.

Figure 3.3: Motor efficiency and power maps.

the ISG efficiency map with a polynomial surface, we should use high order polynomials that are able to capture the steep slopes close to the efficiency holes at low speed and large torque (and at small torque and high speed); this increases the complexity of the formulation and leads to badly scaled derivatives that could undermine the robustness of the

optimization algorithm. To overcome this issue, we propose to directly compute the ISG power for every pair $(\omega_{\text{mot}}, T_{\text{mot}})$ in the efficiency map; the resulting surface in Figure 3.4 is much smoother than the efficiency

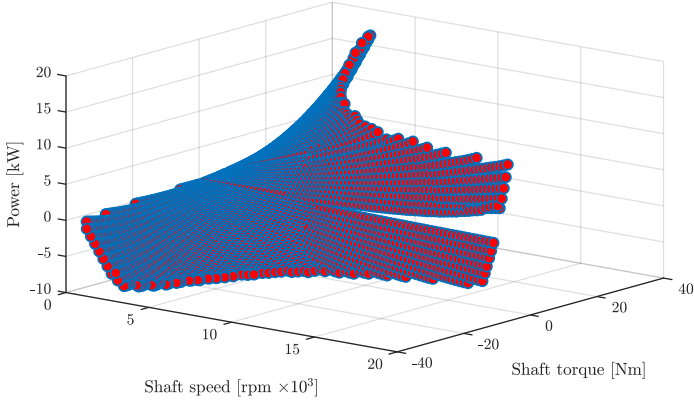


Figure 3.4: Actual motor power computed for each element of the efficiency map from (3.4).

surface and could be approximated with good accuracy by the third order polynomial

$$P_{\text{mot}}(\omega_{\text{mot}}(t), T_{\text{mot}}(t)) = \sum_{j=0}^3 \sum_{i=0}^3 p_{i,j} \omega_{\text{mot}}(t)^j T_{\text{mot}}(t)^i \quad (3.5)$$

resulting in the contours depicted in Figure 3.3b.

3.1.4 Battery System

The Energy Storage System (ESS) comprises of 180 gr/NMC lithium-ion 18650 cylindrical cells arranged in $n_p = 12$ parallel modules with $n_s = 15$ cells in series. Each cell has a nominal voltage of 3.2V and nominal capacity equal to 30Ah, resulting in a 48V battery pack that stores approximately 1.5 kWh of electrical energy in nominal conditions. The maximum discharge/charge power is equal to 17.11 kW and 11.5 kW respectively, corresponding to a maximum cell current equal to 30 A and 20 A respectively. Letting $V(\cdot)$ be the terminal voltage of one cell and $I(\cdot)$ the current applied to it, we compute the the overall battery power at time t as

$$P_{\text{batt}}(t) = V(t) n_s I(t) n_p. \quad (3.6)$$

We assume that the battery cooling system is able to keep the temperature of the cells at a constant value. This is generally not true for standard batteries, in particular for high current values that lead to local temperature gradients; nevertheless, this simplifying assumption is useful to better understand the effect of different temperatures on battery performances and aging, and we can use the analysis to properly size the battery cooling system.

3.1.4.1 Charge/discharge dynamics

In the following we briefly recall the main equations of the electrochemical battery model presented in Chapter 2. The model input is the current $I(t)$ applied to the cell (galvanostatic mode); the output is the terminal voltage $V(t)$ measured between the positive and negative current collectors and result from the sum of the potential and overpotential terms according to

$$V(t) = (U^P(t) - U^n(t)) + (\eta^P(t) - \eta^n(t)) + (\phi_e^P(L, t) - \phi_e^n(0, t)) - R_\Omega I(t). \quad (3.7a)$$

The values and of the cell model parameters have been identified with the same procedure detailed in Chapter 2 and are reported in Table 3.A.1 and 3.A.2 of Appendix i.

The equilibrium potentials $U^i(t)$ depend on the lithium ion concentration at the solid-electrolyte interface (namely on the surface of the electrode particle) $c_{s,e}^i(t)$; defining the stoichiometry ratio as $\theta^i(t) = c_{s,e}^i(t)/c_{s,\max}^i \in [0; 1]$, we can write the functional form of the equilibrium potential at the cathode side from [30] as

$$U^P(\theta^P(t)) = -10.72[\theta^P(t)]^4 + 23.88[\theta^P(t)]^3 - 16.77[\theta^P(t)]^2 + 2.595\theta^P(t) + 4.563$$

and at the anode side from [26] as

$$U^n(\theta^n(t)) = 0.1493 + 0.8493 \exp(-61.79\theta^n(t)) + 0.3824 \exp(-665.8\theta^n(t)) - \exp(39.42\theta^n(t) - 41.92) - 0.03131 \tan^{-1}(25.59\theta^n(t) - 4.099) - 0.009434 \tan^{-1}(32.49\theta^n(t) - 15.74).$$

The kinetic overpotential terms $\eta^i(t)$ are related to the current density $j^i(t) = \mp \frac{I(t)}{A^i L^i}$ by the Butler-Volmer equation, whose solution is

$$\eta^i(t) = \frac{R_g T}{\alpha F} \sinh^{-1} \left[\frac{j^i(t)}{a_s^i i_0^i(t)} \right]. \quad i = p, n \quad (3.7b)$$

The exchange current density $i_0^i(t)$ is related to the concentration at the electrode surface and in the electrolyte, $c_{s,e}^i(t)$ and $c_e^i(t)$ respectively, through

$$i_0^i(t) = k^i \sqrt{c_e^i(t)(c_{s,\max}^i - c_{s,e}^i(t))c_{s,e}^i(t)}. \quad i = p, n \quad (3.7c)$$

The electrolyte overpotential $\Delta \phi_e(t) = \phi_e^p(L, t) - \phi_e^n(0, t)$ is computed by integrating the equation of the conservation of charge in the liquid phase under the assumption of constant current density throughout the electrodes and leads to

$$\Delta \phi_e(t) = \kappa_d (\log[c_e^p(t)] - \log[c_e^n(t)]) - I(t)R_e \quad (3.7d)$$

where $\kappa_d = \frac{2R_g T(1-t_0^+)}{F}(1 + \beta)$. The electrolyte resistance is $R_e = \frac{1}{\kappa \epsilon_e} \left(\frac{L^p}{A^p} + \frac{L^n}{A^n} \right)$, with the electrolyte conductivity κ that depends on the temperature according to the equations detailed in [27], where the authors present a thorough experimental analysis of the electrochemical properties of a LiPF₆-based electrolyte.

The linear-parameter-varying (LPV) state-space realization of the solid diffusion transfer function presented in Section 2.1.1.2, relates explicitly the state-of-charge (SOC) to the surface concentration at the electrodes and allows to take temperature variations into account; the equations are

$$\begin{aligned} \dot{x}(t) &= Ax(t) + Bu(t), \quad \text{with } x \in \mathbb{R}^7, u \in \mathbb{R} \\ y(t) &= Cx(t), \quad \text{with } y(t) = \begin{bmatrix} \tilde{c}_{s,e}^p(t) \\ \tilde{c}_{s,e}^n(t) \\ \widetilde{SOC}(t) \\ \tilde{c}_e^p(t) \\ \tilde{c}_e^n(t) \end{bmatrix} \in \mathbb{R}^5 \end{aligned} \quad (3.8)$$

where the tilde indicates a variation from the equilibrium condition. The state space matrices are reported in (3.9) at page 89.

The solid phase diffusion coefficients D_s^i , the kinetic constants k^i and the activity coefficient β become larger as temperature increases according to the Arrhenius-like equation

$$\Gamma(T) = \Gamma_{\text{ref}} \exp \left[-\frac{E_{\text{act},\Gamma}}{R_g} \left(\frac{1}{T} - \frac{1}{T_{\text{ref},\Gamma}} \right) \right]. \quad (3.10)$$

The reverse trend of R_Ω with temperature is described by the same equation 3.10 but changing the sign inside the exponential term.

3.1.4.2 Battery aging

In Section 2.2 we have designed and validated a semi-empirical model of the capacity degradation of a large sized 26 Ah pouch cell. Using the same model to describe the aging of the cylindrical 2.0 Ah cell considered in this chapter, could result in large modeling errors because of the very different capacity and form factor. For this reason we adopt in this chapter the aging model proposed in [11], that has been validated for a Lithium-ion-phosphate (LFP) 2.6 Ah cylindrical cell. The complexity of the two aging models is comparable, meaning that it is easy to adapt the control strategies obtained in this section to different type of batteries.

Since the diffusion of the solvent reactants through the SEI layer is much slower than the lithium de-insertion dynamics, then the Butler-Volmer equation for the solvent reduction kinetics can be simplified as

$$j_s(t) = -\frac{k_{SEI}(T)}{2A_n(1 + \lambda\theta(t))\sqrt{t}}, \quad (3.11)$$

where $\theta(t) = \exp\left[\frac{F}{RT}(\eta^n(t) + U^n(t) - U_{sei})\right]$. Notice that at higher SOC the half-cell open circuit voltage $U_n(t)$ is small, therefore the side reaction kinetics is faster; following a similar reasoning, a cathodic current at the

$$\begin{aligned}
 A &= \begin{bmatrix} -\frac{189D_s^P}{[R_s^P]^2} & -\frac{3465[D_s^P]^2}{[R_s^P]^4} & 0 & 0 & \frac{189D_s^P(\theta_{100\%}^P - \theta_{0\%}^P)c_{s,max}^P}{[R_s^P]^2} & 0 & 0 \\ 1 & 0 & 0 & 0 & -(\theta_{100\%}^P - \theta_{0\%}^P)c_{s,max}^P & 0 & 0 \\ 0 & 0 & -\frac{189D_s^n}{[R_s^n]^2} & -\frac{3465[D_s^n]^2}{[R_s^n]^4} & -\frac{189D_s^n(\theta_{100\%}^n - \theta_{0\%}^n)c_{s,max}^n}{[R_s^n]^2} & 0 & 0 \\ 0 & 0 & 1 & 0 & (\theta_{100\%}^n - \theta_{0\%}^n)c_{s,max}^n & 0 & 0 \\ 0 & 0 & 0 & 0 & 0 & 0 & 0 \\ 0 & 0 & 0 & 0 & 0 & -\frac{9.8710D_s^{eff}}{L^2} & 0 \\ 0 & 0 & 0 & 0 & 0 & 0 & -\frac{9.5842D_s^{eff}}{L^2} \end{bmatrix}, \\
 B &= \begin{bmatrix} \frac{7}{z^P F A^P L^P} & -\frac{[R_s^P]^2}{15 D_s^P z^P F A^P L^P} & \frac{7}{z^n F A^n L^n} & -\frac{[R_s^n]^2}{15 D_s^n z^n F A^n L^n} & -\frac{1}{Q_N} & \frac{3.1463(t_0^+ - 1)}{\epsilon_e L F A^P} & -\frac{2.9351(t_0^+ - 1)}{\epsilon_e L F A^n} \end{bmatrix}^T \\
 C &= \begin{bmatrix} 1 & 0 & 0 & 0 & 0 & 0 & 0 \\ 0 & 0 & -1 & 0 & 0 & 0 & 0 \\ 0 & 0 & 0 & 0 & 1 & 0 & 0 \\ 0 & 0 & 0 & 0 & 0 & 1 & 0 \\ 0 & 0 & 0 & 0 & 0 & 0 & 1 \end{bmatrix}.
 \end{aligned} \quad (3.9)$$

anode side (during charging) leads to negative surface overpotential $\eta_n(t)$, thus accelerating the SEI formation. The fitting parameter λ weighs the effect of the anode potential on the SEI growth, while the kinetic coefficient for the side reaction $k_{\text{SEI}}(T)$ follows the Arrhenius dependency reported in (3.10). The capacity loss associated to the SEI formation is obtained by integrating the side-reaction rate over time, namely

$$Q_{\text{SEI}}(t) = \int_0^t j_s(t) A_n dt. \quad (3.12)$$

The authors of [11] claim that the increased capacity loss observed after charging and discharging cycles is due to the structural damages that constantly isolate the active material. This phenomenon is well described by the variation of the active material volume fraction that, under the uniform utilization assumption becomes

$$\frac{d\varepsilon_{\text{AM}}(t)}{dt} = -\kappa_\varepsilon(T) |j_n(t)|, \quad (3.13)$$

where again $\kappa_\varepsilon(T)$ depends on temperature according to (3.10). The SOC-dependent capacity loss rate induced by the volume fraction reduction is expressed as

$$\frac{dQ_{\text{AM}}(t)}{dt} = \frac{d\varepsilon_{\text{AM}}(t)}{dt} \text{SOC}(t) V^n c_{s,\text{max}}^n. \quad (3.14)$$

The total capacity loss at time $t > 0$ is modeled by assuming the superposition of the two capacity loss mechanisms, i.e.

$$\begin{aligned} Q_{\text{loss}}(t) &= Q_{\text{SEI}}(t) + Q_{\text{AM}}(t) \\ &= - \int_0^t \frac{k_{\text{SEI}}(T)}{2(1 + \lambda\theta(t))\sqrt{t}} dt \\ &\quad - \int_0^t \kappa_{\text{AM}}(T) \text{SOC}(t) |I(t)| dt, \end{aligned} \quad (3.15)$$

where the constant terms in (3.14) have been condensed in the fitting parameter $\kappa_{\text{AM}}(T)$.

3.2 BATTERY LIFE-AWARE ENERGY MANAGEMENT

In this section we formulate the multi-objective optimal control problem for the definition of the battery life-aware energy management strategies and we detail the adopted solution method. Finally, we present the results of many numerical simulations to assess the effect of different temperatures on the vehicle performance and on battery degradation.

3.2.1 Problem formulation

As discussed in Section 3.1.1, engine and motor speed are constrained to match the velocity profile of the vehicle; this means that we can only regulate engine and motor torque (T_{eng} and T_{mot}), together with the mechanical braking torque T_{brk} and the cell current I to devise our control strategy; we define the control vector as

$$u(t) = [T_{\text{eng}}(t), T_{\text{mot}}(t), T_{\text{brk}}(t), I(t)]^\top.$$

for each t that belongs to the finite-time horizon $[0, t_f]$, where t_f is the length of the selected driving cycle.

In order to take both energy savings and battery aging into account, the cost function shall include a term dependent on the capacity degradation of the battery in addition to the engine fuel consumption rate. We expect the fuel consumption (measured in liters) over the driving cycle to be much higher than the capacity loss (measured as a fraction of the initial nominal capacity). For this reason, instead of directly using these two quantities in the formulation of the objective function, we account for the monetary cost of fuel and battery degradation: we consider an average price of the gasoline in the European Union equal to $\Gamma_{\text{fuel}} = 1.60 \text{ €/liter}$, while we assume that the cost of the entire 1.5 kWh battery pack is approximately equal to² 800€. We assume that a battery pack should be replaced when it reaches 80% of its initial capacity; indeed, after this threshold the degradation is faster and the impedance rise strongly limits the battery power performance. This means that the total cost of the battery must be applied over a capacity loss $Q_{\text{loss}} = 20\%$, resulting in a unitary cost for each percentage point of capacity loss equal to $\Gamma_{\text{age}} = 45 \text{ €/}\%_{\text{loss}}$.

The objective function is formulated as the weighted sum of the cost of fuel consumption over the time horizon $[0, t_f]$ (running cost) and the cost of capacity loss at the end of the driving cycle t_f (terminal cost)

$$J = \alpha \int_0^{t_f} \Gamma_{\text{fuel}} \dot{m}_f(x(t), u(t)) dt + (1 - \alpha) \Gamma_{\text{age}} Q_{\text{loss}}(x(t_f), u(t_f)), \quad (3.16)$$

where the Pareto coefficient $0 \leq \alpha \leq 1$ weighs the two terms. The capacity loss $Q_{\text{loss}}(\cdot)$ is as in (3.15) and the instantaneous fuel consumption rate $\dot{m}_f(\cdot)$ has been defined in (3.3).

The states $x \in \mathbb{R}^7$ follow the battery dynamics detailed in (3.8). The

² If we had considered a plug-in hybrid electric vehicle, we should have taken into account also the price of the electric energy per kWh from the grid.

electrode surface concentrations have to remain within their maximum and minimum values, i.e. $c_{s,\min}^i \leq c_s^i \leq c_{s,\max}^i$, $i = p, n$. The cell voltage (3.7a) should remain within the safety range indicated on the cell datasheet, namely $2.4 V \leq V(t) \leq 4.2 V$, for each $t \in [0, t_f]$. The knowledge of the internal surface concentrations and the constraints on the battery terminal voltage allow to expand the limits on the battery SOC without the risk of incurring in local over-charges or over-discharges, thus guaranteeing the safety conditions; the SOC is therefore constrained to vary within $SOC_{\min} = 15\%$ and $SOC_{\max} = 95\%$. The initial battery SOC is set to $SOC(0) = 50\%$ and the charge sustaining condition, typical of the non-plugin HEV, is enforced by constraining the final battery SOC to remain within a small window around its initial value, namely $SOC(0) - \text{tol} \leq SOC(t_f) \leq SOC(0) + \text{tol}$, where we set $\text{tol} = 2\%$.

Finally, the engine and motor torques have to guarantee the torque split condition in (3.1), while the battery power in (3.6) must equate the electric motor power requirement in (3.4).

3.2.2 Solution method

The *direct* approach, based on a proper discretization of the infinite dimensional optimal control problem, is recommended in [7] for the solution of large scale problems. The resulting finite dimensional problem can be solved by nonlinear programming techniques. In this work we adopt the direct approach for the discretization of the problem described in Section 3.2.1, then we solve the resulting finite dimensional problem with the interior-point algorithm implemented in the state-of-the-art solver Ipopt [28].

We define the equidistant grid $G_N = \{t_0 < t_1 < \dots < t_N = t_f\}$, with constant time step $t_s = \frac{t_N - t_0}{N}$ and grid points $t_j = t_0 + j t_s$, $j = 1, \dots, N$. We set $t_s = 0.5$ s for each driving cycle, therefore the length of the discretization grid is determined by the initial and the final time instants.

We discretize the control by replacing it means of B-spline basis functions of order 1 (piecewise constant functions) on the grid G_N . We then discretize the differential equation (3.8) using the Tustin method, that yields

$$\begin{aligned} x(t_{j+1}) = & \left[\left(I I_{n_x} - \frac{t_s}{2} A \right)^{-1} \left(I I_{n_x} + \frac{t_s}{2} A \right) \right] x(t_j) \\ & + \left[\left(I I_{n_x} - \frac{t_s}{2} A \right)^{-1} B t_s \right] u \left(t_{j+\frac{1}{2}} \right), \quad j = 0, \dots, N-1 \end{aligned} \quad (3.17)$$

where $u\left(t_{j+\frac{1}{2}}\right) = \frac{u_{t_j} + u_{t_{j+1}}}{2}$, I_{n_x} is the $n_x \times n_x$ identity matrix and the continuous state-space matrices A and B are as in (3.8). Finally, we evaluate the objective function (3.16) and the constraints on the grid \mathbb{G}_N .

Ipopt is a gradient based optimizer that requires the gradient of the objective function and the Jacobian of the constraints (and optionally the Hessian of the Lagrange function); we provide the required derivatives with the algorithmic differentiator ADiGator [29]. We solved the optimal control problem running ADiGator and Ipopt on Matlab 2017b on a 2.5 GHz Intel i5 processor with 2 cores and with 16GB of memory.

In the following section we show the results of the simulations that have been run several times with different values of the Pareto coefficient α and at different temperatures.

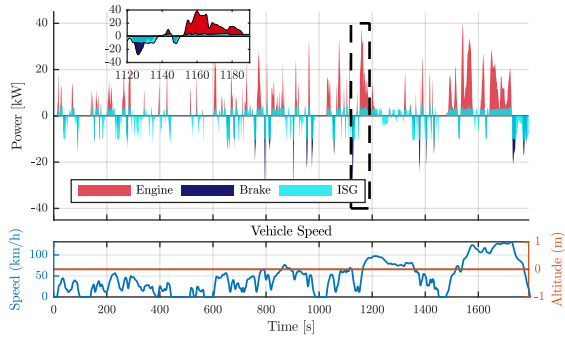
3.2.3 Simulation results

In this section we first show the solution of the energy management problem without considering the battery aging, i.e. we set $\alpha = 1$ in the cost function (3.16). Then, we solve the energy management problem to changing values of the Pareto coefficient; in this way we show how different weights on the two objectives — energy management and battery preserving — affect the control strategy. Finally, we repeat the optimization for changing values of the battery temperature.

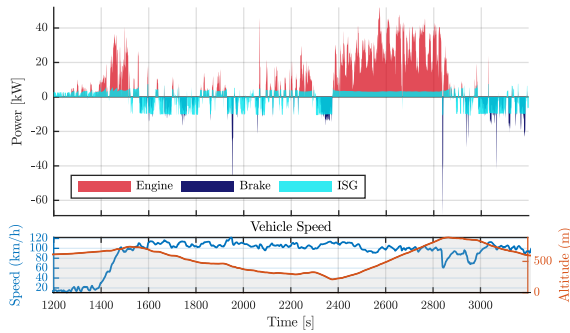
3.2.3.1 Solution to the energy management problem

The optimization has been solved for the four driving cycles in Figure 3.B.1, but we discuss here only two of the: WLTC and Vail2NREL.

First, we set the battery temperature at 30°C and we select the Pareto coefficient $\alpha = 1$ to find a solution that optimizes solely the fuel consumption. In Figure 3.5 we present the optimal power split resulting from the solution of the optimization problem. We see that both in the WLTC and in the Vail2NREL driving cycles the electric machine is able to assist the engine with an approximately constant power; this is possible because most of the braking energy is recovered by the generator and the mechanical brakes intervenes only when the braking maneuver is too severe. It also interesting to notice that the optimal control exploits the last deceleration in both driving cycles to bring the battery SOC to its initial value, as imposed by the constraints detailed in Section 3.2.1 and shown in Figure 3.6 on a cell level. The a-priori knowledge of the road slope in the Vail2NREL driving cycle allows for an intelligent management of the battery, recovering energy during the downhills that is used to assist the engine during the uphills.



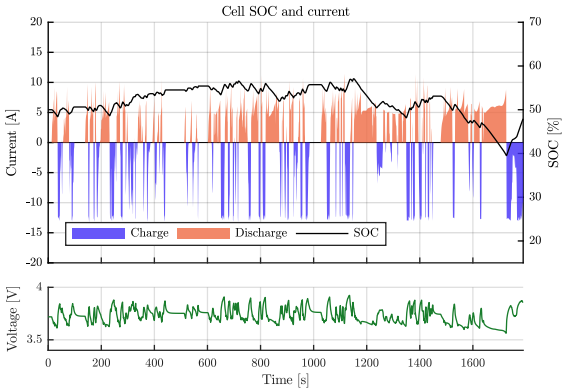
(a) WLTC cycle.



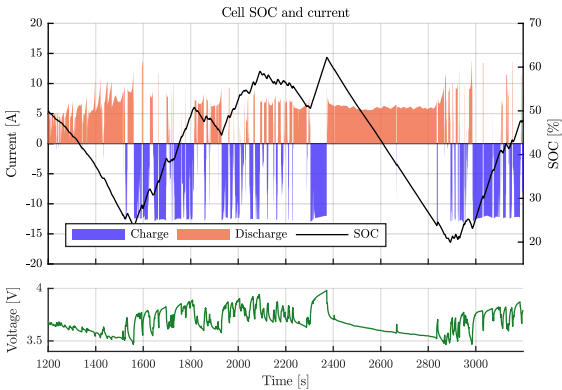
(b) Vail2NREL cycle

Figure 3.5: Optimal power split of the hybrid transmission.

We see from Figure 3.6 that nor the battery current, voltage or SOC bounds are limiting the electric performance, since they lay within their admissible range throughout the driving cycle. This means that the capability of the electric system to recover or release power is restricted by the torque limits of the electric machine, as illustrated in Figure 3.7. Nevertheless, it is clear from Figure 3.7 that the optimal control manages to make the ISG work in the proximity of its highest efficiency regions. This is particularly true when the electric machine is working in motor mode, while when the electric machine is regenerating, even the less efficient regions are exploited: this leads to conclude that, from the electric machine perspective, it is fundamental to recover as much energy as possible, not necessarily in an efficient way.



(a) WLTC cycle.



(b) Vail2NREL cycle

Figure 3.6: Cell current, SOC and voltage.

The fuel savings for the four driving cycles are reported in Table 3.3. The best fuel savings performances are obtained in the WLTC cycle, since the frequent acceleration and deceleration maneuvers — and the resulting charge/discharge profiles — allow to use the battery in the most effective way; the US06 driving cycle exhibits the lowest fuel savings performance, because of the almost constant high speed for most of the cycle time that prevents the battery from re-charging.

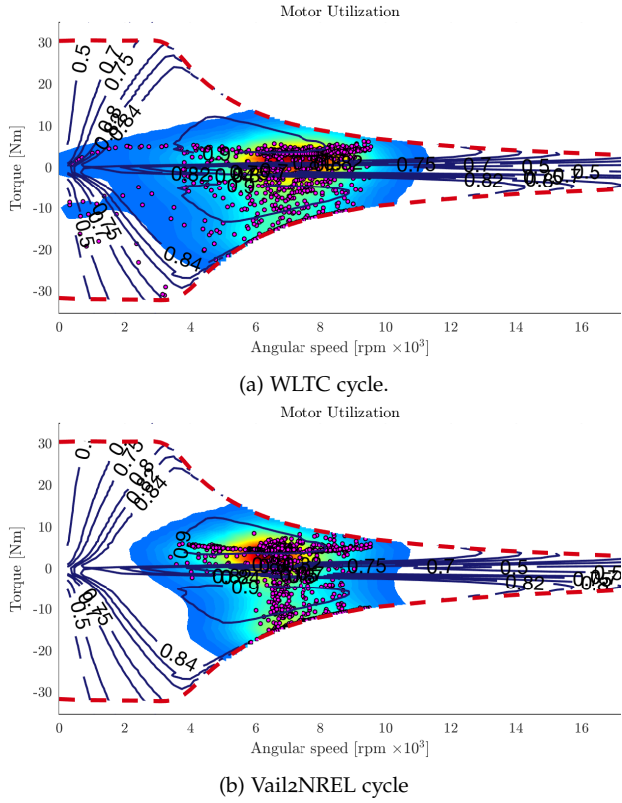


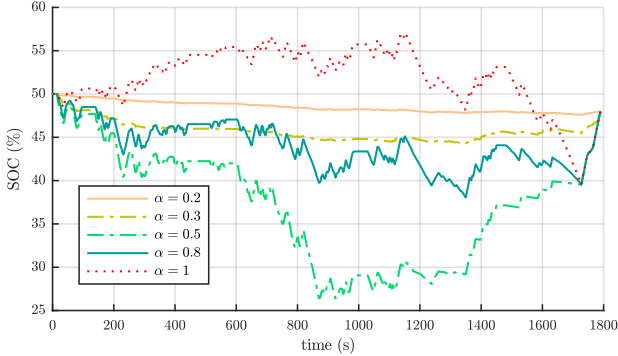
Figure 3.7: Electric machine utilization.

	WLTC	Vail2NREL	US06	NEDC
Only engine (l)	1.04	1.65	0.49	0.51
HEV (l)	0.88	1.45	0.44	0.44
Savings	15.4%	12.1%	10.2%	13.7%

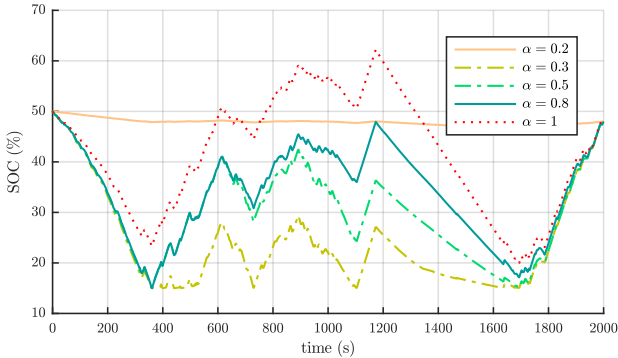
Table 3.3: Fuel savings with optimal energy management control of the hybrid electric vehicle.

3.2.3.2 Solution to changing Pareto coefficient

By reducing the value of the Pareto coefficient α in (3.16) we give more importance to the mitigation of the capacity degradation of the battery, penalizing the fuel consumption minimization.



(a) WLTC cycle.

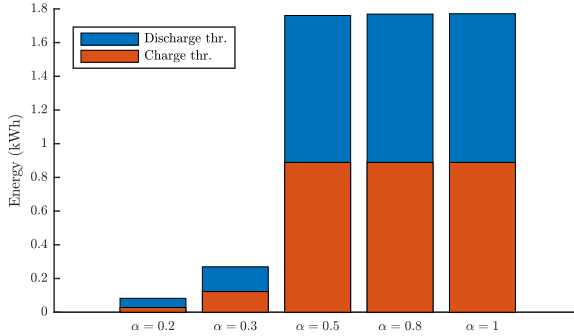


(b) VailzNREL cycle

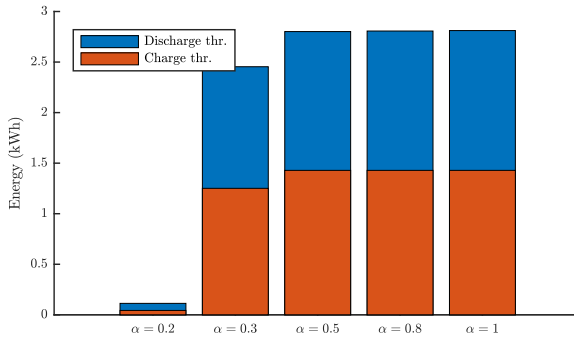
Figure 3.8: Comparison of the battery SOC for different values of the Pareto coefficient α .

In Figure 3.8 we show the SOC profiles at different values of the Pareto coefficient: in both driving cycles the SOC trends look similar for $\alpha \geq 5$, but its average value gets smaller and smaller. For values of the Pareto coefficient close to zero the SOC remains approximately constant around its initial value, because almost no energy is delivered by the battery, nor stored into it as depicted in Figure 3.9; this means that the electric branch of the hybrid power-train is not used to preserve the health of the battery.

This is of course an unwanted behavior, because it does not bring any advantage to the fuel savings performance; to this end we must select higher values of α , in particular, for this powertrain configuration, we choose $\alpha \geq 5$.



(a) WLTC cycle.



(b) VailzNREL cycle

Figure 3.9: Comparison of the battery energy throughput for different values of the Pareto coefficient α .

We reported in Table 3.4 the fuel savings for the four driving cycles and for different values of the Pareto coefficient. We see that, as expected, we got almost no fuel savings (compared to the ICE only solution) for values of α close to zero, meanwhile for $\alpha \geq 0.5$ we manage to obtain quite similar fuel reduction. This result is justified by inspecting the total energy throughput of the battery in Figure 3.9, that is almost identical for the solutions with $\alpha \geq 0.55$, despite the different average states of charge.

Even though the fuel savings remain approximately the same for intermediate values of the Pareto coefficient, we can achieve a significant

(%)	WLTC	Vail2NREL	USo6	NEDC
$\alpha = 0.2$	0.9	1.0	1.4	1.6
$\alpha = 0.5$	14.7	13.7	10.5	13.2
$\alpha = 0.8$	15.2	13.9	10.7	13.6
$\alpha = 1.0$	15.4	14.1	10.7	13.7

Table 3.4: Fuel savings comparison for different values of the Pareto coefficient α . Savings are referred to the fuel consumption with only ICE.

decrease of the battery deterioration as shown in Table 3.5, where we report the percentage capacity degradation reduction w.r.t. the solution with $\alpha = 1$. For $\alpha = 0.2$ we simulate a negligible deterioration of the

(%)	WLTC	Vail2NREL	USo6	NEDC
$\alpha = 0.2$	96.1	96.3	95.0	94.2
$\alpha = 0.5$	27.1	24.5	5.5	11.0
$\alpha = 0.8$	14.1	18.5	1.1	1.8
$\alpha = 1.0$	0	0	0	0

Table 3.5: Reduction of the capacity degradation for $\alpha < 1$.

battery capacity, due to the battery inactivity during the driving cycle. For intermediate values of the Pareto coefficient, namely $0.5 \leq \alpha \leq 0.8$, we found a meaningful reduction of the battery deterioration. This is a remarkable result, since we can slow down battery aging without significantly affecting the fuel savings capabilities of the electric hybrid power-train; indeed, the control strategy computed with $\alpha = 0.5$ in the WLTC driving cycle, allows to obtain almost the same fuel reduction performance while reducing the aging rate by 27%.

The motivation of these results can be found in the degradation model (3.15): first, lower SOC leads to higher values of the open circuit anode-potential $U_n(\cdot)$, slowing down the SEI layer growth; second and most important, the SOC-weighted energy throughput is considerably reduced for lower values of the Pareto coefficient as shown in Figure 3.10, leading to a much slower degradation associated to the charge/discharge cycles of the battery.

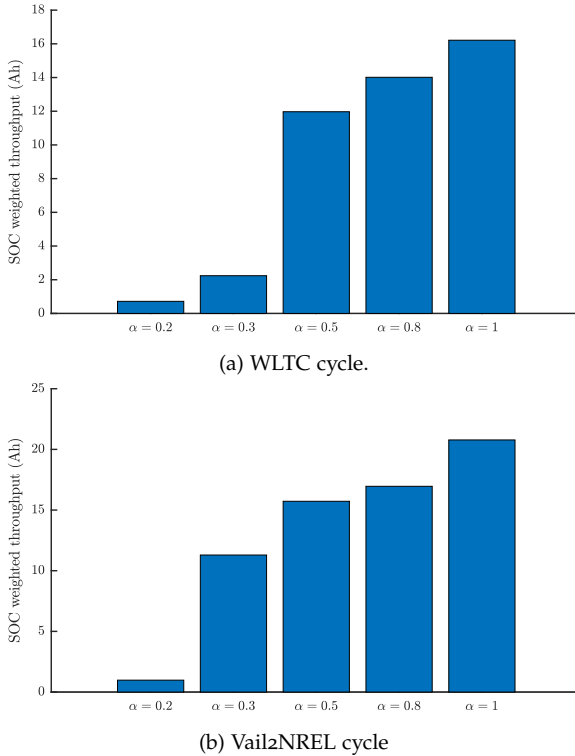


Figure 3.10: Comparison of the SOC-weighted current throughput for different values of the Pareto coefficient α .

In the following we show how the operating temperature of the battery affects both the fuel savings performance and the battery degradation rate.

3.2.3.3 Solution to changing temperature

We have seen in Section 3.1.4 that the temperature accelerates the kinetics of the side reactions that lead to capacity loss and impedance increase, reducing the life span of the battery pack. On the other side, too cold temperatures slow down the diffusion reactions with a consequent increase of the battery impedance, having a detrimental effect on the overall efficiency.

The cooling system of a battery pack is designed to prevent the battery temperature from reaching too high values, in order to extend the battery

life and to avoid unsafe operating conditions (e.g. thermal runaway). The cooling system activates when the temperature of the battery exceeds a certain threshold, that is selected according to a compromise between performance optimization and battery life. In the following we show how such threshold, together with the selection of the Pareto coefficient, influences the optimization results. The Pareto curves of Figure 3.11 have

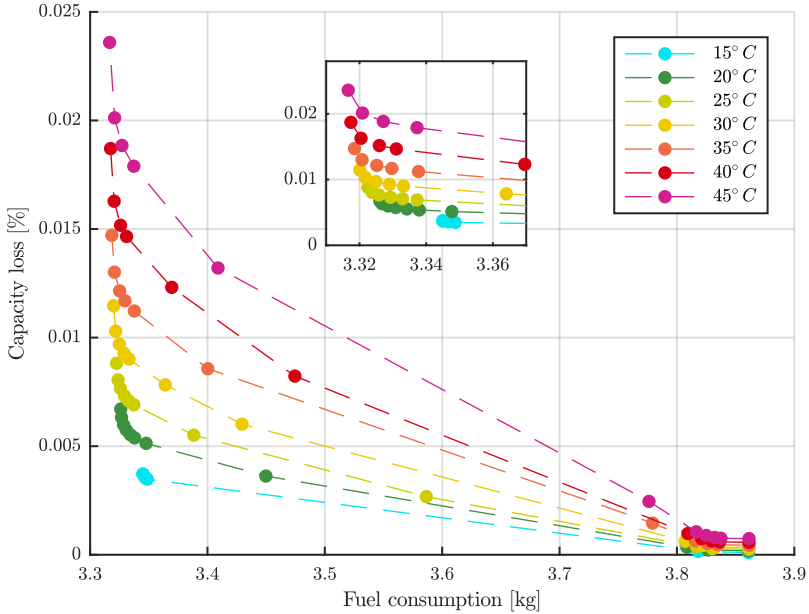


Figure 3.11: Pareto curves for the four concatenated driving cycles.

been drawn by simulating the capacity loss and the fuel consumption for different values of the Pareto coefficient (points with the same color), changing the temperature and concatenating the four driving cycles (WLTC, Vail2Nrel, US06 and NEDC). The Pareto coefficients being equal, there is a clear reduction of the capacity loss at lower temperatures, due to the Arrhenius-like equations governing the side-reaction kinetics. It is interesting to notice that in the leftmost part of the plot, i.e. for higher values of α , a small reduction of the Pareto coefficient leads to a remarkable decrease of the capacity loss together with minor changes of the fuel consumption; this is an important outcome of our work, that proves that we can use control strategies that aim at preserving the battery

life without affecting the fuel savings capability of the electric hybrid power-train.

The fuel-saving performance degradation at lower temperatures are more visible in the left-most part of the plot, where we notice a slight variation of the fuel consumption at different temperatures. For the driving cycles studied in this work, these variations are almost negligible due to the fact the the battery operates far from the imposed constraints on voltage and surface concentration; more severe cycles, or a smaller battery, could result in a greater relevance of the operating temperature on the fuel savings performance.

3.2.3.4 *Conclusions and future work*

In this section we have presented the results obtained with several numerical simulations based on reliable and validated models of the battery aging and dynamics and of the engine and motor efficiency. We found that for certain values of the Pareto coefficient, the multi-objective optimal control problem yield control strategies that allow to extend the battery life up to 15 – 20% without altering the fuel economy of the electric hybrid power-train. We finally saw how the battery temperature influences the capacity losses and the fuel consumptions.

The off-line optimal control solution proposed in this work is a powerful tool that allows to identify the most suitable strategies that optimize the fuel consumptions and extend the lifespan of the battery. We can infer general guidelines from this study to devise rule-based control strategies: first, in order to extend the battery lifespan, it is convenient to make the battery work at low SOC values to slow down the SEI formation, even if this results in higher current demand to provide the same power; also, an average battery temperature between 25° C and 30° C should be kept to get a reasonable trade-off between performance and aging dynamics. It is also interesting to notice that the optimal control strategy makes the electric machine work even in non-efficient regions during regenerative braking, so that to recover the highest amount of energy; on the contrary, when the electric machine works as a motor, the optimal control strategy selects the highest efficiency regions.

Future developments of this project will include a thermal dynamic model of the battery, so that we can take into account the thermal limitations and evaluate different cooling strategies. Moreover, we will use more detailed battery aging models in order to include also the lithium-plating phenomena that take place during battery charge at lower temperatures.

3.3 TOWARDS A RUN-TIME OPTIMIZATION

Model Predictive Control (MPC) allows to formulate and solve a multi-variable optimization problem over a future evolution of a dynamical system, taking into account the system constraints.

Formulating the optimal control problem presented in Section 3.2 in an MPC framework, allows to compute real-time on the Electronic Control Unit (ECU) the optimal power-split compliant with the battery constraints on voltage, SOC and surface concentration and with the control limitations.

Historically, non-linear MPC has been used mainly to control systems characterized by very slow dynamics, such as chemical plants [22]; the recent improvements of the capabilities of embedded computers and the development of more efficient numerical methods (such as FORCES [32], an interior point algorithm designed specifically for embedded systems) made it possible to extend the range of applications to more demanding fields, such as automotive.

We want to prove in this section the effectiveness and the feasibility of the MPC based on an accurate drive-line and battery model for deciding the optimal energy management strategy. We present in this section some preliminary results on the MPC for energy management, we discuss the solution time, the influence of the horizon length on the optimization results and the adaptation of the objective function to shorter prediction horizons.

3.3.1 MPC problem formulation

In receding horizon MPC, the optimal control problem is solved over a finite future horizon $[t_0, t_h]$ with $t_h \ll t_f$, discretized over a grid of $N_h = \frac{t_h - t_0}{t_s}$ intervals, where $t_0 \geq t_j = t_0 + j t_s \geq t_h = t_0 + N_h t_s$ for $j = 0, \dots, N_h$. Only the first element of the control vector is applied, then a new future evolution is predicted based on the current state of the system and the optimization is repeated. A repeated on-line optimization allows to have a continuously updated knowledge of the state of the system thanks to the measurement feedback.

Without an a-priori knowledge of the complete driving cycle, we must enforce the charge-sustaining mode adding a SOC-dependent term to the cost function in (3.16), i.e.

$$\begin{aligned}
 J = & \alpha \int_{t_0}^{t_h} \Gamma_{\text{fuel}} \dot{m}_f(x(t), u(t)) dt \\
 & + (1 - \alpha) \Gamma_{\text{age}} Q_{\text{loss}}(x(t_h), u(t_h)) \\
 & - \rho \text{SOC}(t_h),
 \end{aligned} \tag{3.18}$$

where $\rho < 0$ is a weighting term that is selected based on the desired performance of the energy management strategy. In its most general formulation, the term ρ can vary from one iteration to another to enforce different control behaviors that depend on the initial condition of the system, in this case we say that ρ depends on the initial horizon time, i.e. $\rho = \rho(t_0)$.

3.3.2 Real-time solution of the optimal control problem

Two main assumptions have been made in this study: first, we consider to know precisely the future speed of the vehicle in the horizon window; this is of course not the case in real-life applications; nevertheless, extremely good predictions can be obtained exploiting the on-board Advanced Driving-Assistance Systems (ADAS) as in the co-driver strategy [5] and [2]. Second, we assume to know the states of the system at every iteration of the MPC algorithm, meaning that an accurate battery state estimation algorithm³ (as the ones based on the electrochemical model proposed in [1]) should be implemented.

We run the simulations for the WLTC driving cycle (Figure 3.B.1a) using two different horizon lengths, $t_{h,5} = 5$ s and $t_{h,10} = 10$ s with sampling time equal to $t_s = 0.5$ s, in order to inspect how the prediction horizon affects the MPC performance. We fixed the battery temperature at $T = 30$ °C and the initial state of charge was set to $\text{SOC}(t_0) = 50\%$.

The average solution time for both the 5 s and the 10 s prediction horizon was 100 ms on our Intel i5 machine using Ipopt and the limited-memory BFGS approximation of the Hessian. The MPC solution was updated every 0.5 s; if the solver couldn't provide a solution after this time, we didn't update the solution and the last available control was implemented.

The fuel savings in Table 3.6 are computed for the WLCT driving cycle with respect to the fuel consumption of the ICE-only drive-line. Notice that in the off-line optimization the horizon length is equal to the total

³ The battery state estimation algorithm is not treated in this work.

length of the driving cycle, namely $t_h = t_f$. The fraction of battery aging

Horizon length		$t_h = t_f$	$t_h = 5\text{ s}$	$t_h = 10\text{ s}$
$\alpha = 1.0$	(%)	15.4	13.7	13.9
$\alpha = 0.7$	(%)	15.1	9.7	10.2
$\alpha = 0.5$	(%)	14.7	9.2	9.5

Table 3.6: Comparison of the fuel savings obtained using different horizon lengths of the WLTC cycle. Percentage relative to the ICE-only power-train consumption.

in Table 3.7 is computed with respect to the optimization over the entire cycle time (i.e. $t_h = t_f$) with $\alpha = 1.0$. It can be seen that, as expected, in the

Horizon length		$t_h = t_f$	$t_h = 5\text{ s}$	$t_h = 10\text{ s}$
$\alpha = 1.0$	(%)	0.0	-18.6	-18.4
$\alpha = 0.7$	(%)	14.1	-4.6	-2.6
$\alpha = 0.5$	(%)	27.1	9.1	9.7

Table 3.7: Comparison of the battery aging obtained using different horizon lengths of the WLTC cycle. Percentage relative to the full horizon solution with $\alpha = 1$.

MPC case the fuel savings and the battery life preserving performance degrades with respect to the off-line optimization on the entire cycle time. This is due to the limited knowledge of the future evolution of the system, that prevents the algorithm from finding the best power-split solution.

It is interesting to notice that doubling the length of the horizon window from $t_h = 5\text{ s}$ to $t_h = 10\text{ s}$ does not sensibly affect the results, nor the average solution time that remains around 100 ms. This means that it is sufficient to have a good prediction of the vehicle speed on a short 5 s horizon window to get satisfactory MPC performance.

We can see in Figure 3.12 the both the MPC implementations induce larger SOC variations with respect to the full horizon solution. This means that the battery is charged and discharged more frequently, leading to a higher current throughput that accelerates battery aging, as indicated by the results in Table 3.7. The battery-life preserving performance of the MPC algorithm can be improved by reducing the value of the Pareto coefficient α , giving more importance to the capacity degradation term of the objective function.

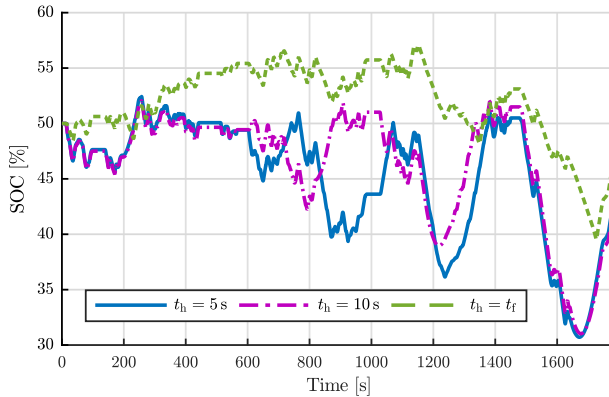


Figure 3.12: Comparison between SOC evolutions with $\alpha = 1$ during WLTC cycle using different horizon lengths.

The behavior of the MPC algorithm can sensibly vary with a different selection of the cost function weights. This allows to obtain the desired control behavior with a suitable calibration of the control parameters without changing the control structure, making it appealing for different applications and driving modes. The proposed nonlinear MPC is based on a validated electrochemical model of the battery which allows to accurately predict the system evolution and avoid unsafe working regions, e.g. too low or too high surface overpotential. The MPC iterations can be solved in a few hundreds of milliseconds, allowing for an update of the solution every 0.5s, which is sufficient for a real-time implementation of the algorithm.

Further studies will address the recursive feasibility problem, in order to guarantee that there always exists a solution which is compliant with the imposed constraints. Moreover, following a hardware-in-the-loop (HIL) approach, we will see if the solution time of the MPC iterations remain unchanged even on an embedded system, suitable for a real-time implementation of the algorithm.

3.4 CONCLUSIONS

In this chapter we have presented a battery-life aware energy management algorithm to get the optimal power split in an electric hybrid power-train of a passenger car. We employed the electrochemical model of the battery, that provides a reliable prediction of the evolution of its states and captures the capacity degradation dynamics.

We studied the effects of different weights (Pareto coefficients) on the objective function that alter the impact of the fuel savings and the battery aging terms. Moreover, we studied the impact of the battery temperature on the final result.

Finally, we proposed some preliminary results on the real-time implementation of the algorithm in a non-linear MPC framework: we showed that the solution time of the optimization problem on a short time horizon is compatible with a real-time update of the solution; moreover, we inspected the influence of the horizon length on the performance of the control algorithm.

BIBLIOGRAPHY OF CHAPTER 3

- [1] Alexander Bartlett, James Marcicki, Simona Onori, Giorgio Rizzoni, Xiao Guang Yang, and Ted Miller. “Electrochemical model-based state of charge and capacity estimation for a composite electrode lithium-ion battery.” In: *IEEE Transactions on control systems technology* 24.2 (2016), pp. 384–399.
- [2] Andrea Bisoffi, Francesco Biral, Mauro Da Lio, and Luca Zaccarian. “Longitudinal jerk estimation of driver intentions for advanced driver assistance systems.” In: *IEEE/ASME Transactions on Mechatronics* 22.4 (2017), pp. 1531–1541.
- [3] Boli Chen, Simos A Evangelou, and Roberto Lot. “Fuel Efficiency Optimization Methodologies for Series Hybrid Electric Vehicles.” In: *2018 IEEE Vehicle Power and Propulsion Conference (VPPC)*. IEEE, 2018, pp. 1–6.
- [4] Boli Chen, Simos A Evangelou, and Roberto Lot. “Impact of optimally controlled continuously variable transmission on fuel economy of a series hybrid electric vehicle.” In: *2018 European Control Conference (ECC)*. IEEE, 2018, pp. 575–580.
- [5] Mauro Da Lio, Francesco Biral, Enrico Bertolazzi, Marco Galvani, Paolo Bosetti, David Windridge, Andrea Saroldi, and Fabio Tango. “Artificial co-drivers as a universal enabling technology for future intelligent vehicles and transportation systems.” In: *IEEE Transactions on intelligent transportation systems* 16.1 (2015), pp. 244–263.
- [6] Simone Formentin, Jacopo Guanetti, and Sergio M Savaresi. “Least costly energy management for series hybrid electric vehicles.” In: *Control Engineering Practice* 48 (2016), pp. 37–51.
- [7] Matthias Gerdts. *Optimal control of ODEs and DAEs*. Walter de Gruyter, 2012.
- [8] Jacopo Guanetti, Simone Formentin, Matteo Corno, and Sergio M Savaresi. “Optimal energy management in series hybrid electric bicycles.” In: *Automatica* 81 (2017), pp. 96–106.
- [9] Xiaosong Hu, Shengbo Li, and Huei Peng. “A comparative study of equivalent circuit models for Li-ion batteries.” In: *Journal of Power Sources* 198 (2012), pp. 359–367.

- [10] Xiaosong Hu, Clara Marina Martinez, and Yalian Yang. "Charging, power management, and battery degradation mitigation in plug-in hybrid electric vehicles: A unified cost-optimal approach." In: *Mechanical Systems and Signal Processing* 87 (2017), pp. 4–16.
- [11] Xing Jin, Ashish Vora, Vaidehi Hoshing, Tridib Saha, Gregory Shaver, R Edwin García, Oleg Wasynczuk, and Subbarao Varigonda. "Physically-based reduced-order capacity loss model for graphite anodes in Li-ion battery cells." In: *Journal of Power Sources* 342 (2017), pp. 750–761.
- [12] Tae-Kyung Lee, Youngki Kim, Anna Stefanopoulou, and Zoran S Filipi. "Hybrid electric vehicle supervisory control design reflecting estimated lithium-ion battery electrochemical dynamics." In: *American Control Conference (ACC), 2011*. IEEE. 2011, pp. 388–395.
- [13] Roberto Lot and Simos A Evangelou. "Green driving optimization of a series hybrid electric vehicle." In: *Decision and Control (CDC), 2013 IEEE 52nd Annual Conference on*. IEEE. 2013, pp. 2200–2207.
- [14] Scott J Moura, Jeffrey L Stein, and Hosam K Fathy. "Battery-health conscious power management in plug-in hybrid electric vehicles via electrochemical modeling and stochastic control." In: *IEEE Transactions on Control Systems Technology* 21.3 (2013), pp. 679–694.
- [15] Scott J Moura, Joel C Forman, Saeid Bashash, Jeffrey L Stein, and Hosam K Fathy. "Optimal control of film growth in lithium-ion battery packs via relay switches." In: *IEEE Transactions on Industrial Electronics* 58.8 (2011), pp. 3555–3566.
- [16] Nikolce Murgovski, Lars Johannesson, Xiaosong Hu, Bo Egardt, and Jonas Sjöberg. "Convex relaxations in the optimal control of electrified vehicles." In: *American Control Conference (ACC), 2015*. IEEE. 2015, pp. 2292–2298.
- [17] Cristian Musardo, Giorgio Rizzoni, Yann Guezennec, and Benedetto Staccia. "A-ECMS: An adaptive algorithm for hybrid electric vehicle energy management." In: *European Journal of Control* 11.4-5 (2005), pp. 509–524.
- [18] Tobias Nüesch, Philipp Elbert, Michael Flankl, Christopher Onder, and Lino Guzzella. "Convex optimization for the energy management of hybrid electric vehicles considering engine start and gearshift costs." In: *Energies* 7.2 (2014), pp. 834–856.
- [19] Simona Onori, Lorenzo Serrao, and Giorgio Rizzoni. *Hybrid Electric Vehicles, Energy Management Strategies*. 2016. ISBN: 978-1-4471-6779-2. DOI: [10.1007/978-1-4471-6781-5](https://doi.org/10.1007/978-1-4471-6781-5). URL: <http://link.springer.com/10.1007/978-1-4471-6781-5>.

- [20] Thomas Miro Padovani, Maxime Debert, Guillaume Colin, and Yann Chamailard. "Optimal energy management strategy including battery health through thermal management for hybrid vehicles." In: *Advances in automotive control (AAC 2013)*. 2013, pp. 384–389.
- [21] Gino Paganelli, Gabriele Ercole, Avra Brahma, Yann Guezennec, and Giorgio Rizzoni. "General supervisory control policy for the energy optimization of charge-sustaining hybrid electric vehicles." In: *JSAE review* 22.4 (2001), pp. 511–518.
- [22] S Joe Qin and Thomas A Badgwell. "A survey of industrial model predictive control technology." In: *Control engineering practice* 11.7 (2003), pp. 733–764.
- [23] Lorenzo Serrao, Simona Onori, and Giorgio Rizzoni. "A comparative analysis of energy management strategies for hybrid electric vehicles." In: *Journal of Dynamic Systems, Measurement, and Control* 133.3 (2011), p. 031012.
- [24] Lorenzo Serrao, Simona Onori, Antonio Sciarretta, Yann Guezennec, and Giorgio Rizzoni. "Optimal energy management of hybrid electric vehicles including battery aging." In: *American Control Conference (ACC), 2011*. IEEE. 2011, pp. 2125–2130.
- [25] Li Tang, Giorgio Rizzoni, and Simona Onori. "Energy management strategy for HEVs including battery life optimization." In: *IEEE Transactions on Transportation Electrification* 1.3 (2015), pp. 211–222.
- [26] Tanvir R Tanim, Christopher D Rahn, and Chao-Yang Wang. "A temperature dependent, single particle, lithium ion cell model including electrolyte diffusion." In: *Journal of Dynamic Systems, Measurement, and Control* 137.1 (2015), p. 011005.
- [27] Lars Ole Valøen and Jan N Reimers. "Transport properties of LiPF₆-based Li-ion battery electrolytes." In: *Journal of The Electrochemical Society* 152.5 (2005), A882–A891.
- [28] Andreas Wächter and Lorenz T Biegler. "On the implementation of an interior-point filter line-search algorithm for large-scale nonlinear programming." In: *Mathematical programming* 106.1 (2006), pp. 25–57.
- [29] Matthew J Weinstein, Michael A Patterson, and Anil V Rao. "Utilizing the Algorithmic Differentiation Package ADiGator for Solving Optimal Control Problems Using Direct Collocation." In: *AIAA Guidance, Navigation, and Control Conference*. 2015, p. 1085.

- [30] Naoaki Yabuuchi, Yoshinari Makimura, and Tsutomu Ohzuku. "Solid-State Chemistry and Electrochemistry of $\text{LiCo}_{1/3}\text{Ni}_{1/3}\text{Mn}_{1/3}\text{O}_2$ for Advanced Lithium-Ion Batteries III. Rechargeable Capacity and Cycleability." In: *Journal of The Electrochemical Society* 154.4 (2007), A314–A321.
- [31] Xingda Yan, James Fleming, and Roberto Lot. "Extending the range of Plug-in Hybrid Electric Vehicles by CVT transmission optimal management." In: *Energy Procedia* 151 (2018), pp. 17–22.
- [32] Andrea Zanelli, Alexander Domahidi, J Jerez, and Manfred Morari. "FORCES NLP: an efficient implementation of interior-point methods for multistage nonlinear nonconvex programs." In: *International Journal of Control* (2017), pp. 1–17.
- [33] Xueyu Zhang and Zoran Filipi. "Optimal supervisory control of the series HEV with consideration of temperature effects on battery fading and cooling loss." In: *SAE International Journal of Alternative Powertrains* 5.2 (2016), pp. 299–307.

APPENDIX OF CHAPTER 3

3.A BATTERY MODEL PARAMETERS

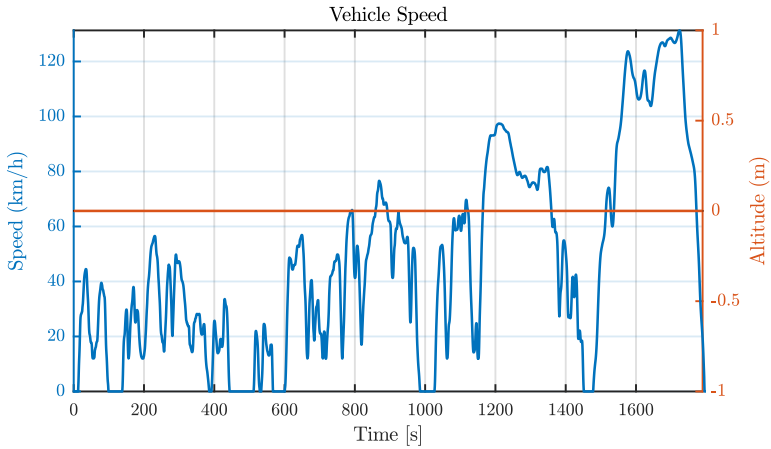
Description	Unit	Symbol	Value
Faraday Constant	C mol^{-1}	F	96487
Gas Constant	J (mol K)^{-1}	R_g	8.3140
Nominal Capacity	Ah	Q_N	2.0
Bruggeman coefficient	–	γ	1.5
Transference number	–	t_0^+	0.38
Mean electrolyte concentration	mol cm^{-3}	$c_{e,\text{avg}}$	$1.2 \cdot 10^{-3}$
Electrode Area	cm^2	A^P	$1.0204 \cdot 10^3$
		A^N	$1.0204 \cdot 10^3$
Layer thickness	cm	L^P	$3.65 \cdot 10^{-3}$
		L^S	$2.50 \cdot 10^{-3}$
		L^N	$4.00 \cdot 10^{-3}$
Volume Fraction	-	ϵ^P	0.6395
		ϵ^S	0.3000
		ϵ^N	0.6500
Max. Li-ion concentration	mol cm^{-3}	$c_{s,\text{max}}^P$	0.0518
		$c_{s,\text{max}}^N$	0.0311
Initial stoichiometry	-	$\theta_{0\%}^P$	0.9518
		$\theta_{0\%}^N$	0.0168
Final stoichiometry	-	$\theta_{100\%}^P$	0.3176
		$\theta_{100\%}^N$	0.9664
Particle Radius	cm	R_s^P	$5 \cdot 10^{-4}$
		R_s^N	$5 \cdot 10^{-4}$
Active surface	cm^{-1}	a_s^P	$3.8373 \cdot 10^3$
		a_s^N	$3.9000 \cdot 10^3$

Table 3.A.1: List of parameters of the gr/NMC 2.0Ah 3.2V cell.

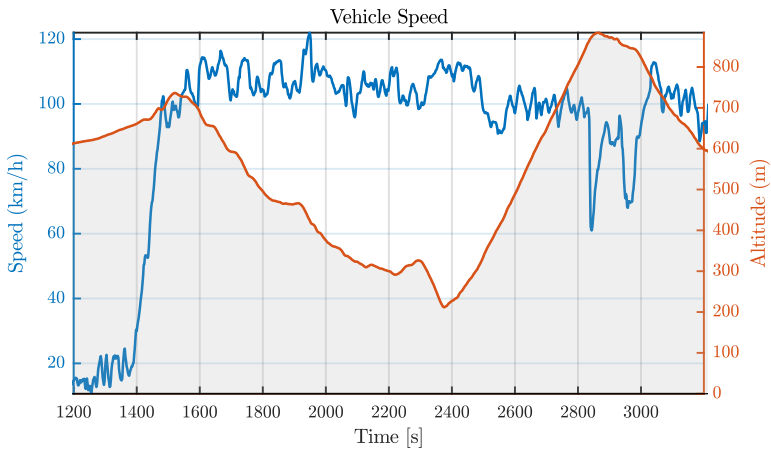
Description	Unit	Symbol	Value
Kinetic coeff. ref. value	$\text{A cm}^{\frac{3}{2}} \text{mol}^{-\frac{3}{2}}$	$k_{\text{ref}}^{\text{P}}$	1
		$k_{\text{ref}}^{\text{n}}$	2.97
- ref. temperature	K	$T_{\text{ref},k}^{\text{P}}$	283
		$T_{\text{ref},k}^{\text{n}}$	296
- activation energy	J mol^{-1}	$E_{\text{act},k}^{\text{P}}$	$8.4720 \cdot 10^4$
		$E_{\text{act},k}^{\text{n}}$	$3.33 \cdot 10^5$
Diffusion coeff. ref. value	$\text{cm}^2 \text{s}^{-1}$	$D_{\text{s,ref}}^{\text{P}}$	$1.314 \cdot 10^{-10}$
		$D_{\text{s,ref}}^{\text{n}}$	$1.001 \cdot 10^{-10}$
- ref. temperature	K	$T_{\text{ref},D_s}^{\text{P}}$	296
		$T_{\text{ref},D_s}^{\text{n}}$	296
- activation energy	J mol^{-1}	$E_{\text{act},D_s}^{\text{P}}$	$1.721 \cdot 10^5$
		$E_{\text{act},D_s}^{\text{n}}$	$1.123 \cdot 10^5$
Contact resistance ref. value		$R_{\Omega,\text{ref}}$	$4.6 \cdot 10^{-3}$
- ref. temperature	K	$T_{\text{ref},R_{\Omega}}$	296
- activation energy	J mol^{-1}	$E_{\text{act},R_{\Omega}}$	$5.67 \cdot 10^3$
Activity coeff. ref. value		β_{ref}	2.35
- ref. temperature	K	$T_{\text{ref},\beta}$	338
- activation energy	J mol^{-1}	$E_{\text{act},\beta}$	$1.164 \cdot 10^3$

Table 3.A.2: List of temperature dependent parameters of the gr/NMC 2.0Ah 3.2V cell.

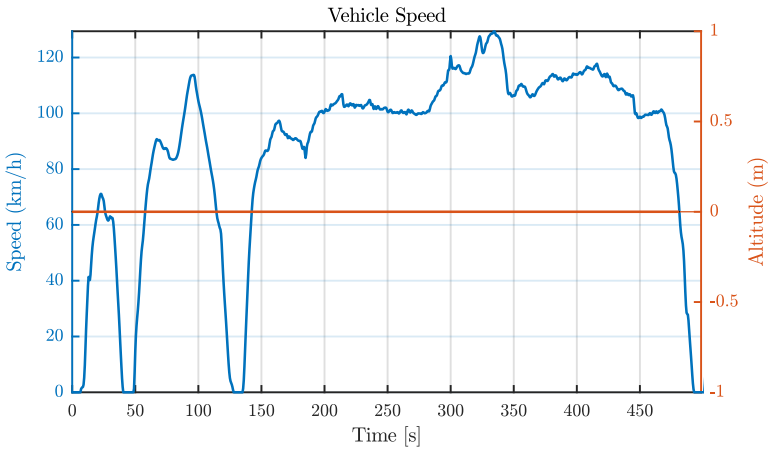
3.B SIMULATIONS RESULT FIGURES



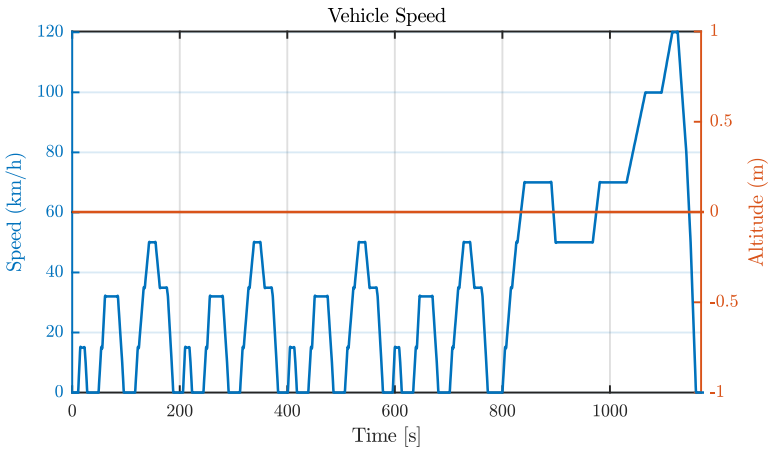
(a) WLTC cycle.



(b) Vail2NREL extra-urban cycle



(c) US06 cycle



(d) NEDC cycle

Figure 3.B.1: Driving cycles considered in this work.

Part II

THE HYBRID HYDROSTATIC TRANSMISSION

HYDROSTATIC TRANSMISSION MODEL

Continuous growth of urban population and the consequent development of suitable infra-structure and transportation systems are bringing to the industrial and academic community's attention the problem of developing environmental sustainable technologies. While research on passenger cars is focusing mainly on the improvement of hybrid electric and full electric architectures [2],[7], the same results cannot be extended to heavy duty vehicles. Indeed, a battery cannot in general comply with the high power demand of the vehicles used in construction, agriculture, mining and forestry, mainly because high and frequent current peaks cause early fading of the battery performances as indicated in [1]. As suggested by Sprengel and Ivantysynova in [15], the limitations of electric hybrids can be overcome by resorting to different and less known technologies like the hydraulic hybrids. These systems are capable of providing considerably high power density by storing more regenerative braking energy compared to their electric counterpart, moreover they are more reliable (typically no maintenance over the vehicle's lifetime) and less subject to aging phenomena. In a hydraulic hybrid transmission, the hydraulic machines are forced to work at the accumulator's current pressure, thus leading to two main issues that inhibit the spread of this technology in standard vehicles: first, the hydraulic motors frequently work at high pressure and small displacement, thus reducing the overall efficiency of the system; secondly, pressures in the accumulators are governed by very slow dynamics and this results in a considerable delay felt by the driver when the pressure in the accumulators is not large enough to generate the demanded torque. To overcome this limit, the authors of [14] propose the so called *Blended Hybrid* transmission that is able to combine the stiffness of the hydrostatic powertrains and the capability of energy recovery of the hybrid systems: in the blended hybrid transmission the accumulators can be detached from the lines through a system of valves, allowing the drivetrain to work as a hydrostatic transmission.

In [3] the authors highlight the importance of a system approach to the fuel economy problem in a series hydraulic hybrid transmission and propose heuristic control strategies that are tested on an Engine In the Loop experimental setup; a similar study has been performed in [5] for a series hydraulic hybrid transmission mounted on a 4×4 conventional vehicle, while in [4] the authors prove the effectiveness of a parallel

hydraulic hybrid transmission implemented on a 6×6 medium tactical truck for the reduction of fuel consumption. These studies demonstrate the interest in the HHT technology and its effectiveness in improving fuel economy, but a validation of the model on a full powertrain and a formal approach to the fuel savings problem is missing in the literature for this kind of architecture; in this work we try to fill this gap by first validating the HHT model using data from a prototype vehicle [13] and then we study the fuel savings performance of the powertrain using numerical techniques from the optimization theory.

In this chapter we focus on the blended type Series Hydraulic Hybrid Transmission (SHHT) developed and design by Dana: Spicer[®] PowerBoost[®] is a series hybrid-hydraulic powertrain for off-highway vehicles and material-handling equipment. The technology is intended for application driven by hydrostatic transmissions, whose typical driving cycle comprises of frequent bursts of accelerations and decelerations, and lifting and lowering maneuvering, where most of the energy can be recuperated. By using hydraulic accumulators, the system recovers a part of the energy that would otherwise be wasted, and uses this energy to help power the vehicle.

The system dynamics are characterized by several discrete actuation (valves and clutch) and continuous controls of the hydraulic machines. The series hybrid-hydraulic powertrain considered in this paper differs from the others presented in the literature, since regenerative phase is attained by inverting the configuration of the accumulators valves, rather than inverting the motors displacement as proposed in [3], [5] and [6]. Indeed, this allows the use of standard commercial bent-axis motors, for which negative displacement is not possible. The transmission architecture is shown in Fig. 4.1, where we can see that all the hydraulic lines reach the valve block, called PowerBoost[®] hub, in the upper part of the image; this is the core of the SHHT transmission, because it manages the connection of the hydraulic accumulators to the lines allowing for the regeneration of the braking energy or the release of extra-power to assist the hydraulic motors. The latter are connected to a mechanical transmission that brings the power to the rest of the driveline up to the wheels.

Continuously variable transmission ratios and energy recovery in hydraulic accumulators improve the overall efficiency of the powertrain, but requires a sophisticated control strategy in order to fully exploit SHHT fuel reduction capability.

The hydraulic hybrid transmission operates in two different modes: hydrostatic mode (HYS) and hybrid mode (HYB). In hydrostatic mode the internal combustion engine (ICE) drives a hydraulic variable displace-

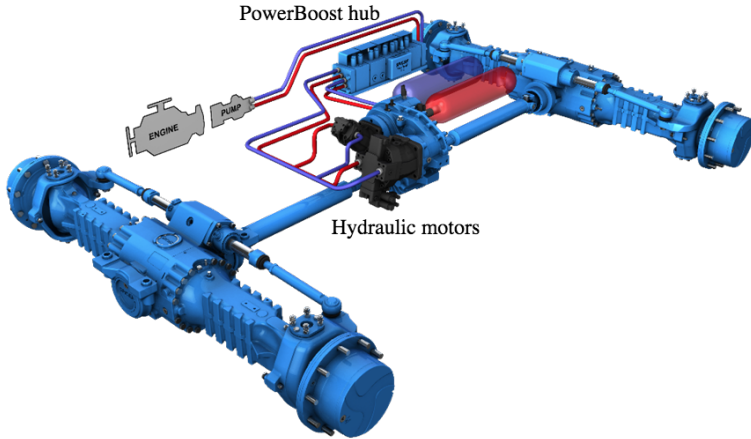


Figure 4.1: Dana Spicer[®] PowerBoost[®] driveline.

ment pump/motor (PM) that pressurizes the oil in the hydraulic circuit; the circuit is connected to two hydraulic motors that convert hydraulic energy into mechanical energy, delivering torque and speed to the vehicle wheels through a gear box and to the rest of the driveline (driveshafts and axles). In hybrid mode, a valve system (PowerBoost Hub) connects two bladder type hydraulic accumulators (one at high pressure and one at low pressure) to the hoses, allowing kinetic energy recovery and power boosting. The overall system dynamics switches between these two operating modes, according to the valves configuration.

In this section we present the mathematical model of the powertrain subsystems, then we proceed with parameters identification and finally we validate the model on data collected in an experimental campaign on a telehandler vehicle thoroughly described in [13].

4.1 MODEL DESIGN

In this section we introduce the subsystems of the Spicer[®] PowerBoost[®] transmission. First, we propose in Section 4.1.1 a model for the hydrostatic transmission only, with no accumulators connected to the lines. This allows to identify the parameters of the hydraulic lines, without the complexity of the hybrid functionalities. The hydraulic accumulators are modeled as a separate subsystem in Section 4.1.2, while in Section 4.1.3 we study the valve block that connects the accumulators to the lines of

the hydrostatic transmission. Finally, the longitudinal dynamic equations of the telescopic handler are treated in Section 4.1.4.

4.1.1 *Hydrostatic sub-system*

The configuration of the telehandler transmission system with two propulsion motors is given in Fig. 4.2. The internal combustion engine drives

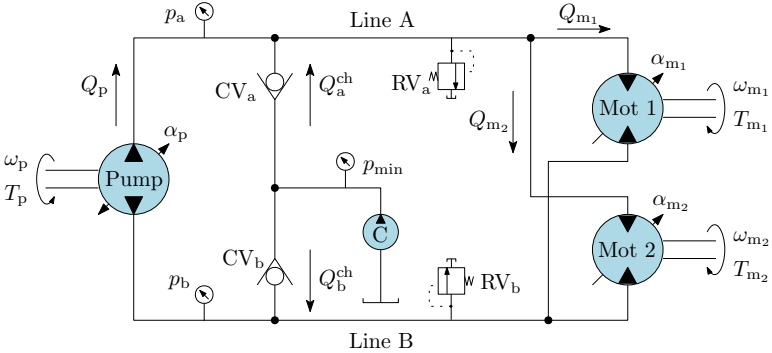


Figure 4.2: Scheme of the transmission in hydrostatic mode. The check valves CV_a and CV_b regulate the flow from the charge pump C, while RV_a and RV_b are the two relief valves.

the variable displacement swash plate piston pump, which rotates with angular velocity $\omega_p = \omega_{ice}$, generating an ideal oil flow rate equal to

$$Q_p^{id} = \omega_p \alpha_p D_p. \tag{4.1}$$

All symbols are listed in Table 4.3. The flow generated by the pump is absorbed by two variable displacement axial piston motors, that in stationary conditions rotate with angular velocities ω_{m1} and ω_{m2} respectively according to

$$Q_{m_i}^{id} = \omega_{m_i} \alpha_{m_i} D_{m_i}, \quad i = 1, 2 \tag{4.2}$$

where the superscript ^{id} means that we refer to an ideal quantity. The second motor is smaller than the first motor, in particular $D_{m1} > D_{m2}$. Small construction defects and wear of the seals cause oil leakage in the hydraulic machine, that, together with finite oil compressibility, reduces the oil flow at the output port. These effects are taken into account

by volumetric efficiency of the hydraulic machine η^v , whose physical interpretation has been given in [4] and [11] according to

$$\eta^v = 1 - \overbrace{\frac{C_s}{|\alpha|S}}^{\text{laminar leak}} - \overbrace{\frac{\Delta p}{\beta}}^{\text{compressibility leak}} - \overbrace{\frac{C_{st}}{|\alpha|\sigma}}^{\text{turbulent leak}} < 1 \quad (4.3)$$

where $S = \frac{\mu\omega}{\Delta p}$ and $\sigma = \frac{\omega D^{1/3}}{\left(2\frac{\Delta p}{\rho}\right)^{1/2}}$. It is important to notice that the volumetric efficiency depends on the rotational speed ω , the displacement fraction α and the pressure difference Δp between the input and output of the hydraulic machine. Volumetric efficiency is always smaller than one, thus the actual flow generated by the machine working as a pump is smaller than the ideal one and the actual flow processed by the machine working as a motor to keep a certain velocity is greater than the ideal one, namely

$$Q_p = Q_p^{\text{id}} \eta_p^v, \quad Q_{m_i} = \frac{Q_{m_i}^{\text{id}}}{\eta_{m_i}^v} \quad i = 1, 2. \quad (4.4)$$

The torque generated by the hydraulic motors is proportional to the pressure difference between line A (p_a) and line B (p_b) according to

$$T_{m_i}^{\text{id}} = \alpha_{m_i} D_{m_i} (p_a - p_b). \quad i = 1, 2 \quad (4.5)$$

Similarly, the torque required by the machine working as a pump to increase the pressure in the hoses is

$$T_p^{\text{id}} = \alpha_p D_p (p_a - p_b). \quad (4.6)$$

Also in this case non-idealities of the hydraulic machines, such as mechanical and viscous friction and hydrodynamical losses causes a mismatch between the actual and the ideal generated torque. The so called mechanical (or torque) efficiency η^t is well described by the physical model presented in [4] and [11]:

$$\eta^t = 1 - \overbrace{\frac{C_v S}{|\alpha|}}^{\text{viscous loss}} - \overbrace{\frac{C_f}{|\alpha|}}^{\text{mech. friction}} - \overbrace{C_h \alpha^2 \sigma^2}^{\text{hydrod. loss}} < 1, \quad (4.7)$$

with S and σ as in (4.3). The actual torque required by the machine working as a pump is greater than the ideal one, while the actual torque generated by the machine working as a motor is smaller than the ideal one, namely

$$T_p = \frac{T_p^{\text{id}}}{\eta_p^t}, \quad T_{m_i} = T_{m_i}^{\text{id}} \eta_{m_i}^t, \quad i = 1, 2. \quad (4.8)$$

The principle of conservation of mass in a hydraulic system with single inlet and single outlet gives us an insight of the pressure dynamics in the hydraulic system [12]. The evolution of the pressure in the lines on time is described by the *continuity equation* for a compressible fluid, that relates the difference of the flow at the input and at the output of a control volume to the pressure variation rate. Given an entering flow rate Q_{in} and an outgoing flow rate Q_{out} the pressure dynamic in the constant control volume is written as

$$\frac{dp}{dt} = \frac{\beta}{V}(Q_{\text{in}} - Q_{\text{out}}) = \frac{\beta}{V}\Delta Q, \quad (4.9)$$

where β is the bulk modulus of the fluid and V is the value of the control volume.

In order to prevent cavitation, a constant displacement pump (charge pump) is present in the hydraulic circuit, as represented in Fig. 4.2. This allows to maintain pressure inside the lines above the minimum threshold p_{min} . Charge pump is modeled by a proportional controller that regulates the pressure in the circuit by introducing the flow Q^{ch} , while the check valves CV_a and CV_b allow oil flow only when the pressure in the line goes below the minimum threshold. Flow generated by the charge pump and entering the lines can be described by the unidirectional proportional controller of the form

$$Q_i^{\text{ch}} = \max\{K_{\text{ch}}(p_{\text{min}} - p_i), 0\}, \quad i = a, b. \quad (4.10)$$

where K_{ch} is the gain of the proportional controller. Similarly, two relief valves RV_a and RV_b on both hoses ensure that pressure does not exceed maximum allowable value p_{max} ; the flow Q_{ref} from the relief valves is modeled as

$$Q_i^{\text{rel}} = \max\{K_{\text{rel}}(p_i - p_{\text{max}}), 0\}, \quad i = a, b. \quad (4.11)$$

Finally, we add the auxiliary term Q_i^{loss} to the total amount of fluid in the lines that takes into consideration unmodeled nonlinearities and uncertainties in volumetric efficiency:

$$Q_i^{\text{loss}} = c^{\text{loss}} \sqrt{p_i}, \quad i = a, b, \quad (4.12)$$

where c^{loss} is a constant parameter identified with experimental data.

Thanks to the characterization of all the flow rates in the lines, we can write pressure dynamics for the two lines as

$$\frac{dp_a}{dt} = \frac{\beta}{V}(Q_p - Q_{m_1} - Q_{m_2} - Q_a^{\text{loss}} + Q_a^{\text{ch}} - Q_a^{\text{rel}}) \quad (4.13a)$$

$$\frac{dp_b}{dt} = \frac{\beta}{V}(Q_{m_1} + Q_{m_2} - Q_p - Q_b^{\text{loss}} + Q_b^{\text{ch}} - Q_b^{\text{rel}}). \quad (4.13b)$$

4.1.2 Hydraulic accumulator sub-systems

The energy recovery task is handed over to the bladder type hydraulic accumulator, assembled with a membrane that separates the oil from an inert gas (in our case nitrogen). First studies on hydraulic type accumulators for regenerative systems are addressed in [9],[11] and [10]. When the oil is pumped into the accumulator, the pressure of the sealed gas rises, with a consequent increase in its internal energy; during a boost acceleration event, the compressed gas in the bladder expands and pushes the oil out of the accumulator, returning the stored energy to the system. In order to prevent cavitation, a low pressure accumulator (or reservoir) is required, since large amount of oil has to be available during charge and discharge events.

Otis and Pourmovahed assert in [8] that state dynamics of the accumulator gas can be modeled considering energy equations and thermodynamics relations for the gas during a transformation; they employ Benedict-Webb-Rubin equation of state for non-ideal gas to represent the dependency of pressure from temperature and specific volume. Since the final purpose of the presented model is the definition of the constraints of the optimal control problem, we must keep its formulation as simple as possible and thus accept some degree of approximation. To this end we regard the sealed nitrogen inside the accumulators as an ideal gas, whose internal state is described by the equation of state for ideal gas, i.e.

$$p_i V_i = n_i R T_i, \quad i = hp, lp, \quad (4.14)$$

where $R = 8.314 \frac{\text{J}}{\text{mol K}}$ is the universal gas constant, n_i is the number of moles of nitrogen inside the bladder, T_i and V_i are the gas temperature and volume respectively. Obviously, the error introduced by this approximation must be assessed with experimental validation.

The variation of gas volume V_i is equal and opposite to the oil flow rate pumped into the accumulator, namely:

$$\frac{dV_i}{dt} = -Q_i \quad i = hp, lp. \quad (4.15)$$

Accumulator temperature dynamics is attained from internal energy balance and from the thermodynamic relation describing the energy variation for a real gas:

$$m_i \frac{du_i}{dt} = \underbrace{m_i c_v \frac{T_s - T_i}{\tau}}_{\text{heat transport}} - \underbrace{p_i \frac{dV_i}{dt}}_{\text{work}} \quad (4.16)$$

$$du_i = c_v dT_i + \left[T_i \left(\frac{\partial p_i}{\partial T_i} \right)_{V_i} - p_i \right] \frac{dV_i}{m_i}, \quad i = \text{hp, lp}. \quad (4.17)$$

Combining (4.14)-(4.17) we can write the temperature dynamics of the gas inside the accumulators as

$$\frac{dT_i}{dt} = \frac{(T_s - T_i)}{\tau} + \frac{p_i}{c_v m_i} Q_i, \quad i = \text{hp, lp}. \quad (4.18)$$

Pressure dynamics can be obtained differentiating (4.14) w.r.t. time, namely

$$\frac{dp_i}{dt} = \frac{p_i}{T_i} \frac{dT_i}{dt} + \frac{p_i^2}{(n_i R T_i)} Q_i, \quad i = \text{hp, lp}. \quad (4.19)$$

4.1.3 Power Boost hub sub-system

Hydraulic accumulators are connected to the transmission lines by means of a set of valves contained in the PowerBoost Hub subsystem, whose scheme is depicted in Fig. 4.3. PowerBoost Hub is a crucial element of the hybrid transmission, and allows to handle energy recovery phase without inverting the motor displacements as in [3], [16] and [5]. As an example, suppose that motors have positive angular velocity (the vehicle is moving forward), thus the oil flows from line A to line B; when the driver brakes, power hub connects high pressure accumulator to line B and reservoir to line A, addressing the oil flow from the reservoir to the high pressure accumulator. According to (4.19) the internal pressure of the accumulator gas increases, and so does its internal energy. In this configuration, the negative pressure difference $\Delta p = p_a - p_b$ imposed to the circuit generates a negative (braking) torque to the motors as in (4.5).

The following assumptions limit the combination of valves configurations and highlight the switching behavior of the system dynamics:

- (i) volume of the oil in the accumulators is much larger than the volume in the hoses;
- (ii) opening dynamics of the valves in the PowerBoost hub are neglected;

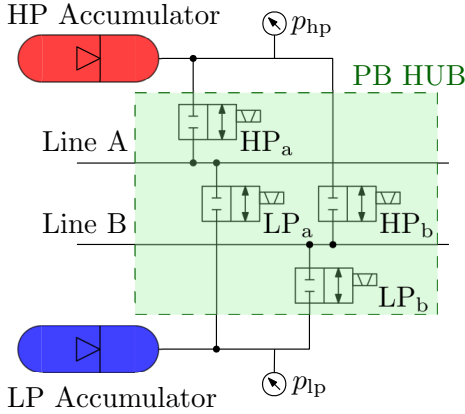


Figure 4.3: Conceptual scheme of the PowerBoost Hub that connects the accumulators to the lines.

- (iii) dynamics of gas pressure in the accumulators are much slower than dynamics introduced by continuity equation;
- (iv) the accumulators are always connected at the same time and to different lines.

Assumption (i) and (iii) imply that, when the accumulator is connected to the line, pressure in the hose reaches almost instantly the one in the accumulator and remains stucked to it evolving with the same dynamics. Assumption (iv) allows PowerBoost Hub to switch among the three different configuration in Table 4.1, where the discrete control $\zeta = \{-1, 0, 1\}$ determines the valves arrangement.

Pressure switching dynamics inside the circuit can be now defined for every working condition, namely

$$\dot{p}_a = \begin{cases} \dot{p}_{hp} + \frac{1}{v}(p_{hp} - p_a) & \zeta = +1 \\ \dot{p}_{lp} + \frac{1}{v}(p_{lp} - p_a) & \zeta = -1 \\ \dot{p}_a^{\text{hyd}} & \zeta = 0, \end{cases} \quad (4.20a)$$

$$\dot{p}_b = \begin{cases} \dot{p}_{lp} + \frac{1}{v}(p_{lp} - p_b) & \zeta = +1 \\ \dot{p}_{hp} + \frac{1}{v}(p_{hp} - p_b) & \zeta = -1 \\ \dot{p}_b^{\text{hyd}} & \zeta = 0. \end{cases} \quad (4.20b)$$

Value of ζ	Operational Mode	Valves			
		HP _a	HP _b	LP _a	LP _b
$\zeta = 1$	Boost fwd & Regen bkw	1	0	0	1
$\zeta = -1$	Boost bkw & Regen fwd	0	1	1	0
$\zeta = 0$	Hydrostatics	0	0	0	0

Table 4.1: Valves configuration in the PowerBoost Hub. When $HP_i, LP_i = 0$ the corresponding valve is closed, when $HP_i, LP_i = 1$ the corresponding valve is open, with $i = \{a, b\}$.

Superscript ^{hyd} indicates that the corresponding pressure dynamics evolves according to the continuity equation in (4.13a) and (4.13b) as in hydrostatic mode, while pressure dynamics in the accumulators p_{hp} and p_{lp} are detailed in (4.19). In hybrid mode (i.e. when $\zeta \neq 0$), for a small enough time constant v , pressure in the hose reaches rapidly the value of pressure in the connected accumulator.

4.1.4 Mechanical powertrain and longitudinal dynamics

To conclude the analytic analysis of the transmission we detail in this section the mechanical part of the powertrain and introduce a simple model for the longitudinal dynamics. The scheme of the complete vehicle driveline is depicted in Fig. 4.4. Torque generated by hydraulic motors is blended by Dana 318 CVT, that connects the primary and secondary motors to the main shaft with transmission ratio τ_{m_1} and τ_{m_2} respectively. The primary motor can be disconnected at high speed by means of a multidisk wet clutch and re-engaged for high torque demands. Torque at transmission output is

$$T_{\text{trans}} = \begin{cases} T_{m_1} \tau_{m_1} + T_{m_2} \tau_{m_2} & \varphi = 1 \\ T_{m_2} \tau_{m_2} & \varphi = 0 \end{cases} \quad (4.21)$$

where the discrete control $\varphi \in \{0, 1\}$ determines whether the clutch is engaged ($\varphi = 1$) or disengaged ($\varphi = 0$). Torque is then transmitted to the wheels through the transmission ratio of the differential (τ_{diff}) and the wheel hub (τ_{hub}), whose values are listed in Table 4.2. Torque transmitted

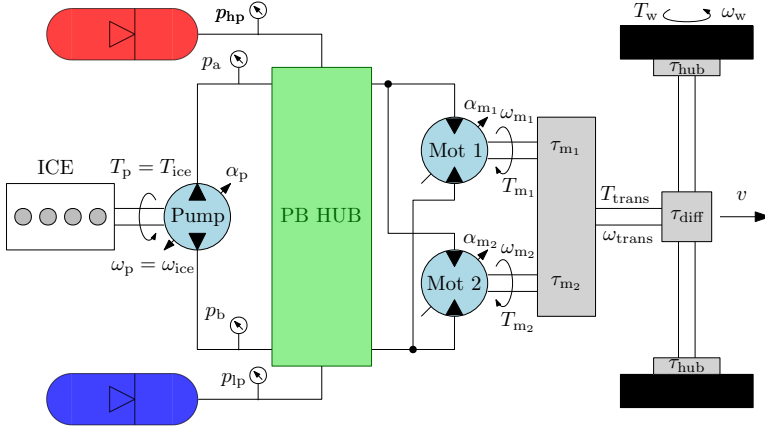


Figure 4.4: Architecture of the driveline.

Member	Symbol	Value
Motor 1	τ_{m_1}	3.560
Motor 2	τ_{m_2}	1.330
Differential	τ_{diff}	2.818
Wheel hub	τ_{hub}	6.000

Table 4.2: Transmission ratios.

to the wheels accelerates the telehandler and overcomes the road friction force and aerodynamic drag

$$\begin{aligned}
 T_w &= T_{trans} \tau_{diff} \tau_{hub} \\
 &= r_w \left(m_v \frac{dv}{dt} + \kappa_1 m_v g \sin(\gamma) |v| + \kappa_2 m_v g v \cos(\gamma) \right)
 \end{aligned}
 \tag{4.22}$$

where v is the vehicle speed and γ is the road slope. Table 4.3 summarizes the longitudinal dynamics parameters identified with experimental data. The axial piston pump is powered by a 83 kW diesel engine. Engine fuel consumption (measured in [l/h]) is approximated by a polynomial function of engine torque T_{ice} and angular velocity ω_{ice} , that is

$$\delta m_f = \left(c_{f_1} + c_{f_2} \omega_{ice}^4 + c_{f_3} T_{ice}^4 + c_{f_4} \omega_{ice} T_{ice} \right) H(T_{ice})
 \tag{4.23}$$

where ω_{ice} is measured in rpm and T_{ice} in Nm, and $H : \mathbb{R} \rightarrow \mathbb{R}$ is the Heaviside step function and c_{f_i} are fitting coefficients. Maximum and

Symbol	Value	Unit
r_w	0.5450	m
κ_1	0.0620	—
κ_2	0.0029	$\frac{s}{m}$

Table 4.3: Parameters longitudinal dynamics.

minimum torques $T_{\max}(\omega_{\text{ice}})$ and $T_{\min}(\omega_{\text{ice}})$ depend on engine speed and are fitted by cubic splines. The torque delivered by the engine has to fulfill the torque request of the pump and accelerate the engine flywheel. Moreover, we need to take account of additional torque demand that comes from the auxiliary elements in the circuit (charge pump, telescopic boom and steering system). We compute torque request at engine as

$$T_{\text{ice}} = T_p + J_{\text{ice}}\dot{\omega}_{\text{ice}} + T_{\text{aux}}, \quad (4.24)$$

where T_{aux} is a constant torque demand from the auxiliary members, J_{ice} is the average generalized inertia of the engine and T_p is computed from pump displacement and line pressure difference according to (4.6) and considering mechanical efficiency (4.7).

The overall states, controls and the ODE describing the dynamics of the system are summarized in Table 5.A.1 in Appendix ii.

4.2 MODEL VALIDATION

4.2.1 Experimental setup

Dana's prototype telehandler in Fig 4.5 was instrumental in the development of the powertrain model. This prototype has the ability to perform multiple types of operation involving traction and work functions such as lifting, handling, digging, silage, loading, and transport. These scenarios are formalized into a set of driving cycles performed at Dana's own test facility [13]. Figure 4.6 represents the layout of the test track at Dana's facility in Arco, Italy. It consists of a flat area paved with asphalt and concrete, surrounded by guard-rails.

4.2.2 Performance assessment

The powertrain is provided with several sensors (we are mostly interested in pressure and speed sensors) to allow a good characterization of the vehicle behavior. As an example Fig 4.7 illustrates the comparison between



Figure 4.5: Tele-boom handler used for experimental campaign.

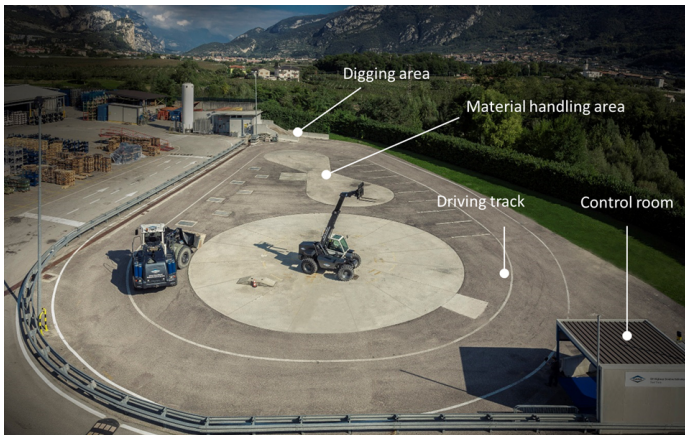


Figure 4.6: Test track at Dana's facility in Arco, TN - Italy.

measured and experimental pressure. A good correspondence is observed both in hydrostatic mode and in hybrid mode, where pressure in the lines matches pressure in the accumulators (i.e. when $\xi = \pm 1$). When the vehicle is in hydrostatic mode (i.e. $\xi = 0$), the estimated pressure has some spikes that are not present in the measured data. This is due to the

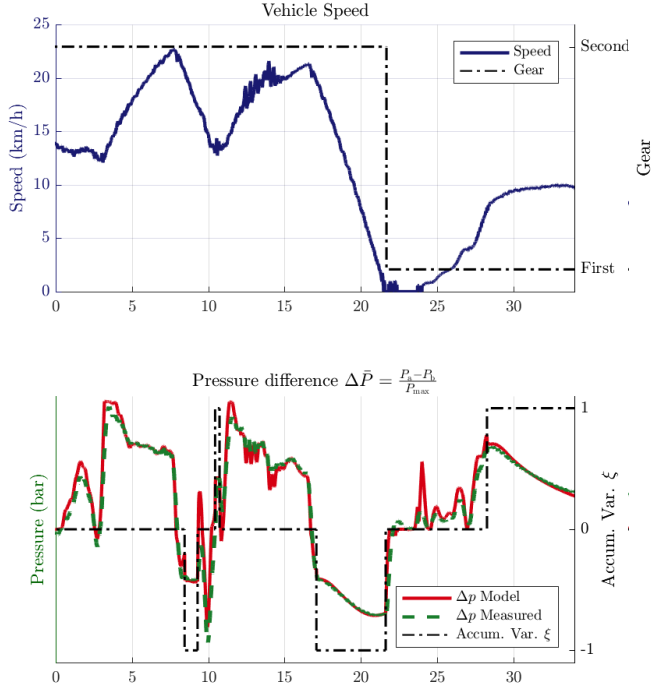


Figure 4.7: Comparison between measured and estimated pressure.

fact that pressure dynamics in hydrostatic mode is very sensitive to small variations of pump and motors flow (and consequently displacement), since the multiplying term $\frac{\beta}{V}$ in (4.9) is large. Nevertheless, the model is able to properly represent the main dynamics of the system, with a fitting equal to $\text{fit} = 1 - \text{NMSE} = 93\%$, where NMSE is the normalized mean square error.

BIBLIOGRAPHY OF CHAPTER 4

- [1] Anthony Barré, Benjamin Deguilhem, Sébastien Grolleau, Mathias Gérard, Frédéric Suard, and Delphine Riu. “A review on lithium-ion battery ageing mechanisms and estimations for automotive applications.” In: *Journal of Power Sources* 241 (2013), pp. 680–689. ISSN: 03787753. DOI: [10.1016/j.jpowsour.2013.05.040](https://doi.org/10.1016/j.jpowsour.2013.05.040)Review. URL: <http://dx.doi.org/10.1016/j.jpowsour.2013.05.040>.
- [2] C.C. Chan. “The state of the art of electric and hybrid vehicles.” In: *Proceedings of the IEEE* 90.2 (2002), pp. 247–275. ISSN: 00189219. DOI: [10.1109/5.989873](https://doi.org/10.1109/5.989873). URL: <http://ieeexplore.ieee.org/lpdocs/epic03/wrapper.htm?arnumber=989873>.
- [3] Zoran Filipi and Young Jae Kim. “Hydraulic Hybrid Propulsion for Heavy Vehicles: Combining the Simulation and Engine-In-the-Loop Techniques to Maximize the Fuel Economy and Emission Benefits.” In: *Oil & Gas Science and Technology – Revue de l’Institut Français du Pétrole* 65.1 (2010), pp. 155–178. ISSN: 1294-4475. DOI: [10.2516/ogst/2009024](https://doi.org/10.2516/ogst/2009024).
- [4] Zoran Filipi et al. “Combined optimisation of design and power management of the hydraulic hybrid propulsion system for the 6x6 medium truck.” In: *International Journal of Heavy Vehicle Systems* 11.3/4 (2004), p. 372. ISSN: 1744-232X. DOI: [10.1504/IJHVS.2004.005458](https://doi.org/10.1504/IJHVS.2004.005458).
- [5] Young Jae Kim and Zoran Filipi. “Simulation Study of a Series Hydraulic Hybrid Propulsion System for a Light Truck.” In: *SAE Paper 2007-01-4151* 724 (2007), pp. 776–790. ISSN: 0148-7191. DOI: [10.4271/2007-01-4151](https://doi.org/10.4271/2007-01-4151).
- [6] Sisay Molla and Beshah Ayalew. “Power management strategies for a series hydraulic hybrid drivetrain.” In: *International Journal of Powertrains* 1.1 (2011), p. 93. ISSN: 1742-4267. DOI: [10.1504/IJPT.2011.041911](https://doi.org/10.1504/IJPT.2011.041911).
- [7] Simona Onori, Lorenzo Serrao, and Giorgio Rizzoni. *Hybrid Electric Vehicles, Energy Management Strategies*. 2016. ISBN: 978-1-4471-6779-2. DOI: [10.1007/978-1-4471-6781-5](https://doi.org/10.1007/978-1-4471-6781-5). URL: <http://link.springer.com/10.1007/978-1-4471-6781-5>.

- [8] D. R. Otis and a. Pourmovahed. "An Algorithm for Computing Nonflow Gas Processes in Gas Springs and Hydropneumatic Accumulators." In: *Journal of Dynamic Systems, Measurement, and Control* 107.1 (1985), p. 93. ISSN: 00220434. DOI: [10.1115/1.3140714](https://doi.org/10.1115/1.3140714).
- [9] A. Pourmovahed. "Energy storage capacity of gas-charged hydraulic accumulators." In: *23rd Thermophysics, Plasmadynamics and Lasers Conference* (1988). DOI: [10.2514/6.1988-2656](https://doi.org/10.2514/6.1988-2656). URL: <http://arc.aiaa.org/doi/10.2514/6.1988-2656>.
- [10] A. Pourmovahed, N. H. Beachley, and F. J. Fronczak. "Modeling of a Hydraulic Energy Regeneration System—Part II: Experimental Program." In: *Journal of Dynamic Systems, Measurement, and Control* 114.1 (1992), p. 160. ISSN: 00220434. DOI: [10.1115/1.2896498](https://doi.org/10.1115/1.2896498).
- [11] A. Pourmovahed, N. H. Beachley, and F. J. Fronczak. "Modeling of a Hydraulic Energy Regeneration System: Part I—Analytical Treatment." In: *Journal of Dynamic Systems, Measurement, and Control* 114.1 (1992), p. 160. ISSN: 00220434. DOI: [10.1115/1.2896498](https://doi.org/10.1115/1.2896498).
- [12] M Galal Rabie and Ph. D. *Fluid power engineering*. Vol. 28. McGraw-Hill New York, NY, USA, 2009.
- [13] Lorenzo Serrao, Giulio Ornella, Luca Balboni, Maximiliano Giorgio Bort, Carl Dousy, and Fabrizio Zendri. "A telehandler vehicle as mobile laboratory for hydraulic-hybrid powertrain technology development." In: *10th International Fluid Power Conference* (2016).
- [14] Michael Sprengel and Monika Ivantysynova. "Investigation and Energetic Analysis of a Novel Hydraulic Hybrid Architecture for On-Road Vehicles." In: *The 13th Scandinavian International Conference on Fluid Power, SICFP2013, June 3-5, 2013, Linköping, Sweden* (2013), pp. 87–98. URL: http://mechatronic.iei.liu.se/sicfp2013/SICFP2013{_}investigation{_}and{_}energetic{_}analysis{_}of{_}a{_}novel{_}hydraulic{_}hybrid{_}architecture{_}for{_}on{_}road{_}vehicles.pdf.
- [15] Michael Sprengel, Tyler Bleazard, Hiral Haria, and Monika Ivantysynova. "Implementation of a novel hydraulic hybrid powertrain in a sports utility vehicle." In: *IFAC-PapersOnLine* 28.15 (2015), pp. 187–194. ISSN: 24058963. DOI: [10.1016/j.ifacol.2015.10.027](https://doi.org/10.1016/j.ifacol.2015.10.027). URL: <http://dx.doi.org/10.1016/j.ifacol.2015.10.027>.
- [16] Tri Vien Vu, Chih Keng Chen, and Chih Wei Hung. "A model predictive control approach for fuel economy improvement of a series hydraulic hybrid vehicle." In: *Energies* 7.11 (2014), pp. 7017–7040. ISSN: 19961073. DOI: [10.3390/en7117017](https://doi.org/10.3390/en7117017).

The hydrostatic hybrid transmission presented in Chapter 4 is designed to reduce fuel consumptions by making the engine operate at its best working point and by recovering the kinetic energy of the vehicle that would be otherwise wasted during deceleration maneuvers. The torque required at the wheels may be achieved by infinitely many combinations of the control variables listed in Table 5.A.1 in Appendix ii, due to the redundancy of the actuations. We fully exploit the architecture of the powertrain only if we wisely select, among the infinitely many control combinations, the one that maximizes the fuel savings. Many techniques have been proposed in the literature for the control of the hydrostatic hybrid vehicles, Molla and Ayalew in [14] classify them into three groups: heuristic rule-based techniques, instantaneous optimization and finally optimization over a time horizon. The latter group is in general not suitable for on-line implementation, since high computational effort and time are required to find the optimal control action. On the other hand, the offline optimal control analysis serves to define the best case performances of the system, making it possible to compare different architectures or system configurations (e.g. accumulators pre-charge pressure, gear ratios, etc.) using a fair metrics. Moreover, off-line optimal solutions can be used to draw simpler —and faster— heuristic rules that can run real-time on a vehicle control unit (e.g. for the selection of threshold values in the thermostatic SOC control in [12]).

In this chapter we formulate the energy management problem as a finite-horizon optimal control problem based on the dynamical system presented in Chapter 4. The usage of a validated model ensures that the proposed control strategy is compliant with the actual system limitations and that the fuel savings result is credible.

In Chapter 4 we have seen that the pressure dynamics (4.20a), (4.20b) and the longitudinal dynamics (4.22) switch among different statuses, that are determined by the discrete controls φ and ζ ; contrarily, the pump and motor displacement and the engine speed rate may assume any real value within their domain. An optimal control problem that involves continuous-valued control variables and discrete control variables is called *mixed-integer optimal control problem* (MI-OCP).

Three different approaches can be employed to find the solution of an optimal control problem: *dynamic programming*, *direct approach*, and *indi-*

direct approach (compare [1],[3],[11]). Dynamic Programming is the most suited technique to deal with discrete control variables, since it is based on the discretization of both the state and control space, but its computational complexity grows with the number of states and controls, making it impossible to use in large scale optimal control problems. The indirect approach, based on the Pontryagin maximum principle, was the first method used to solve the MI-OCP in [4], but the complex switching of the adjoint variables makes it arduous to apply to solve more general problems. Direct approach is based on the discretization on a time grid that reduces the infinite dimensional optimal control problem to a finite dimensional non-linear programming (NLP) optimization that can be tackled with efficient gradient based solvers (SNOPT [10], Ipopt [21], worhp [5]). Direct solution approach proved to be effective in many practical application examples [18], [13]. A comprehensive investigation on direct and indirect solution methods is provided in [9] and [2].

Direct approach and branch&bound techniques have been employed in [7] to solve the time optimal problem for an automobile with gear shift in a double-lane change maneuver; branch&bound works well with few discretization points, thus it is not suitable for problems with fast dynamics. Gerdt proposes in [8] a novel approach based on a variable time transformation to solve problems with partially discrete control set. In this chapter we solve the mixed-integer optimal control problem for energy management using the outer-convexification and relaxation technique proposed in [16], [17], [19] and [20]: the control space is augmented to transform the discrete controls into binary variables, then the problem is *relaxed* allowing the binary variables to vary in a continuous interval; this approximation transforms the MI-OCP in a standard optimal control problem that can be solved using common solution techniques, such as the *direct approach* detailed in Chapter 1. To avoid chattering effect in the solution and to enforce the integer feasibility of the control variable we introduce the switching penalty presented in [15].

5.1 PROBLEM FORMULATION

5.1.1 *Mixed-Integer Optimal Control*

The objective is to minimize fuel consumption over a driving cycle, by imposing the vehicle speed from measured data. Vehicle speed is allowed to assume values within a “tube” of thickness ε_v around the reference value v_{dc} imposed by the driving cycle; this flexibility eases the numerical solution of the optimal control, while bounding the velocity tracking error and it also accommodates for inaccuracies in the longitudinal model

dynamics. If we want to pursue a fair comparison among different control strategies we should select small values of ε_v , so that controlled vehicle speed becomes closer to the speed imposed by the driving cycle.

The aim of optimal control for energy management is the minimization of fuel consumption over a predefined driving cycle and a fixed time horizon $[0 t_f]$. We want to minimize the Lagrange Term

$$J = \int_0^{t_f} \delta m_f(\mathbf{x}(t)) dt, \quad (5.1)$$

where the fuel consumption rate (4.23) depends only on the differential states of the system.

Finally, we require that engine torque (4.24) remains within the maximum and minimum speed admissible values by imposing the following path constraints:

$$\begin{aligned} c_1(\mathbf{x}(t)) &= T_{\text{ice}}(\mathbf{x}(t)) - T_{\text{max}}(\mathbf{x}(t)) \leq 0 \\ c_2(\mathbf{x}(t)) &= T_{\text{min}}(\mathbf{x}(t)) - T_{\text{ice}}(\mathbf{x}(t)) \leq 0. \end{aligned} \quad (5.2)$$

Introducing the fully connected sets $\mathcal{X} \subset \mathbb{R}^{n_x}$ and $\mathcal{U} \subset \mathbb{R}^{n_u}$ defined by the lower and upper bounds on continuous states and controls and the finite set $\Omega := \{\boldsymbol{\nu}^1, \boldsymbol{\nu}^2, \dots, \boldsymbol{\nu}^{n_w}\} \subset \mathbb{R}^{n_v}$, containing all the values that the integer control can assume, yields the compact formulation of the MI-OCP:

$$\min_{\mathbf{u}, \boldsymbol{\nu}} J \quad (5.3a)$$

$$\text{s.t. } \dot{\mathbf{x}}(t) - \mathcal{F}(\mathbf{x}(t), \mathbf{u}(t), \boldsymbol{\nu}(t)) = \mathbf{0}_{\mathbb{R}^{n_x}} \quad (5.3b)$$

$$\psi(\mathbf{x}(0), \mathbf{x}(t_f)) = \mathbf{0}_{\mathbb{R}^{n_\psi}} \quad (5.3c)$$

$$\mathbf{c}(\mathbf{x}(t)) \leq \mathbf{0}_{\mathbb{R}^{n_c}} \quad (5.3d)$$

$$\mathbf{x}(t) \in \mathcal{X}, \quad \mathbf{u}(t) \in \mathcal{U}, \quad \boldsymbol{\nu}(t) \in \Omega, \quad (5.3e)$$

where $\mathcal{F} : \mathbb{R}^{n_x} \times \mathbb{R}^{n_u} \times \mathbb{R}^{n_v} \rightarrow \mathbb{R}^{n_x}$ represents the dynamics equations listed in Table 5.A.1, $\psi : \mathbb{R}^{n_x} \times \mathbb{R}^{n_x} \rightarrow \mathbb{R}^{n_\psi}$ maps the boundary conditions and $\mathbf{c} : \mathbb{R}^{n_x} \rightarrow \mathbb{R}^{n_c}$ represents the path constraints. In our case $n_c = 2$, namely $\mathbf{c}(\mathbf{x}(t)) := \text{col}(c_1(\mathbf{x}(t)), c_2(\mathbf{x}(t)))$, with $c_1(\cdot)$ and $c_2(\cdot)$ defined in (5.2).

5.1.2 Regularized functions

Since gradient based solution methods require derivative both of the constraints and the objective functions, we replace the *Heaviside* function

in (4.23) and the \max function in (4.10) with their smooth approximations, namely

$$H(x) \approx \lim_{\kappa \rightarrow 0} \frac{1}{2} + \frac{1}{2} \tanh\left(\frac{x}{\kappa}\right)$$

$$\max(x, y) \approx \lim_{\kappa \rightarrow 0} \frac{1}{2} (x + y + \sqrt{(x - y)^2 + \kappa}),$$

with $\kappa > 0$.

5.1.3 Outer convexification and relaxation

The first step towards the solution of MI-OCPs proposed in [16] is the outer convex relaxation of the integer variable $\nu(\cdot) \in \Omega$, by introducing a binary control $w_i(t) \in \{0, 1\}$ for every element ν^i of the finite set Ω . Then system dynamics (5.3b) can be rewritten as

$$\dot{\mathbf{x}}(t) - \sum_{i=1}^{n_w} \mathcal{F}(\mathbf{x}(t), \mathbf{u}(t), \nu^i) w_i(t) = \mathbf{0}_{\mathbb{R}^{n_x}} \quad (5.4)$$

and the bijection between every feasible integer control $\nu(\cdot) \in \Omega$ and the binary function $\mathbf{w}(\cdot) = \text{col}[w_1(\cdot), \dots, w_{n_w}(\cdot)] \in \{0, 1\}^{n_w}$ is guaranteed by imposing the special ordered set type one condition:

$$\sum_{i=1}^{n_w} w_i(t) = 1. \quad (5.5)$$

Subset $\Omega = \{-1, 0, 1\} \times \{0, 1\}$ has cardinality $n_w = 6$, therefore we replace integer controls $\nu(\cdot) \in \Omega \subset \mathbb{R}^2$ with binary variables $\mathbf{w}(\cdot) \in \{0, 1\}^6$. In other words, we increase the control space from n_v integer controls to $n_w > n_v$ binary controls by means of a suitable coordinate change. Binary control $w_i(\cdot) \in \{0, 1\}^{n_w}$ selects the system dynamics obtained with the combination of discrete controls ν^i . Finally, the relaxation of MI-OCP is attained by replacing the binary control $\mathbf{w}(\cdot) \in \{0, 1\}^{n_w}$ with the contin-

uous variable $\tilde{\mathbf{w}}(\cdot) = \text{col}[\tilde{w}_1(\cdot), \dots, \tilde{w}_{n_w}(\cdot)] \in [0, 1]^{n_w}$. The outer convex relaxed form of (5.3) writes as

$$\min_{\mathbf{u}, \tilde{\mathbf{w}}} J \quad (5.6a)$$

$$\text{s.t. } \dot{\mathbf{x}}(t) - \sum_{i=1}^{n_w} \mathcal{F}(\mathbf{x}(t), \mathbf{u}(t), \nu^i) \tilde{w}_i(t) = \mathbf{0}_{\mathbb{R}^{n_x}} \quad (5.6b)$$

$$\psi(\mathbf{x}(0), \mathbf{x}(t_f)) = \mathbf{0}_{\mathbb{R}^{n_\psi}} \quad (5.6c)$$

$$\mathbf{c}(\mathbf{x}(t)) \leq \mathbf{0}_{\mathbb{R}^{n_c}} \quad (5.6d)$$

$$\sum_{i=1}^{n_w} \tilde{w}_i(t) = 1 \quad (5.6e)$$

$$\mathbf{x}(t) \in \mathcal{X}, \quad \mathbf{u}(t) \in \mathcal{U}, \quad \tilde{\mathbf{w}}(t) \in [0, 1]^{n_w}. \quad (5.6f)$$

5.2 SOLUTION TO OPTIMAL CONTROL PROBLEM

5.2.1 Direct full discretization method

Direct discretization approach is defined by the operations surveyed in [9]. First, we define the equidistant time grid

$$\mathbb{G}_N := \{t_0, t_1, \dots, t_N\}, \quad t_0 = 0 < t_1 < \dots < t_N = t_f, \quad (5.7)$$

with N grid intervals and constant step size $h = \frac{t_f - t_0}{N}$. In our problem we select a discretization grid with $h = 0.01$ s. We discretize controls by means of B-spline basis function of order 1 (piecewise constant functions) on the discrete time interval, then we proceed with state discretization applying a suitable discretization rule to ODE (5.6b). Finally, control and state constraints in (5.6) are evaluated only on the grid \mathbb{G}_N in (5.7). The discretized Lagrange cost function becomes

$$J = \sum_{i=0}^N \delta m_i(t_i) h. \quad (5.8)$$

We employ *Ipopt* [21] for the solution of the resulting highly-structured large-scale nonlinear optimization problem and provide the symbolic gradient of objective function and Jacobian of the constraints with ADiGator [22, 23].

5.2.2 Sum-Up rounding

The main idea to find the solution of MI-OCP (5.3) is to first solve its relaxation (5.6) and then adopt a suitable rounding strategy to reconstruct

the binary variable $\mathbf{w}(\cdot) \in \{0, 1\}^{n_w}$ from the continuous optimal control $\tilde{\mathbf{w}}(\cdot) \in [0, 1]^{n_w}$. In this work we adopt the *sum-up rounding* strategy presented by Sager in [16] and [17]: consider the piecewise constant control function

$$\tilde{w}_j(t) = \tilde{w}_{j,i} \in [0, 1], \quad t \in [t_i, t_{i+1}), \quad (5.9)$$

with $j = 1, \dots, n_w$ and $i = 0, \dots, N - 1$, the sum-up rounding for the special ordered set type one condition (5.5) is defined as

$$\begin{aligned} \hat{w}_{j,i} &= \sum_{k=0}^i \tilde{w}_{j,k} h - \sum_{k=0}^{i-1} w_{j,k} h \\ w_{j,i} &= \begin{cases} 1 & \{\hat{w}_{j,i} \geq \hat{w}_{q,i} \forall q \neq j\} \wedge \{j < q \forall q : \hat{w}_{j,i} = \hat{w}_{q,i}\} \\ 0 & \text{otherwise.} \end{cases} \end{aligned} \quad (5.10)$$

The rounding strategy considers rounding error on previous steps to minimize the cumulated error and guarantees that the solution error is a multiple of the size of the grid step h as proved in [20].

5.2.3 Multi-time switching penalty

Optimal control function $\tilde{\mathbf{w}}(\cdot)$ can, in principle, be sensibly different from the binary control $\mathbf{w}(\cdot)$, therefore rounding strategy (5.10) leads to unfeasible chattering in the solution. Rieck et al. in [15] propose to augment cost function with a switching cost J_{SC} that penalizes the number of switches and enforces binary feasibility of the control function. Considering the piecewise constant control (5.9) on the grid G_N , the switching cost is defined as

$$\begin{aligned} J_{SC} &= \sum_{j=1}^{n_w} \sum_{i=1}^{N-1} [\tilde{w}_{j,i-1} + \tilde{w}_{j,i}(1 - 2\tilde{w}_{j,i-1}) + \\ &\quad \tilde{w}_{j,i+1} + \tilde{w}_{j,i}(1 - 2\tilde{w}_{j,i+1})], \end{aligned} \quad (5.11)$$

thus the overall cost function becomes

$$\bar{J} = J + \alpha J_{SC} \quad (5.12)$$

where α is a scaling factor such that the order of magnitude of the auxiliary term is comparable with the objective J that is defined in (5.8).

5.3 OPTIMIZATION RESULTS

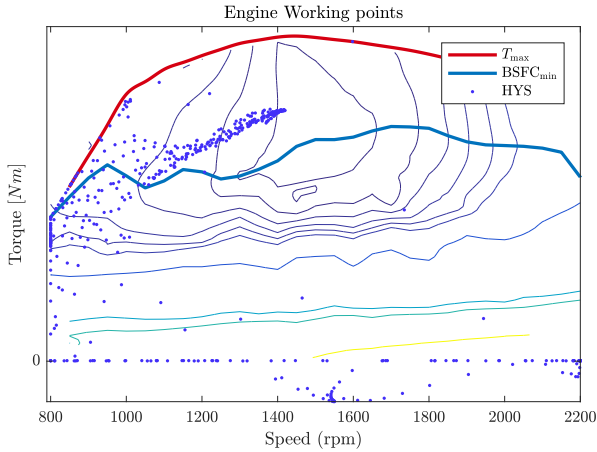
The mixed-integer optimal control problem introduced in Sec. 5.1 has been solved for two different operating modes: in the first configuration

(hydrostatic mode) the valves in the PB Hub are enforced to remain closed, preventing the accumulators from connecting to the lines; in the second configuration (hybrid mode), the accumulators can be connected to the hoses. In order to guarantee a fair comparison between the two strategies, we impose that, in hybrid mode, the initial and final pressures of the high pressure accumulator coincide; therefore, we add to the boundary conditions (5.6d) the condition $p_{\text{hp}}(0) = p_{\text{hp}}(t_f)$. We report in this work the solution to the the optimal energy management problem for two real driving cycles, whose velocity profiles (measured on the prototype vehicle) are reported in Figure 5.2. We solved the NLP problem with Ipopt in Matlab R2016b on a 2.9 GHz Intel Core i5 processor and it took about 15 min to find the solution.

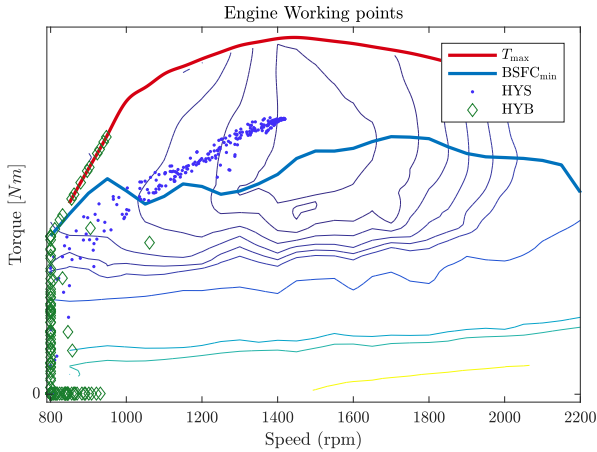
Figure 5.1 illustrates the engine utilization points on the BSFC map for the two architectures; BSFC_{\min} is the minimum brake specific fuel consumption curve, computed by selecting, for each speed, the torque corresponding to the highest efficiency value. It is somewhat surprising to notice that the optimal control strategy tends to move the engine utilization towards low torque and low speed regions instead of high efficiency regions, because they correspond to lower fuel consumption rates. This is in good accordance with the results presented in [6], where the best heuristic control strategy was not the one running at the “efficiency sweet spot”. This explains why, by comparing Figures 5.1a and 5.1b, we see that the main effect of using the hybrid architecture is a further shift of the engine working points towards the lower-left side of the engine map. In hybrid mode the braking action is demanded to the accumulators allowing for the regeneration of the otherwise wasted kinetic energy; the energy stored in the accumulators is then used to assist the engine by making it work in the region of the engine map corresponding to lower fuel consumptions.

The optimal gear selection and the contribution of the engine and accumulators power to the overall power at the wheels are reported in Figure 5.2; obviously, the output power is always lower than the engine power due to the system inefficiencies, except when the accumulators are connected in boost mode, adding extra-power to the output. It is interesting to notice that sometimes, during the regenerative braking, it is convenient to use the engine to further charge the accumulator (e.g. in Figure 5.2a at 30 s or in Figure 5.2b at 40 s). The first gear, with both hydraulic motors connected to the output shaft, is engaged when a large amount of torque is required at low speed.

In Figure 5.3 the optimal pump/motor displacements and flows are drawn for the two driving cycles. It is interesting to notice that the pump displacement saturates when the vehicle speed is large; this permits to



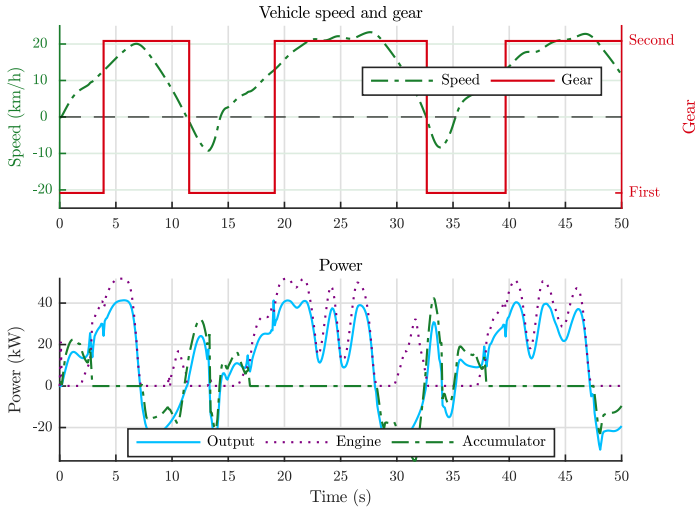
(a) Engine working points in Hydrostatic mode.



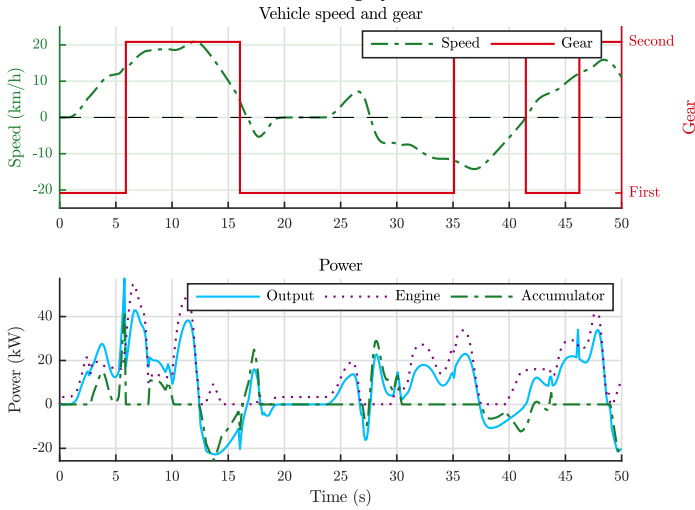
(b) Engine working points in Hybrid mode.

Figure 5.1: Engine working points in the two working modes.

get high flow values even with lower input speed, allowing the engine to work at lower speed. When in second gear, the primary hydraulic motor (M1) is detached from the output shaft and its displacement remains approximately constant, while the smaller secondary motor (M2) processes all the flow that comes from the pump and the accumulators.



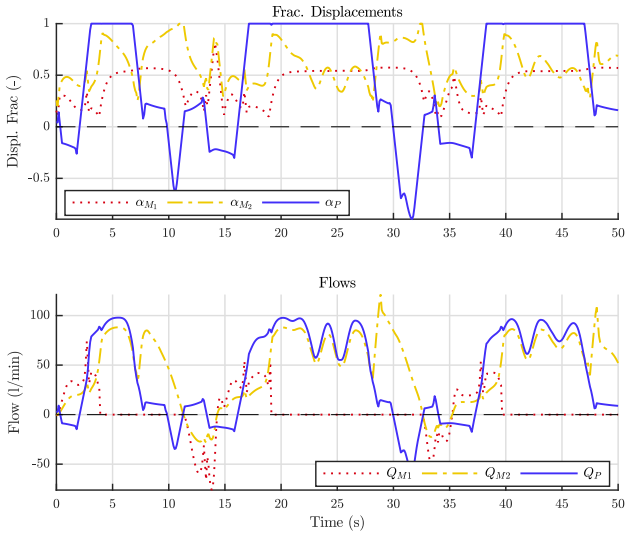
(a) Driving cycle 1.



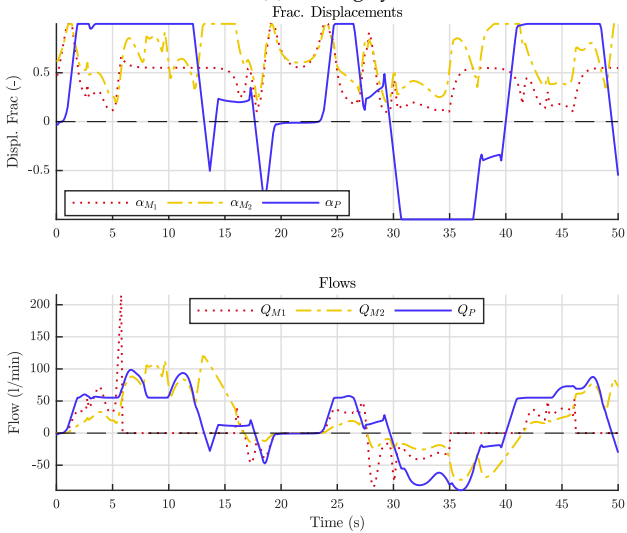
(b) Driving cycle 2.

Figure 5.2: Speed, power and optimal gear selection in hybrid mode.

The PowerBoost hub configuration is illustrated in Figure 5.4 for the two driving cycles. The colored areas correspond to the valve block configurations, represented by the variable ζ . In hybrid mode (blue and



(a) Driving cycle 1.



(b) Driving cycle 2.

Figure 5.3: Pumps and motor displacements in hybrid mode.

red area), the pressure in the line matches the pressure of the connected accumulator, while in hydrostatic mode (green areas) the pressure in

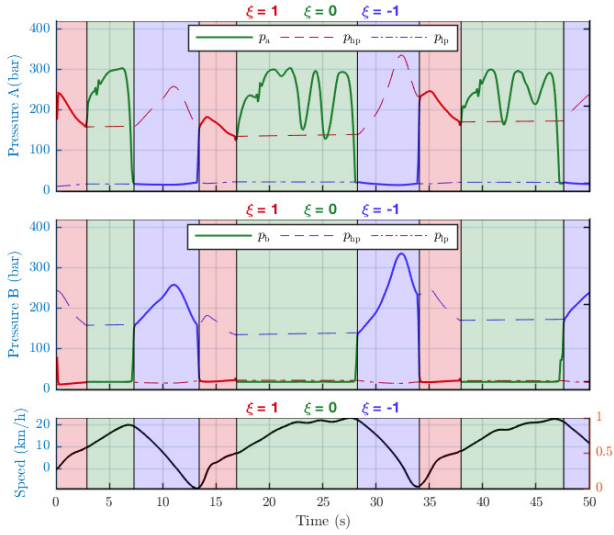
the lines evolves independently according to the continuity equation in (4.13a) and (4.13b). The effectiveness of the accumulator action is more evident when the vehicle is changing direction: the initial deceleration is used to charge the accumulator and the stored energy is then used to assist the acceleration in the opposite direction, sensibly reducing the power demand on the engine. In all the driving cycles, as expected, the accumulators are used when higher accelerations are required, while the system works in hydrostatic mode (green areas) when slower speed variations are demanded.

The optimal usage of the accumulators increases the fuel efficiency of an exceptional 12% (on average on the two driving cycles) compared to the driveline with only the hydrostatic transmission. This proves the effectiveness of the PowerBoost technology, as well as the soundness of the proposed optimal control technique.

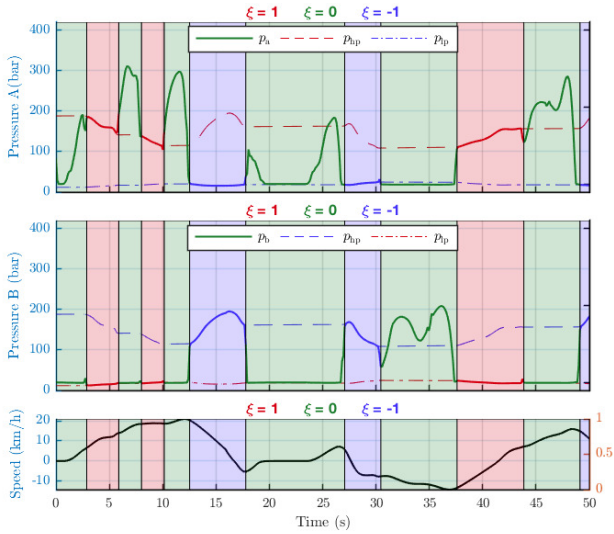
5.4 CONCLUSIONS

In this chapter we solved the energy management optimization problem in the framework of the mixed-integer optimal control, proving the performances of the direct discretization approach together with outer convexification of the integer controls on a realistic application. The optimal strategies have been computed and simulated using a realistic and validated powertrain model of an off-highway vehicle for material handling. This is the first time that such an extensive analysis has been made on this technology. Optimal control results show a good improvement in fuel consumption for the configuration with hydraulic accumulators, thanks to the recovery of the kinetic energy during regenerative braking that is released during high acceleration maneuver to assist the internal combustion engine, resulting in the overall reduction of the fuel consumptions.

The optimal control strategy has been computed off-line, and, due to the long time required to find a solution, cannot be implemented run-time in this form. In next phases of this project we will use the optimal control results discussed in this thesis to devise heuristic control strategies and improve the fuel economy of the system. Thanks to the implementation of such heuristic strategies, we will be able to validate on the vehicle the control strategies attained in this work.



(a) Driving cycle 1.



(b) Driving cycle 2.

Figure 5.4: Lines and accumulators pressures in hybrid mode.

BIBLIOGRAPHY OF CHAPTER 5

- [1] E. Bertolazzi, F. Biral, and M. Da Lio. “Real-time motion planning for multibody systems: Real life application examples.” In: *Multibody System Dynamics* 17.2-3 (2007). cited By (since 1996) 22, pp. 119–139. DOI: [10.1007/s11044-007-9037-7](https://doi.org/10.1007/s11044-007-9037-7). URL: <http://www.scopus.com/inward/record.url?eid=2-s2.0-33947493288&partnerID=40&md5=2f7a56e7aa941a0f8ba6491a92ddebfa>.
- [2] John T. Betts. *Practical Methods for Optimal Control and Estimation Using Nonlinear Programming*. 2010, p. 434. ISBN: 9780898716887. DOI: [10.1137/1.9780898716887](https://doi.org/10.1137/1.9780898716887).
- [3] Francesco Biral, Enrico Bertolazzi, and Non-member Paolo Bosetti. “Notes on Numerical Methods for Solving Optimal Control Problems.” In: *IEEJ Journal of Industry Applications* 5.2 (2015), pp. 154–166. DOI: [10.1541/ieejjia.5.154](https://doi.org/10.1541/ieejjia.5.154).
- [4] HG Bock and RW Longman. “Computation of optimal controls on disjoint control sets for minimum energy subway operation.” In: *Proceedings of the American Astronomical Society. Symposium on Engineering Science and Mechanics, Taiwan*. 1982.
- [5] Christof Büskens and Dennis Wassel. “The esa nlp solver worhp.” In: *Modeling and optimization in space engineering*. Springer, 2012, pp. 85–110.
- [6] Zoran Filipi and Young Jae Kim. “Hydraulic Hybrid Propulsion for Heavy Vehicles: Combining the Simulation and Engine-In-the-Loop Techniques to Maximize the Fuel Economy and Emission Benefits.” In: *Oil & Gas Science and Technology – Revue de l’Institut Français du Pétrole* 65.1 (2010), pp. 155–178. ISSN: 1294-4475. DOI: [10.2516/ogst/2009024](https://doi.org/10.2516/ogst/2009024).
- [7] Matthias Gerdt. “Solving mixed-integer optimal control problems by branch&bound: A case study from automobile test-driving with gear shift.” In: *Optimal Control Applications and Methods* 26.1 (2005), pp. 1–18. ISSN: 01432087. DOI: [10.1002/oca.751](https://doi.org/10.1002/oca.751).
- [8] Matthias Gerdt. “A variable time transformation method for mixed-integer optimal control problems.” In: *Optimal Control Applications and Methods* 27.3 (2006), pp. 169–182. ISSN: 01432087. DOI: [10.1002/oca.778](https://doi.org/10.1002/oca.778).

- [9] Matthias Gerdts. *Optimal control of ODEs and DAEs*. Vol. 1. 2012. ISBN: 9788578110796. DOI: [10.1017/CB09781107415324.004](https://doi.org/10.1017/CB09781107415324.004). arXiv: [arXiv:1011.1669v3](https://arxiv.org/abs/1011.1669v3).
- [10] Philip E Gill, Walter Murray, and Michael A Saunders. "SNOPT: An SQP algorithm for large-scale constrained optimization." In: *SIAM review* 47.1 (2005), pp. 99–131.
- [11] Leonardo Giovanini. "Optimal control applications and methods literature survey (No. 10)." In: *Optimal Control Applications and Methods Literature Survey* 30.2 (2009), pp. 217–219. ISSN: 01432087. DOI: [10.1002/oca.879](https://doi.org/10.1002/oca.879). URL: <http://doi.wiley.com/10.1002/oca.879>.
- [12] Young Jae Kim and Zoran Filipi. "Simulation Study of a Series Hydraulic Hybrid Propulsion System for a Light Truck." In: *SAE Paper 2007-01-4151* 724 (2007), pp. 776–790. ISSN: 0148-7191. DOI: [10.4271/2007-01-4151](https://doi.org/10.4271/2007-01-4151).
- [13] Christian Kirches, Sebastian Sager, Hans Georg Bock, and Johannes P. Schl. "Time-optimal control of automobile test drives with gear shifts." In: *Optimal Control Applications and Methods* 31.3 (), pp. 137–153. ISSN: 01432087. DOI: [10.1002/oca.892](https://doi.org/10.1002/oca.892). URL: <http://doi.wiley.com/10.1002/oca.939>.
- [14] Sisay Molla and Beshah Ayalew. "Power management strategies for a series hydraulic hybrid drivetrain." In: *International Journal of Powertrains* 1.1 (2011), p. 93. ISSN: 1742-4267. DOI: [10.1504/IJPT.2011.041911](https://doi.org/10.1504/IJPT.2011.041911).
- [15] Matthias Rieck, Guillermo P Falcon, Matthias Gerdts, and Florian Holzapfel. "Periodic Full Circuit Race Line Optimization under Consideration of a Dynamic Model with Gear Changes." In: 0.4 (2016), pp. 1470–1475.
- [16] Sebastian Sager. "Numerical methods for mixed-integer optimal control problems." In: *Praxis* 2005 (2005), p. 219. URL: <http://scholar.google.com/scholar?hl=en&btnG=Search&q=intitle:Numerical+methods+for+mixed+integer+optimal+control+problems+{#\%}5Cnhttp://sager1.de/sebastian/downloads/Sager2005.pdf>.
- [17] Sebastian Sager. "Reformulations and algorithms for the optimization of switching decisions in nonlinear optimal control." In: *Journal of Process Control* 19.8 (2009), pp. 1238–1247. ISSN: 09591524. DOI: [10.1016/j.jprocont.2009.03.008](https://doi.org/10.1016/j.jprocont.2009.03.008). URL: <http://dx.doi.org/10.1016/j.jprocont.2009.03.008>.

- [18] Sebastian Sager. "A benchmark library of mixed-integer optimal control problems." In: *Mixed Integer Nonlinear Programming* (2012), pp. 1–39. URL: http://link.springer.com/chapter/10.1007/978-1-4614-1927-3{_}22.
- [19] Sebastian Sager, Hans Georg Bock, and Moritz Diehl. "Solving mixed-integer control problems by sum up rounding with guaranteed integer gap." In: *SICON* (2007), pp. 1–13.
- [20] Sebastian Sager, Hans Georg Bock, and Moritz Diehl. "The integer approximation error in mixed-integer optimal control." In: *Mathematical Programming* 133.1-2 (2012), pp. 1–23. ISSN: 00255610. DOI: [10.1007/s10107-010-0405-3](https://doi.org/10.1007/s10107-010-0405-3).
- [21] Andreas Wächter and Lorenz T Biegler. "On the implementation of an interior-point filter line-search algorithm for large-scale nonlinear programming." In: *Mathematical programming* 106.1 (2006), pp. 25–57.
- [22] Matthew J Weinstein, Michael A Patterson, and Anil V Rao. "Utilizing the Algorithmic Differentiation Package ADiGator for Solving Optimal Control Problems Using Direct Collocation." In: *AIAA Guidance, Navigation, and Control Conference*. 2015, p. 1085.
- [23] Matthew J Weinstein and Anil V Rao. "Algorithm: ADiGator, a Toolbox for the Algorithmic Differentiation of Mathematical Functions in MATLAB Using Source Transformation via Operator Overloading." In: ().

APPENDIX OF CHAPTERS 3 AND 5

5.A LIST OF SYMBOLS

	Description	Symbol	Unit	Min/Max	$\mathcal{F}(x, u, \nu)$
States (x)	Pressure line A	p_a	bar	20/400	(4.20a)
	Pressure line B	p_b	bar	20/400	(4.20b)
	Engine Speed	ω_{ice}	rpm	800/2200	$\tau_{ice}\dot{\omega}_{ice} + \omega_{ice} = u_{ice}$
	Motor 1 Displ.	α_{m_1}	(-)	0.1/1	$\dot{\alpha}_{m_1} = u_{m_1}$
	Motor 2 Displ.	α_{m_2}	(-)	0.2/1	$\dot{\alpha}_{m_2} = u_{m_2}$
	Pump Displ.	α_p	(-)	-1/1	$\dot{\alpha}_p = u_p$
	Vehicle Speed	v	m/s	$v_{dc} \mp \varepsilon_v$	(4.22)
	HP temperature	T_{hp}	K	10/800	(4.18)
	HP pressure	p_{hp}	bar	95/400	(4.19)
	LP temperature	T_{lp}	K	10/800	(4.18)
LP pressure	p_{lp}	bar	12/60	(4.19)	
Continuous Controls (u)	Displ. rate motor 1	u_{m_1}	1/s	-0.5/0.5	
	Displ. rate motor 2	u_{m_2}	1/s	-0.5/0.5	
	Displ. rate pump	u_p	1/s	-0.5/0.5	
	Speed rate engine	u_{ice}	1/s	-1000/2200	
Discrete Controls (ν)	Gear engaged	φ	(-)	0/1	
	PowerHub Variable	ζ	(-)	-1/{0, +1}	

Table 5.A.1: List of States and Controls of the Optimal Control Problem.

Variable name	Symbol
Maximum displacement	D_p, D_{m_1}, D_{m_2}
Oil bulk modulus	β
Volume of the hose	V
Laminar leak coeff.	C_s
Turbulent leak coeff.	C_{st}
Viscous loss coeff.	C_v
Mech. friction coeff.	C_f
Hydrodyn. losses coeff.	C_h
Oil dynamic viscosity	μ
Oil density	ρ
Constant volume specific heat of gas	c_v
N ₂ mass in accumulators	m_{hp}, m_{lp}
N ₂ moles in accumulators	n_{hp}, n_{lp}
Accumulator time constant	τ
Universal gas constant	R
Wheel radius	r_w
Vehicle mass	m_v
Road slope	γ
Rad friction coeff.	κ_1
Drag coeff.	κ_2
Flow rate	Q_p, Q_{m_1}, Q_{m_2}
Torque	T_p, T_{m_1}, T_{m_2}
Volumetric efficiency	$\eta_p^v, \eta_{m_1}^v, \eta_{m_2}^v$
Mechanical efficiency	$\eta_p^t, \eta_{m_1}^t, \eta_{m_2}^t$
Prop. gain check valve	K_{ch}
Prop. gain relief valve	K_{rel}
Coeff. for unmodeled losses	c^{loss}

Table 5.A.2: List of Parameters. Subscripts p, m₁, m₂ refer to pump, motor 1 and motor 2. Subscripts hp, lp refer to high and low pressure accumulators respectively.

Part III

OPTIMIZATION OF THE CONTROLLER
PARAMETERS

6.1 INTRODUCTION

According to the global trend of reducing carbon emissions and improving efficiency some of the main goals for the next generation of transmission systems are an improved fuel economy and a better productivity. With this goal in mind, Dana-Rexroth Transmission Systems is developing a novel Continuous Variable Transmission (CVT) system that combines both fuel efficiency and performance. The best solution to fully satisfy the efficiency and performance requirements is using a Hydromechanical Variable Transmission (HVT). This novel transmission was introduced by Dana-Rexroth in [10] and references therein.

The HVT developed by Dana-Rexroth can also switch among several drive ranges that extend the range of possible working speeds. The switch is performed by coordinating two wet clutches suitably actuated by electro-proportional valves. In order to obtain a smooth clutch shift, a correct control of the torques transmitted by each clutch is critical. For this reason, Dana-Rexroth is developing a closed-loop pressure control scheme able to precisely modulate the transferred torque. The control design is challenging because of some restrictive specifications and hardware limitations. The requirements for the closed loop are: 1) a non-overshooting response, 2) a rise time smaller than 75 milliseconds. Moreover the control should be “easy” enough to be implemented with a limited computation power.

Several controllers are present in the literature but most of them are specific for dry clutches where the piston position is directly available. For example nonlinear geometric approaches are presented in [8] and [7]. In [8] a differential flatness based approach is considered while in [7] the authors use a feedback linearization to control the filling phase. These methods are rather elegant but are sensitive to modeling error and uncertainties. A different, and more robust, approach is presented in [11] where a nonlinear sliding-mode controller and observer are used. However this method is computationally expensive and requires a correct initialization of the observer. In our work the approach is more similar in spirit to the one presented in [6], where a linear model is employed. However experimental results show that a nonlinear DC gain is present in the plant, for this reason a nonlinear invertible output function is

added at the output, obtaining a so-called Wiener model. Similar to [12], the final goal of this work will be to develop a torque control for CVT transmissions.

The work is organized as follows: the experiment is described in Section 6.2. Section 6.3 explains the identified model. Section 6.4 illustrates the control system design and closed-loop experiments are reported in Section 6.5. All the units are normalized in this work due to confidentiality constraints and proofs are omitted due to space limitations.

6.2 EXPERIMENT DESCRIPTION AND GOALS

The goal of this work is the synthesis of a suitable control for wet clutches, this corresponds to precisely controlling the oil pressure inside the clutch (the output) selecting the right amount of current (input) in the electro-proportional valve. In this way the two coaxial shafts exert an exact force against each other, and the proper amount of torque is transmitted. The control for the valve current has been studied in [3].

Due to technological constraints the only available pressure sensor is located just after the valve and no pressure sensor is available in the clutch chamber. However, it is reasonable to assume that when the piston reaches the end of stroke, the gradient pressure in the line is negligible and the measured pressure coincides with the one inside the clutch chamber.

The stroke of the piston ends when all the oil among the disks is squeezed out and the shafts come to a contact transmitting only dry torque (because of the dry friction). The instant just before the end of the stroke of the piston is called *kiss point* or *incipient sliding point* [4]. In this work we consider only the system after the kiss point, but a control strategy encompassing the overall system is desirable.

Experimental tests have shown a delay between the commanded current and a change in the pressure. This delay is small and sometimes variable. We can roughly estimate this time delay as the time between the rising point of the output and the rising point of the step input. The latter can be easily detected, but the former can be only estimated. If we determine experimentally the smallest window that certainly contains the rising point, the estimated rising point of the output is the intercept between the two interpolating lines of the n_s samples before the rising window and the n_s samples after, where n_s is less than the number of samples before the first peak, as depicted in Fig. 6.1. Repeating this procedure on different datasets we find a pure delay of approximately 10 ms.

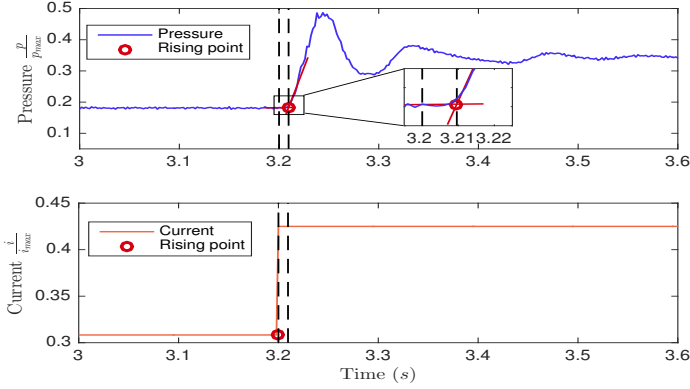


Figure 6.1: Time delay between the commanded step current and the pressure response.

6.3 PLANT MODEL AND IDENTIFICATION

In this section we propose a system model identification technique based on a convex optimization, that captures the main dynamics of the system and takes into account the most important nonlinearity while maintaining a simple structure.

6.3.1 Model selection

The response of the pressure in the clutch chamber to a current step input can be seen in Fig. 6.1. The dynamics recalls the behavior of a second order system with two complex conjugate poles inducing the oscillations. The peculiar shape of the peaks, that seem to elongate and get thinner, suggest that this nonlinear behavior can be described by a quadratic output nonlinearity at the output. This model, i.e., a transfer function in cascade interconnection with a static invertible output nonlinearity is called *Wiener model* [9]. We propose a model of the form:

$$g(s) \triangleq \frac{y_\ell(s)}{u(s)} = \frac{1 + \alpha_1 s}{1 + \beta_1 s + \beta_2 s^2} \quad (6.1a)$$

$$y(t) = \varphi(y_\ell(t)), \quad (6.1b)$$

where $g(s) : \mathbb{C} \rightarrow \mathbb{C}$ is the transfer function, $\alpha_1, \alpha_0, \beta_1 \in \mathbb{R}$ are the coefficients, $y_\ell(s), u(s)$ are respectively the output (pressure) and the input (current) in the Laplace domain and $\varphi : \mathbb{R} \rightarrow \mathbb{R}$ is the static output nonlinearity. The function φ is assumed to be continuous and

with continuous inverse, so that one can obtain the linear output y_ℓ from the real measurements y by inverting φ . Notice that in (6.1) we have arbitrarily assigned the DC gain of the transfer function $\lim_{s \rightarrow 0} g(s) = 1$ without loss of generality ¹.

6.3.2 Identification of the output nonlinearity

Since the static nonlinearity φ is invisible to the dynamics of the system, a reasonable approach for the identification of the non-linear model is to inspect the steady state input-output pairs $(y_{ss}, u_{ss}) \in \mathbb{R}^2$. The equation that relates the steady-state pairs in (6.1) is $y_{ss} = \varphi(y_{\ell,ss}) = \varphi(u_{ss})$, thanks to the unitary DC gain.

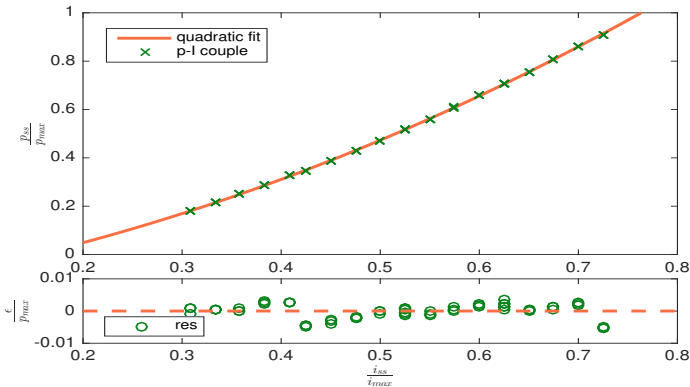


Figure 6.2: Interpolation of the steady-state pairs (top) and residuals (bottom) normalized on the maximum pressure p_{max} .

Fig. 6.2 shows the result of the interpolation of the steady states with a quadratic function of the form

$$y_{ss} = \varphi(u_{ss}) \triangleq a_0 + a_1 u_{ss} + a_2 u_{ss}^2. \tag{6.2}$$

¹ A non unitary DC gain of the transfer function $g(s)$ can be easily incorporated in the Wiener nonlinearity φ

The parameters $a_0, a_1, a_2 \in \mathbb{R}$ are found interpolating $N \in \mathbb{N}_{\geq 3}$ steady-state pairs; the resulting linear regression has the form

$$\underbrace{\begin{bmatrix} y_{ss1} \\ y_{ss2} \\ \vdots \\ y_{ssN} \end{bmatrix}}_z = \underbrace{\begin{bmatrix} 1 & u_{ss1} & u_{ss1}^2 \\ 1 & u_{ss2} & u_{ss2}^2 \\ \vdots & \vdots & \vdots \\ 1 & u_{ssN} & u_{ssN}^2 \end{bmatrix}}_X \underbrace{\begin{bmatrix} a_0 \\ a_1 \\ a_2 \end{bmatrix}}_a, \quad (6.3)$$

and the parameters vector $a \in \mathbb{R}^3$ is easily obtained as $a = (X^T X)^{-1} X^T z$, as long as the Vandermonde matrix X contains $N \geq 3$ linear independent pairs.

As expected, the quadratic function (6.2) fits well the steady-state values and the inverse φ^{-1} of the nonlinear function (6.2) maps the measured output y to the variable y_ℓ .

6.3.3 Model identification

In this section we discuss the technique adopted for the identification of the transfer function in (6.1). Let us consider a generic transfer function with unitary DC gain $G(s)$ of the form

$$G(s) = \frac{y_\ell(s)}{u(s)} = \frac{1 + \alpha_1 s + \dots + \alpha_q s^q}{1 + \beta_1 s + \dots + \beta_n s^n}, \quad (6.4)$$

where $q \in \mathbb{N}$ is the number of zeros of the transfer function and $n \in \mathbb{N}$ is the number of poles; the coefficients $\alpha_1, \dots, \alpha_q, \beta_1, \dots, \beta_n$ are the $q + n$ parameters to identify.

Expanding (6.4) and recalling that the inverse Laplace transform $\mathcal{L}^{-1}[s^j y_\ell(s)](t) = y_\ell^{(j)}(t)$, where $y_\ell^{(j)}(t)$ denotes the j -th derivative of the function $y_\ell(t)$, yields

$$\underbrace{\begin{bmatrix} y_\ell^{(1)}(t_s) & \dots & y_\ell^{(1)}(mt_s) \\ \vdots & & \vdots \\ y_\ell^{(n)}(t_s) & \dots & y_\ell^{(n)}(mt_s) \\ -u^{(1)}(t_s) & \dots & -u^{(1)}(mt_s) \\ \vdots & & \vdots \\ -u^{(q)}(t_s) & \dots & -u^{(q)}(mt_s) \end{bmatrix}}_\Phi \underbrace{\begin{bmatrix} \beta_1 \\ \vdots \\ \beta_n \\ \alpha_1 \\ \vdots \\ \alpha_q \end{bmatrix}}_\theta = \underbrace{\begin{bmatrix} u(t_s) - y_\ell(t_s) \\ \vdots \\ u(mt_s) - y_\ell(mt_s) \end{bmatrix}}_d \quad (6.5)$$

where $t_s \in \mathbb{R}$ is the sampling time of the collected dataset and $m \in \mathbb{N}$ is the number of samples in the dataset. Again the vector $\theta \in \mathbb{R}^{n+q}$ of

the unknown parameters is obtained as $\theta = (\Phi^T \Phi)^{-1} \Phi^T d$, as long as $m \geq (n + q)$. Notice that the regressor $\Phi \in \mathbb{R}^{m \times (n+q)}$ contains the first n derivatives of the output y_ℓ and the first q derivatives of the input u . If we apply a filter \mathcal{F} both to the input and the output of the system, the dynamics relating the new signals \tilde{y}_ℓ and \tilde{u} is described by the same transfer function $G(s)$. This is a consequence of the commutative and associative properties of linear systems; that is, if we have several SISO LTI systems in cascade, the output of the overall cascade does not depend on the order of the systems. We may apply the filter proposed in [5]

$$\mathcal{F} = [F_0(s) \ F_1(s) \ \dots \ F_n(s)]^T = \frac{[I \ sI \ \dots \ s^n I]^T}{(1 + \tau s)^n} \tag{6.6}$$

to the input u and output y_ℓ , choosing $\tau \in \mathbb{R}$ in order to preserve the most important dynamics of the system. We get the \tilde{y}_ℓ and \tilde{u} signals and their first n and q derivatives respectively. In this way we may construct the vector d and regressor Φ thus obtaining parameters vector θ .

According to (6.1), the identified transfer function is a second order transfer function with two complex conjugate poles with negative real part and one zero with positive real part. The identified system is a non-minimum phase system and approximates the delay by way of the small undershoot depicted in Fig. 6.3. This is not surprising as non-minimum phase systems are also typically used to represent delays in Padé approximations.

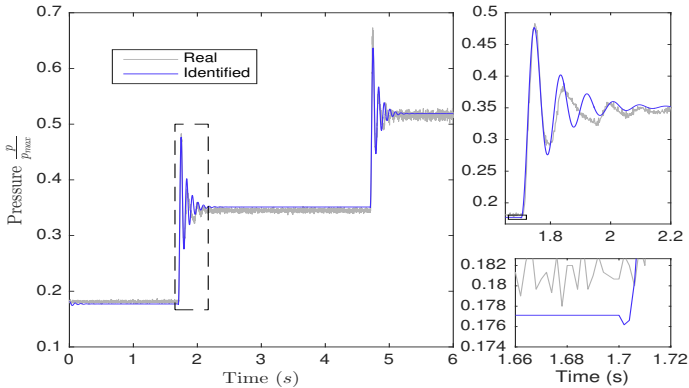


Figure 6.3: Validation of the identified model.

In Fig. 6.3 the real and simulated outputs are overlapped on some validation data, showing a good matching of the two curves. Given the identified output, y_{id} , the real response y_{real} and its mean value \bar{y}_{real} ,

the goodness of fit (GoF) is computed using the normalized root mean square error (NRMSE), i.e.

$$\text{GoF} = 100 (1 - \|y_{\text{id}} - y_{\text{real}}\| / \|y_{\text{real}} - \bar{y}_{\text{real}}\|). \quad (6.7)$$

In this experiment the goodness of fit is $\text{GoF} \approx 94\%$. Note that, even if the main dynamics of the system is well captured, there are still some unmodeled nonlinearities visible in the secondary oscillations. Nevertheless, such a degree of accuracy is sufficient for our goal, since we want to avoid the overshooting caused by the first oscillation.

6.4 CONTROL SYNTHESIS

In this section we describe the adopted LMI-based strategy for the design of an output feedback dynamic controller consisting of an observer combined with a static feedback from the estimated state. First, in Section 6.4.1 we describe the design of the observer as a suitable trade-off between speed of convergence and noise rejection. Then in the subsequent Section 6.4.2 we describe the adopted strategy for the design of the state-feedback gains as a suitable trade-off between the aggressiveness of the control action versus the ability to induce a non-overshooting response.

First, let us consider the following minimal realization for the transfer function in (6.1):

$$\left[\begin{array}{c|c} A & b \\ \hline c^\top & \end{array} \right] = \left[\begin{array}{cc|c} -\beta_1/\beta_2 & 1/\sqrt{\beta_2} & \alpha_1/\beta_2 \\ -1/\sqrt{\beta_2} & 0 & 1/\sqrt{\beta_2} \\ \hline 1 & 0 & \end{array} \right] \quad (6.8)$$

and the associated Wiener model

$$\dot{x} = Ax + bu + w_1, \quad y = \varphi(c^\top x) + w_2, \quad (6.9)$$

where $x \in \mathbb{R}^2$ is the state, $u \in \mathbb{R}$ is the input, $y \in \mathbb{R}$ is the output and $w_1 \in \mathbb{R}^2$, $w_2 \in \mathbb{R}$ are disturbances that take into account respectively the model uncertainties and the noise.

Assumption 1. Plant (6.9) is exponentially stable, namely matrix A is Hurwitz. Moreover, pair (c^\top, A) is observable.

Figure 6.4 summarizes the overall control scheme. Since the plant corresponds to a (non-minimum phase) linear filter followed by a nonlinearity, the linear controller is selected by inverting the nonlinearity φ , thereby

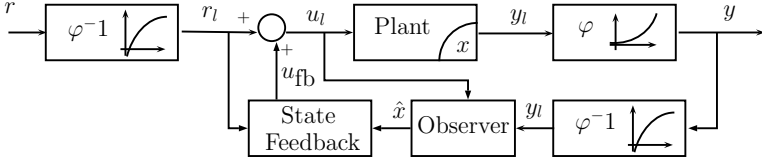


Figure 6.4: Block diagram of the proposed control algorithm consisting of the nonlinearity inversion φ^{-1} , an observer and a state feedback.

virtually accessing the linear output y_ℓ (denoted once again y_ℓ in the figure, under the assumption of a perfect knowledge of the nonlinearity) and then filtering the linear output to obtain a state estimate \hat{x} that is used in a state feedback solution driving to zero the tracking error with respect to an external reference.

6.4.1 LMI-based observer design

We propose implementing the following Luenberger observer for dynam-
ics (6.9), (6.8):

$$\begin{aligned} \dot{\hat{x}} &= A\hat{x} + bu + L(y_\ell - \hat{y}_\ell) \\ \hat{y}_\ell &= c^T\hat{x}, \end{aligned} \tag{6.10}$$

where gain L should be selected to induce suitable stability properties of the estimation error dynamics and disturbance rejection. Defining the estimation error as $e := x - \hat{x}$, the error dynamics can be computed from (6.9), (6.10) as:

$$\dot{e} = (A - Lc^T)e + Lw_2, \tag{6.11}$$

where we set $w_1 = 0$ because for our application the effect of w_2 is dominant. Following well known Lyapunov formulations of the bounded real lemma (see, e.g, [1]), we suggest selecting the observer gain L according to the following LMI-based convex optimization parametrized by $\alpha > 0$:

minimize γ , subject to:
 $P > 0, Y, \gamma$

$$\begin{aligned} \text{He}(PA - Yc^T) &\leq -2\alpha P \\ \text{He} \begin{bmatrix} PA - Yc^T & Y & 0 \\ 0 & -\frac{\gamma}{2} & 0 \\ I & 0 & -\frac{\gamma}{2} \end{bmatrix} &< 0, \end{aligned} \tag{6.12}$$

which is evidently linear in the optimization variables and where we used $\text{He}(X) = X + X^\top$. The following proposition establishes useful properties of the proposed selection:

Proposition 1. *Given any value of $\alpha > 0$, the LMI (6.12) is always feasible under Assumption 1. Moreover, consider any triple P, Y, γ satisfying the constraints in (6.12). Then selecting:*

$$L := P^{-1}Y, \quad (6.13)$$

the error dynamics (6.11) is such that the \mathcal{H}_∞ norm from w_2 to e is smaller than γ , and the matrix $A - Lc^\top$ has eigenvalues with real part smaller than or equal to $-\alpha$.

Proof. Feasibility of the LMI follows from standard pole placement theory combined with the observability assumption. The remaining part of the proof is a standard application of the bounded real lemma and the use of quadratic Lyapunov functions. In particular, defining $V_e(e) := e^\top P e$ (which is positive definite due to the constraint $P > 0$, performing a Schur complement on the last constraint of (6.12) and left- and right-multiplying by $\begin{bmatrix} e \\ w_2 \end{bmatrix}$, we obtain (after replacing $Y = PL$):

$$\langle \nabla V_e, \dot{e} \rangle + \frac{1}{\gamma} e^\top e - \gamma w_2^\top w_2 < 0,$$

which can be integrated on both sides to obtain the desired bound on the \mathcal{L}_2 gain from w_2 to e (equivalently, the \mathcal{H}_∞ norm). Regarding the speed of convergence α , this follows from noticing that the first inequality in (6.12) implies $\text{He}(P(A - Lc^\top + \alpha I)) < 0$ which only holds with a positive definite P if $A - Lc^\top$ has convergence abscissa smaller than $-\alpha$. \square

Remark 1. Proposition 1 emphasizes that the LMI-based design tool corresponding to (6.12) and (6.13) can be an effective means for performing the design of L while establishing a trade-off between the guaranteed speed of convergence of the observer dynamics (corresponding to α) and the level of disturbance rejection from the sensor noise w_2 to the estimation error e . The suggested use of this tool is to fix increasing values of α and then determine a trade-off curve between α and γ providing a range of optimal selections of the observer gain L . For our specific transfer function (6.1), such a trade-off curve is represented in Figure 6.5. The specific operating point on this curve will be selected to be the one corresponding to a black dot in the figure. Such a selection is mainly performed by fixing a sufficiently large convergence rate α once the state feedback gains are selected, as illustrated later in Section 6.5. \lrcorner

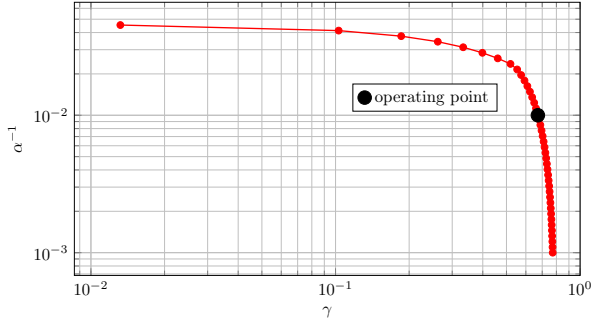


Figure 6.5: Trade-off curve between α and γ for the observer gain selection, based on construction (6.12), (6.13) applied to the identified transfer function.

6.4.2 LMI-based state feedback design

Due to the specific observer/controller structure of Figure 6.4, we may address the goal of non-overshooting stabilization within the simplified context wherein the control action is performed in feedback from the actual state, rather than its estimate. Then, in this section, we will propose an LMI-based convex procedure for the selection of the stabilizing gain K in such a way to obtain a non-overshooting response within the feedforward/feedback architecture:

$$\begin{aligned} u &= r_l + u_{fb}, \\ u_{fb} &= -K\tilde{x}, \quad \tilde{x} := x - x_r := x + A^{-1}b r_l, \end{aligned} \tag{6.14}$$

From Assumption 1 x_r is unique due to the fact that the open-loop dynamics is exponentially stable (therefore A is nonsingular).

The design of the stabilizer gain K is performed here by imposing the non-overshooting condition under the simplifying assumption of zero estimation error, namely $\hat{x} = x$, which means that the tracking error \tilde{x} is ruled by the next differential equation:

$$\begin{aligned} \dot{\tilde{x}} &= A\tilde{x} + Bu_{fb} = (A - BK)\tilde{x}, \\ \tilde{y}_\ell &= C\tilde{x}. \end{aligned} \tag{6.15}$$

In particular, within the above setting we represent the non-overshooting condition by imposing that when $\tilde{y}_\ell = 0$, then we have that $\dot{\tilde{y}}_\ell \approx 0$. More specifically, we will cast some conservative bounds aiming at establishing:

$$\tilde{y}_\ell = 0 \quad \Rightarrow \quad |\dot{\tilde{y}}_\ell| \leq \kappa_y |\tilde{x}|, \tag{6.16}$$

while minimizing bound κ_y . To the end of providing designs that lead to a small value of κ_y in (6.16), we rewrite (6.16) as follows:

$$|c^T(A - BK)\tilde{x}| \leq \kappa_y |\tilde{x}|, \quad \forall \tilde{x} : c^T \tilde{x} = 0. \quad (6.17)$$

Note that for the planar dynamics under consideration the least upper bound on κ_y can be explicitly computed as follows:

$$\kappa_y^* := |c^T(A - BK)c^\perp|, \quad (6.18)$$

where $c^\perp \in \mathbb{R}^2$ is the unique unit column vector such that $c^T c^\perp = 0$. To see that selection (6.18) satisfies (6.17) notice that any \tilde{x} satisfying $c^T \tilde{x} = 0$ can be written as $c^\perp \zeta$, where $\zeta \in \mathbb{R}$ satisfies $|\zeta| = |\tilde{x}|$, so that one has: $|c^T(A - BK)\tilde{x}| = |c^T(A - BK)c^\perp \zeta| = |c^T(A - BK)c^\perp| |\zeta| = \kappa_y^* |\tilde{x}|$.

Similar to the previous section, we perform our design as a suitable trade-off, which will then be useful for the practical selection of the controller gain among a set of possible ones. To this end, we parametrize the family of possible selections by way of a vector of upper bounds κ_u on $|K|$, otherwise understood as the level of aggressiveness of the arising controller. The proposed design consists in two steps, described subsequently in the remainder of this section and summarized in Remark 2 below.

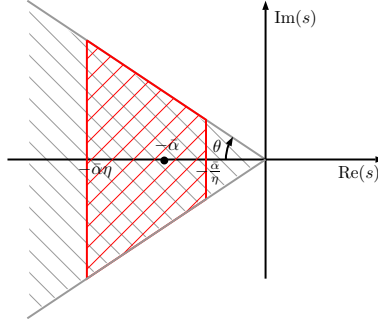


Figure 6.6: Region of the complex plane where the closed-loop poles are confined in the design optimization.

In the first step of the design we characterize the maximum achievable convergence rate $\bar{\alpha}$ that can be obtained with a pre-specified value of κ_u , under the constraint that the damping factor ζ of the two (possibly complex conjugate) closed loop poles be satisfying $|\cos(\theta)| \leq \zeta$ (this constraint corresponds to imposing that the closed-loop poles belong to a conic region in the left half plane, represented by the shaded grey area in

Figure 6.6). In particular, in the first step we solve the following problem:

$$\begin{aligned}
 &\text{maximize } \bar{\alpha}, \text{ subject to:} \\
 &\quad Q > I, X, \bar{\alpha} \\
 &\quad M + M^T \leq -2\bar{\alpha}Q, \\
 &\quad \begin{bmatrix} (M + M^T) \sin \theta & (M - M^T) \cos \theta \\ (M^T - M) \cos \theta & (M + M^T) \sin \theta \end{bmatrix} \leq 0 \\
 &\quad \begin{bmatrix} Q & X^T \\ X & \kappa_u^2 \end{bmatrix} \geq 0
 \end{aligned} \tag{6.19}$$

where we used the shortcut notation $M \triangleq AQ - BX$. Note that the constraints in (6.19) are non convex due to the product between variables $\bar{\alpha}$ and Q . However they can still be solved conveniently because they are quasi-convex in the optimization variables (they constitute a so-called generalized eigenvalue problem [1]). The next proposition establishes a few useful properties of the above mentioned optimization.

Proposition 2. *Under Assumption 1, for any value of $\kappa_u \geq 0$ there exists a large enough selection of $\theta \in [0, \pi/2]$ such that optimization (6.19) is feasible.*

Moreover, for any feasible solution of (6.19), selecting $K = XQ^{-1}$ the following properties hold for the closed loop: 1) the gain K satisfies $|K| \leq \kappa_u$; 2) the closed-loop poles have a convergence rate at least equal to $\bar{\alpha}$; 3) the closed-loop damping factor ζ satisfies $|\zeta| \leq \cos(\theta)$.

Proof. Feasibility follows from the fact that with $\theta = \frac{\pi}{2}$ the third constraint in (6.19) reduces to $M + M^T \leq 0$ and then the assumption that A be Hurwitz implies that $X = 0$ is a feasible solution for any non-negative value of κ_u .

Concerning the three properties of feasible solutions, item 2) is a straightforward consequence of the first constraint in (6.19) (see the similar steps in the proof of Proposition 1)) and item 3) is a direct application of the results in [2, eqn. (13)]. The proof is completed by showing item 1). To this end, first note that using $X = KQ$, we can obtain

from the third constraint in (6.19) that $\begin{bmatrix} Q^{-1} & K^T \\ K & \kappa_u^2 \end{bmatrix} \geq 0$. Then we may use

$Q^{-1} \leq I$ to obtain $\begin{bmatrix} I & K^T \\ K & \kappa_u^2 \end{bmatrix} \geq 0$ and performing a Schur complement we get $|K|^2 = KK^T \leq \kappa_u^2$, as to be proven. \square

The second step of the proposed construction consists in determining a solution to an optimization problem attempting to minimize quantity

κ_y in equation (6.16) while constraining the closed-loop poles to lay in a conic region in the left half plane. Given a selection of η , we solve the following LMI-based convex optimization:

$$\begin{aligned}
 & \underset{Q>I, X, \kappa_1>0, \kappa_2, \tau}{\text{minimize}} && \kappa_1 + \kappa_2, \text{ subject to:} \\
 & M + M^T \leq && -2\frac{\bar{\alpha}}{\eta}Q, \\
 & M + M^T \geq && -2\bar{\alpha}\eta Q, \\
 & \begin{bmatrix} (M + M^T) \sin \theta & (M - M^T) \cos \theta \\ (M^T - M) \cos \theta & (M + M^T) \sin \theta \end{bmatrix} \leq && 0 \\
 & \begin{bmatrix} Q & X^T \\ X & \kappa_u^2 \end{bmatrix} \geq && 0 \\
 & \begin{bmatrix} 2Q + \frac{\kappa_1}{2} & (c^T M)^T & -I \\ c^T M & \kappa_2 & 0 \\ -I & 0 & \frac{\kappa_1}{2} I + \tau c c^T \end{bmatrix} > && 0,
 \end{aligned} \tag{6.20}$$

where we used again the shortcut notation $M = AQ - BX$. The optimization in (6.20) is a heuristic one with the goal of providing reduced values of the nonlinear objective $\kappa_1\kappa_2$, indeed it is proven below that this product is an upper bound for the quantity κ_y in (6.17).

Proposition 3. *Under Assumption 1, if $\bar{\alpha}$, θ and κ_u come from a feasible solution to the constraints in (6.19), then there exists a large enough parameter $\eta \geq 1$ such that problem (6.20) is feasible.*

Moreover, for any feasible solution of (6.20), selecting $K = XQ^{-1}$ the following properties hold for the closed loop: 1) the gain K satisfies $|K| \leq \kappa_u$; 2) the closed-loop poles have a convergence rate at least equal to $\frac{\bar{\alpha}}{\eta}$; 3) the closed loop damping factor ζ satisfies $|\zeta| \leq \cos(\theta)$; 4) relation (6.17) is satisfied along solutions with $\kappa_y = \sqrt{\kappa_1\kappa_2}$.

Proof. Feasibility follows from the fact that there exists η sufficiently large such that the red region in Figure 6.6 contains the positions of the poles obtained by the feasible solution for (6.19) assumed in the theorem. Then that solution is also a feasible solution for (6.20) as long as κ_1 and κ_2 are selected sufficiently large so that the last constraint of (6.20) holds.

Regarding the properties of the feasible solutions, items 1)–3) are a straightforward consequence of the fact that the first, third and fourth constraints in (6.20) coincide with the constraints in (6.19) with $\bar{\alpha}$ replaced by $\frac{\bar{\alpha}}{\eta}$. We finish the proof by showing item 4). Performing a Schur com-

plement on the last inequality of (6.20), and using $Q = Q^\top$, and $Q \geq I$, we obtain:

$$\begin{bmatrix} Q + Q^\top + \frac{\kappa_1}{2} Q^\top Q - (\frac{\kappa_1}{2} I + \tau c c^\top)^{-1} & (c^\top M)^\top \\ c^\top M & \kappa_2 \end{bmatrix} > 0,$$

where $\Sigma := \frac{\kappa_1}{2} I + \tau c c^\top$ is invertible from its positive definiteness. Then, exploiting $(Q - \Sigma^{-1})^\top \Sigma (Q - \Sigma^{-1}) \geq 0$, we obtain $Q + Q^\top - \Sigma^{-1} \leq Q^\top \Sigma Q$, which implies, also using $M = (A - BK)Q$,

$$\begin{bmatrix} Q^\top (\kappa_1 I + \tau c c^\top) Q & (c^\top (A - BK) Q)^\top \\ c^\top (A - BK) Q & \kappa_2 \end{bmatrix} \geq 0, \tag{6.21}$$

or equivalently

$$\begin{bmatrix} \kappa_1 I + \tau c c^\top & (c^\top (A - BK))^\top \\ c^\top (A - BK) & \kappa_2 \end{bmatrix} \geq 0, \tag{6.22}$$

which, after being multiplied by κ_2 and after a Schur complement, implies:

$$|c^\top (A - BK) \tilde{x}|^2 \leq \kappa_1 \kappa_2 |\tilde{x}|^2 + \kappa_2 \tau |c^\top \tilde{x}|^2, \tag{6.23}$$

thus, when $c^\top \tilde{x} = 0$, we can take a square root and prove (6.17) with $\kappa_y = \sqrt{\kappa_1 \kappa_2}$. □

#	κ_u	$\bar{\alpha}$	κ_y^*	$\sqrt{\kappa_1 \kappa_2}$	Color
1	0	~	~	~	•
2	8.9	92.0	825.3	2932.3	•
3	14.4	140.4	1042.3	3031.6	•
4	23.4	194.1	1098.9	3362.6	•
5	37.9	264.0	1171.3	3823.5	•
6	61.6	354.9	1265.6	4482.5	•
7	100.0	471.6	1388.6	5439.6	•

Table 6.1: Values resulting from the optimization discussed in Remark 2 and corresponding color in the curves of Figure 6.7.

Remark 2. The properties established in Propositions 2 and 3 suggest that the feedback gain K be selected as follows: first a set of different levels of aggressiveness of the feedback κ_u are fixed, spanning an experimentally reasonable range for the size of gain K . Then for each of them optimization (6.19) is performed, possibly adjusting the parameter θ if the LMIs are infeasible (feasibility is guaranteed by Proposition 2 for a large enough θ). This first step provides a number of values for $\bar{\alpha}$, each of them corresponding to a different selection of κ_u . As a second step, optimization (6.20) is solved for each one of the $(\kappa_u, \bar{\alpha})$ pairs with the same value of θ , possibly adjusting parameter η (feasibility is guaranteed by Proposition 3 for a large enough η).

For the plant identified in this work, the values of κ_u listed in Table 6.1 have been selected and the resulting values of $\bar{\alpha}$ have been obtained applying optimization (6.19) by fixing $\theta = \pi/4$. Table 6.1 also reports for the specific selections of κ_u , the value obtained for $\sqrt{\kappa_1\kappa_2}$ after solving optimization (6.20) with $\eta = 5$. According to Proposition 3, this value of $\sqrt{\kappa_1\kappa_2}$ corresponds to an upper bound for the quantity κ_y^* defined in equation (6.18). Also κ_y^* is reported for completeness: note that there is a significant level of conservativeness in the estimate $\sqrt{\kappa_1\kappa_2}$, however despite this fact the optimizer is capable of reducing κ_y^* to a reasonably small value, thereby eliminating the overshoot in the curves of Figures 6.7–6.8. ┘

6.5 GAINS SELECTION AND EXPERIMENTS

6.5.1 Gain selection

The selection of the state feedback gain K in the scheme of Figure 6.4 has been performed by first generating a number of possible closed-loop responses following the strategy described in Remark 2. The corresponding values are listed in Table 6.1 and for each one of these selections, Figure 6.7 shows the corresponding state responses obtained when simulating dynamics (6.9), with the state feedback $u = -Kx$. Clearly, the responses expected experimentally are worse because the scheme of Figure 6.4 also involves the state observer, and the linear non-minimum phase plant dynamics is an approximation for an actual linear plant with input delay and minimum phase dynamics.

Among the possible responses shown in Figure 6.7, we selected the slow red bold solution because it leads to gains well ranged for keeping the control action within the saturation limits. Moreover, this selection allowed picking a relatively faster observation error dynamics, which was still within a reasonable range, compatible with the real-time imple-

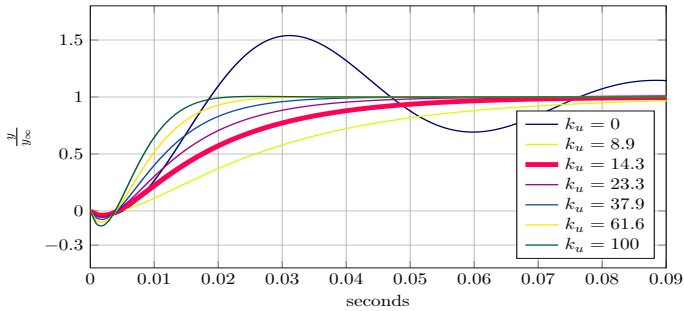


Figure 6.7: Simulated step responses of the state-feedback loop (no observer) with the selections of Table 6.1. The bold curve corresponds to the experimental gains.

mentation on the industrial product. In particular, based on the response time of roughly 50 ms of the state feedback selection (see the red curve in Figure 6.7), we selected the observer gain from Figure 6.5 imposing the inverse of the convergence rate α^{-1} (which is a rough estimate of the response time) as 10 ms (see the black dot in Figure 6.5).

Before experimentation, the selected gains have been tested by way of three simulations:

1. *State feedback*: A first simulation corresponding to the same scenario reported in Figure 6.7 and corresponding to the *state-feedback* scheme, without the observer, corresponding to (6.9), with the state feedback $u = -Kx$;
2. *Output feedback without delay*: A second simulation implementing the full scheme of Figure 6.4 corresponding to (6.9), with the observer (6.10) and the input selection $u = r_l - K(\hat{x} - x_r)$, with the plant model consisting in the identified non-minimum phase system;
3. *Output feedback with delay*: A third more realistic situation consisting in the use of the same controller but the plant replaced by a minimum phase linear dynamics (whose identification has been performed following similar steps to those listed in Section 6.3) having a large variable delay (between 0 and 20ms) at its input, consistently with the identification illustrated in Figure 6.1.

Note that the insertion of the observer dynamics causes a slight deterioration of the response (red vs blue curves) due to the observation error. Moreover, the more realistic situation of the presence of a large variable

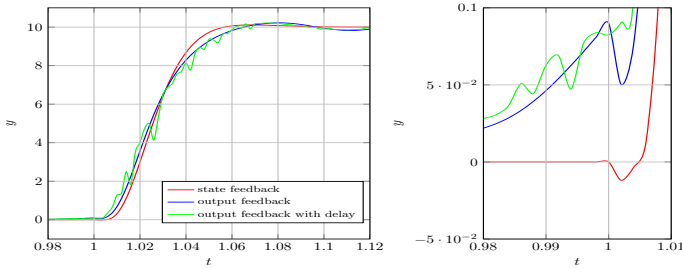


Figure 6.8: Simulation of the step responses in the three considered scenarios: state feedback (red), output feedback without delay (blue) and output feedback with delay (green).

delay (between 0 and 20ms) at the plant input (green curve), leads to a very similar response, even though the zoom at the right of the figure shows a substantial difference in the nature of the plant response.

6.5.2 Experimental validation of the control scheme

In this section we present the results of the implementation of the control strategy proposed in this chapter on one of the clutches of the Dana Rexroth HVT transmission. The experimental data prove the validity of the proposed control technique for achieving a non-overshooting and relatively fast output response of the closed loop. In Fig. 6.9 the output the open and closed loop response is shown.

The proposed control strategy is effective on the second pressure step, where the clutch chamber is completely filled and there is no flow of oil. The first pressure drop corresponds to the filling phase, when the pressure measurement is not representative of the actual actuation pressure of the clutch because the oil in the chamber is still flowing. The closed loop effectively reduces the oscillations of the pressure response, avoiding the overshoot. The rise time is approximately 60 ms, which is within the required 75 ms. The performances of the asymptotic observer are illustrated in Fig. 6.10, reporting the estimate \hat{x} of the plant state together with output $y = x_1$.

The observer follows the actual value of x_1 and acts as a low-pass filter reducing the measurement noise. The observer estimate presents a small undershoot, due to the fact that the identified model used in the observer is non-minimum phase to take into account the delay.

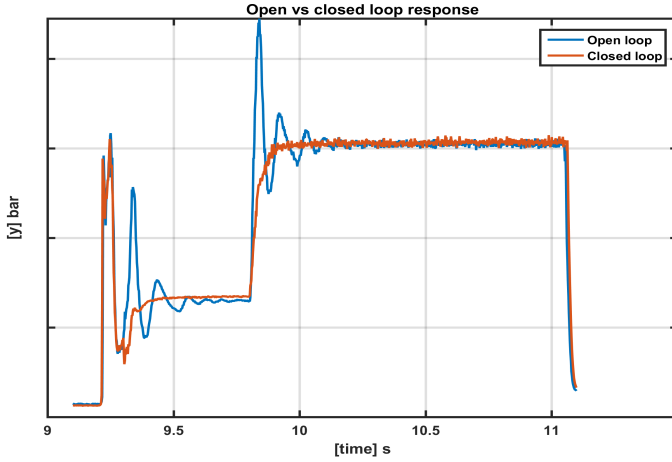


Figure 6.9: Experimental closed loop response.

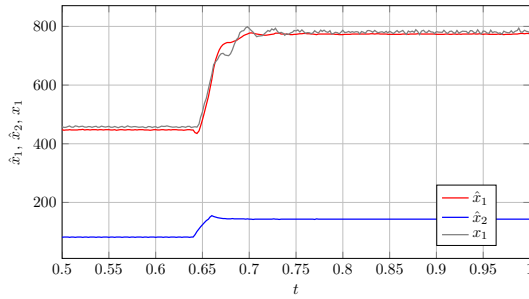


Figure 6.10: Comparison between the measure and the estimate of the state x_1 .

6.6 CONCLUSION

This work reports on the design of an observer/controller pair for the wet clutches of an HVT. The interest of the proposed design is especially in the identification approach and in the new method proposed to obtain non-overshooting responses. Experimental results confirm the effectiveness of our approach.

BIBLIOGRAPHY OF CHAPTER 6

- [1] S. Boyd, L. El Ghaoui, E. Feron, and V. Balakrishnan. *Linear Matrix Inequalities in System and Control Theory*. Society for Industrial and Applied Mathematics, 1994.
- [2] M. Chilali and P. Gahinet. " H_∞ design with pole placement constraints: an LMI approach." In: *IEEE Transactions on Automatic Control* 41.3 (1996), pp. 358–367.
- [3] M Cordioli, M Mueller, F Panizzolo, F Biral, and L Zaccarian. "An adaptive reset control scheme for valve current tracking in a power-split transmission system." In: *Control Conference (ECC), 2015 European*. IEEE. 2015, pp. 1884–1889.
- [4] Lars Eriksson and Lars Nielsen. *Modeling and control of engines and drivelines*. John Wiley & Sons, 2014.
- [5] F. Forni, S. Galeani, and L. Zaccarian. "An almost Anti-Windup scheme for plants with magnitude, rate and curvature saturation." In: *Proceedings of the 2010 American Control Conference*. 2010, pp. 6769–6774. DOI: [10.1109/ACC.2010.5531621](https://doi.org/10.1109/ACC.2010.5531621).
- [6] M Goetz, MC Levesley, and DA Crolla. "Dynamics and control of gearshifts on twin-clutch transmissions." In: *Proceedings of the institution of mechanical engineers, Part D: Journal of Automobile Engineering* 219.8 (2005), pp. 951–963.
- [7] Hongtao Hao, Tongli Lu, Jianwu Zhang, and Bin Zhou. "A new control strategy of the filling phase for wet dual clutch transmission." In: *Proceedings of the Institution of Mechanical Engineers, Part C: Journal of Mechanical Engineering Science* (2015), p. 0954406215590187.
- [8] Joachim Horn, Joachim Bamberger, Peter Michau, and Stephan Pindl. "Flatness-based clutch control for automated manual transmissions." In: *Control Engineering Practice* 11.12 (2003), pp. 1353–1359.
- [9] Lennart Ljung. *System Identification: Theory for the User*, PTR Prentice Hall Information and System Sciences Series. 1999.
- [10] M. Mueller, W. Scandella, and S. Mutschler. *Power-split transmission for a traction drive and method for controlling the transmission*. US Patent 9,243,701. 2016. URL: <https://www.google.ch/patents/US9243701>.

- [11] Xingyong Song and Zongxuan Sun. "Pressure-based clutch control for automotive transmissions using a sliding-mode controller." In: *Mechatronics, IEEE/ASME Transactions on* 17.3 (2012), pp. 534–546.
- [12] Paul D Walker, Nong Zhang, and Richard Tamba. "Control of gear shifts in dual clutch transmission powertrains." In: *Mechanical Systems and Signal Processing* 25.6 (2011), pp. 1923–1936.

VEHICLE LATERAL VELOCITY ESTIMATION

7.1 INTRODUCTION

Control of vehicle dynamics is a firmly established field in the automotive industry. The possibility to change the dynamical behavior of a vehicle using an electronic control unit (ECU) leads to tremendous improvement in passengers safety and comfort. Remarkable examples are Traction Control (TC), which maximizes the tire-road friction forces through longitudinal slip control [24], and the Electronic Stability Control (ESC), which prevents vehicles from spinning, by reducing the under/oversteering behavior [22].

In the latter class of algorithms the side-slip angle plays a pivotal role, since it is directly related to the vehicle instability, see for example [12] and [19]. The side-slip angle identifies the orientation of the vehicle with respect to the longitudinal direction and is therefore representative of the lateral velocity component, which plays a fundamental role in the ESC design.

However, an accurate measurement of the lateral velocity requires expensive devices such as optical sensors [27], two-antenna GPS [8] or lateral tire forces sensors [15], which are usually not available on commercial cars. For these reasons many techniques have been proposed to reconstruct lateral velocity based on measurements provided by cheap sensors such as accelerometers, gyroscopes and wheel encoders. Two approaches became popular in the literature: the first one employs an observer based on a “physical” linearized model of the vehicle dynamics, while the second one is an observer based on a purely kinematic model of the vehicle [30].

The observer built upon the physical model has good robustness properties, it rejects sensor noise and biases, but usually requires a precise knowledge of the vehicle parameters, such as the cornering stiffness, inertia and mass. The cornering stiffness are usually time varying and difficult to predict during fast maneuvers, and for this reason a vast number of solutions have been proposed in the literature. Some example are adaptive control techniques [13], robust control [9] and on-line parameters estimation [26, 28, 31] just to cite a few. Further improvements can be obtained including non-linear models of the tire-road contact forces in

the observer dynamics [2, 11, 20], but once again a good knowledge of the model parameters is required.

The observer built upon the kinematic model is more appealing, since its estimate does not depend on the physical parameters of the vehicle, and consequently it is robust with respect to parameters uncertainties, [5, 18, 19]. However, it provides reliable estimates only for high yaw-rates and in the absence of bias on the acceleration measurements (e.g. when the vehicle travels on a flat road). To compensate for these accelerations related to gravity, many techniques have been developed, see for example bank and grade road angle approaches [21, 29], or disturbance observer based techniques in [6, 7, 16].

However, robustness to acceleration bias can also be improved by increasing the observer gain, with a consequent (and undesired) increase of the noise sensitivity. To reduce this sensitivity we propose here a modified version of the well-known kinematic observer presented in [5], where we introduce an adaptive dead-zone function at the output injection term. This dead-zone mechanism has been recently proposed in [3] for Linear Time Invariant (LTI) systems. In this work we show that the same technique can be easily adapted for the kinematic observer which is a Linear Parameter Varying (LPV) system. The noise reduction attained with the dead-zone mechanism allows for a selection of a larger observer gain, which attenuates the deterioration of the estimate caused by the bias on the acceleration measurements. The effectiveness of the proposed observer is shown by means of numerical simulations on the 8 degrees of freedom non-linear vehicle model.

The outline of this chapter is organized as follows. Section 7.2 presents vehicle model and the kinematic model. Section 7.3 briefly recall the well-known kinematic observer and investigates the effect of sensor noise. Section 7.4 introduces the dead-zone observer structure and contains the main results and proofs. Numerical results are reported and discussed in Section 7.5. Finally, conclusions are offered in Section 7.6.

Notation: We denote by \mathbb{R}^n the set of real vectors of dimension n . Given a constant $c \in \mathbb{R}$ we write $\mathbb{R}_{\geq c}$ to denote the subset $[c, \infty) \subset \mathbb{R}$. Given two vectors $x \in \mathbb{R}^n$, $y \in \mathbb{R}^m$, $(x, y) := [x^\top y^\top]^\top \in \mathbb{R}^{n+m}$. For a matrix $M \in \mathbb{R}^{n \times m}$, M^\top denotes its transpose. For square invertible matrices $M \in \mathbb{R}^{n \times n}$, M^{-1} denotes the inverse of M and $M^{-\top}$ its inverse transpose, $M > 0$ ($M \geq 0$) denotes positive definiteness (semi-definiteness) of M , and $\text{He}(M) := (M + M^\top)$. The symbol $\text{co}(\cdot)$ denotes the standard (closed) convex hull operation and sat (resp. dz) is the standard saturation (resp. dead-zone) function. Finally \mathbb{E} denotes the expectation operator.

7.2 VEHICLE MODELS

In this section we briefly recall two models that are commonly employed to design and test the effectiveness of the lateral-speed estimation algorithms. The models are presented in decreasing order of complexity and accuracy. The first model is called “double track”, and includes detailed formulas for tire forces, load transfers and roll motion. The second is a “kinematic” model, which links accelerations to the longitudinal and lateral velocity in the vehicle reference frame. We use this model to build the kinematic observer proposed in [5] and add the dead-zone mechanism.

7.2.1 Double track model

It is widely accepted in the literature [1, 4, 10, 25] that vehicle dynamics models including a fairly good representation of the roll motion are sufficiently accurate to study and design integrated chassis control for active suspension and steering and traction/braking torque distribution. Among those models, the double track model is the simplest one. The double track model is an 8 Degrees Of Freedom (DOF), which describes the motion of the chassis with respect to the unsprung masses as the rotation about a fixed roll axis. This motion is completed by the dynamics associated to the wheel rotation, and a detailed tire model [17] that also considers the camber effect for a better prediction of the handling properties [14]. Details regarding this model can be found in [25] and are not reported here for space reasons. In Section 7.5 we use the double track model to test the effectiveness of the kinematic observer proposed in Section 7.4.

7.2.2 Kinematic model

The kinematic model is probably the simplest model that we can consider. The acceleration vector $u = (a_x, a_y) \in \mathbb{R}^2$ is directly sensed by the accelerometers mounted on the chassis, projected along the longitudinal/lateral directions and then integrated obtaining the velocity $x = (v_x, v_y) \in \mathbb{R}^2$. The resulting model is a Linear Parameter Varying (LPV) system of the following form

$$\begin{cases} \dot{x} = A(r)x + u \\ y = Cx, \end{cases} \quad (7.1)$$

where $r \in \mathbb{R}$ is the time varying parameter representing the yaw-rate. Notice that in this model the velocity vector is the state, the acceleration

is the input and $y = v_x \in \mathbb{R}$ is the measured output. The matrices in (7.1) are defined as

$$A(r) := \begin{bmatrix} 0 & r \\ -r & 0 \end{bmatrix}, \quad C := \begin{bmatrix} 1 & 0 \end{bmatrix}.$$

It is important to remark that the pair $(C, A(r))$ is detectable if and only if r is different from zero.

7.3 KINEMATIC OBSERVER

In this section we briefly recall the kinematic observer proposed by Farrelly and Wellstead in [5], and we show that in presence of a lateral acceleration bias the estimation error is proportional to the observer gain. This suggests that increasing the gain allows us to achieve better performance. The price to pay is an observer more sensitive to noise.

7.3.1 A yaw-rate dependent kinematic observer

In [5] Farrelly and Wellstead proposed a Luenberger-like kinematic observer with a yaw-rate dependent observer gain. The observer has the following form:

$$\begin{cases} \dot{\hat{x}} = A(r)\hat{x} + u + L(r)(\hat{y} - y) \\ \hat{y} = C\hat{x}, \end{cases} \quad (7.2)$$

where the observer gain $L(r) \in \mathbb{R}^2$ is yaw-dependent and defined as

$$L(r) := \begin{bmatrix} -2\alpha|r| \\ (1 - \alpha^2)r \end{bmatrix}, \quad (7.3)$$

where $\alpha \in \mathbb{R}_{>0}$ is a tunable parameter. The parameter α assigns the speed of converge of the error dynamics. Indeed, at constant yaw-rate, the two eigenvalues associated to $(A(r) + L(r)C)$ are both located at $-\alpha|r|$, for $i = 1, 2$. It is worth to notice that (7.2) with the gain selection (7.3) is a linear parameter varying (LPV) system and the location of the eigenvalues is not enough to establish stability. However, the authors in [5] provide a suitable Lyapunov function that guarantees stability for all uniformly non-zero evolution of r . Since its proposal, the kinematic-observer in (7.2) has been widely studied in the literature, e.g. [19] and [30], and many experimental implementations have been developed to test its performance. It turns out that, despite its simplicity, the kinematic-observer provides good estimates even during driving conditions where

the vehicle dynamics is far from being linear. However, as pointed out in [18], the selection of the parameter α is especially critical, as it entails the well-known trade-off between bandwidth (speed of converge of the error dynamics) and sensitivity to noise.

7.3.2 The effect of input/output noise

To implement the kinematic-observer in (7.2) few measurements are required. The longitudinal speed $y = v_x$ is usually estimated starting from an average of the left and right non-tractive wheels rotational speed $\omega_l, \omega_r \in \mathbb{R}$ as $v_x = R \frac{\omega_l + \omega_r}{2}$, where $R \in \mathbb{R}_{>0}$ is the wheel rolling radius. However, this estimate is correct only in the absence of slip between the wheels and the ground. This immediately suggests that in slipping conditions v_x can be affected by noise and biases. The yaw-rate r and the accelerations $u = (a_x, a_y)$ are obtained by the gyroscopes and accelerometers commonly integrated in standard Inertial Measurement Unit (IMU), but are easily affected by the shape of the road. For example the bank angle $\vartheta \in \mathbb{R}$ induces a lateral acceleration bias which is given by

$$\Delta a_y = -g \sin(\vartheta), \quad (7.4)$$

where g is the gravitational acceleration. This bias can damage fully and degrade the lateral speed estimation, see for example [18]. Many hardware and software compensation techniques have been proposed, see for example [8, 18, 21, 31], and [32] just to cite a few. However it is desirable to design an observer that is intrinsically able to mitigate the effects of measurements noise/biases, both at the input u and at the output y . This desirable behavior can be obtained by increasing the value of α in the observer gain (7.3). For example if we consider a bias of the form (7.4) at the input u , the error dynamics associated with the observer (7.2) yields

$$\dot{e} = (A(r) + L(r)C)e + \begin{bmatrix} 0 \\ \Delta a_y \end{bmatrix}, \quad (7.5)$$

where $e := \hat{x} - x$ is the estimation error. Assuming a non-zero yaw-rate r and $\alpha \in \mathbb{R}_{>0}$ the steady state error results

$$e = [A(r) + L(r)C]^{-1} \begin{bmatrix} 0 \\ \Delta a_y \end{bmatrix} = \frac{1}{\alpha} \begin{bmatrix} -\frac{1}{\alpha r} \\ -\frac{2|r|}{r^2} \end{bmatrix} \Delta a_y. \quad (7.6)$$

We can notice that larger values of α lead to smaller estimation errors. We stress also that for a fixed α , the estimation error is larger at smaller

yaw-rates and this is consistent with the intuition that when r approaches zero, the kinematic model (7.1) is increasingly less observable.

By incrementing α we increase the robustness to bias/noise at the input, but we also reduce the noise rejection capability of the observer with respect to high frequency noise at the output y . This behavior is undesirable when dealing with noisy measurements of the longitudinal speed and, for this reason, in the following section, we propose a dead-zone modification of the kinematic observer.

7.4 DEAD-ZONE BASED KINEMATIC OBSERVERS

In this section we briefly recall the main features of the Dead-zone Observer (DO) proposed in [3]. The central idea is to modify the classical Luenberger observer with an adaptive dead-zone function at the output injection term, as illustrated in Subsection 7.4.1. This choice introduces a peculiar mechanism that reduces the sensibility to high frequency noise, and leaves open the possibility to increase the observer gain. This feature is desirable since a large observer gain can be used to dominate nonlinearities or to reduce the effect of unmodeled dynamics. We mimic this idea and we propose a dead-zone mechanism for the kinematic-observer (7.2) in Subsection 7.4.2.

7.4.1 Overview on dead-zone observers

We start by briefly recalling the main results obtained in [3], adapting the presentation to Multiple Inputs Single Output (MISO) plants. Let us start by considering a Linear Time Invariant (LTI) detectable plant of the following form

$$\begin{cases} \dot{x} = Ax + Bu \\ y = Cx, \end{cases} \quad (7.7)$$

where $x \in \mathbb{R}^n$ is the state, $u \in \mathbb{R}^m$ is the input and $y \in \mathbb{R}$ is the output. The Dead-zone Observer for (7.7) proposed in [3] has the following form

$$\begin{cases} \dot{\hat{x}} = A\hat{x} + Bu + Ldz_{\sqrt{\sigma}}(\hat{y} - y) \\ \hat{y} = C\hat{x} \end{cases} \quad (7.8)$$

where $\hat{x} \in \mathbb{R}^n$ is the estimated state, $\hat{y} \in \mathbb{R}$ is the estimated output and $dz_{\sqrt{\sigma}} : \mathbb{R} \rightarrow \mathbb{R}$ is an adaptive dead-zone function defined as $dz_{\sqrt{\sigma}}(s) := \text{sign}(s)(|s| - \min\{|s|, \sqrt{\sigma}\})$. The amplitude of the dead-zone is equal to

$2\sqrt{\sigma}$, where $\sigma \in \mathbb{R}_{\geq 0}$ evolves dynamically according to the following adaptation law

$$\dot{\sigma} = -\lambda\sigma + \gamma(\hat{y} - y)^2. \quad (7.9)$$

Now let us define the estimation error as $e := \hat{x} - x$ and recall that $\text{sat}_{\sqrt{\sigma}}(y) + \text{dz}_{\sqrt{\sigma}}(y) = y$, where $\text{sat}_{\sqrt{\sigma}} : \mathbb{R} \rightarrow \mathbb{R}$ is the standard saturation function (whose saturation level is $\sqrt{\sigma}$). Then, after a few manipulations, we obtain the following equivalent representation for the interconnection (7.8)-(7.9),

$$\begin{cases} \dot{e} = (A + LC)e - L\text{sat}_{\sqrt{\sigma}}(Ce) \\ \dot{\sigma} = -\lambda\sigma + \gamma(Ce)^2 \end{cases} \quad \sigma \in \mathbb{R}_{\geq 0}. \quad (7.10)$$

We notice that the σ -adaptation is tuned by $\gamma \in \mathbb{R}_{\geq 0}$, and by $\lambda \in \mathbb{R}_{> 0}$, which are design parameters. Notice also that $\mathbb{R}_{\geq 0}$ is a forward invariant set for (7.9).

Intuitively, observer (7.10) works as follows: in the absence of noise \hat{y} converges asymptotically to y and the adaptation parameter σ converges to zero. In this scenario, the dead-band shrinks to zero and the dead-zone function converges to the identity map recovering the classical Luenberger observer. On the contrary, in the presence of noise or unmodeled dynamics, the adaptation mechanism (7.9) is forced by a persistently non zero $(\hat{y} - y)$ and σ remains bounded away from zero. This non zero value of σ creates a “tube” around $(\hat{y} - y) = 0$, where a mismatch (e.g. noise) does not affect the observer dynamics. We can think that inside this tube the observer runs partially in open-loop fashion and that the dead-zone cuts everything inside the dead-band.

The drawback is that this mechanism partially disconnects (7.8) from the output measurements and may have a destabilizing effect on the observer dynamics. To ensure stability of the origin for (7.10) the authors in [3] propose a Linear Matrix Inequality (LMI) synthesis. The LMI formulation is the following:

$$\text{He} \begin{bmatrix} PA + ZC + \gamma C^T C & -Z \\ \mu C & -\mu - \lambda \end{bmatrix} < 0, \quad (7.11)$$

where the optimization variables are $0 < P = P^T \in \mathbb{R}^{n \times n}$, $\lambda \in \mathbb{R}_{> 0}$, $\gamma, \mu \in \mathbb{R}_{\geq 0}$ and $Z \in \mathbb{R}^n$. This formulation allows for a convenient trade-off between the speed of adaptation (corresponding to large values of λ) and the filtering action (corresponding to large values of γ). Any feasible solution to (7.11), with the selection $L := P^{-1}Z$, provides a choice of the parameters (λ, γ, L) that guarantees Global Asymptotic Stability (GAS) of

the origin $(e, \sigma) = (0, 0)$ for (7.10). We also recall from [3], that a necessary and sufficient condition for the feasibility of (7.11) is the detectability of the pair (C, A) . Therefore (7.11) is always feasible for any linear detectable plant. Finally we remark that (7.11) is still a feasible LMI if a stabilizing observer gain L is a-priori fixed: we just need to substitute Z with the product PL in (7.11).

7.4.2 Yaw-rate dependent dead-zone observer

In this subsection we propose to augment the kinematic observer (7.2) with the dead-zone mechanism illustrated in (7.8), (7.9). The proposed kinematic dead-zone observer has the following form

$$\begin{cases} \dot{\hat{x}} = A(r)\hat{x} + u + L(r)\text{dz}_{\sqrt{\sigma}}(\hat{y} - y) \\ \hat{y} = C\hat{x}, \end{cases} \quad (7.12)$$

where $L(r) \in \mathbb{R}^2$ is defined in (7.3). We immediately notice that in contrast to (7.8), matrix $A(r)$ and the observer gain $L(r)$ are parameter varying and depend on the yaw-rate r . It is easy to verify that for small values of $|r|$ the observer gain $L(r)$ is small as well and observer (7.12) is less sensitive to noise. For this reason, we propose to scale the σ -dynamics in (7.9) according to $|r|$ in the following way

$$\dot{\sigma} = -\lambda|r|\sigma + \gamma|r|(\hat{y} - y)^2. \quad (7.13)$$

Following the same steps as in Subsection 7.4.1 we define the estimation error as $e := \hat{x} - x$ and, with the selection (7.13), we obtain the following LPV variation of dynamics (7.14):

$$\begin{cases} \dot{e} = A_{\text{CL}}(r)e - L(r)\text{sat}_{\sqrt{\sigma}}(Ce) \\ \dot{\sigma} = -\lambda|r|\sigma + \gamma|r|(Ce)^2 \end{cases} \quad \sigma \in \mathbb{R}_{\geq 0}, \quad (7.14)$$

where for simplicity of notation we defined the following closed-loop matrix $A_{\text{CL}}(r) := A(r) + L(r)C$, whose explicit expression is reported below

$$\left[\begin{array}{c|c} A_{\text{CL}}(r) & L(r) \end{array} \right] := \left[\begin{array}{cc|c} -2\alpha|r| & r & -2\alpha|r| \\ -\alpha^2 r & 0 & (1 - \alpha^2)r \end{array} \right]. \quad (7.15)$$

In order to recover the LMI-based formulation in [3] we assume that the yaw rate is uniformly bounded away from zero, i.e., that $|r(t)| \geq \epsilon$ for all $t \in \mathbb{R}_{\geq 0}$ where $\epsilon \in \mathbb{R}_{> 0}$ is not necessarily known. Although this may seem restrictive, in practice it is not possible to obtain reliable estimates

of the lateral velocity when the yaw rate is too small, due the very nature of the kinematic model (7.1). We are now ready to state the main result of the chapter.

Theorem 1. *Consider the observer (7.14). Assume that the following LMI in the optimization variables $0 < P = P^\top \in \mathbb{R}^{2 \times 2}$, $\gamma \in \mathbb{R}_{\geq 0}$, $\lambda, \mu \in \mathbb{R}_{> 0}$ is feasible:*

$$\text{He} \begin{bmatrix} PA_{\text{CL}}(1) + \gamma C^\top C & -PL(1) \\ \mu C & -\mu - \lambda \end{bmatrix} < 0. \quad (7.16)$$

Then for any $\epsilon \in \mathbb{R}_{> 0}$ and for any value of $r \in (-\infty, -\epsilon]$, or $r \in [\epsilon, \infty)$, the error dynamics (7.14) is Globally Asymptotically Stable (GAS) to the origin.

Proof. The proof is carried out in two steps. First we show that (7.16) implies GAS of the origin for (7.14) as long as $r \in [\epsilon, \infty)$. Second, we show that the GAS property holds also when $r \in (-\infty, -\epsilon]$. Let us start considering the following candidate Lyapunov function $V(e, \sigma) := e^\top P e + 2\sigma$. We remark that $P = P^\top > 0$ and that $\sigma \in \mathbb{R}_{\geq 0}$ so that $V(e, \sigma)$ is proper and positive definite. Differentiating with respect to time yields

$$\begin{aligned} \dot{V}(e, \sigma) &= e^\top A_{\text{CL}}(r)^\top P e + e^\top P A_{\text{CL}}(r) e \\ &\quad - 2e^\top P L(r) \text{sat}_{\sqrt{\sigma}}(C e) \\ &\quad - 2\lambda |r| \sigma + 2\gamma |r| (C e)^2, \end{aligned} \quad (7.17)$$

and then consider the following inequalities

$$2\mu |r| \text{sat}_{\sqrt{\sigma}}(C e) (C e - \text{sat}_{\sqrt{\sigma}}(C e)) \geq 0 \quad (7.18a)$$

$$2\lambda |r| (\sigma - \text{sat}_{\sqrt{\sigma}}^2(C e)) \geq 0, \quad (7.18b)$$

where (7.18a) is a global sector condition for the saturation function and (7.18b) simply states that σ is always greater than the square of a saturation function whose amplitude is $\sqrt{\sigma}$. Summing up (7.18) to (7.17) we obtain the following upper-bound

$$\begin{aligned} \dot{V}(e, \sigma) &\leq \begin{bmatrix} e \\ \text{sat}_{\sqrt{\sigma}}(C e) \end{bmatrix}^\top \begin{bmatrix} \text{He}(P A_{\text{CL}}(r)) + 2\gamma |r| C^\top C \\ -L(r)^\top P + \mu |r| C \\ -PL(r) + \mu |r| C^\top \\ -2|r|(\mu + \lambda) \end{bmatrix} \begin{bmatrix} e \\ \text{sat}_{\sqrt{\sigma}}(C e) \end{bmatrix} \leq 0, \end{aligned} \quad (7.19)$$

for all $(e, \sigma) \neq 0$. Equation (7.19) can be strengthened and conveniently re-written in a strict LMI like form as follows

$$\text{He} \begin{bmatrix} PA_{\text{CL}}(r) + \gamma|r|C^{\top}C & -PL(r) \\ \mu|r|C & -|r|(\mu + \lambda) \end{bmatrix} < 0, \quad (7.20)$$

where r ranges in the interval $[\epsilon, \infty)$. It is important to notice that inequality (7.20) does not imply asymptotic convergence, but only stability: however we can represent the LPV model as a differential inclusion and invoke the invariance principle presented in [23] to conclude that if (7.20) holds for all $r \in [\epsilon, \infty)$, then (7.14) is Globally Asymptotically Stable (GAS).

Now recalling that $r \in [\epsilon, \infty)$ notice that the entries of (7.15) are homogeneous of degree one with respect to r , so that $A_{\text{CL}}(r) = rA_{\text{CL}}(1)$ and $L(r) = rL(1)$. Collecting a scaling factor $|r|$ from Equation (7.20), this last one reduces to (7.16), showing GAS for uniformly positive yaw-rates. We conclude the proof by showing that any feasible solution to (7.20) with $r = r^* \in [\epsilon, \infty)$ is also a feasible solution to (7.20) with $r = -r^* \in (-\infty, \epsilon]$. This idea is formally stated in Lemma 1.1 below, which concludes the proof of the case $r \in (-\infty, -\epsilon]$. \square

Lemma 1.1. *Assume that $(P^*, \gamma^*, \mu^*, \lambda^*)$ is a feasible solution to (7.20) associated to a positive yaw-rate $r = r^* \in [\epsilon, \infty)$, and consider the non-singular diagonal matrix $T := \text{diag}(1, -1) \in \mathbb{R}^{2 \times 2}$. Then $(TP^*T, \gamma^*, \mu^*, \lambda^*)$ is a feasible solution to (7.20) with $r = -r^* \in (-\infty, -\epsilon]$.*

Proof. First we notice that feasibility of the LMI (7.20) is not affected by congruence transformations. We pre/post-multiply (7.20) by $\text{diag}(T, 1) \in \mathbb{R}^{3 \times 3}$ and we obtain the equivalent condition

$$\text{He} \begin{bmatrix} TPA_{\text{CL}}(r)T + \gamma|r|TC^{\top}CT & -TPL(r) \\ \mu|r|CT & -|r|(\mu + \lambda) \end{bmatrix} < 0. \quad (7.21)$$

Using the expression in (7.15) it is easy to verify that the following equalities hold

$$A_{\text{CL}}(r)T = TA_{\text{CL}}(-r) \quad (7.22a)$$

$$TC^{\top}CT = C^{\top}C \quad (7.22b)$$

$$L(r) = TL(-r). \quad (7.22c)$$

Plugging (7.22) into (7.21) we retrieve (7.20) with parameters $(TP^*T, \gamma^*, \mu^*, \lambda^*)$ and following the same steps as in the proof of Theorem 1 we conclude GAS for $r \in (-\infty, \epsilon]$. It is interesting to notice that matrix $TP^*T \in \mathbb{R}^{2 \times 2}$

has the same elements as P but with a sign inversion of the off-diagonal terms, namely

$$P^* := \begin{bmatrix} p_{11} & p_{12} \\ p_{12} & p_{22} \end{bmatrix} \Leftrightarrow TP^*T := \begin{bmatrix} p_{11} & -p_{12} \\ -p_{12} & p_{22} \end{bmatrix},$$

where we remark that $TP^*T > 0$ if and only if $P^* > 0$. \square

The combination of Theorem 1 and Lemma 1.1 provides a desirable unified design strategy, which is independent of the sign of r , and provides guarantees for any value of r uniformly bounded away from zero. We do not include the defective point $r = 0$ (where we know that the system is not detectable), even if Theorem 1 suggests that the same observer can also be used for cases where r keeps changing sign and spends little time around zero. However a rigorous stability analysis for that scenario is not carried out in this preliminary work. We also remark that LMI (7.16) is always feasible because pair $(C, A(1))$ is detectable: the proof of this fact follows similar steps to those reported in [3]. As a consequence, we can think of the dead-zone mechanism as an augmentation of the original observer (7.2), which improves its performance.

7.4.3 LMI-based optimization

In this subsection we use the LMI constraint (7.16) to formulate an optimization problem with the goal to optimize the noise rejection capability of the dead-zone observer (7.12).

In general there are infinitely many solutions to (7.16) and we propose to choose the one that maximizes the effect of noise on the adaptation dynamics. A good idea is to select the largest possible value of γ , once an upper bound $\lambda_{\max} \in \mathbb{R}_{>0}$ has been fixed for the σ -adaptation speed λ . The resulting optimization problem can be cast as follows

$$\begin{aligned} & \max_{\gamma, \lambda, \mu, P} \gamma, & \text{subject to:} \\ & \text{He} \begin{bmatrix} PA_{\text{CL}}(1) + \gamma C^T C & -PL(1) \\ \mu C & -\mu - \lambda \end{bmatrix} < 0 & (7.23) \\ & P = P^T > 0, \quad \lambda_{\max} \geq \lambda > 0 \\ & \mu \geq 0, \quad \gamma \geq 0. \end{aligned}$$

The upper-bound $\lambda_{\max} \in \mathbb{R}_{>0}$ avoids an excessive mismatch between the plant and the dead-band adaptation dynamics.

7.5 SIMULATION RESULTS

In this section we assess the effectiveness of the proposed method. We compare the performance of the kinematic observer (7.2) with the one of the dead-zone observer (7.12) in the presence of noise ν affecting measurement $y = Cx + \nu$. We perform numerical simulations on the double track model described in Subsection 7.2.1.

We show that the dead-zone observer allows for a selection of larger values of α in the observer gain (7.3), without affecting the sensitivity to measurement noise. To quantify this sensitivity we use two indicators that provide a quantitative appraisal of the signal noise and of the quality of the estimation: the Signal to Noise Ratio (SNR) and the Goodness of Fit (GoF) computed using the Normalized Root Mean Squared Error (NRMSE). The SNR of the estimate \hat{x} corrupted by noise $\nu \in \mathbb{R}$ is defined as

$$\text{SNR}_{\text{dB}} := 10 \log \left(\frac{\mathbb{E}\{\hat{x}^\top \hat{x}\}}{\mathbb{E}\{\nu^\top \nu\}} \right),$$

while the GoF is defined as

$$\begin{aligned} \text{GoF} &:= 1 - \text{NRMSE} \\ &:= 1 - \frac{\|x - \hat{x}\|}{\|x - \mathbb{E}\{x\}\|}. \end{aligned}$$

We remark that $\text{GoF} = 1$ indicates a perfect match between the estimate \hat{x} and the real value x .

In order to achieve a fair comparison between the two methods, we first fix α of the kinematic observer gain, then we gradually increase α of the dead-zone observer gain until the SNR of the two estimates coincides. We see that, given a similar SNR, parameter α in the dead-zone observer can be roughly doubled. The longitudinal speed is selected constant and equal to $v_x = 13.9$ m/s, and a step-like steering angle is applied at the front wheels. The output measurement $y = v_x + \nu$ is corrupted by the high frequency (500 Hz) uniform random noise ν with amplitude range ± 0.034 m/s. At $t = 10$ s the vehicle encounters a banked road with inclination $\vartheta = 1.4^\circ$ that results in a lateral acceleration measurement bias Δa_y as in (7.4). The σ -adaptation parameters are computed solving the convex optimization problem in (7.23) setting $\lambda_{\max} = 300$ are $\gamma = 225.37$ and $\lambda = 299.9$. We remark that Lemma 1.1 guarantees that γ and λ are valid design parameters also for negative yaw rates. The estimation results are depicted in Fig. 7.1, where we can see that for $t < 10$ s, namely when the road is flat, a good estimate is achieved by both the

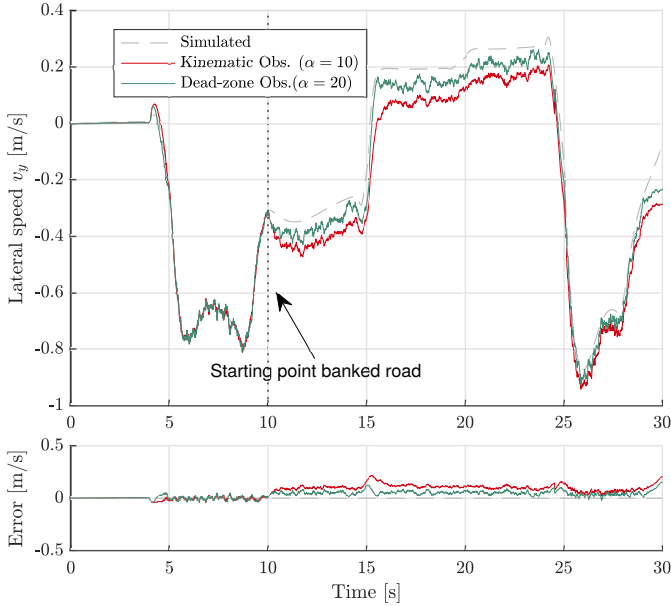


Figure 7.1: Comparison between the simulated (dashed line) and the estimated lateral velocity with the kinematic observer (green solid line) and the dead-zone observer (red solid line) during a step-like steering maneuver on the double track model, see Subsection 7.2.1.

kinematic and the dead-zone observers. When the vehicle encounters the banked road after $t = 10$ s, the estimates degrade, but the larger α value of the dead-zone observer reduces sensibly the error induced by the acceleration bias. This result is supported by the value of the GoF in Table 7.1, where the similar SNR of the two estimates is reported as well. It is also interesting to look at Fig. 7.2, where the dead-zone action

	α	SNR	GoF
Kinematic Observer	10	42.5 dB	75.50 %
Dead-zone Observer	20	40.3 dB	86.93 %

Table 7.1: Parameter α and performance indicator for the sinusoidal steering test on the non-linear model.

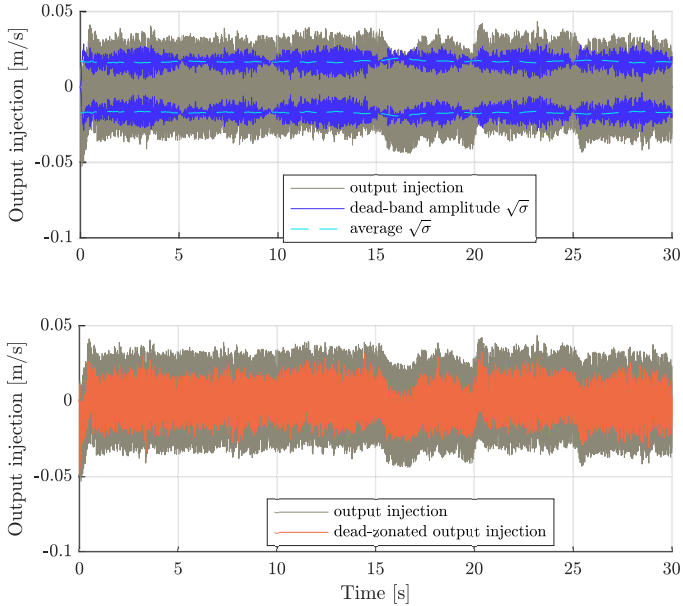


Figure 7.2: Dead-zone “tube” overlapped to the output injection term (top) and filtering action of the dead-zone (bottom).

can be visually interpreted. The dead-zone mechanism cuts the part of the output injection term (gray line top plot) which is trapped inside the dead-band (blue lines top plot); the resulting output injection term is shown in orange in the bottom plot.

7.6 CONCLUSIONS

In this work we modified the well-known kinematic observer based on a LPV generalization of the adaptive dead-zone mechanism discussed in [3]. This adaptive dead-zone mechanism reduces the sensitivity to high frequency noise and allows for larger values of the observer gain. We have shown that stability of the LPV error dynamics can be re-formulated in a LMI form. We showed the LMI feasibility under the necessary condition of detectability of the linearized kinematic model and we characterized solutions for positive and negative yaw rates. Finally, we tested the effectiveness of our approach by means of numerical simulations on a

non-linear vehicle model. Implementation of the proposed methodology on an experimental setup will be the subject of future investigations.

BIBLIOGRAPHY OF CHAPTER 7

- [1] John T. Cameron and Sean Brennan. "A comparative, experimental study of model suitability to describe vehicle rollover dynamics for control design." In: *Proceedings of IMECE2005. 2005 ASME International Mechanical Engineering Congress and Exposition*. 2005.
- [2] B. C. Chen and F. C. Hsieh. "Sideslip angle estimation using extended Kalman filter." In: *Vehicle System Dynamics* 46.SUPPL.1 (2008), pp. 353–364. DOI: [10.1080/00423110801958550](https://doi.org/10.1080/00423110801958550).
- [3] M Cocetti, S Tarbouriech, and L Zaccarian. "On dead-zone observers for linear plants." In: *Submitted to Proceedings of 2017 IEEE American Control Conference* (). URL: <http://homepages.laas.fr/lzaccari/submitted/CocettiACC18.pdf>.
- [4] Nicola Dal Bianco, Roberto Lot, and Marco Gadola. "Minimum time optimal control simulation of a GP2 race car." In: *Proc IMechE Part D: J Automobile Engineering* 1.16 (2017). DOI: [10.1177/0954407017728158](https://doi.org/10.1177/0954407017728158).
- [5] J. Farrelly and P. Wellstead. "Estimation of vehicle lateral velocity." In: *Proceedings of the 1996 IEEE International Conference on Control Applications* November (1996), pp. 552–557. ISSN: 1085-1992. DOI: [10.1109/CCA.1996.558920](https://doi.org/10.1109/CCA.1996.558920). URL: <http://ieeexplore.ieee.org/lpdocs/epic03/wrapper.htm?arnumber=558920>.
- [6] Hiroshi Fujimoto and Naoki Takahashi. *Cornering stiffness and slip angle estimation of electric vehicle for direct yaw-moment control*. Vol. 39. 16. IFAC, 2004, pp. 496–501. DOI: [10.3182/20060912-3-DE-2911.00087](https://doi.org/10.3182/20060912-3-DE-2911.00087).
- [7] Hiroshi Fujimoto, Take Saito, Akio Tsumasaka, and Toshihiko Noguchi. "Motion Control and Road Condition Estimation of Electric Vehicles with Two In-wheel Motors." In: (2004).
- [8] J Christian Gerdes. "Estimation of Vehicle Roll and Road Bank Angle." In: (2004), pp. 2110–2115.
- [9] J Bosche A El Hajjaji. *An Output Feedback Controller Design for Lateral Vehicle Dynamic*. Vol. 41. 1. IFAC, 2008, pp. 5670–5675. ISBN: 9781123478. DOI: [10.3182/20080706-5-KR-1001.00956](https://doi.org/10.3182/20080706-5-KR-1001.00956).
- [10] Bridget C. Hamblin, Ryan D. Martini, John T. Cameron, and Sean N. Brennan. "Low-Order Modeling of Vehicle Roll Dynamics." In: *Proceedings of the 2006 American Control Conference*. 2006.

- [11] Lars Imsland, Tor A. Johansen, Thor I. Fossen, Håvard Fjær Grip, Jens C. Kalkkuhl, and Avshalom Suissa. "Vehicle velocity estimation using nonlinear observers." In: *Automatica* 42.12 (2006), pp. 2091–2103. DOI: [10.1016/j.automatica.2006.06.025](https://doi.org/10.1016/j.automatica.2006.06.025).
- [12] EK Liebmenn, K Meder, J Schuh, and G Nenninger. "Safety and performance enhancement: The Bosch electronic stability control (ESP)." In: *SAE Paper 20004.2004* (2004), pp. 21–0060.
- [13] Chia-Shang Liu and Huei Peng. "A State and Parameter Identification Scheme for Linearly Parameterized Systems." In: *Journal of Dynamic Systems, Measurement, and Control* 120.4 (1998), p. 524. ISSN: 00220434. DOI: [10.1115/1.2801496](https://doi.org/10.1115/1.2801496).
- [14] Xiao-Pei Lu, Konghui Guo, Dang Lu, and Yin-Lin Wang. "Effect of tire camber on vehicle dynamic simulation for extreme cornering." In: *Vehicle System Dynamics* 44.sup1 (2006), pp. 39–49. DOI: [10.1080/00423110600867309](https://doi.org/10.1080/00423110600867309).
- [15] Kanghyun Nam, Hiroshi Fujimoto, and Yoichi Hori. "Lateral stability control of in-wheel-motor-driven electric vehicles based on sideslip angle estimation using lateral tire force sensors." In: *IEEE Transactions on Vehicular Technology* 61.5 (2012), pp. 1972–1985.
- [16] Kenji Natori, Roberto Oboe, and Kouhei Ohnishi. "Stability Analysis and Practical Design Procedure of Time Delayed Control Systems With." In: 4.3 (2008), pp. 185–197.
- [17] Hans B. Pacejka. *Tire and Vehicle Dynamics (Third Edition)*. Third Edition. Oxford: Butterworth-Heinemann, 2012, p. 697. ISBN: 978-0-08-097016-5.
- [18] Giulio Panzani, Matteo Corno, Mara Tanelli, Sergio M Savaresi, Andrea Fortina, and Sebastiano Campo. "Control-oriented vehicle attitude estimation with online sensors bias compensation." In: *ASME 2009 Dynamic Systems and Control Conference*. American Society of Mechanical Engineers. 2009, pp. 819–826.
- [19] Giulio Panzani, Matteo Corno, Mara Tanelli, Annalisa Zappavigna, Sergio M. Savaresi, Andrea Fortina, and Sebastiano Campo. "Designing on-demand four-wheel-drive vehicles via active control of the central transfer case." In: *IEEE Transactions on Intelligent Transportation Systems* 11.4 (2010), pp. 931–941. ISSN: 15249050. DOI: [10.1109/TITS.2010.2055858](https://doi.org/10.1109/TITS.2010.2055858).

- [20] Gridsada Phanomchoeng, Rajesh Rajamani, and Damrongrit Piyabongkarn. "Nonlinear observer for bounded Jacobian systems, with applications to automotive slip angle estimation." In: *IEEE Transactions on Automatic Control* 56.5 (2011), pp. 1163–1170. ISSN: 00189286. DOI: [10.1109/TAC.2011.2108552](https://doi.org/10.1109/TAC.2011.2108552).
- [21] Damrongrit Piyabongkarn, Rajesh Rajamani, John A. Grogg, and Jae Y. Lew. "Development and experimental evaluation of a slip angle estimator for vehicle stability control." In: *IEEE Transactions on Control Systems Technology* 17.1 (2009), pp. 78–88. ISSN: 10636536. DOI: [10.1109/TCST.2008.922503](https://doi.org/10.1109/TCST.2008.922503).
- [22] Rajesh Rajamani. *Vehicle dynamics and control*. Springer Science & Business Media, 2011.
- [23] Ricardo G Sanfelice, Rafal Goebel, and Andrew R Teel. "Invariance principles for hybrid systems with connections to detectability and asymptotic stability." In: *IEEE Transactions on Automatic Control* 52.12 (2007), pp. 2282–2297.
- [24] Sergio M Savaresi and Mara Tanelli. *Active braking control systems design for vehicles*. Springer Science & Business Media, 2010.
- [25] Taehyun Shim and Chinar Ghike. "Understanding the limitations of different vehicle models for roll dynamics studies." In: *Vehicle System Dynamics* 45.3 (2007), pp. 191–216. DOI: [10.1080/00423110600882449](https://doi.org/10.1080/00423110600882449).
- [26] C. Sierra, E. Tseng, A. Jain, and H. Peng. "Cornering stiffness estimation based on vehicle lateral dynamics." In: *Vehicle System Dynamics* 44.SUPPL. 1 (2006), pp. 24–38. ISSN: 00423114. DOI: [10.1080/00423110600867259](https://doi.org/10.1080/00423110600867259).
- [27] Zehang Sun, George Bebis, and Ronald Miller. "On-road vehicle detection using optical sensors: A review." In: *Intelligent Transportation Systems, 2004. Proceedings. the 7th International IEEE Conference on*. IEEE, 2004, pp. 585–590.
- [28] S Bottelli M Tanelli and I Boniolo S M Savaresi. "Online estimation of vehicle load and mass distribution for ground vehicles." In: (2014), pp. 8439–8444.
- [29] H E Tseng. "Dynamic Estimation of Road Bank Angle." In: 3114.October (2017). DOI: [10.1076/vesd.36.4.307.3547](https://doi.org/10.1076/vesd.36.4.307.3547).

- [30] a. Y. Ungoren, H. Peng, and H. E. Tseng. "A study on lateral speed estimation methods." In: *International Journal of Vehicle Autonomous Systems* 2.1/2 (2004), pp. 126–144. ISSN: 1471-0226. DOI: [10.1504/IJVAS.2004.004458](https://doi.org/10.1504/IJVAS.2004.004458). URL: <http://www.inderscience.com/link.php?id=4458>.
- [31] A. Vahidi, A. Stefanopoulou, and H. Peng. "Recursive least squares with forgetting for online estimation of vehicle mass and road grade: Theory and experiments." In: *Vehicle System Dynamics* 43.1 (2005), pp. 31–55. ISSN: 00423114. DOI: [10.1080/00423110412331290446](https://doi.org/10.1080/00423110412331290446).
- [32] Vincent Winstead and Ilya V. Kolmanovsky. "Estimation of road grade and vehicle mass via model predictive control." In: *Proceedings of 2005 IEEE Conference on Control Applications, 2005. CCA 2005.* (2005), pp. 1588–1593. ISSN: 1085-1992. DOI: [10.1109/CCA.2005.1507359](https://doi.org/10.1109/CCA.2005.1507359). URL: <http://ieeexplore.ieee.org/lpdocs/epic03/wrapper.htm?arnumber=1507359>.

CONCLUSIONS

In this chapter we summarize the main results of this thesis and we give an outlook over the future directions that can be developed from this work.

The necessity to cope with the issue of a more sustainable mobility brought to the development of power-train solutions able to cut down noxious emissions and to reduce the need of fossil fuels. Hybridization has been accepted as a mid-term solution able to ferry the global mobility towards full emission-free alternatives. In this view, an increasingly number of hybrid power-trains have been spreading in the automotive industry, both in passenger cars, where electric-hybrid vehicles are an established reality, and in heavy duty and off-highway vehicles, where alternative solutions have been proposed to fulfill the high power demand.

The increased complexity of these new architectures, that adds degrees of freedom to the energy management problem, should be suitably controlled with the aim of improving the overall efficiency of the system. The thorough knowledge of the powertrain subsystems allows to draw optimal control strategies to fully exploit the vehicle capabilities.

The optimal control results are tightly linked to the reliability of the mathematical models of the powertrain components, especially under varying environmental conditions or when the system operates close to its working limits.

In the three parts of this work we have proven the effectiveness of the optimization approach to different problems arising in vehicular technology: the energy management problem of a electric-hybrid transmission, the definition of control strategies for a hydraulic series-hybrid powertrain for an off-highway vehicle and finally the design and tuning of low level control algorithms.

8.1 ENERGY MANAGEMENT OF AN ELECTRIC HYBRID VEHICLE

In Part [i](#) we proposed optimal control trajectories to maximize the fuel efficiency of a parallel electric-hybrid passenger car, exploiting the validated model of the aging mechanisms of the lithium-ion battery in order to extend its life.

We first detailed in Chapter [2](#) the physics-based model of the the lithium-ion battery, that describes the voltage dynamics and the internal

state of the electrochemical cell throughout a wide range of temperatures, states-of-charge and current profiles. We proposed a reduced-order approximation of the full-order model, yielding a simpler representation suitable for control and estimation purposes, yet retaining good accuracy, also at varying temperatures. The physics-based electrochemical battery model allows to relate the aging mechanisms of the cell with the internal states of the electrodes; this permits to formulate an aging model partially based on the physics of the electrochemical processes. Thanks to an extensive experimental campaign on the 26 Ah NMC cell used in the new high-performance Ferrari road car *F-173*, we were able to characterize the electrochemical model and the aging model over a wide range of operating conditions with good accuracy. The aging model was able to capture many different mechanisms, spanning from Solid-Electrolyte-Interphase layer growth to faster aging at high temperature and high SOC, from anode overhang effect to the lithium plating during charges at low temperature.

In Chapter 3 we used the battery models developed in Chapter 2, slightly adapted to the different application, as a basis for the formulation of an optimal control problem for the concurrent maximization of fuel savings and battery lifespan in a parallel hybrid vehicle. We found that a promising strategy to reduce the battery deterioration, while maintaining good fuel savings capabilities, is to operate the battery at lower SOC: indeed, diminishing the SOC-weighted current throughput has a dramatic effect on the battery aging, leading to a reduction of the capacity degradation of the battery up to 25% for some driving cycles, leaving fuel consumptions almost unaltered.

We finally showed that the proposed optimal control formulation is promising also for a run-time implementation in a non-linear Model Predictive Control (MPC) framework, given the fast computational time and the good results even with a relative short (5s) prediction horizon.

Future researches should be addressed to the implementation of the optimal control algorithms in a real scenario, in order to experimentally validate the obtained results. Moreover, a relatively simple extension of this work would be to include a thermal model of the battery, in order to draw predictive thermal management strategies.

8.2 MIXED-INTEGER OPTIMAL CONTROL OF A HYDROSTATIC POWERTRAIN

In Part ii, we studied a hydrostatic series-hybrid transmission for a telescopic handler — a vehicle widely used on construction sites or in the

farms — where the energy recovery is obtained by means of high-power hydraulic accumulators.

We start by modeling the multi-physics domains of the hydrostatic hybrid transmission: the equations of motions are used to describe the longitudinal dynamics, the pressure in the hydrostatic transmission is governed by the continuity equation and the hydraulic accumulators are modeled by the intertwined pressure and temperature dynamics of a non-ideal gas that undergoes an adiabatic transformation. A system of four valves connects the hydraulic accumulators to the hydrostatic lines, generating a switched dynamics behavior. The valve configuration is modeled as the integer control, while motors and pump speed and displacement are the continuous control. This model, comprising of both integer and continuous control, is called *mixed-integer* system.

We were able to test the entire vehicle at Dana's testing facility, proving the goodness of our relatively simple model in capturing the main dynamics of the entire system in real operating scenario.

The coexistence of integer and continuous control variables increases the complexity of the optimal control formulation; we approached the *mixed-integer* optimal control problem in Chapter 5 using convexification and relaxation techniques to transform the MI-OCP in a standard continuous optimal control problem that can be solved using common solution techniques, such as the *direct approach* detailed in Chapter 1.

8.3 OPTIMIZATION FOR THE DESIGN OF THE CONTROLLER

In Part [iii](#) we addressed two controller design problem using linear convex optimization algorithms. Formulating the controller design problem as a Linear Matrix Inequality allows to systematically calibrate the parameters of controller to reach a desired control performance.

This is done in Chapter 6 to prevent pressure overshoot of a wet clutch, acting on an electro-actuated valve. The precise control of the engaging pressure of a clutch is of paramount importance to guarantee a smooth torque transmission to the wheels during gear shifting. We proposed a method for the identification of the pressure dynamics and for the automatic calibration of the optimal state-feedback parameters.

In Chapter 7, the LMI approach have been used to select the optimal parameter of a state observer for the estimation of the lateral velocity of a vehicle. The proposed observer guarantees improved noise rejection performance thanks to a deadzone nonlinearity acting on the output injection term. The lower sensitivity to noise of the proposed approach allows for the selection of larger observer gains, that guarantee a faster convergence of the estimation.

DECLARATION

I declare that this thesis was composed by myself, that the work contained herein is my own except where explicitly stated otherwise in the text, and that this work has not been submitted for any other degree or professional qualification except as specified.

Trento, October 2019



Luca De Pascali